Structural Evolution of Silica Aerogel under a Microwave Field

By

Carlos Eduardo Folgar

Dissertation submitted to the faculty of the Virginia Polytechnic Institute and State University in partial fulfillment of the requirements for the degree of

Doctor of Philosophy

in

Materials Science and Engineering

David E. Clark, Chair
Carlos Suchicital
Dwight Viehland
Gary R. Pickrell

May 10, 2010
Blacksburg, Virginia

Keywords: Silica Aerogel, Microwave Processing of Materials, Single Mode Microwave System, Sol-Gel Processing, Temperature Measurements

Structural Evolution of Silica Aerogel under a Microwave Field

Carlos Eduardo Folgar

ABSTRACT

Structure evolution of silica aerogel was studied in microwave- and conventionally processed samples over the temperature range from 25 to 1200°C. The samples were produced using sol-gel processing and dried under carbon dioxide supercritical conditions. After drying, the monolithic samples received a thermal treatment at different programmed temperatures in two different ovens, conventional and microwave. The microwave process was performed using a single mode microwave oven at 2.45GHz. Dielectric properties were measured using the cavity perturbation method, and structural characterization was carried out using a variety of techniques, including absorption surface analysis, Helium pycnometry, Archimedes principle, Fourier transform infrared spectroscopy, X-ray diffraction, and high resolution microscopy. The data obtained revealed that structural differences do exist between microwave- and conventionally processed samples.

Three different regions were identified from the structural characterization of the samples. Regions I exhibited a structure densification at temperatures between 25 and 850°C. Region II was characterized by a bulk densification in the temperature range from 850 to 1200°C. Region III was represented by the onset of crystallization above 1200°C. Explanation and possible causes behind the structural differences observed in each region are provided. In general, the structure evolution observed in microwave- and conventionally processed samples followed the same order, but occurred at lower temperature for the microwave process.

Dedication

I dedicate this dissertation to the inspiration of my life, my parents (Alicia and Francisco Folgar), my wife (Mitzi) and my two boys (Carlos and Rodrigo).

Acknowledgements

I would like to express my sincere gratitude to my advisor Dr. David Clark for his valuable guidance and advice. His concerns about the quality of this work and my academic goals encouraged me to do my best. I am thankful to Dr. Carlos Suchicital whose generosity and suggestions toward my academic goals and personal life are highly appreciated. I am grateful to Diane Folz for all her invaluable assistance.

I would like to thank the members of my advisory committee for their contributions to my development as a materials science and engineering student. I took classes with Dr. Dwight Viehland and Dr. Gary Pickrell; their excitement when they were teaching inspired my work in materials science.

Thanks to all the present and former members in Dr. Clark's research group. Thanks to Patricia Mellodge for her assistance with the software for the single mode microwave oven. Special thanks to Raghu Thridandapani and Morsi Mahmoud for many scientific discussions, but even more, for their friendship.

I would like to give a special recognition to different people who provided invaluable technical assistance throughout this work. Thanks to Dr. Donald Hutcheon from Microwave Properties North for guidance in the development of the microwave dielectric measurement equipment. Thanks to Mr. John Gerling from Gerling Applied Engineering for many technical discussions about microwave generation and transmission. Thanks to Dr. John West for introducing me to the field of sol-gel processing. Thanks to Mr. Peter Winter from Heitronics for invaluable discussions about infrared temperature measurements, and thanks to Dr. James Thomas who donated the main components of the single mode microwave oven to our lab.

I want to thank my loving parents, brothers, and sisters for their support throughout my life. Thanks to my brother and my sister, Francisco and Zonia. Their continuous support throughout my graduate student life encouraged me to reach my academic goals. I would like to thank my wife Mitzi and my sons, Carlos and Rodrigo, for their endless love that has always lighted my life.

Finally, thanks…God, I am here because You want me to be here.

Table of Content

List of Figures

List of Tables

List of Equations

List of Symbols

This list presents the symbols used in this study and does not include SI unit abbreviations, atomic symbols, acronyms, or standard mathematical symbols.

σ_e	Electronic conduction
σ_i	Ionic conduction
ε^*	Complex permittivity
ε'	Relative dielectric constant
ε''	Relative dielectric loss
ε_o	Permittivity of free space
ε''_{eff}	Effective dielectric loss factor
μ_o	Permeability of free space
μ''_{eff}	Effective magnetic loss factor
ρ_B	Bulk density of the material
σ	Stefan–Boltzmann constant
ε_m	Emissivity of the material
ε_R	Emissivity radius at two different wavelengths
$\%P$	Percent total porosity
$\%Pc$	Percent closed pores
$\%Po$	Percent open pores
$\frac{P}{Po}$	Relative pressure
$\Delta\sigma$	Difference in horizontal stresses
μ_c	Permeability of the cavity
μ_s	Permeability of the sample
a	Radius of the unit cell cylinder
a	Dimension of the waveguide or cavity on the *x* axis

A	Constant for the distribution of the electric field in the empty cavity
A_{CS}	Cross-sectional area of the adsorbate
Att	Value of the attenuation produced to measure the actual power
b	Dimension of the waveguide or cavity on the y axis
C	Capacitance
c	Speed of light
Cp	Specific heat at constant pressure
cps	Cycles per second
d	Diameter of the pore
d	Spacing between atomic planes
$\boldsymbol{E}$	Electric field
e	Eccentricity of the ellipsoid of rotation
e'	Dielectric constant
e''	Dielectric loss
E_c	Electric field in the empty cavity
e''_{eff}	Effective dielectric loss
e_m	Emittance
Em	Maximum electric field on the sample
E_o	Maximum electric field of the sinusoidal voltage signal
E_{rms}	Root mean square of the electric field
Es	Electric field on the susceptor
E_s	Electric field in the sample
Ex, Ey, Ez	Component of the electric field along its respective axis
f_c	Cut-off frequency
f_c	Resonant frequency of the empty cavity
F_m	Calibration constant to use a cylindrical sample
f_o	Operating frequency
f_s	Resonant frequency of the sample
F_{SH}	Shape factor of the static electric field
Fw	Area that represents the field of view of the pyrometer
G_{ac}	Polarization conductance

G_{dc}	Ohmic conductance
$\boldsymbol{H}$	Magnetic field
h	Plank's constant
H_c	Magnetic field in the empty cavity
H_{rms}	Root mean square of the magnetic field
H_s	Magnetic field in the sample
Hx, Hy, Hz	Component of the magnetic field along its respective axis
Hz	Hertz
i	Imaginary operator
I_C	Charging current
I_L	Total loss current
I_O	Loss current from ohmic conduction
I_P	Loss current from polarization
I_T	Total current
K	Slope of the densification rate
K	Boltzmann constant
k"	Dielectric loss
$K(t\text{-}to)$	Rate at which the cylinders densify by viscous flow
k*	Complex dielectric constant
k'	Dielectric constant
K_c	Constant to adjust the distribution of the electric field at the location of the sample inside the cavity
l	Propagation mode on the z axis
L_c	Length of the cavity
m	Propagation mode along the x axis
M_d	Distance from the pyrometer sensor to the sample
n	Propagation mode along the y axis
N	Avogadro's number
n_C	Number of moles in the cell chamber
n_E	Number of moles in the expansion chamber
P	Pressure

P_a	Atomic polarization
P_a	Atmospheric pressure
P_{av}	Power absorbed inside the material
P_C	Capillary pressure
Pc	Supercritical pressure
P_d	Dipolar polarization
P_e	Electronic polarization
P_H	Helium gas pressure
P_i	Interfacial polarization
P_m	Power measured
P_{out}	Actual power at the measured point
P_R	Power reflected by the cavity
P_T	Total power supplied to the cavity
Pv	Specific volume of the pores
P_W	Power loss on the walls of the cavity
$\mathbf{P}_y$	Poynting vector
q	Stored charge
Q	Heat generated
Q	Activation energy
Q_c	Quality factor of the empty cavity
Q_s	Quality factor of the sample
r	Pore radius
r_H	Hydraulic radius
SA	Specific surface area
S_t	Total surface area of the sample
t	Time
T	Temperature
T_a	Ambient temperature
tanδ	Dissipation factor
Tc	Supercritical temperature
T_C	Critical temperature

T_c	Temperature calculated to use in a multi-wavelength pyrometer
T_P	Predetermined temperature
T_t	True temperature of a material obtained using a multi-wavelength pyrometer
V	Voltage
V	Volume of the material
V_A	Apparent volume
V_B	Bulk volume
V_C	Volume of the cell chamber
V_{cp}	Volume of the closed pores
V_E	Volume of the expansion chamber
V_{op}	Volume of the open pores
V_s	Seebeck voltage
V_S	Volume of the sample
V_s	Volume of the solid material not including pores
V_T	Total volume of the sample, including the pores
W	Weight of the gas absorbed at a relative pressure
W_{BB}	Thermal radiation emitted by a black body
W_D	Weight of the sample
W_{GB}	Thermal radiation emitted by a gray body
W_m	Weight of the adsorbate monolayer that covers the surface
W_{NB}	Thermal radiation emitted by a non-black body
W_{NG}	Thermal radiation emitted by a non-gray body
Ws	Weight of the sample with open pores filled with the liquid
Wss	Weight of the saturated sample when it is submerged in the liquid
W_λ	Energy radiated
β	Propagation constant
γ	Specific surface energy of the vapor-liquid interface
δ	Loss angle
ε_c	Dielectric constant of the cavity
$\varepsilon_{m(\lambda)}$	Emissivity function

ε_s	Dielectric constant of the sample
η	Viscosity
θ	Contac angle
θ	Half of the angle between the incident and diffracted X-rays
λ_c	Wavelength of the cut-off frequency
λ_g	Guide wavelength of a cavity or waveguide
λ_i	One of the wavelengths used by the multi-wavelength pyrometer
λ_o	Microwave wavelength
ρ_A	Apparent density
ρ_{TR}	True density
χ_e	Complex electric susceptibility
χ_m	Complex magnetic susceptibility
ω	Angular frequency
ω_c^*	Resonant complex angular frequency of the cavity
ω_s	Resonant angular frequency of the sample

CHAPTER I

Introduction

It is well-known that processing materials using microwave energy sometimes produces unusual effects. For example, variation in processing time and temperature when compared to conventional processing. A common objective in the microwave community has been to provide a scientific explanation for these observations. This investigation shows the existence of these differences when processing gels and provides an explanation for these results, specifically through a study on silica aerogel.

This chapter presents a brief introduction to sol-gel processing, microwave energy, and conventional and microwave heating. An overview of the subsequent chapters in this dissertation is also provided.

1.1 Sol-gel processing

Investigators in the early 19^{th} century observed that the hydrolysis of tetraethyl orthosilicate (TEOS, $Si(OC_2H_5)_4$) under acid conditions produced silica (SiO_2) in the form of a "glass-like material" [1]. During the 1930s, Geffcken demonstrated that alkoxides could be used in the preparation of oxide films [2]. Around the same time, Kistler [3] invented a process to dry silica gel under supercritical conditions. Later, in the 1960s, intensive work from the ceramic science and industry communities confirmed that a wide variety of shapes and homogeneous ceramic powders could be produced using sol-gel processing. During the 1970s, a major advancement in sol-gel processing techniques was generated when Yoldas [4] and Yamane et al

[5] demonstrated that monolithic ceramics could be produced by careful drying of gels; this development would later become one of the driving forces for significant research in sol-gel science.

This study describes the steps of the sol-gel process that yield monolithic SiO_2 dried under supercritical conditions. The emphasis is on silica aerogel and on the structure transformation upon further heat treatment (after drying).

Silica aerogel is a highly porous material that has one of the lowest thermal conductivities, lightest weights, and lowest dielectric constants [6] of any man-made material. Because of these characteristics, aerogel has great potential for use in many fields of technology, including electronic, optical, and energy storage. Properties of this material are directly influenced by its structure which can be affected by several factors, including chemical composition, physical parameters, and the thermal process used for its preparation [7]. Chapter II provides more detailed information about the process used to make this material, its main properties, and structural characteristics.

1.1.1 Advantages in sol-gel processing

Some of the reasons for the particular value and interest in sol-gel processing of materials include [8, 9]:

1. Temperatures required for the synthesis stages are low, frequently close to room temperature.
2. Highly porous materials can be prepared using this method.

3. Control of the pore size and surface area can be achieved by chemical modification of the precursors.
4. Since liquid precursors are used, it is possible to cast ceramic materials in complex shapes without the need for machining or melting.
5. Better homogeneity of the final product can be obtained due to the mixing of the liquid precursors at the molecular level.
6. High purity of starting materials and reduced risk of contamination resulting from diffusion of species from the container at high temperatures can lead to higher purity of the final product.

1.1.2. Limitations of sol-gel processing

Even though sol-gel processing presents many advantages, there are some limitations that one has to take into account, such as [10]:

1. Precursors are often expensive and sensitive to moisture.
2. The process is time-consuming, particularly when careful drying is required.
3. If monolithic samples are required, cracking during drying presents significant challenges.

If these limitations can be overcome, sol-gel derived materials may provide advantages in applications where the required properties cannot be achieved using other processes.

1.2 Microwave energy

Microwaves are defined as a portion of the electromagnetic spectrum that lies between 300MHz and 300GHz with wavelengths between 1m and 1mm, respectively. Figure 1.1 shows the microwave range with some of the major applications existing at various frequencies. It also shows some of the frequencies used for microwave processing of materials. During World War II, microwave applications emerged in the area of communication (radar and radio). Since then, this technology has been used for many different applications. Essentially, the areas where microwaves have been used include: 1) communication and information transfer, 2) processing/manufacturing, 3) diagnostics/analysis, 4) medical treatment, and 5) weapons [11].

While communication had always been a strong area of microwave applications, in the 1950s, processing/manufacturing became one of the leading areas due to the appearance of industrial and home microwave ovens. By the 1960s, most of the investigations performed in materials processing were related to drying applications and were being conducted primarily in modified home microwave ovens. Home microwave ovens operate at 2.45GHz because at that frequency, water, a major ingredient in food, is a good microwave absorber. During the 1970s, while drying alumina, Sutton [12] observed that microwaves not only removed the water, but also heated the ceramic. It is important to point out that, during those experiments, the oven operated at 2.45GHz, but not all ceramic materials absorb microwaves at that frequency. In subsequent years, industry and academia have worked at trying to explain the effects of microwave processing, knowing that the word “processing” involves not only the application of radiation, but also transmission, detection, control, and generation [13]. A typical system design for microwave processing of materials is shown in Fig. 1.2.

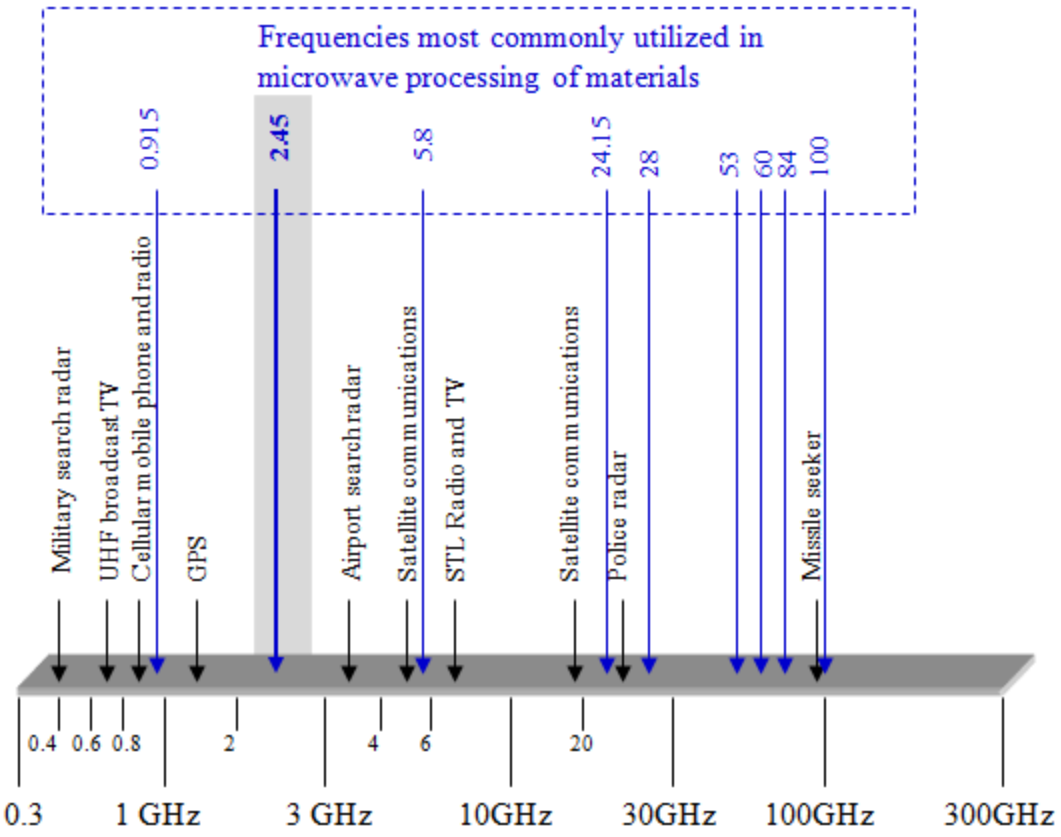

Fig. 1.1: The microwave spectrum. The 2.45GHz frequency is the most commonly used in microwave ovens and used in this study.

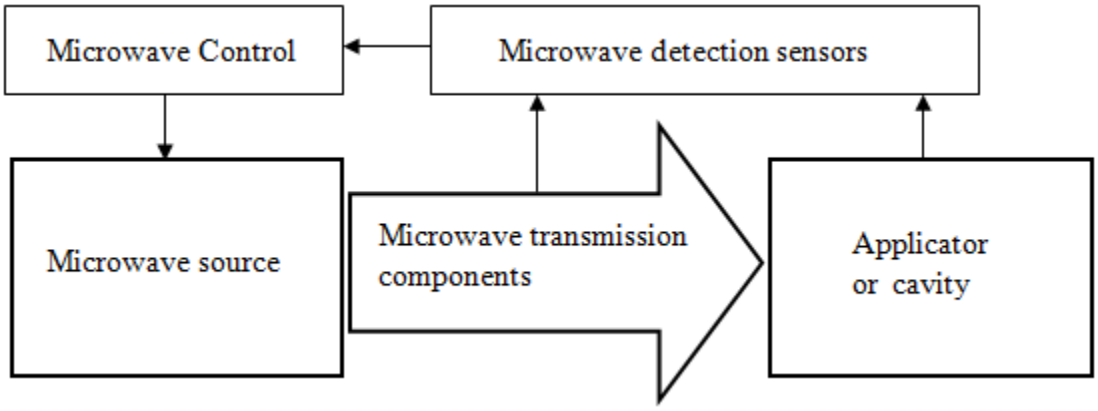

Fig. 1.2: Organization of a typical system for microwave processing of materials.

Microwave generators include magnetrons, klystrons, traveling wave tubes, backward wave oscillators, and cross field amplifiers [14, 15]. This section provides an operative

description of the magnetron (Fig. 1.3), as it is the microwave source for the equipment used in this study (also used in the home microwave oven).

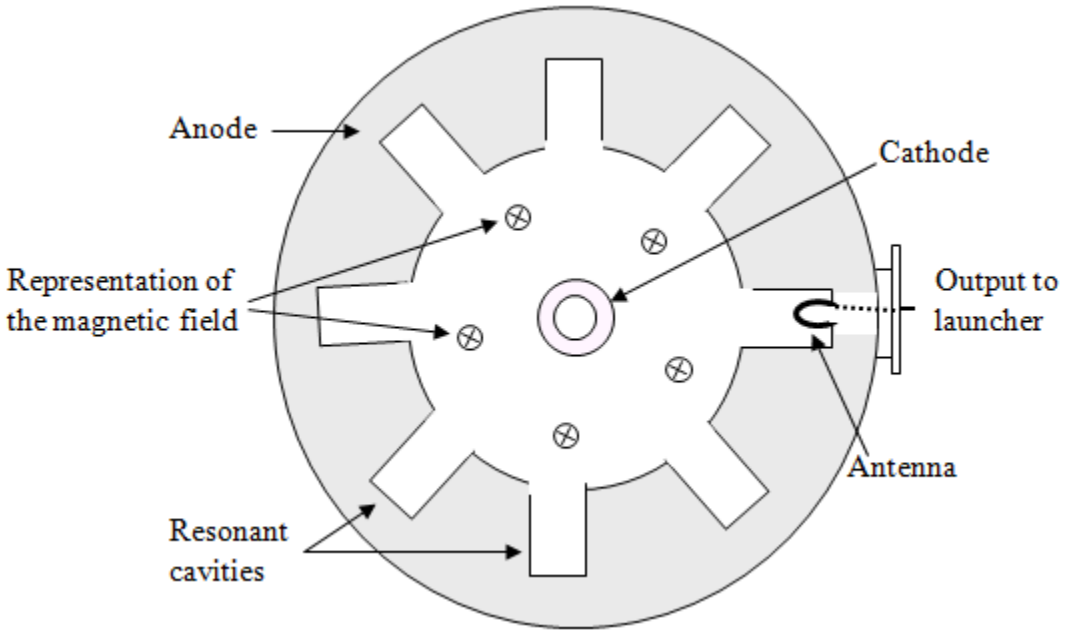

Fig. 1.3: Schematic of the internal circuit of the magnetron.

The magnetron is a high-vacuum electronic valve consisting of a magnetic field perpendicular to the electric field between the cathode and the anode [16]. The magnetic field is supplied by permanent magnets or electromagnets. The electric field is provided by an external high-voltage transformer which maintains the anode at a higher voltage relative to the cathode. Under this large difference in electric potential, electrons are emitted from the cathode to the anode. Due to the magnetic field being perpendicular to the electrons' path, a force is introduced on the electrons, causing them to travel in a quasi-circular path around the cathode. This rotational behavior depends on the strength of the electric and magnetic fields, and on the distance between the cathode and the anode. The anode has a set of resonant cavities where the electrons are induced to enter. The continuous change in polarity of the electric field produces a

rotation of the electron cloud in the cavities of the anode. Microwave power is then generated in the cavities (at their resonant frequency) by the oscillation of the electrons. This microwave power is extracted by an antenna located in one of the cavities and then is transmitted to a launcher waveguide. During this process, substantial heat dissipation takes place at the anode due to the electrons that reach it with high velocity, and their kinetic energy is converted to heat. The main efficiency loss in the magnetron is due to the heat which must be removed by air or liquid to prevent over heating.

1.3 Conventional and microwave heating

There are fundamental differences between microwave and conventional heating. In conventional heating, energy is transferred to the material by one or a combination of the following mechanisms: convection, conduction, and/or radiation of heat from the material surface to its interior. The main mechanisms by which this heat is conducted through the entire body are electron, phonon, or photon conductivity. In contrast, microwave heating is the product of energy delivered directly to the material. This heating is the conversion of electromagnetic energy to thermal energy due to the material's molecular interaction with the electromagnetic field. Therefore, microwave heating is initially an energy conversion rather than a heat transfer [17]. Thus, because of the difference in the way energy is deposited in the material, heat can be generated internally throughout the volume of the body [18, 19].

Using conventional methods, heat transfer in ceramics and polymers is a slow process, since generally they have low thermal conductivities. Rapid heating rates usually induce large thermal gradients that can produce thermal stresses or structural inhomogeneities. In the case of

microwave heating, the potential for reducing processing times exists due primarily to the volumetric nature of heat transfer. Also, molecular interaction with the electromagnetic field can cause selective heating of one component of a sample. When different materials are in contact, microwaves will selectively couple with the material with highest dielectric loss, or different frequencies can be used to couple selectively with each of the materials. The characteristic of selective heating can be advantageous in many applications, such as joining of ceramics, or driving chemical reactions by selective heating of reactants [20].

Even though there are cases where microwave heating offers advantages over conventional methods, the different mechanisms of energy using microwaves have generated new processing challenges. For example, non-uniform application of the electromagnetic field in the material can result in non-uniform heating. Also, as a material is processed, it may undergo chemical and/or physical changes that may influence its microwave absorption, and difficulties can arise in processing, modeling, or control. Therefore, it is critical to understand the role played by each of the components particular to microwave processing (Fig. 1.2), as well as microwave interaction with materials.

1.4 Goal, objectives, and motivation

According to the literature, it is well-known that the structure of the dried silica-gel changes significantly when it is heated in a conventional oven/furnace [10, 21]. This structure evolution depends on the chemical and physical parameters involved in the gel's composition and the thermal process used for its preparation. Generally, a dried silica gel consists of an amorphous silica matrix containing a distribution of pore sizes. Several stages of structure

evolution are observed when silica gel is heated in a conventional oven, which are explained in Chapter II, Section 2.3.

For several years, microwave energy has been used to densify and crystallize materials [22]. In many of those cases, a different structure than the one obtained with a conventional oven has been observed [23]. In addition, a substantial reduction of time has been reported when compacts of amorphous silica particles were sintered [24], and different pore size distribution has been obtained when porous silica gel (xerogel) was dried using microwaves [25].

The **main goal** of this research is to determine if there are differences in structure evolution between the conventional and microwave process and if so, show what they are and explain the reasons why they occurred in silica aerogel.

In order to reach this goal, five **objectives** are proposed

1. Develop a method for the reliable and consistent production of silica aerogel (Section 4.1.2).
2. Design and build a single mode microwave system appropriate for processing silica aerogel (Section 4.2).
3. Develop a reliable method for temperature measurements in a single mode microwave oven (Section 4.4.2).
4. Design and construct an apparatus for measuring the dielectric properties as a function of temperature at 2.45GHz (Section 4.5).
5. Develop a suitable methodology for characterizing the structure of aerogels (Section 4.6).

The main **motivation** for this work is to better understand the structure evolution in silica aerogel under the influence of a microwave field, so this knowledge can be used by future researchers to control aerogel's properties through process design.

1.5 Dissertation overview

This dissertation combines two advanced techniques, sol-gel processing and microwave processing of materials. The focus is on the effects produced by microwave processing techniques on silica aerogel. Explanations of both techniques and important information about the equipment used are provided.

Chapters II and III provide literature reviews on sol-gel processing and microwave processing of materials. Specifically, Chapter II focuses on the technique used to make silica aerogel and an explanation of the fundamental steps in sol-gel processing. Chapter III is divided into an explanation of the two critical aspects of microwave processing of materials: microwave materials interactions and microwave equipment engineering. Chapter IV details the experimental procedures performed in sol-gel and microwave processing operations. Also, detailed information about the equipment used is provided. Criteria used for designing and building the microwave processing equipment and dielectric characterization apparatus are described. The results of this investigation are presented in Chapter V. Chapter VI presents a discussion of the results observed, and conclusions drawn from this study are provided in Chapter VII. Chapter VIII presents future work in different areas related to this study. In addition, supporting information and calculations are presented in the appendices.

References

1. Hench, L.L. and J.K. West, *The sol-gel process.* Chem. Rev., 1990. **90**: p. 33-72.
2. Klein, L.C., Editor. *Sol gel technology for thin film, fibers, preforms, electronics and specialty shapes*. 1988. Noyes Publications.
3. Kistler, S.S., *Coherent expanded aerogels.* Journal of Physical Chemistry, 1932. **36**: p. 52-64.
4. Yoldas, B.E., *Preparation of glasses and ceramics from metal-organic compounds.* Journal of Materials Science, 1977. **12**(6): p. 1203-1208.
5. Jamane, M., S. Aso, and T. Sakaino, *Preparation of a gel from a metal alkoxide and its properties as a precursor of oxide glass.* Journal of Material Science, 1978. **13**(4): p. 865-870.
6. Fricke J. and Tillotson T., *Aerogels: production, characterization, and applications.* Thin Solid Films, 1997. **297**: p. 212-223.
7. Elias, A.E., *Pore size effects on the thermal stability of sol-gel derived silica monoliths, M.S. Thesis in Material Science and Engineering*. 1989. University of Florida: Gainesville, Florida. p. 172.
8. Casu, M., M. Casula, A. Corrias, and G. Paschina, *Textural characterization of high temperature silica aerogels.* Journal of Non-Crystalline Solids, 2003. **315**: p. 97-106.
9. Wang, S.-H., *Sol-gel derived silica optics, Ph.D. Dissertation in Materials Science and Engineering*. 1988. University of Florida: Gainesville, Florida.
10. Fricke, J., Editor. *Aerogels*. Springer Proceeding in Physics. Vol. 6. 1986. Springer-Verlan: Berlin, Germany.
11. Clark, D., D. Folz, C. Folgar, and M. Mahmoud, Editors. *Microwave Solutions for Ceramic Engineers*. 2005. The American Ceramic Society: Westerville, Ohio.
12. Sutton, W.H., *Microwave firing of high alumina ceramics.* Material Research Society Proccedings, 1988. **124**: p. 376-386.
13. Reader, H.C., *Understanding microwave heating systems: a perspective on state-of-the-art*, in *8th International Conference on Microwave and High-Frequency Heating*, M. Willert-Porada, Editor. 2001. Springer: Germany. p. 3-14.
14. Metaxas, A.C. and R.J. Meredith, *Industrial Microwave Heating*. 1983. London, United Kingdom: Peter Peregrinus Ltd.
15. Scott, A.W., *Understanding Microwaves*. 1993. New York, New York: John Wiley & Sons, Inc.
16. Chan, C.T. and H.C. Reader, *Understanding Microwave Heating Cavities*. 2000. Boston, Massachusetts: Artech House, Inc.
17. Roussy, G. and J.A. Pearce, *Foundations and Industrial Applications of Microwaves and Radio Frequency Fields*. 1995. West Sussex, England: John Wiley & Sons Ltd.
18. Sutton, W.H., *Microwave Processing of Ceramic Materials.* Ceramic Bulletin, 1989. **68**(2): p. 376-386.
19. Thostenson, E.T. and T.W. Chou, *Microwave processing: fundamentals and applications.* Composites: Part A: Applied Science and Manufacturing, 1999. **30**: p. 1055-1071.
20. Schiffman, R.F. *Commercializing microwave systems: paths to succes or failure*. in *Microwaves: Theory and Application in Materials Processing III*. 1995. Cincinnati, Ohio: The American Ceramic Society.

21. Brinker, C.J. and G.W. Scherer, *Sol-Gel Science*. 1990. New York, New York: Academic Press.
22. Bouajaj, A., M. Ferrari, and M. Montagna, *Crystallization of Silica Xerogels: A Study by Raman and Fluorescence Spectroscopy.* Journal of Sol-Gel Science and Technology, 1997. **8**: p. 391-395.
23. Hirao, K., M.I. Jones, M.E. Brito, and M. Toriyama, *Microwave Sintering of Silicon Nitride Ceramics*, in *Advances in Microwave and Radio Frequency Processing*, M. Willert-Porada, Editor. 2001. Springer: Bayreuth, Germany. p. 533 - 540.
24. Zhong, J.P., et al, *Microwave Densification of Porous Silica Gel*, in *Microwaves: Theory and Application in Materials Processing II*, C. David, W. Tinga, and J. Joseph Laia, Editors. 1993. The American Ceramic Society: Westerville, Ohio.
25. Folgar, C., D. Folz, C. Suchicital, and D. Clark. *Drying Silica-Gel Using Microwaves*. in *Microwaves and Radio Frequency Applications*. 2004. Austin, Texas: The Microwave Working Group, Ltd.

CHAPTER II

Silica Gel

2.1 Sol-gel processing

Sol-gel processing is a method that involves the conversion of a sol into a gel that eventually becomes a solid porous material. A wet gel is a three-dimensional solid network enclosing a continuous liquid phase and is formed from sols interconnected together with pores of submicrometer dimensions [1]. A sol is a suspension of colloidal particles in a liquid, and colloidal particles are solid particles with diameters from 1-100nm [2].

In general, there are two main approaches used to make monolithic silica [3, 4]. One starts with a colloidal solution, and the other is initiated with the hydrolysis and polycondensation of alkoxide precursors. The first approach uses colloidal powders to make silica gel by growing a network composed of an array of discrete colloidal particles. This approach is a physical gel because there is no formation of the colloidal particles; they are already contained in one of the precursors.

In the present study, the second approach is used. Here, the silica gel is produced by the formation of an interconnected three-dimensional network that is the result of the simultaneous hydrolysis and polycondensation of a metal alkoxide precursor. This methodology will be described in more detail in subsequent sections of this chapter.

2.2 Processing stages in silica gel production

During processing, there are several stages that determine the type of gel produced. They depend on the mode of preparation, precursors (starting materials), and conditions under which sol-gel processing is performed. A general sequence of the stages involved in the production of silica gel is shown in Fig. 2.1. This sequence is divided into three parts according to the processing conditions under which silica gel has been produced for this study. Part I involves the stages that were performed at room temperature. Part II includes the drying process performed under supercritical conditions in an autoclave. Part III consists of the heat treatment applied to silica gel samples at ambient pressure and at different pre-determined temperatures in a conventional furnace or a microwave oven. The structure evolution in Part III is the focus of this dissertation. The different stages of the process as highlighted by Fig. 2.1 are detailed in the following sections.

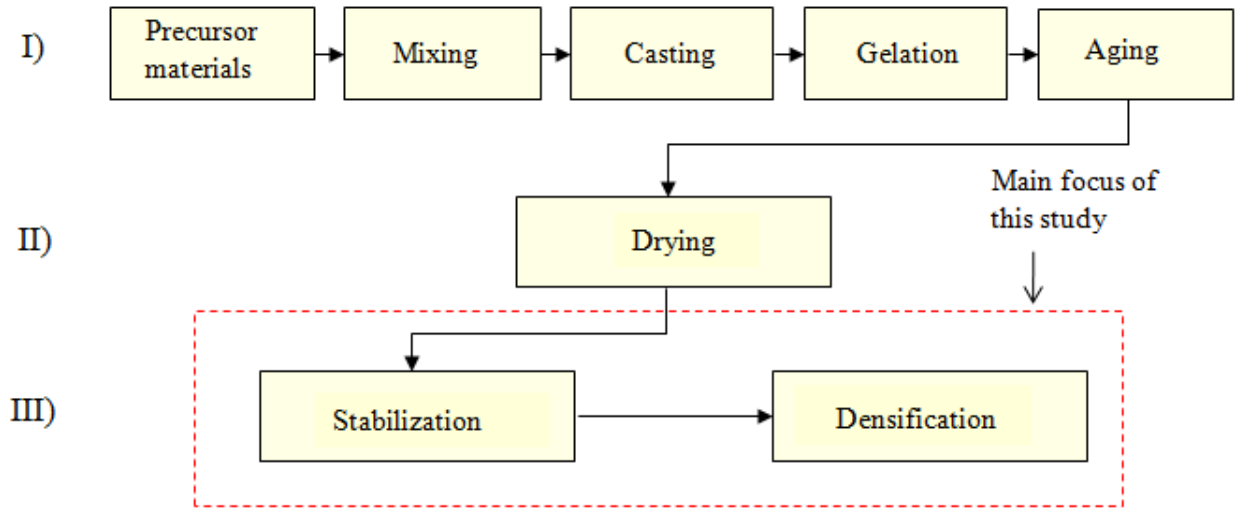

Fig. 2.1: General stages involved in the production of silica gel.

2.2.1 Precursor materials

The precursors most extensively used in sol-gel processing to make silica gel are metal alkoxides, which are metal-organic compounds. These compounds have an organic bond attached to a metal or metalloid atom. The most frequently used organic compounds to make silica gel are silicon alkoxides, such as tetraethyl orthosilicate (TEOS, $Si(OC_2H_5)_4$) and tetramethyl orthosilicate (TMOS, $Si(OCH_3)_4$).

2.2.2 Mixing

Mixing of the precursor materials is produced when a liquid alkoxide is hydrolyzed with water; it is further stirred to obtain a homogeneous solution. The reaction following mixing is known as *hydrolysis* and is illustrated in Eq. 2.1 using TMOS, the alkoxide used in this research.

$$TMOS + 4(H_2O) \rightarrow Si(OH)_4 + 4(CH_3OH) \qquad (2.1a)$$

Eq. 2.1a also can be represented as follows:

$$H_3CO{-}\underset{\displaystyle OCH_3}{\overset{\displaystyle OCH_3}{\underset{|}{\overset{|}{Si}}}}{-}OCH_3 + 4(H_2O) \rightarrow HO{-}\underset{\displaystyle OH}{\overset{\displaystyle OH}{\underset{|}{\overset{|}{Si}}}}{-}OH + 4(CH_3OH) \qquad (2.1b)$$

or $$\equiv Si{-}OCH_3 + 4(H_2O) \rightarrow \equiv Si{-}OH + 4(CH_3OH) \qquad (2.1c)$$

The silicon hydroxyl groups (Si─OH) interact with each other to produce siloxane bonds (≡O─Si─O≡), plus water as a by-product. This interaction is known as *condensation* (Eq. 2.2).

$$HO{\equiv}Si{-}OH + HO{\equiv}Si{-}OH \rightarrow HO{\equiv}Si{-}O{-}Si{\equiv}OH + H_2O \qquad (2.2)$$

Condensation continues, forming a three-dimensional network through a reaction known as *polymerization* (Eq. 2.3). The polymerization reaction then continues, even during subsequent stages of the process.

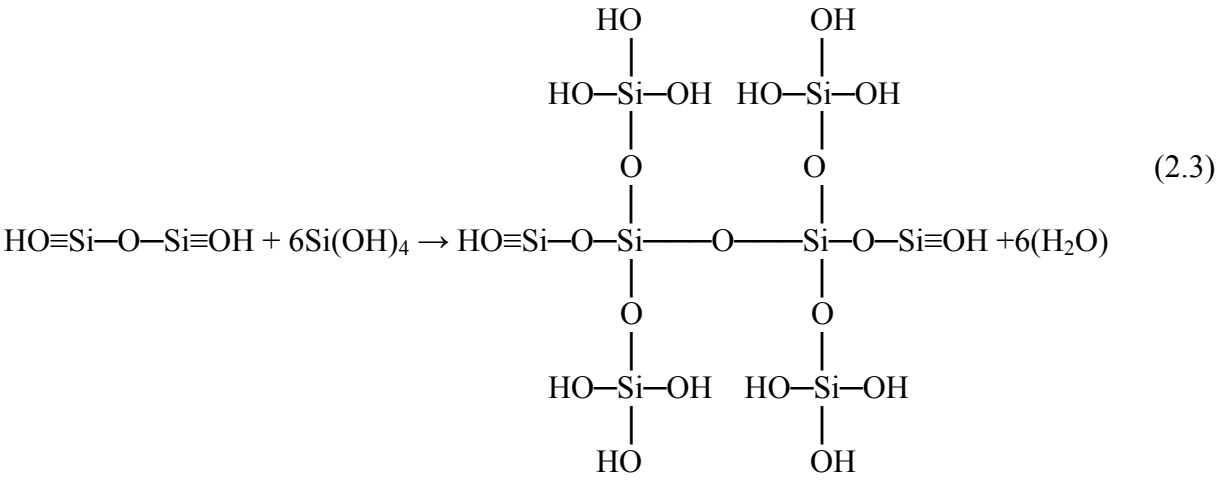

(2.3)

2.2.3 Casting

After becoming partially polymerized, the solution is cast. Casting consists of pouring the solution into a container (mold) before its viscosity becomes too high. The container should meet several requirements [5]:

1. Shape: Determines the shape of the final piece.
2. Surface quality: Influences the final quality of the product's surface, as well as the ability to remove the sample from the container.
3. Cleanliness: Prevents any contamination in the final product.
4. Composition: Eliminates any reaction between the sol and the container.

2.2.4 Gelation

Condensation and *polymerization* lead to the formation of particles in the sol that subsequently form clusters. These clusters link together, forming a three-dimensional network that extends across the mold in which it is contained. While the three-dimensional network is growing, its viscosity increases, converting the network into a gelled material that can support stress elastically. This process is known as gelation, and the time it takes is defined as the gelation time (t_{gel}) [6]. Many researchers have demonstrated that t_{gel} depends on several factors, such as pH of the solution, R ratio (moles of water / moles of silicon alkoxide), types of catalyst, solvent, and temperature [3, 7]. Any variation of these processing parameters will influence the kinetics of the hydrolysis and condensation reactions; consequently, they also will affect the viscosity and time for gelation to occur.

2.2.5 Aging

After the gel is cast and has become a solid, it is maintained in the mold or placed in another container with a solvent. Polycondensation then continues and syneresis occurs in the solid wet sample. Syneresis is the shrinkage of the gelled sample as liquid is released from the pores [6-8]. This contraction may be due to any of three mechanisms:

1. The effects of increased bridging bonds from the condensation reactions.
2. Dissolution and reprecipitation of the silica primary particulates onto the walls of the network.
3. Attachment of unreacted oligomers from the gelation process or addition of new monomers after the gelation stage.

As a result, during aging, the thickness of the walls between the pores grows, porosity decreases, and strength and stiffness of the sample increase. Therefore, it is advisable to age monolithic gels to minimize, as much as possible, cracking of the material during subsequent stages of the production process.

2.2.6 Drying

During drying, extensive amounts of solvent and by-products from the condensation reactions are removed from the solid wet sample. This stage is characterized by additional shrinkage of the gel structure that is usually proportional to the amount of liquid evaporated [9]. As the liquid in the pores (pore liquid) evaporates, a concave liquid/vapor meniscus is formed inside the pores (Fig. 2.2a) producing capillary pressures, as described by the Laplace's equation (Eq. 2.4).

$$P_C = 2\gamma(\cos\theta)/r \tag{2.4}$$

Where, P_C = capillary pressure

γ = specific surface energy of the vapor-liquid interface

θ = contact angle

r = pore radius

This capillary pressure puts the liquid into tension (L, Fig. 2.2b) [10, 11]. To maintain Pore I in equilibrium, it is required to have horizontal and vertical forces with the same magnitude, but opposite direction than those horizontal and vertical components of the liquid tension (L_x and Ly). The weight of the liquid (W_L) equilibrates with Ly, and Lx is equilibrated with the Sx force produced by the solid phase. The total stress in Pore I (σ_1) on a face normal to

the *x* direction is the sum of the horizontal force components (L_x and S_x) divided by the area of the face for both the liquid and the solid phases. Equilibrium also must be maintained between different pores (Pore I, Pore II, Fig. 2.2a), but because there are variations in pore size, differences in capillary pressure are induced that produce differences in stresses ($\Delta\sigma = \sigma_2 - \sigma_1 \neq 0$). Since capillary pressure depends on the size of the pore, the smaller the pore, the higher the P_C as is manifested in Eq. 2.4. When the pores are small (< 20nm), the differences in capillary pressures can produce large $\Delta\sigma$ that can fracture the monolithic gel [12], as is illustrated in Fig. 2.2a. Fracturing during the drying process is a major problem in the formation of monolithic gels [6, 13]. Typical capillary pressures that can occur in a 10nm pore are between 4 and 14MPa, based in Eq. 2.4 ($\gamma \cos\theta$ between 20 to 70 ergs/cm^2 [7]).

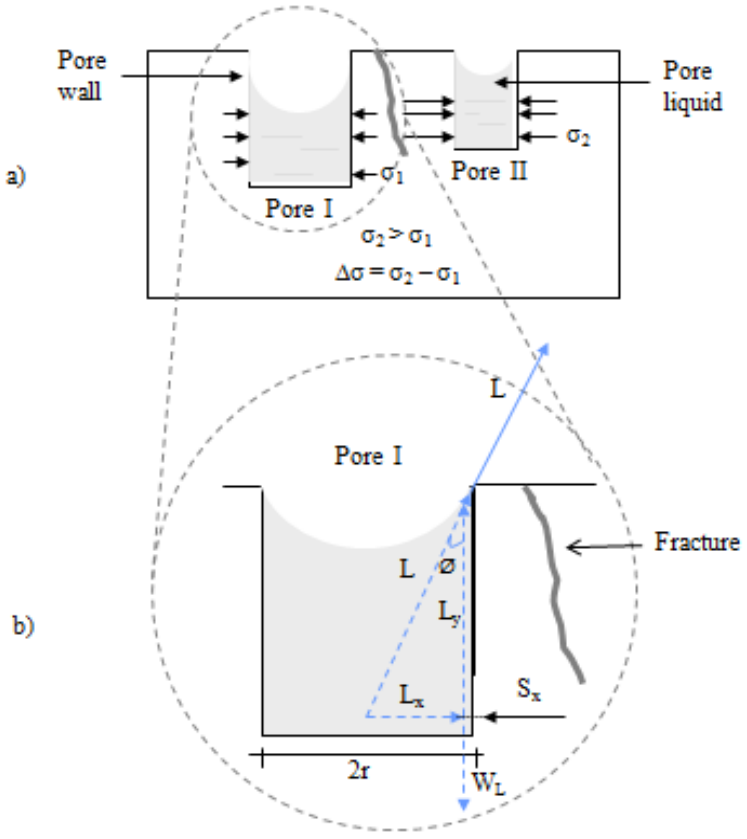

Fig. 2.2: Stresses in a monolithic silica gel body: a) evaluation of forces in Pore I; b) horizontal stresses in different pore size.

Fracture of the gel can be avoided by controlling different factors, such as

1. Synthesizing the gel with a larger pore size, lower surface area, or larger angle of contact.
2. Increasing the strength and stiffness of the material during aging.
3. Removing the liquid under supercritical conditions.

The silica gel obtained by drying under supercritical conditions is known as aerogel. This material and the technique to produce it were used in this study; further details will be mentioned in subsequent paragraphs.

In the supercritical drying technique, the wet solid sample is subjected to a thermal/pressure process in an autoclave (critical point drier). During this process, the liquid inside the pores is removed when it is above its critical temperature (Tc) and critical pressure (Pc) because it is converted into a supercritical fluid. This conversion avoids the development of the meniscus inside the pores; consequently, capillary forces are eliminated [14, 15]. The next step in this process is to convert the super fluid into gas that then is taken to ambient conditions and removed from the autoclave. At this point, a dried silica gel known as an aerogel is obtained. Using this technique, the gel texture is only slightly modified and almost preserves its original dimensions.

The critical point drying technique can use two different processes: one requires high temperature and high pressure because the solvent used is passed to its critical point; the other process requires low temperature and high pressure. In this work, the latter is used and requires that the solvent be replaced by liquid carbon dioxide (CO_2), which is removed under critical conditions as the process continues. Table 2.1 lists values of Tc and Pc for some of the most common liquids used. Figure 2.3 illustrates this process in a CO_2 phase diagram, and the arrows inside the diagram show the procedure followed by the thermal/pressure process. Black dots

represent the beginning and the end of the cycle during which the autoclave does not have CO_2. Green dots illustrate the trajectory followed by the CO_2 inside the autoclave. Chapter V, section 5.2 explains in more detail the procedure performed using this technique during the drying process.

Table 2.1: Critical temperature and pressure of common liquids used in the critical point drying technique [7, 16].

Liquid substance	**Formula**	**Tc (°C)**	**Pc (atm)**
Carbon dioxide	CO_2	31.1	73
Methanol	CH_3OH	240.0	78
Ethanol	C_2H_5OH	243.0	63
Water	H_2O	374.0	22

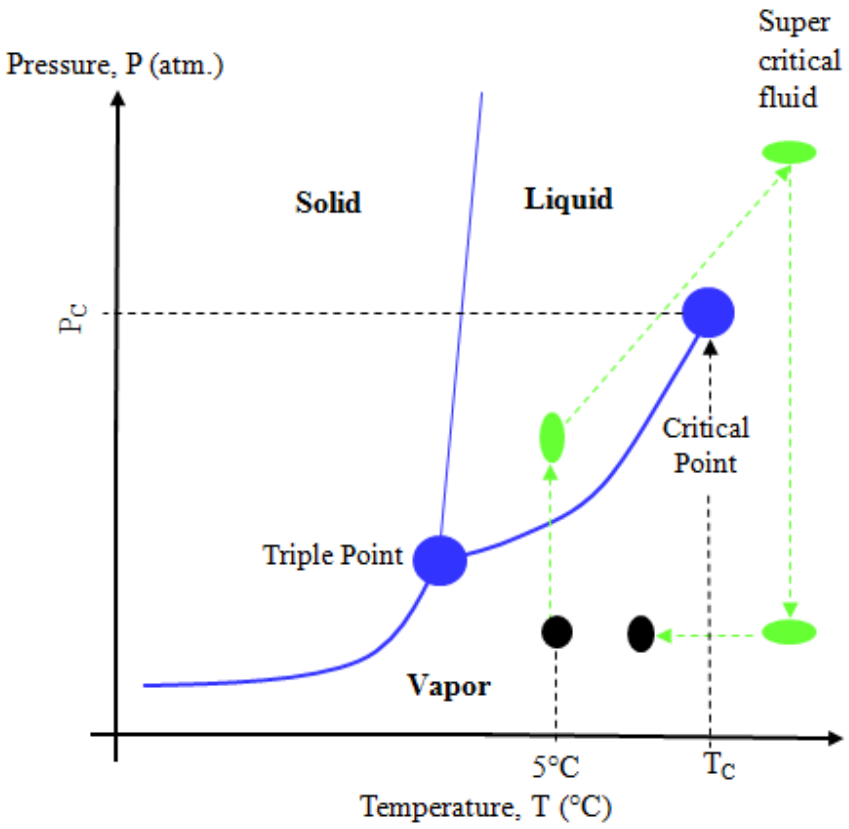

Fig. 2.3: Procedure to dry silica gel in an autoclave overimposed on the CO_2 phase diagram.

2.2.7 Stabilization

After drying, silica gel still has a large number of silanol groups (Si ─ OH) on the surface [6, 7]. Such high OH content can reduce the transparency of the material or produce structural changes in an ambient environment. The objective of stabilization is to remove these groups from the pore surface, which can be achieved through a thermal or chemical treatment.

Thermal stabilization involves removing the hydroxide groups (i.e., chemical water) through a thermal treatment in the range of 500-800°C. As the temperature increases, condensation reactions progress (Eq. 2.2), and OH groups are gradually lost. This treatment prepares the material to be used at a given temperature without reversible structural changes because it reduces the surface area and the contact angle and consequently, the sensitivity to

rehydration stresses. However, sometimes even though a large amount of OH is removed, sintering due to subsequent heating starts before stabilization is complete [17, 18]. Sintering contributes to pore closure in the gel, but chemical water may get trapped and lead to bloating or foaming of the gel in the final stages of sintering. In these cases, chemical stabilization is employed to eliminate additional surface silanol groups.

During chemical stabilization, different chloride or fluoride compounds are often utilized to react with the hydroxyl groups, forming a product that can be desorbed at temperatures from 400-800°C. For example, chloride (Cl_2) can react with the silicon hydroxide groups to form hydrochloric acid (HCl), which then is desorbed at temperatures higher than 700ºC [7]. Complete elimination of the OH groups increases the formation of Si ─ O ─ Si bonds, which improves the transparency of the material and is especially important for applications in optical devices.

2.2.8 Densification

After the silica gel is dried, a porous amorphous solid material with some by-products is obtained. Subsequent heating of the silica gel will produce stabilization of the material and reduce or eliminate some pores, resulting in a partially or fully densified gel.

There are different parameters that influence the temperature at which densification occurs, including pore size, surface area, and composition of the material. Researchers have reported that densification sometimes starts as low as 200°C or as high as 1000ºC [19, 20]. In those cases where silica gel has been acid-catalyzed, the material has a high concentration of chemical water, which reduces the viscosity and favors the beginning of densification at low temperatures. In most cases, the surface area decreases when the temperature increases [21].

However, it has been shown that some silica gels display an increase in surface area at temperatures in the range of 200-400°C, followed by a decrease in the same parameter as the temperature increases. This behavior has been attributed to desorption of water or inorganic materials [22]. It is difficult to predict when densification will occur because of all the different factors mentioned, but physical properties can be measured, and the changes in densification can be quantified.

According to Brinker and Scherer [7, 23], there are four primary mechanisms responsible for densification:

1. Capillary contraction as a result of the increase in energy when silanol groups are removed.
2. Condensation – polymerization reactions which produce siloxane groups and involve loss of water and inorganic materials.
3. Structural relaxation which is due to the diffusive motion of atoms.
4. Viscous flow which is associated with the mass flow produced by the decrease in surface energy.

To describe the silica gel densification (e.g. sintering), a model that represents a convenient geometry of the gel structure was adopted. The model was consistent with measured values of surface area, pore size, and density. In this study, a cubic array of cylinders model based on the Frenkel approach [7, 24] is used and the method is described in Chapter VI, Section 6.4.1.

2.3 Structure evolution of silica aerogel in a conventional heating system

It is known that the structure of silica gel changes significantly throughout all its production stages. This structural evolution depends on the chemical and physical parameters

attributed to its composition, and the thermal process used for its preparation. This section provides an overview of the structural changes in silica aerogel (obtained after it has been dried) during heat treatment in a conventional oven/furnace between ambient temperature and 1200°C.

Aerogel is produced using the critical point drying technique that reduces the capillary pressure and allows the production of large monolithic samples. To study the structure changes after aerogel is dried, it is important to know its conditions in the dried state. Dried aerogels have very low density, high porosity, very low thermal conductivity, and very low dielectric constant. Typical values are shown in Table 2.2.

Table 2.2: Typical values of properties in dried silica aerogels.

Parameter	Value
Bulk density	0.1 – 0.4 g/cm^3 [22, 25]
Percent of total porosity	80 – 95 % [26]
Surface area	800 – 1600 m^2/g [21]
Thermal conductivity	4 - 11 mW/m-K [27]
Dielectric constant	1.0 – 2.0 [28]

When an aerogel is heated in a conventional oven/furnace, several stages of evolution are observed. Over the temperature range under study, the following discussion provides a description of the stages observed.

Generally, a dried silica gel consists of an amorphous silica matrix containing a distribution of pore sizes. A comparison between different dried silica gels that have been acid-catalyzed using TMOS as the metal alkoxide is shown in Fig. 2.4 [29]. This figure shows the pore size distribution ($Dv_{(d)}$) of two types of silica gels (xerogel and aerogel) dried using three different methods. A xerogel is produced when the wet solid material is dried by evaporation of the liquid at atmospheric pressure and is then heated.

In Figure 2.4, the method used to dry one of the xerogels was a conventional oven; the other two xerogels were dried using microwaves at different frequencies, and the aerogel was dried using a critical point drier (autoclave). This figure shows that xerogels have a narrow distribution of pore size, while aerogels have a wider distribution of pores and larger pore sizes. These differences are characteristics existing in each of these types of silica gels at the moment that they are dried. The pore distribution shown for aerogels in Fig. 2.4 is representative of the dried gel used in this study.

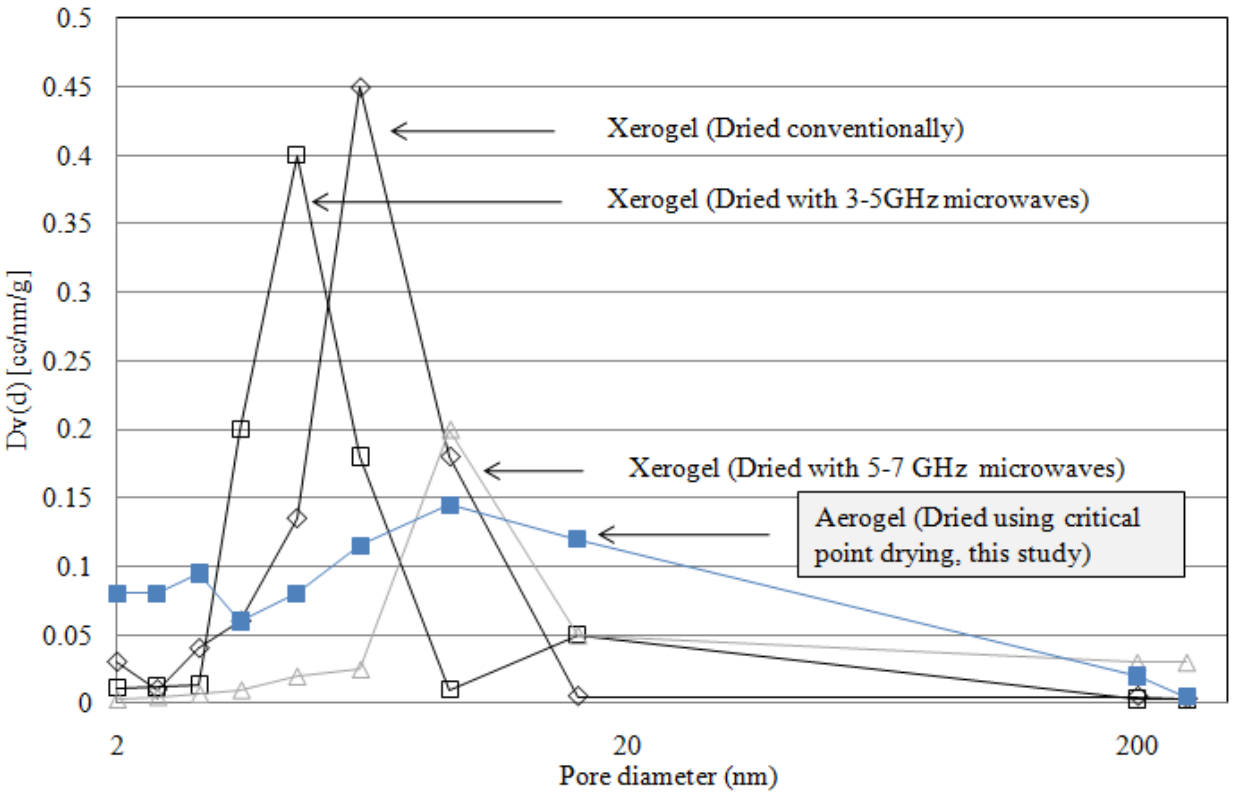

Fig. 2.4: Pore size distribution analysis of two types of silica gel (xerogel and aerogel) obtained by using nitrogen adsorption/desorption techniques. Author's own work [29] reprinted with kind permission of The Microwave Working Group, Ltd. (permission granted appendix F1).

In addition, the silica gel dried using microwave energy exhibited different distributions of pore size (Fig. 2.4). The microwave oven used to process the silica gel in Fig. 2.4 was a multimode cavity with variable frequency. The researchers demonstrated that when xerogel was dried using microwaves, a change in microwave frequencies produced a difference pore size distribution.

Drying and stabilization also are characterized by little if any reduction in pore volume and surface area. This observation was confirmed by Casu et al [21] who presented a study on aerogels (A1 SiO_2 and A2 SiO_2) and xerogel ($XSiO_2$) using TEOS as a precursor, in which little variation in surface area was observed for aerogel at temperatures lower than 700°C (Fig. 2.5).

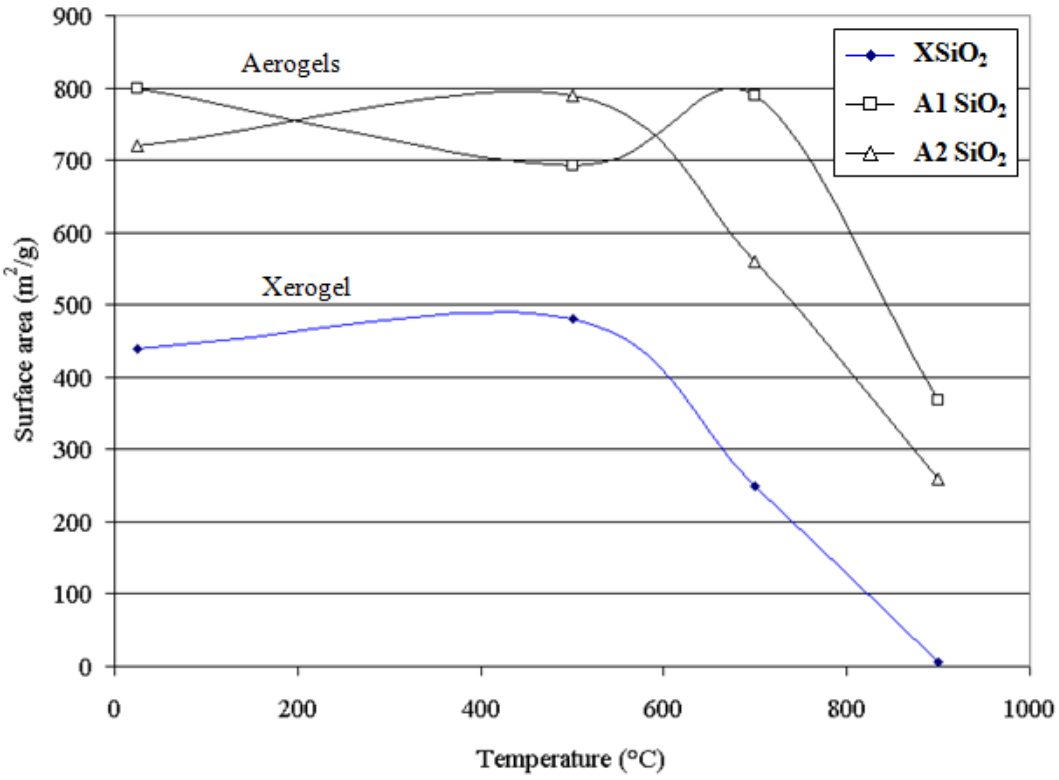

Fig. 2.5: Surface area changes in TEOS silica gels over the temperature range from 25 to 900ºC. $XSiO_2$ is the xerogel, and A1 SiO_2 and A2 SiO_2 are the aerogels. Based on data from Casu et al [21].

During dehydration and partial densification, there is a substantial decrease in pore volume due to the reduction of large pores, and a narrow distribution of pore sizes (700 – 1000°C). Moreover, shrinkage without weight losses has been reported, which has been associated with structural relaxation and continuous polycondensation reactions[30]. This behavior is also illustrated in Fig. 2.5 when aerogels (A1 SiO_2 and A2 SiO_2) present a substantial reduction in surface area in the range of 700 – 900°C.

In conventional processing, densification is complete usually between 1000 and 1200°C. During this stage, silica aerogel shows a rapid shrinkage as a result of viscous flow, allowing the pores in the gel to collapse. For example, Fig. 2.6 shows the variation of surface area (S), pore volume (Vp), and density (ρ) of an aerogel derived from TMOS and base-catalyzed. A substantial reduction in S and Vp can be seen at temperatures close to 1150ºC. In addition, aerogel reaches a density similar to fused silica (2.2 g/cm^3). At this temperature, the porosity is almost negligible; however, if chemical stabilization is not performed before densification (some products do not require it), bloating may be observed.

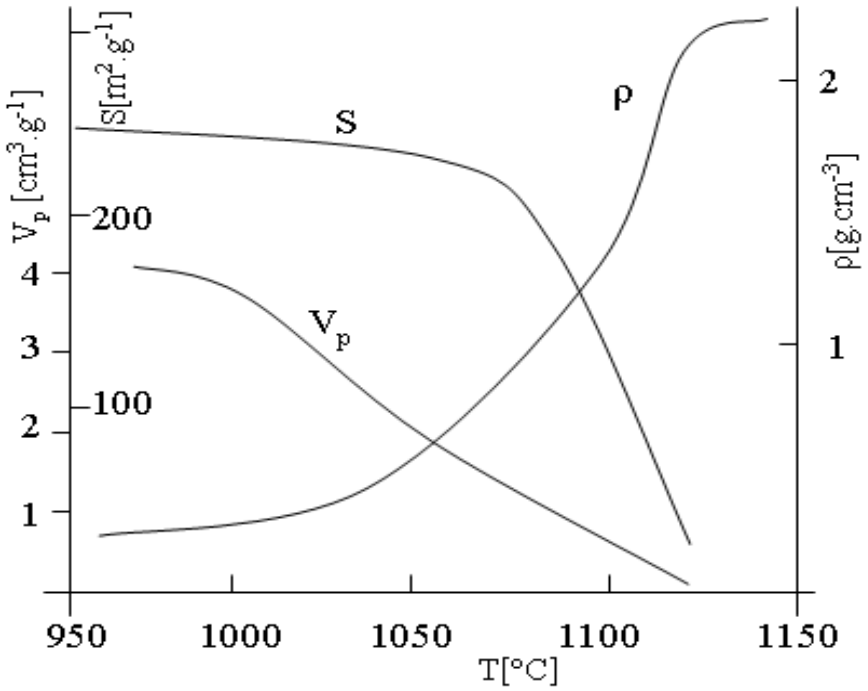

Fig. 2.6: Variation of surface area (S), volume of pores (Vp), and density (ρ) during sintering in a TMOS-derived aerogel. From [31]. With kind permission of Springer Science + Business Media (permission granted appendix F2).

Subsequent stages may include nucleation, crystallization and growth, which could occur at temperatures between 1200 and 1500ºC. Values of the different parameters shown in this section describe a typical behavior, but they may change according to the chemical and physical parameters of the aerogel composition and thermal treatment used after it is dried.

References

1. Zarzycki, J., M. Prassas, and J. Phalippou, *Synthesis of glasses from gels: the problem of monolithic gels.* Journal of Materials Science, 1982. **17**: p. 3371-3379.
2. Davis, J.T. and E.K. Rideal, *In Interfacial Phenomena*, in *Academic Press*. 1963.
3. Hench, L.L. and J.K. West, *The sol-gel process.* Chem. Rev., 1990. **90**: p. 33-72.
4. Bengisu, M., *Engineering Ceramics*. 2001. New York, New York: Springer.

5. Vasconcelos, W.L., *Topological Evolution and Properties of Sol-Gel Silica Monoliths*, *Ph.D. Dissertation in Materials Science and Engineering*. 1989. University of Florida: Gainesville, Florida.

6. Hench, L.L., *Sol-Gel Silica*. Materials Science and Process Technology Series, Bunshad Rointan F., McGuire Gary E., and Rossnagel Stephen M., Editors. 1998. Westwood: Noyes Publications.
7. Brinker, C.J. and G.W. Scherer, *Sol-Gel Science*. 1990. New York, New York: Academic Press.
8. Latorre, G.P. and J.K. West, *Chemical Processing of Advanced Materials*, Hench L.L. and West J. K., Editors. 1992. New York, New York: Wiley. 891.
9. Smith, D.M., G.W. Scherer, and J.M. Anderson, *Shrinkage during drying of silica gel.* Journal of Non-Crystalline Solids, 1995. **188**: p. 191-206.
10. Scherer, G.W. and D.M. Smith, *Cavitation during drying of a gel.* Journal of Non-Crystalline Solids, 1995. **189**: p. 197-211.
11. Scherer, G.W., *Effect of drying on properties of silica gel.* Journal of Non-Crystalline Solids, 1997. **215**: p. 155-168.
12. Siouffi, A.M., *Silica gel-based monoliths prepared by the sol-gel method: facts and figures.* Journal of Chromatography A, 2003. **1000**: p. 808-818.
13. Klein, L.C., Editor. *Sol gel technology for thin film, fibers, preforms, electronics and specialty shapes*. 1988. Noyes Publications.
14. Dieudonne, P., A.H. Alaoui, P. Delord, and J. Phalippou, *Transformation of nanostructure of silica gels during drying.* Journal of Non-Crystalline Solids, 2000. **262**: p. 155-161.
15. Alie, C., et al, *Textural properties of low-density xerogels.* Journal of Non-Crystalline Solids, 2000. **270**: p. 77-90.
16. Fricke, J., Editor. *Aerogels*. Springer Proceeding in Physics. Vol. 6. 1986. Springer-Verlan: Berlin, Germany.
17. Wright, J.D. and N.A. Sommerdijk, *Sol-Gel Materials Chemistry and Applications*. 2001. London, Great Britain: Taylor & Francis.
18. Hench, L.L., J.K. West, B.F. Zhu, and R. Ochoa. *Gel-silica hybrid optics*. in *SPIE-The International Society for Optical Engineering*. 1990. San Diego, California: SPIE.
19. Mulder, C.A.M., J.G.V. Lierop, and G. Frens, *Densification of SiO2-xerogels to glass by Ostwald ripening.* Journal of Non-Crystalline Solids, 1986. **82**: p. 92-96.
20. Hegde, N.D. and V. Rao, *Effect of processing temperature on gelation and physical properties of low density TEOS based silica aerogels.* Journal of Sol-Gel Science and Technology, 2006. **38**: p. 55-61.
21. Casu, M., M. Casula, A. Corrias, and G. Paschina, *Textural characterization of high temperature silica aerogels.* Journal of Non-Crystalline Solids, 2003. **315**: p. 97-106.
22. Orgaz-Orgaz, F., *Gel to Glass Conversion:Densification Kinetics and Controlling Mechanisms* Journal of Non-Crystalline Solids, 1988. **100**: p. 115-141.
23. Brinker, C.J. and G.W. Scherer, *Sol - Gel - Glass: I. Gelation and Gel Structure.* Journal of Non-Crystalline Solids, 1985. **70**: p. 301-322.
24. Kuczynski, G.C., *Study of the sintering of glass.* Journal of Applied Physics, 1949. **20**: p. 1160-1163.

25. Lemay, J.D., T.M. Tillotson, L.W. Hrusbesh, and R.W. Pekala, *Microstructural dependence of aerogel mechanical properties*, in *Better Ceramics Through Chemistry IV*, Brian Zelinski, Jeffrey Brinker, David Clark, and Donald Ulrich, Editors. 1990. Materials Research Society: San Francisco, California. p. 321-324.
26. Hrubesh, L.W., T.M. Tillotson, and J.F. Poco, *Characterization of ultralow-density silica aerogels made from a condensed silica precursor*, in *Better Ceramics through chemistry IV*, Brian Zelinski, Jeffrey Brinker, David Clark, and Donald Ulrich, Editors. 1990. Materials Research Society: San Francisco, California. p. 315-320.
27. Caps, R. and J. Fricke, *Radiactive Heat Transfer in Silica Aergel*, in *Aerogels*, J. Fricke, Editor. 1985. Springer-Verlag: Berlin, Germany. p. 110-115.
28. Hrubesh, L.W., L.E. Keene, and V.R. Latorre, *Dielectric properties of aerogels.* Material Research Society, 1993. **8**: p. 1736 - 1741.
29. Folgar, C., D. Folz, C. Suchicital, and D. Clark. *Drying Silica-Gel Using Microwaves*. in *Microwaves and Radio Frequency Applications*. 2004. Austin, Texas: The Microwave Working Group, Ltd.
30. Yoldas, B.E., *Preparation of glasses and ceramics from metal-organic compounds.* Journal of Materials Science, 1977. **12**(6): p. 1203-1208.
31. Zarzycki, J. and T.Woignier, *Aerogels: Precursors or End Materials?*, in *Aerogels*, J. Fricke, Editor. 1985. Springer-Verlag: Berling, Germany. p. 42-48.

CHAPTER III

Microwave Processing of Materials

3.1 Microwave interactions with materials

Microwaves have frequencies in the electromagnetic spectrum between 300MHz and 300GHz. One of the most common characteristics of microwave heating is that the heat in a material is generated from inside out instead of from the surface to the inside, as in conventional heating. In most cases, such internal heating results in rapid and uniform heating.

Based on their degree of interaction with microwaves, materials are classified generally in four categories: transparent, opaque, absorbing, and partially absorbing [1], as shown in Fig. 3.1. Transparent materials do not absorb any significant amount of energy when microwaves pass through them. Opaque materials reflect microwaves (good examples are conductors, such as metals). Absorbing materials allow for the penetration and absorption of microwaves, and partial absorbers are a combination of two or more of the categories mentioned.

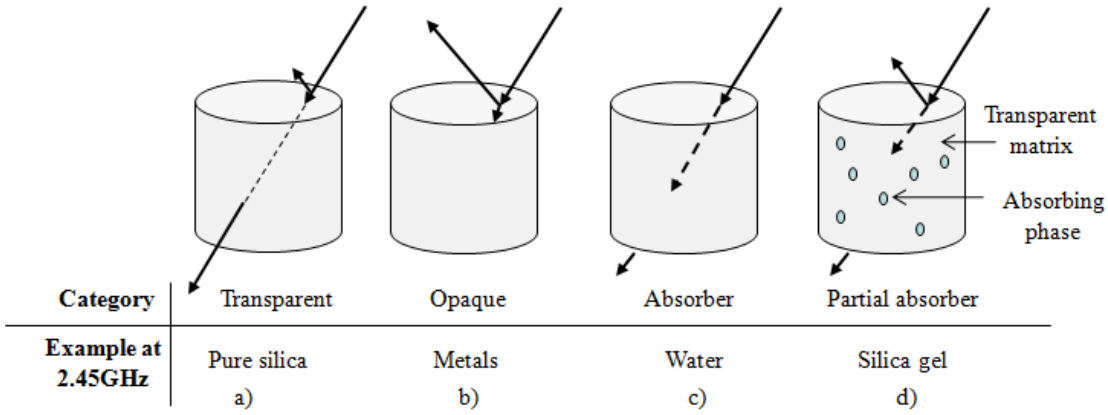

Fig. 3.1: Material classification based on microwave interaction: a) transparent, b) opaque, c) absorber, d) partial absorber. Silica gel is composed of a transparent matrix and absorbing phase and is thus a partial absorber.

When microwaves are absorbed by a material, the electric field (***E***) in the affected volume induces translation and rotation of charged particles (e.g. electrons, ions or dipoles). The resistance to these motions due to inertial, elastic, and frictional forces causes losses and attenuation of the electromagnetic field, resulting in internal heating [2, 3].

3.2 Dielectric materials

The two primary mechanisms that produce losses when microwaves interact with materials are long-range and short-range motion of charged particles [4]. Long-range motion of the charge is known as conduction, which involves the motion of the electrons or ions that are the charge carriers when an ***E*** is applied. In metals and semiconductors, the electrical charge is transported by the electrons and is known as electronic conduction (σ_e). The losses in σ_e are generated due to resistance losses. For ionic materials, the charge displacement is carried out by the ions and is known as ionic conduction (σ_i). These losses in σ_i occur when the electrically charged particles move and collide with other particle species in the material. These conduction losses are observed in the low frequency range. When the frequency increases, the time for the charged particle displacement decreases; consequently, the charged particles cannot be transported in the direction of the field.

Short-range motion of the charge is known as polarization and is the result of the interaction of ***E*** with a dielectric material. In this case, the charge transportation is through oscillation, orientation, or rotation of electric dipoles. There are different types of polarizations that produce losses when the dipoles present resistance to the movement under an alternating field. These losses are mainly exhibited at high frequencies [5].

3.3 Types of polarization

There are four types of polarization in ceramic materials, and they are the result of the displacement of the charged particles from their equilibrium position, forming dipoles which try to follow the direction of the electric field (Fig. 3.2).

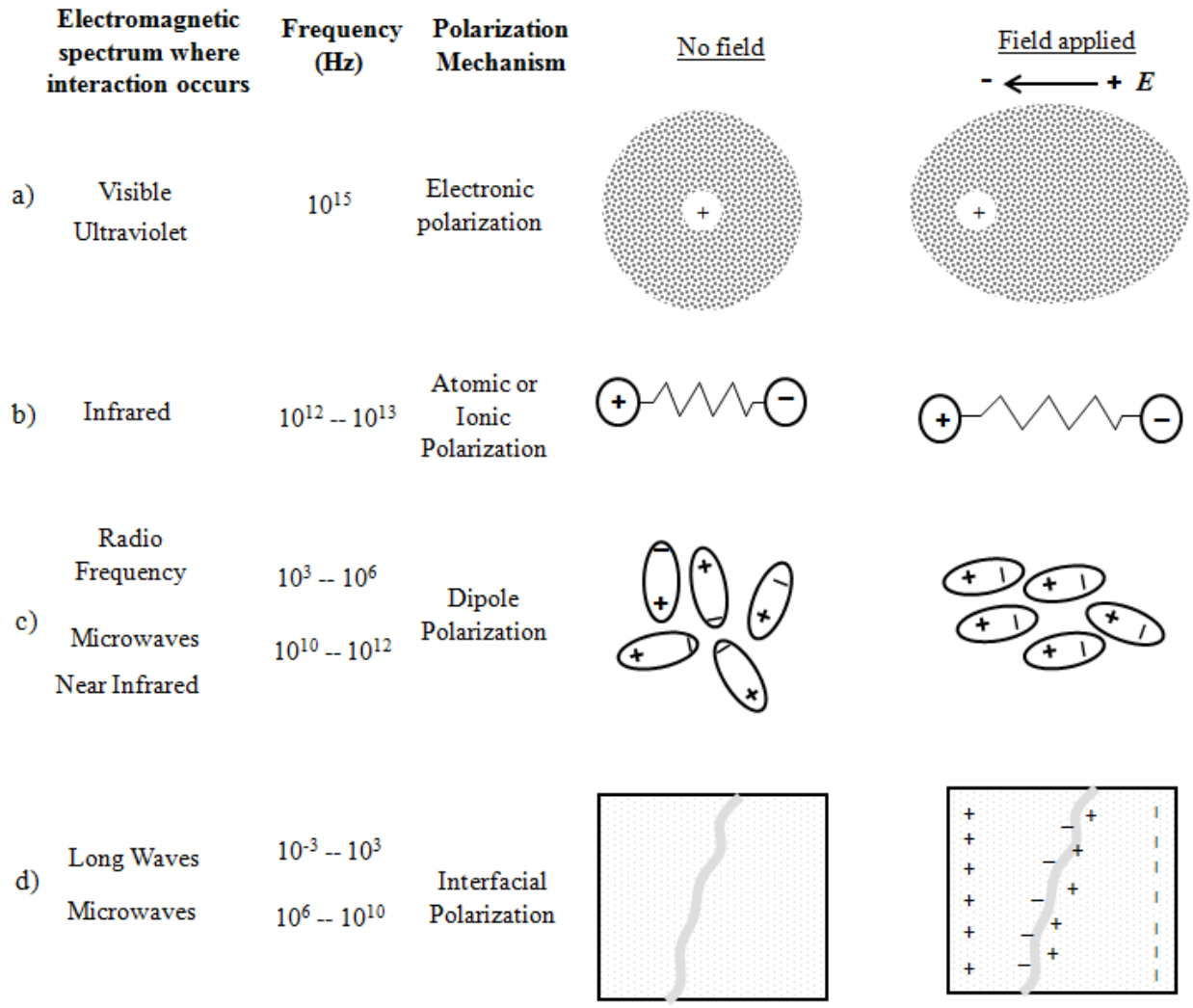

Fig. 3.2: Polarization types with and without an electric field applied: a) electronic, b) atomic, c) dipole, and d) interfacial space charge polarization.

Each type of polarization is described in more detail below:

1. Electronic polarization is the effect of the electrons' displacement in the atoms relative to the positive atom nucleus in an electrical field (Fig. 3.2a). This process takes around 10^{-15} sec and corresponds approximately to the frequency of ultraviolet light.
2. Atomic or ionic polarization is the result of the movement of the ions relative to one another inside the molecule, as shown in Fig. 3.2b. This process requires from 10^{-12} to 10^{-13} sec and corresponds to the frequency of infrared radiation. A similar polarization in ionic crystals arises with the displacements of oppositely charged ions requiring 10^{-12} sec, which corresponds to the far infrared frequency. Ionic polarization gives rise to resonance absorption at a narrow frequency range, characteristic of the bond strength between the ions.
3. Dipolar polarization is the perturbation of the thermal motion of ionic or molecular dipoles, producing a net dipolar orientation in the direction of an applied field (Fig. 3.2c). Because of this behavior, this polarization is also known as orientation polarization and is probably one of the most important in the microwave range. There are two primary mechanisms that take effect in orientation polarization. The first is the rotation of the permanent dipoles against the elastic restoring forces to the equilibrium position. This process also is referred to as deformation polarization and takes $10^{-10} – 10^{-12}$ sec at room temperature. This mechanism is not common in ceramic materials, but is important for a diversity of liquids, gasses, and polar solids. The second mechanism is the rotation of dipoles between two equilibrium positions. It involves a spontaneous alignment of the dipoles in one of the equilibrium positions when an electrical field is applied. As the

frequency of the electric field increases, the dipoles cannot follow the direction of the field. This type of polarization requires times between 10^{-9}-- 10^{-12} sec and 10^{-3} – 10^{-6} sec.

4. Interfacial polarization results from the accumulation of charges at the interfaces between phases that have differences in dielectric constant and conductivity. The interfaces between phases, impurities, or second phases act as physical barriers that reduce charge displacement (Fig. 3.2d). This polarization is observed over two ranges of frequencies. One range is between 10^{-3} and 10^{3} Hz and is due to an accumulation of charge (localized polarization) on the barriers. The other range is between 10^{6} and 10^{10} Hz and occurs when one of the phases is highly conductive and dominates the total loss in the dielectric [6].

The important mechanisms resulting in microwave heating for most ceramics are dipole and interfacial polarizations because they are active in the microwave frequency range [6, 7]. The electromagnetic spectrum, including the frequency range where each polarization mechanism occurs, is shown in Fig. 3.2.

3.4 Dielectric constant and dielectric loss

The stored charge (q) in a dielectric can be expressed as a function of the applied voltage (V) and the capacitance (C):

$$q = V/C \quad \text{(Coulombs)} \tag{3.1}$$

The charging current can be expressed as

$$I_C = dq/dt \quad \text{(Ampere)} \tag{3.2}$$

where, t = time

Combining 3.1 and 3.2, one can obtain

$$I_C = C\,(dV/dt) \tag{3.3}$$

In the case of a sinusoidal voltage, $V = V_o\exp[i(\omega t)]$, the I_C becomes

$$I_C = i\omega C V_o \exp[i(\omega t)] \tag{3.4}$$

$$\omega = 2\pi f_o \tag{3.5}$$

where, ω = angular frequency (Radians)

$i = (-1)^{1/2}$

f_o = operating frequency (Hz = cps = sec^{-1})

In an ideal dielectric, the total current would be the I_C current and would lead the voltage by 90°. In a real dielectric, there are loss currents arising from ohmic conduction and polarization (discussed previously) that can be expressed as [4]

$$I_O = G_{dc}\,V \tag{3.6}$$

$$I_P = G_{ac}\,V \tag{3.7}$$

where G_{dc} and G_{ac} are the dc and ac conductance in units of ohm^{-1}, and the loss current (I_L) is equal to the summation of the ohmic current (I_O) and the polarization current (I_P), as in Eq. 3.8.

$$I_L = I_O + I_P = (G_{dc} + G_{ac})V \tag{3.8}$$

The loss current is in phase with V because G_{ac} and G_{dc} are not complex, and the total current (I_T) of the capacitor filled with a dielectric corresponds to the summation of I_C and I_L according to Eq. 3.9.

$$I_T = I_C + I_L = (i\omega C + G_{dc} + G_{ac})V \tag{3.9}$$

The vectorial representation of Eq. 3.9 is given in Fig. 3.3. As can be seen, I_T in a real dielectric leads the voltage by an angle $((\pi/2)-\delta)$, where δ is the loss angle.

In addition, the charge stored in a real dielectric can be expressed as

$$q = CV = kC_oV \tag{3.10}$$

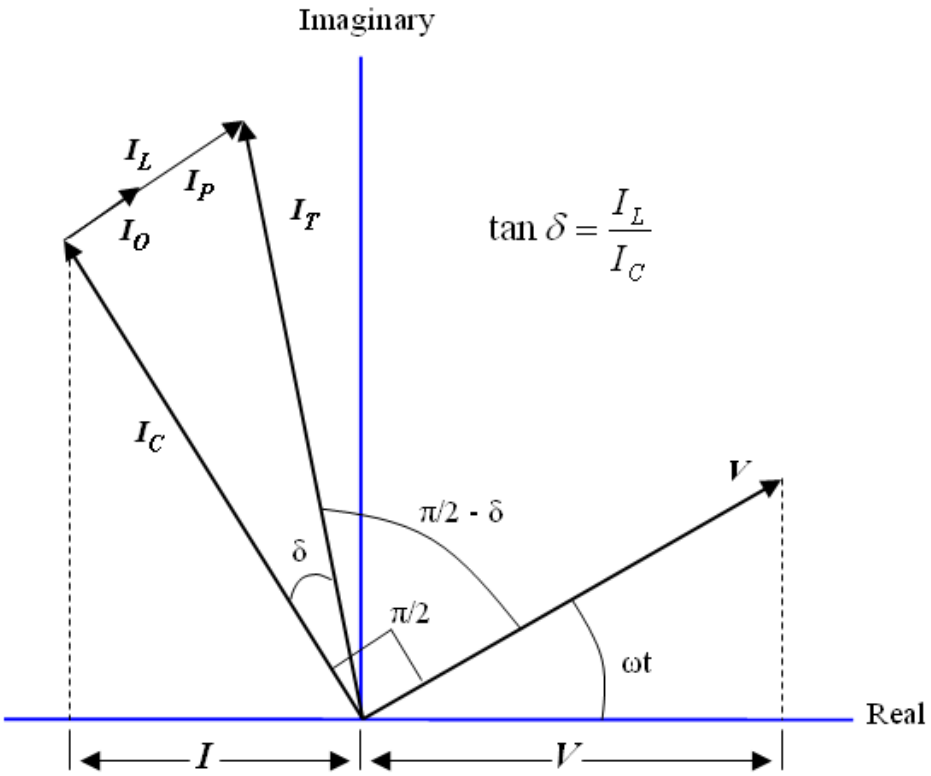

Fig. 3.3: Vectorial representation of the currents in a dielectric (I_C, I_L, and I_T) from Hench and West [4]. With kind permission of John Wiley & Sons, Inc. (permission granted, appendix F3).

Using Eq. 3.2, I_T can be expressed as

$$I_T = kC_oi\omega V \tag{3.11}$$

Knowing that I_T is equal to the summation of the charging and loss currents, Eq. 3.11 becomes

$$I_T = I_C + I_L = kC_oi\omega V = (i\omega C + G_{dc} + G_{ac})V \tag{3.12}$$

Rearranging Eq. 3.12 yields

$$k = C/C_o - [i(G_{dc} + G_{ac})]/\omega C_o \tag{3.13}$$

Equation 3.13 shows that the total current inside a real dielectric having charging and loss currents is expressed as a function of one complex parameter, k. This parameter will be called the complex dielectric constant (k*). The real part of k* is

$$k' = C/C_o \tag{3.14}$$

The imaginary part of k* is

$$k'' = (G_{dc} + G_{ac})/\omega C_o \tag{3.15}$$

also expressed as

$$k^* = k' - ik'' \tag{3.16}$$

The value of k' indicates the ability of the material to store charges when it is under an ***E*** and is called the dielectric constant. The value of k" indicates the losses exhibited by the material when it is under an ***E*** and is referred to as the dielectric loss factor. The ratio of the dielectric loss factor to the dielectric constant (k"/k') is equal to the ratio of the loss current to the charging current (I_L/I_C) and is called the loss angle, dissipation factor or tanδ.

Another way of expressing the complex dielectric constant of a real dielectric is as a function of complex permittivity (ε^*)

$$\varepsilon^* = \varepsilon' - i\varepsilon'' \tag{3.17}$$

$$k^* = k' - ik'' = \varepsilon^*/\varepsilon_o = \frac{\varepsilon'}{\varepsilon_o} - i\frac{\varepsilon''}{\varepsilon_o} \tag{3.18}$$

where, ε_o = permittivity of free space = 8.85×10^{-2} F/m

In addition, from Fig. 3.3, the dissipation factor can be expressed as

$$\tan\delta = (\text{loss current/charging current}) = \varepsilon''/\varepsilon' = k''/k' \tag{3.19}$$

It is difficult to separate all types of losses due to long-range motion (conduction) from those due to short-range motion (polarization); consequently, all of them have been designated with only one term, the effective loss factor, ε''_{eff}, given by [6, 8]

$$\varepsilon''_{eff} = \varepsilon''(\omega) + \sigma_{dc}/(\varepsilon_o\omega) = \varepsilon''_{sc}(\omega) + \varepsilon''_{o}(\omega) + \varepsilon''_{a}(\omega) + \varepsilon''_{e}(\omega) + \sigma_{dc}/(\varepsilon_o\omega) \qquad (3.20)$$

where $\varepsilon''(\omega)$ represents the losses related with polarization (frequency dependent), and the $\sigma_{dc}/(\varepsilon_o\omega)$ is associated with the losses from dc conductivity. The subscripts of the different components refer to the diverse polarization mechanisms: space charge or interfacial (sc), orientation (o), atomic (a), and electronic (e). It is common to find in the literature that ε''_{eff} is referred to as dielectric loss when the mechanism of interaction between microwaves and the material is unknown or involves more than one mechanism.

One empirical observation is that ceramics with ε''_{eff} between 10^{-2} and 5 are good candidates for microwave heating. Ceramics with $\varepsilon''_{eff} < 10^{-2}$ will be difficult to heat, and those materials with $\varepsilon''_{eff} > 5$ will experience most of the heating on the surface and not in the bulk [2, 6]. However, it should be understood that for this observation to be valid, conditions such as distribution of electric field, temperature, power applied, or position inside the cavity must be optimal. For example, silica aerogel has a dielectric loss at room temperature of 0.27 (2.45GHz). It is not possible to heat this material inside a multimode cavity applying 1200W, but it is possible to heat it in a single mode cavity under a higher electrical field and at much lower input power (more details are provided in Chapter IV and V).

3.5 Microwave power dissipation

Any time that an electromagnetic (EM) wave propagates, it transports energy. When this energy flows through a closed surface, it can be calculated from the integration of the Poynting[1] vector **P** [9]:

$$\mathbf{P} = \boldsymbol{E} \times \boldsymbol{H} = (V/\mathrm{m})(\mathrm{A/m}) = (\mathrm{Watts/m^2}) \tag{3.21}$$

where, V = volts

A = amps

m = meters

Here, $\boldsymbol{E}$ and $\boldsymbol{H}$ are the electric and magnetic components of the electromagnetic field, respectively.

When EM energy is applied to a material, microwave effects result in dissipation of the energy volumetrically inside the material, usually in the form of heat. By using Eq. 3.21, the power absorbed inside a material of volume (v) can be obtained as P_{av} and given by Eq. 3.22 [6]. Appendix A provides the details of the P_{av} deduction.

$$P_{av} = \omega\, \varepsilon_o\, \varepsilon''_{eff}\, E^2_{rms}\, v \ \ (\mathrm{Watts}) \tag{3.22}$$

Where $E_{rms} = E_o/\sqrt{2}$ is the root mean square of the electric field inside the material (V/m), and E_o is the maximum electric field of the sinusoidal voltage signal. The root mean square is used as an average of $\boldsymbol{E}$; consequently, it is assumed that the field is uniform throughout the volume, and that the material is in thermal equilibrium. If the material exhibits magnetic losses, a permeability (μ) term must be added to Eq. 3.22:

$$P_{av} = \omega\, \varepsilon_o\, \varepsilon''_{eff}\, E^2_{rms}\, v \ + \ \omega\, \mu_o\, \mu''_{eff} H^2_{rms}\, v \tag{3.23}$$

[1] Postulated by the English physicist, John H. Poynting, in 1884.

In the case where the material is inside a microwave cavity, the total power supplied to the cavity (P_T) is greater than P_{av} because there are some losses on the walls (P_W) of the cavity, and some power may be reflected (P_R) to the source (Eq. 3.24).

$$P_T = P_{av} + P_W + P_R \tag{3.24}$$

In most cases, P_W is very small compared to P_T and is considered to be negligible. The power reflected by the load is the result of the mismatch between the impedance of the load (Z_L) and the impedance of the source (Z_S). The impedance (Z) is defined as the ratio of the electric field to the magnetic field, as shown in Eq. 3.25.

$$Z = \mathbf{E}/\mathbf{H} \text{ (ohms)} \tag{3.25}$$

In practice, there are different components used to match or minimize the differences between these impedances (Z_L and Z_S), such as a tuner, an iris, and a variable short circuit. These components of a microwave system will be explained in more detail in Chapter IV, Section 4.2.

Assuming that the microwave irradiation results in uniform heating in a material of mass M, the microwave power necessary to raise the temperature from T_o to T (ΔT) is [6, 10, 11]

$$P_{av} = Q/t = M\, C_p\, (\Delta T)/t \tag{3.26}$$

where Q is the heat generated (J), t is the time (sec) and C_p is the specific heat (J/Kg °C) at constant pressure. Using Eq. 3.22 and 3.26, the rise of temperature can be expressed as a function of the bulk density (ρ_b=M/v) of the material (Eq. 3.27).

$$(\Delta T)/t = \omega\, \varepsilon_o\, \varepsilon''_{eff}\, E^2_{rms} / (\rho_b\, C_p) \quad (°C/s) \tag{3.27}$$

As illustrated by Eq. 3.21 – 3.27, the power absorbed and temperature rise by a material when microwave energy is applied depend on two factors. One factor is related to the material characteristics (ε''_{eff}, μ''_{eff}, ρ_b, C_p), and the other is associated with the microwave source

characteristics (ω, E_{rms}, H_{rms}, P_T). Therefore, it is very important to establish the optimal equipment set-up to process a given material. Consequently, the microwave source has to be chosen according to the process required.

3.6 Thermal runaway

Effective dielectric loss is a material characteristic that generally is low at room temperature but increases at elevated temperatures. Even though this is not true for all materials, a typical behavior of ε''_{eff} as a function of temperature for ceramic materials is shown in Fig. 3.4.

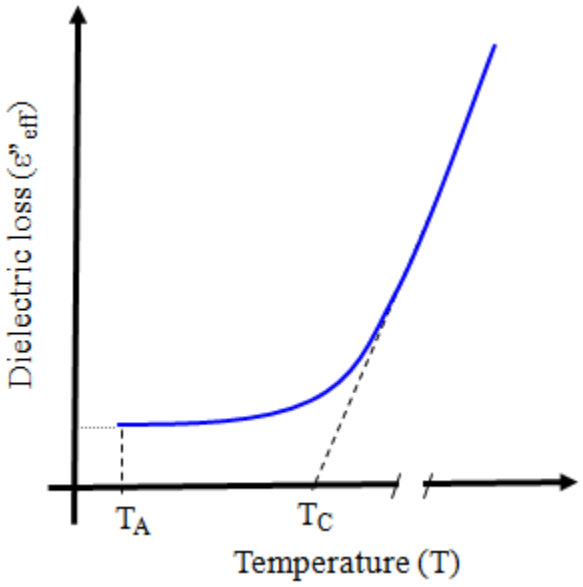

Fig. 3.4: Condition of thermal runaway.

This figure illustrates a significant change in the slope of ε''_{eff} versus temperature ($d\varepsilon''_{eff}/dT$) which is evident at temperatures higher than T_c (critical temperature). Below T_c, the material is difficult to heat, even when the microwave power is increased. However, once the material reaches T_c, either through microwave absorption or through an external source, the heating rate ($\Delta T/\Delta t$) increases significantly. If the microwave power applied to the material

continues after T_c, then ε''_{eff} increases very rapidly. Based on Eq. 3.27, the increase of ε''_{eff} results in a further temperature rise and in a steep rise in heating referred to as thermal runaway [12]. One way to control thermal runaway is to limit the power applied to the material, which is the method used in this research.

3.7 Microwave hybrid heating

The change of ε''_{eff} as a function of temperature has led to the development of microwave hybrid heating (MHH), a technique where the material is heated initially using a method other than or in addition to microwaves. Once the material's ε''_{eff} has increased sufficiently, the sample becomes a more efficient microwave absorber, and its temperature can reach much higher levels than by the initial method alone. Microwave hybrid heating can be performed using two different techniques.

1. Heating the sample or product outside the microwave cavity with an external heat source and then introducing the sample into the cavity.
2. Heating the sample inside the microwave cavity with the aid of a susceptor material (microwave absorbing material) while microwave energy is applied to both materials at the same time. This is the technique used in the present study for processing the silica gel.

These techniques can produce different results depending on what type of microwave cavity is used. The EM field on the sample has characteristics that are influenced by the cavity design and thus a given material will respond to the field differently in a different microwave cavity. Therefore, it becomes important to have some understanding of the different types of microwave cavities.

3.8 Microwave cavities

The microwave cavity or applicator is the device that transfers the microwave energy to the product. This device is basically a metallic enclosure where the signal undergoes multiple reflections from the walls [13]. Size and shape of the cavity and microwave frequency must be optimized to ensure a high conversion efficiency of the microwave energy to the sample. The main types of cavities are the multimode and the single mode. A mode is a particular distribution of the electromagnetic field in a cavity or transmission line and is the product of the interaction of two or more traveling waves [6].

A multimode is a type of cavity in which different patterns of electromagnetic waves are present, and the total field is the summation of all excited modes. The multiple modes are the result of the multiple reflections of the signal in a cavity that has lineal dimensions much larger than the microwave wavelength (λ_o) used. The larger the number of modes, the more uniform the heating. In addition, a more uniform radiation of the product is obtained using mode stirrers and/or product movement inside the microwave field, as shown in Fig. 3.5. However, multimode cavities also produce a non-continuous distribution of low and high field intensities; consequently, the position of the product in the cavity is critical. Analysis of the field distribution is difficult, especially after the introduction of a sample which can shift the energy distribution significantly.

In a single mode cavity, only one mode is excited. The primary advantage with this type of cavity is that the field distribution can be precisely determined [10]. This knowledge allows the operator to position the sample where it is more convenient to process it. One of the limitations is that these cavities usually are small in the plane normal to the propagation of microwaves, which restricts the size of the sample to be processed.

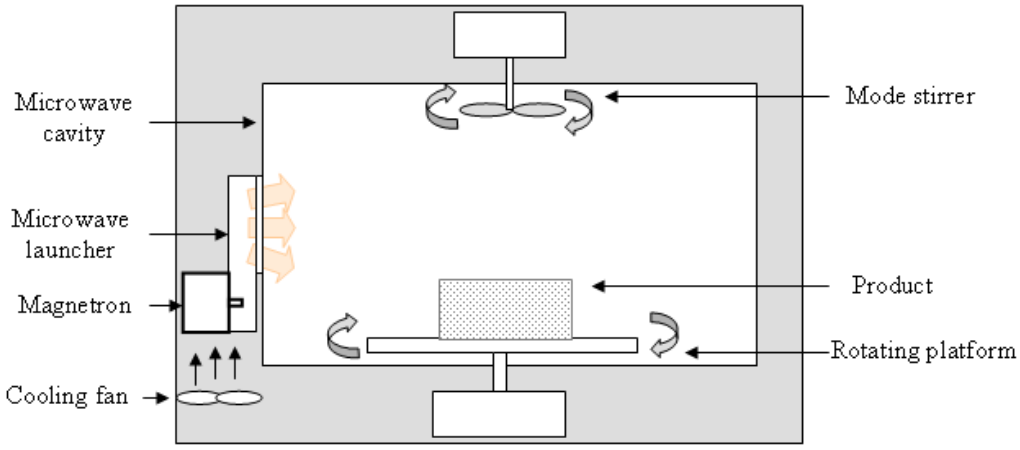

Fig. 3.5: Microwave cavity with mode stirrer and rotating platform.

There are different types of single mode cavities. Depending on the mode of propagation, the two main classifications for rectangular and cylindrical cavities are transverse magnetic (TM) and transverse electric (TE) modes. The TM mode corresponds to the mode in which the magnetic field is transverse to the direction of propagation, and in the TE modes, the electric field is transverse to the direction of propagation [6, 13]. In this dissertation, a TE rectangular single mode cavity is used and will be discussed in further detail in subsequent paragraphs.

3.9 TE rectangular single mode cavity

In a single mode cavity, the distribution of the electromagnetic field is defined by the resonant frequency. The maximum power transmitted to the cavity occurs at this frequency and is reached when the length of the cavity (L_c) is a multiple of half of the guide wavelength ($\lambda_g/2$). The guide wavelength is the distance that a microwave signal travels in one cycle inside a waveguide. It is different than the wavelength of the microwave frequency (λ_o), because it is

modified by the presence of the waveguide walls and by the dielectric material that fills the waveguide. The guide wavelength is given by Eq. 3.28 [6].

$$\lambda_g = \frac{2L_c}{l} = \frac{\lambda_o}{\sqrt{1-\left(\frac{\lambda_o}{\lambda_c}\right)^2}} \tag{3.28}$$

where, l = number of nodes in the propagation direction

λ_c = wavelength of the cutoff frequency

The cutoff frequency (f_c) is the minimum frequency that can be transmitted in a waveguide or cavity. This frequency is a function of the waveguide dimensions and the propagation mode, as given by Eq. 3.29 [6, 14].

$$\lambda_c = \frac{c}{f_c} = \frac{1}{\sqrt{\mu\varepsilon} f_c} = \frac{2}{\sqrt{\left(\frac{m}{a}\right)^2 + \left(\frac{n}{b}\right)^2}} \tag{3.29}$$

Where, c = speed of light

m, n = modes of propagation

a = dimension of the waveguide or cavity along the x axis

b = dimension of the waveguide or cavity along the y axis

The TE rectangular cavities are designated with the TE_{mnl} nomenclature, where $m, n,$ and l are integers that specify the mode of propagation of $\boldsymbol{E}$ along the x, y, and z axes, respectively. It is a common practice to specify the mode of propagation using only m and n subscripts. In that case, l is assumed to be equal to one. Also, it is a standard convention that the direction of propagation lies along the z axis, and the longest side of the waveguide is along the x axis; consequently, $a > b$, as shown in Fig. 3.6a.

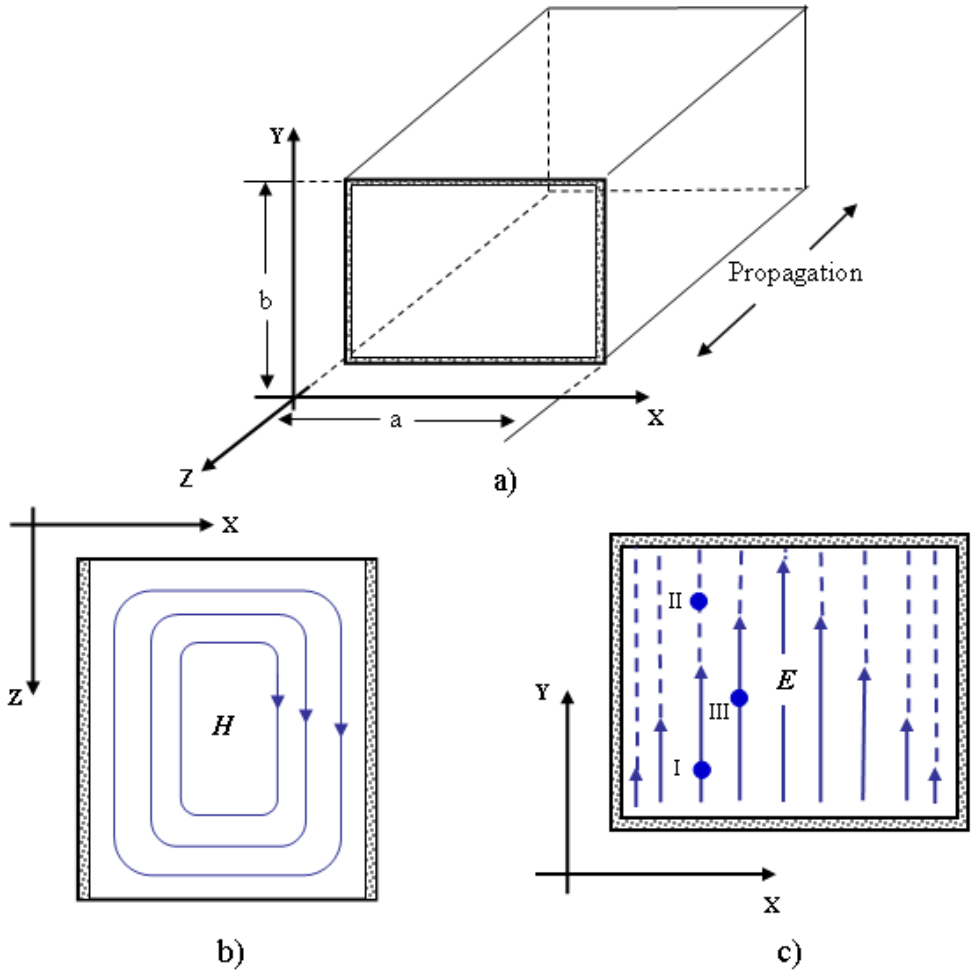

Fig. 3.6: TE_{10} rectangular waveguide and its field propagations: a) rectangular waveguide dimensions, b) magnetic field distributions, and c) electric field.

The distribution of the field in the TE_{mnl} rectangular cavity is derived from the solution in time and space of the Maxwell equations [15]. Since $\boldsymbol{E}$ is perpendicular to the direction of propagation (z), this mode is characterized by $\boldsymbol{E}$ in the z direction equal to zero (E_Z=0).

3.10 Field distribution in a TE_{10} rectangular cavity

The mode with the lowest f_c is called the dominant mode. Since commercial waveguides have $a=2b$, the lowest f_c occurs for the TE_{10} (m = 1 and n = 0). For this mode, the respective fields are [6]

$$E_z = E_x = H_y = 0 \tag{3.30}$$

$$E_y = E_{yo} \sin\left(\frac{\pi x}{a}\right) \sin(\beta z) \tag{3.31}$$

$$H_x = H_{xo} \sin\left(\frac{\pi x}{a}\right) \cos(\beta z) \tag{3.32}$$

$$H_z = H_{zo} \cos\left(\frac{\pi x}{a}\right) \sin(\beta z) \tag{3.33}$$

Where E_{yo}, $H_{xo,}$ H_{zo} are constants that represent the maximum magnitude of the field in the axis analyzed, and β is the propagation constant (Eq. 3.34).

$$\beta = \frac{2\pi}{\lambda_g} = \omega\sqrt{\mu\varepsilon}\sqrt{1-\left(\frac{f_c}{f_o}\right)^2} \tag{3.34}$$

The distribution of $\boldsymbol{H}$ and $\boldsymbol{E}$ fields of the TE_{10} mode are presented in Figure 3.6b and 3.6c, respectively, by the arrows inside the cavity. This mode of propagation has an $\boldsymbol{H}$ field tangential to the direction of propagation with two components, H_x and H_z, forming closing loops, as shown in Fig. 3.6b. The electric field has only one component, E_y, and its magnitude describes one half sinusoid variation along the x axis, as represented by the arrows in Fig. 3.6c. It is important to identify from Eqs. 3.30 – 3.33 that the maximum of $\boldsymbol{E}$ and $\boldsymbol{H}$ occur when x = $a/2$, but have a difference in phase on z of $\frac{\lambda_g}{4}$. Therefore, one can choose where to have more electrical or magnetic interaction with the sample.

Generally, the terminology "variation" is used to describe one half sinusoid change of the field in a single mode cavity or waveguide. Using the nomenclature TE_{10}, the subscript 1 indicates that $\boldsymbol{E}$ has only one variation along the x axis, and the subscript 0 indicates that $\boldsymbol{E}$ has no variation (constant $\boldsymbol{E}$) along the y axis. Every arrow in Fig. 3.6c represents how the magnitude of $\boldsymbol{E}$ changes along the x axis. Also, the arrows and dashed lines represent the presence of $\boldsymbol{E}$ along the y axis on a position x. In this case, the electric field magnitude is constant for every specific x position along the y axis. For example, E_I (magnitude of the electric field at position I in Fig. 3.6c) is equal to E_{II}, but it is lower than E_{III}.

The subscript l in the TE_{mnl} nomenclature indicates the number of variations of the $\boldsymbol{E}$ field along the z axis. As can be seen in Eq. 3.28, along a resonant cavity with a L_c length, every variation of $\boldsymbol{E}$ along z occurs at $\frac{\lambda_g}{2}$. For example, a TE_{103} mode has a distribution of the field as shown in Fig. 3.7. This figure shows that $\boldsymbol{E}$ has three variations along the z axis. Since there are three variations of $\boldsymbol{E}$ along z, the total length of the cavity is equal to $1\frac{1}{2}\lambda_g$, and every maximum or minimum of $\boldsymbol{E}$ is at $\frac{\lambda_g}{4}$ along the propagation direction.

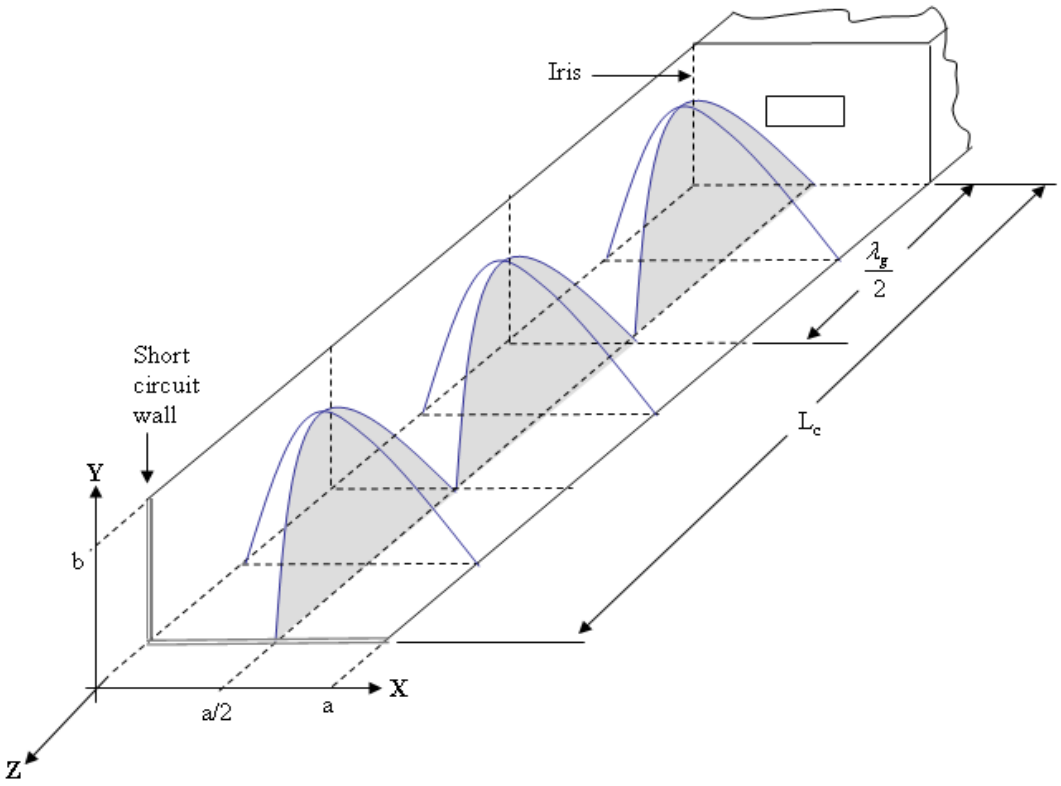

Fig. 3.7: Distribution of the electric field in a TE_{103} cavity, the primary cavity used in this study.

The electric field at any point in the single mode cavity is the resultant of the superposition of a forward wave and a reflected wave. When these two waves are in phase, a maximum magnitude of the field is reached. If they are out of phase, minimum points are obtained. The repetition of the superposition of these waves produces what is known as a standing wave [16]. In addition, Fig. 3.7 shows an iris and a short-circuit wall. The iris separates the microwave source from the applicator. The size and shape of the iris' aperture determines the transfer of power into the cavity. Also, instead of closing the other end of the cavity with a fixed wall, a variable short-circuit wall is moved to restore the original mode when the load is introduced. Consequently, the cavity can be tuned for heating a variety of materials.

3.11. Quality factor of the cavity

Resonant cavities lose energy by power dissipation in the walls (resistive losses) and by dielectric losses if the cavity is loaded. The losses in a cavity are usually expressed in term of the quality factor (Q) of the cavity, defined by Eq. 3.35.

$$Q = 2\pi \frac{\text{total store energy}}{\text{energy dissipated per period}} \tag{3.35}$$

The Q of a cavity is a unique value which depends on the resonant mode, shape of the cavity, and material of the cavity [17]. In practice, Q is defined as a measure of the sharpness of the response of a cavity to an input signal and is expressed by Eq. 3.36 [18].

$$Q = \frac{1}{\tan\delta} = \frac{\varepsilon'}{\varepsilon''} = \frac{f_r}{f_2 - f_1} \tag{3.36}$$

Each of the parameters represented in Eq. 3.36 is the total parameter for the cavity loaded or unloaded. For example, if the cavity is loaded, the ε'' represents the total dielectric loss of the cavity and the load. Also, f_r is the resonant frequency; f_1 and f_2 represent the frequencies at which power at the f_r is reduced by 50%.

Knowing the power supplied (P_T) to a cavity and power transmitted (P_t) through the cavity, the coefficient of transmission (S_{21}) can be obtained (Eq. 3.37). Plotting S_{21} as a function of frequency, Q can be calculated (Fig. 3.8a). In the same way, Q can be obtained by plotting the coefficient of reflection (S_{11}, Eq. 3.38) if the power reflected (P_R) from the cavity is known (Fig. 3.8b) [13].

$$S_{21} = P_t/P_T \tag{3.37}$$

$$S_{11} = P_R/P_T \tag{3.38}$$

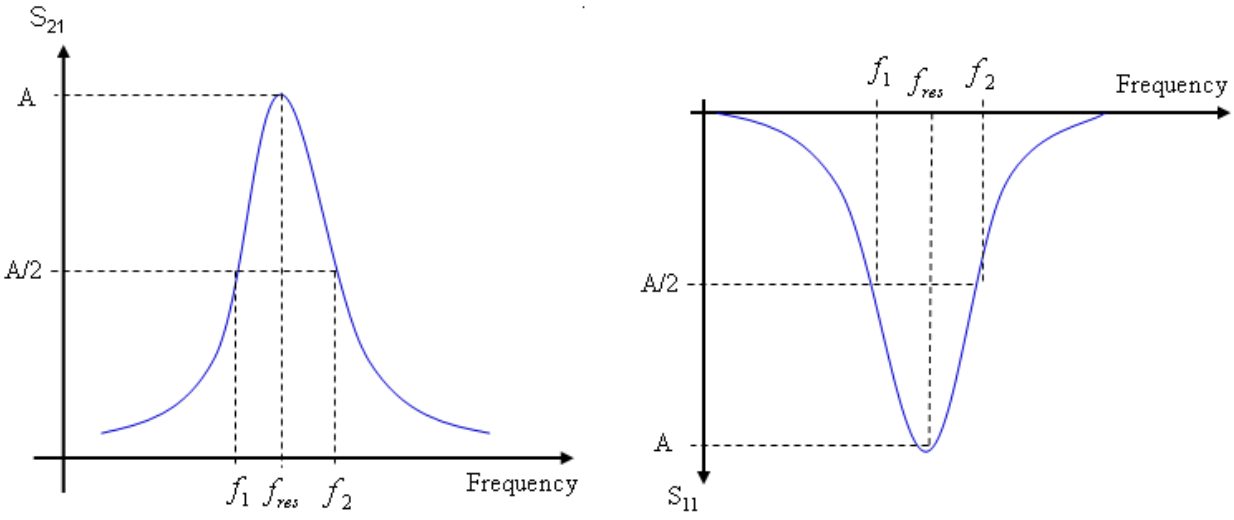

a) b)

Fig. 3.8: The resonant frequency of a cavity: a) at the positive peak of the coefficient of transmission, b) at the negative peak of the coefficient of reflection.

3.12 Power in a TE_{10} rectangular cavity

The power propagating in a rectangular waveguide or applicator is given by the Poynting vector, introduced in Eq. 3.21. In the case of a TE_{10} rectangular cavity, the direction of propagation is along the *z* axis. Therefore, the power of the propagation wave is provided by the z component of the Poynting vector, shown in Eq. 3.39 [10].

$$P_{10} = \frac{ab}{Z_{TE}} \frac{E_{RMS}^2}{2} \tag{3.39}$$

Where Z_{TE} is the impedance of the TE waveguide or cavity and is given by

$$Z_{TE} = \frac{\omega\mu}{\beta} = \frac{\eta}{\sqrt{1-\left(\frac{f_c}{f_o}\right)^2}} \tag{3.40}$$

Here, $\eta = \sqrt{\mu/\varepsilon}$ and is known as the impedance characteristic of the medium. When the medium in the cavity is air or vacuum, η is equal to 377Ω. It can be seen in Eq. 3.39 that by knowing the E_{RMS} value inside the cavity, the power also can be obtained. The applicator presented in Fig. 3.7 is a standard cavity and further information can be found in the literature [6, 10, 14].

In this cavity, the sample can be positioned in a place where the intensity of ***E*** is optimum for processing the particular material. This is probably the best advantage of a single mode cavity. The subsequent chapter in this study will provide complementary information about the use of a TE_{10} single mode cavity.

References

1. Sutton, W.H., *Microwave Processing of Ceramic Materials*, in *Microwave Solutions for Ceramic Engineers*, David E. Clark, Diane C. Folz, Carlos E. Folgar, and Morsi M. Mahmoud, Editors. 2005. The American Ceramic Society: Westerville, Ohio. p. 35-66.
2. Clark, D., D. Folz, C. Folgar, and M. Mahmoud, Editors. *Microwave Solutions for Ceramic Engineers*. 2005. The American Ceramic Society: Westerville, Ohio.
3. Newnham, R.E., S.J. Jang, M. Xu, and F. Fones, *Fundamental Interaction Mechanisms Between Microwaves and Matter*, in *Microwaves: Theory and Application in Materials Processing*, David E. Clark, Frank D. Gac, and Willard H. Sutton, Editors. 1991. The American Ceramic Society: Westerville, Ohio. p. 51-68.
4. Hench, L.L. and J.K. West, *Principles of Electronic Ceramics*. 1990: John Wiley & Sons, Inc.
5. Atong, D., *Microwave - Inducted Combustion Synthesis of Al2O3 - TiC Powder*, *Ph.D. Dissertation in Materials Science and Engineering*. 2000. University of Florida: Gainesville, Florida.
6. Metaxas, A.C. and R.J. Meredith, *Industrial Microwave Heating*. 1983. London, United Kingdom: Peter Peregrinus Ltd.

7. Fathi, Z., *Surface Modification of Sodium Aluminosilicate Glasses using Microwave Energy*, *Ph.D. Dissertation in Materials Science and Engineering*. 1994. University of Florida: Gainesville, Florida.
8. *Microwave Processing of Materials*. Committee on Microwave Processing of Materials. 1994. Washington, D.C.: National Academy Press.
9. Pozar, D.M., *Microwave Engineering*. 2005. Amherst, MA: John Wiley & Sons, Inc.
10. Roussy, G. and J.A. Pearce, *Foundations and Industrial Applications of Microwaves and Radio Frequency Fields*. 1995. West Sussex, England: John Wiley & Sons Ltd.
11. Gaskell, D.R., *Introduction to the Thermodynamics of Materials*. Fourth Edition ed. 2003. New York: Taylor & Francis.
12. Janney, M.A. and H. Kimrey, *Microwave Sintering of Alumina.* Ceramic Powder Science II, Ceram. Trans., 1988. **1**: p. 919-924.
13. Scott, A.W., *Understanding Microwaves*. 1993. New York, New York: John Wiley & Sons, Inc.
14. Chan, C.T. and H.C. Reader, *Understanding Microwave Heating Cavities*. 2000. Boston, Massachusetts: Artech House, Inc.
15. Hayt, W.H. and J.A. Buck, *Engineering Electromagnetics*. Sixth edition ed. 2001. New York: McGraw-Hill.
16. Wu, X., *Experimental and Theorical Study of Microwave Runaway Materials*, *Ph.D. Dissertation in Mechanical Engineering*. 2002. Virginia Polytechnic Institute and State University: Blacksburg, Virginia.
17. Balanis, C.A., *Advanced engineering electromagnetics*. 1989. New York, New York: John Wiley & Sons.
18. Altschuler, H.M., *Dielectric constant*, in *Handbook of microwave measurements*, Max Sucher and Jerome Fox, Editors. 1963. Polytechnic Press: New York, New York. p. 495-548.

CHAPTER IV

Experimental Procedure

This chapter presents a description of the sample preparation, set-ups, and characterization techniques used. The sample preparation is according to the production process presented in Chapter II. The description of set-ups used includes a brief summary of the equipment and justification for their arrangements. Some parameters measured or calculated for better use of the equipment are provided. Also, a detailed procedure to measure the temperature of a material under a microwave field is presented. The final section includes a description of the characterization techniques used and important considerations when applying these techniques. In general, standard characterization techniques are used in this study. The design and construction of a system to measure the dielectric properties of the silica gel in the microwave frequency range is described.

4.1 Production of samples

Monolithic silica aerogel samples were produced by following a procedure depicted in Fig. 2.1. As mentioned in Section 2.2 of Chapter II, the production process was divided into three parts.

4.1.1 Part I of the production process

Part I includes the following stages: precursor materials, mixing, casting, gelation, and aging (Fig. 4.1). All of these stages were performed at room temperature and ambient pressure.

1. Precursor materials

The procedure followed to make silica aerogel samples included the use of TMOS as the silicon source, water to hydrolyze the silicon alkoxide, and a mixture of dilute nitric acid and dilute hydrofluoric acid as the catalyst. This is a standard procedure developed by H. Wang and described in the literature [1, 2]. The precursor materials utilized are given in Table 4.1.

a)

b)

c)

Fig. 4.1: Stages performed in Part I of the production process: a) precursor materials and mixing, b) casting and gelation, c) aging.

Table 4.1: Materials for preparation of acid-catalyzed silica aerogel.

Components	Formula	Volume	Supplier (product #)
DI water	H_2O	46 ml	Local
70% Nitric acid	HNO_3	0.6 ml	Fisher Scientific (UN2031)
50% Hydrofluoric acid solution	HF	0.2 ml	Fisher Scientific (UN1790)
TMOS	$Si(OCH_3)_4$	19.5 ml	Alfa Aesar (40251)

2. Mixing

During mixing of the chemical components, hydrolysis, condensation, and polymerization reactions took place (Eq. 2.1, 2.2, 2.3, respectively).

The standard procedure to mix the precursor materials was as follows:

a) Pour 46 ml of DI water into a clean beaker.

b) Place the beaker in a hot-stirring plate at a temperature between 28-30°C.

c) Mix 0.6 ml of 70% HNO_3 and 0.2 ml of 50% HF (catalysts) into the beaker using a Teflon®-coated magnetic bar.

d) Stir for 3 min to get a homogeneous solution.

e) Add 19.5 ml of TMOS to the acid solution while it continues to be stirred for approximately 1 min.

f) When the viscosity of the solution increases but is still being stirred, the solution is cast into the molds.

3. Casting

The requirements for choosing the mold that were mentioned in Chapter II were considered. The mixed sol was cast from the beaker into a mold that corresponded to the desired shape. Several attempts using different types of molds were carried out. Some of them were unsuccessful due to cracking upon removal from the mold. The sample must not come out from the mold with cracks. If it does, the cracks will propagate in subsequent production stages (especially during drying), and production of a sample that can retain the shape of the mold becomes extremely difficult. A custom-made mold was used to avoid this problem. The tip section of 60cc polystyrene syringes was cut off, leaving cylindrical tubes with a piston, as shown in Fig. 4.1b. Using these molds, cylindrical samples were obtained with no cracks by pushing the syringe's plunger carefully.

4. Gelation

When the mixed sol was poured into the mold, it took the shape and surface of the mold. The gelation step was finalized in the mold and as a result, a wet solid sample was obtained. However, at this moment the sample could not be removed because it was not strong enough to retain its shape.

5. Aging

Aging was performed in two stages: one was carried out in the mold and the other took place in a container of ethanol.

a) Aging in the mold: Ethanol (C_2H_5OH) was poured into the molds (with samples) allowing polycondensation reactions to take place for 8h at room temperature.

During this period, mechanical properties of the sample increased sufficiently to allow the sample could be removed from the mold and passed it to another container to continue aging.

b) Aging in a container: After the samples were removed from the mold, they were maintained in a container with C_2H_5OH, aging for six days, as shown in Fig. 4.1c. During this time, the samples achieved sufficient strength to resist the stresses that may develop in the drying stage.

4.1.2 Part II of the production process

In Part II of the production process, drying of the silica aerogel samples took place. This process was performed in a critical point drier (CPD) using liquid CO_2 under specific pressure and temperature conditions. Liquid CO_2 was passed through different pressure-temperature stages, as explained in Section 2.2.6 and shown in Fig. 2.3. An experimental procedure, which lasted about three days, was developed to produce dried silica aerogel using the critical point drying technique. Fig. 4.2 shows the path followed by the procedure in capital letters (A – E), and it is explained as follows:

1. The wet gel and C_2H_5OH were loaded into a CPD at 5°C, and the chamber was filled with liquid CO_2 (A-B)[3]. A chiller (Thermo NESLAB model RTE7) circulated water around the CPD chamber to control the temperature.
2. The solvent, C_2H_5OH, was removed by repeated purging (around 50ml every 3h) while the chamber was kept full of CO_2 (B).
3. While the chamber temperature was slowly raised (0.3 °C/min) above 31ºC, the pressure increased (B-C).
4. When the pressure was greater than 74 atm, the CO_2 became a supercritical fluid. Subsequently, the pressure was brought below 74 atm while keeping the temperature at

40ºC, and the supercritical fluid passed into the gas phase. The gas in the chamber was vented gradually (C-D, 0.4 atm/min), and the temperature was brought down slowly to ambient temperature (D-E, 2h). Fig. 4.3 shows the set-up used to make silica aerogel samples.

Monoliths of dried silica aerogel could be reliably produced in this manner and samples are shown in Fig. 4.4. The fogginess of the samples is due to the high degree of porosity [4]. **Development of this procedure and successful production of sol-gel samples satisfied objective one for this study.**

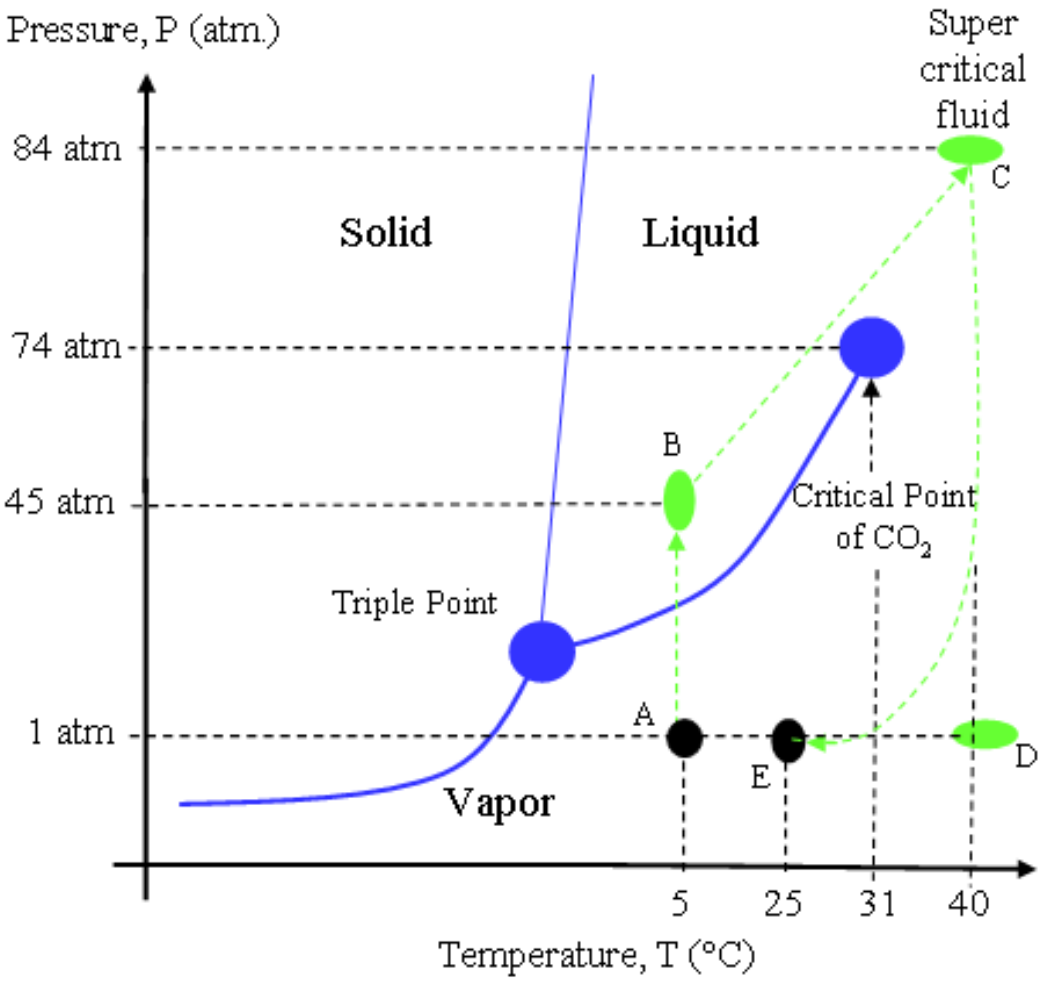

Fig. 4.2: Procedure to dry silica aerogel in a CPD imposed on a CO_2 phase diagram.

Fig. 4.3: Set-up used to make dried aerogel samples.

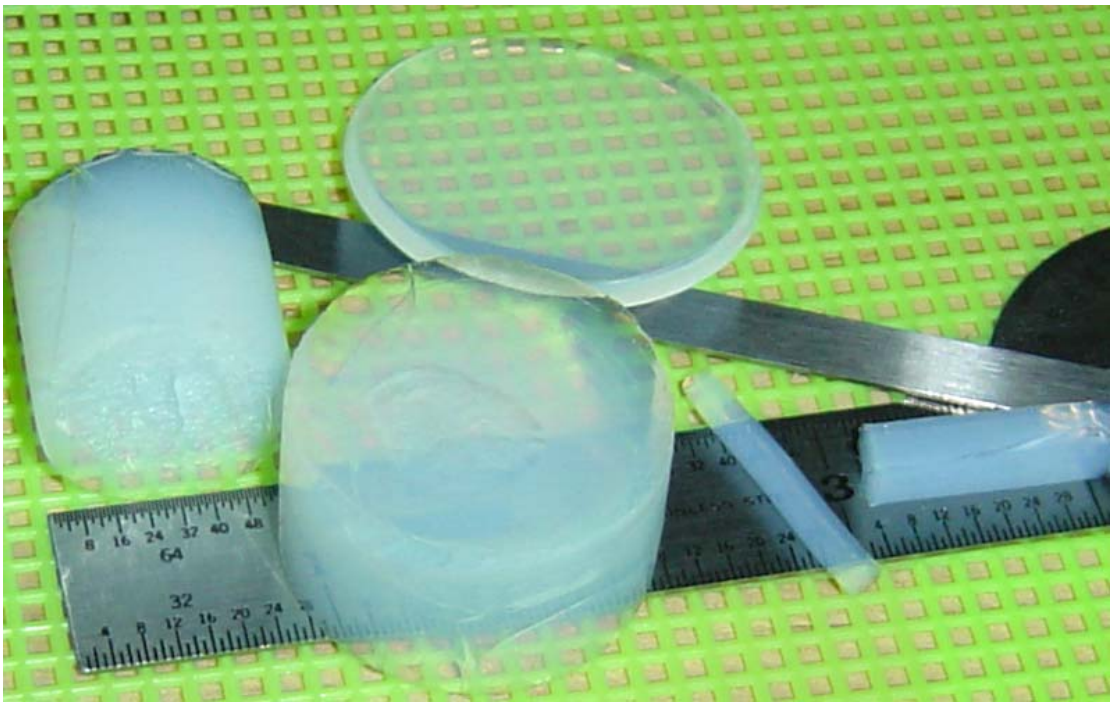

Fig. 4.4: Monolithic silica aerogel samples after being dried in a CPD with CO_2.

4.1.3 Part III of the production process

This part includes the stabilization and densification stages which took place during a heat treatment applied to the sample. The structure evolution during these stages is the main focus of this dissertation.

Monolithic dried aerogel samples received a thermal treatment at ambient pressure for 30 min at a predetermined temperature (T_P) and then were characterized. The thermal treatment followed a temperature profile shown in Fig. 4.5, and the predetermined temperature was different for each sample, so the structure characterization as a function of the thermal history could be obtained.

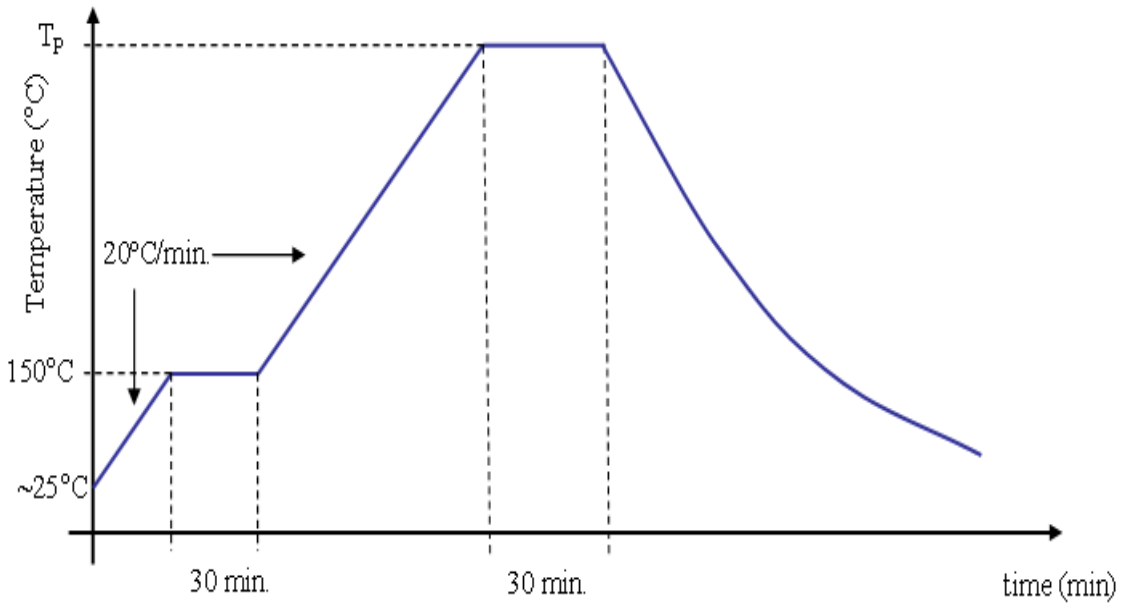

Fig. 4.5: Typical temperature profile for conventional and microwave heat treatments.

Samples were heated in a conventional or microwave oven, and both ovens followed the same temperature profile. The conventional heat treatment was performed in an electric furnace. This furnace monitored the temperature using a thermocouple that was close to the wall of the furnace (common practice in ovens and furnaces). However, if this thermocouple did not

measure temperature on or close to the sample, the temperature could be different between the position of the sample and the furnace's thermocouple. In this case, substantial differences in temperature were observed between those two positions (around 60°C at temperatures lower than 800ºC). Consequently, a parallel system that monitored the temperature of the furnace (on the wall) and the temperature on the sample surface was installed (Fig. 4.6). Thus, the temperature provided in the results section was measured on the silica aerogel sample using the parallel system.

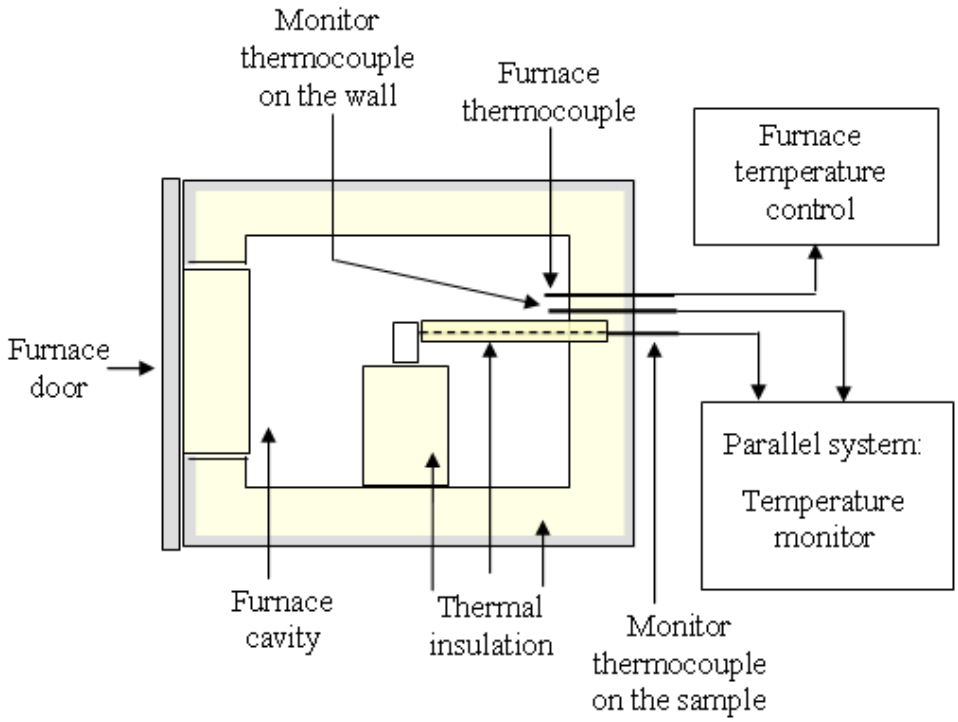

Fig. 4.6: Lateral view of the conventional furnace cavity with the parallel temperature monitoring system.

In addition, the internal temperature of the sample was measured for a few samples at low (150ºC), medium (500ºC) and high temperature (1000ºC). The objective was to determine if there was a substantial difference between internal and surface temperature (TCIn and TCSu,

respectively) during the 30 min at T_p. These heat treatments in both systems (conventional and microwave) showed small differences between both temperatures (≤20°C). An example of these temperature profiles is shown in Fig. 4.7 for the conventional furnace and in Fig. 6.3 for a microwave oven. In the conventional process, the time that it took the temperature from inside the sample to reach the surface temperature was approximately 68 seconds (calculated data), while experimentally, the time was less than 30 seconds. The difference in these values may have been due to heat flow to the thermocouple tip inside the sample that caused an unexpected similarity between the inside and outside temperature readings, reflected in the data in Fig. 4.7. The results obtained for structural characterization of the samples were not affected by this difference because samples were heated for 30 min to ensure temperature uniformity throughout.

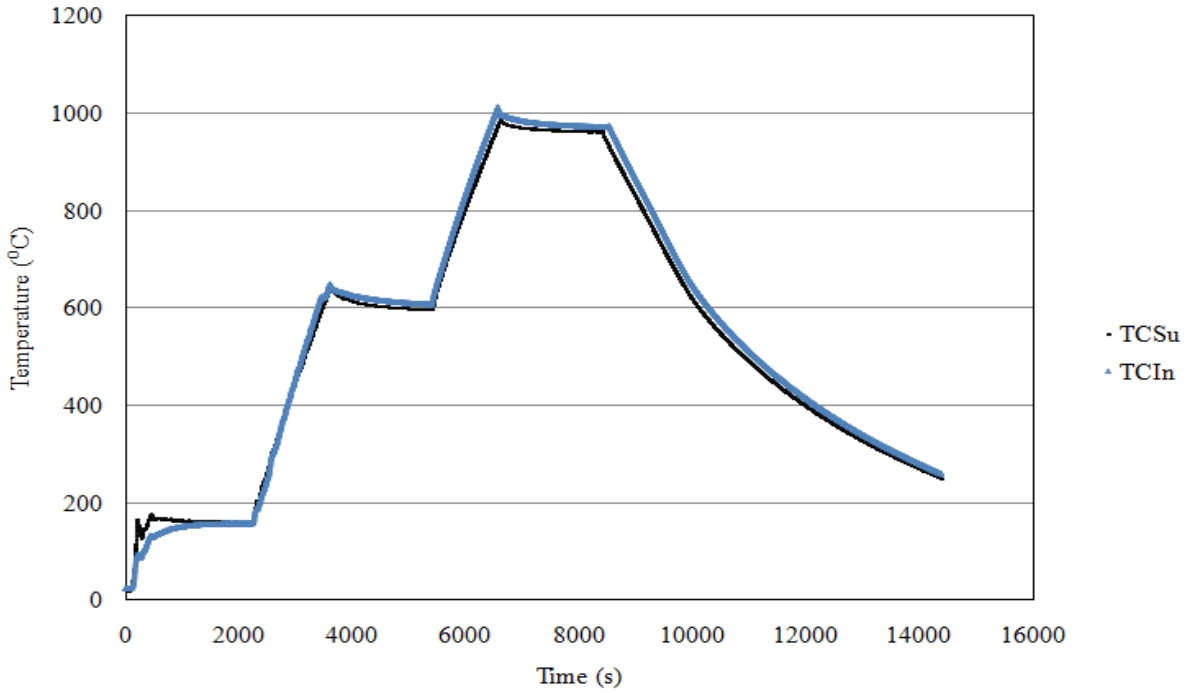

Fig. 4.7: Temperature profile of a silica aerogel sample in a conventional oven where the TCSu and TCIn are the surface and internal temperature of the sample, respectively.

The microwave heat treatment of the samples was performed in a single mode microwave system with a TE_{103} cavity. Since silica aerogel exhibited a very low dielectric loss at low temperature, the sample was heated from room temperature using a hybrid heating set-up inside the cavity. Temperature measurements in the microwave cavity were carried out using infrared pyrometers (IRP) and thermocouples (TC). More details about the microwave system and temperature measurements are provided in the following sections.

4.2 Single mode microwave system

A single mode microwave system operating at 2.45GHz was designed and built (by the author) to process dried aerogel samples. Fig. 4.8 shows a picture of the system with its main components. Fig. 4.9 is a schematic of the system with the following capabilities:

1. Control of temperature and applied power.
2. Tuning forward power, reflected power and distribution of $\boldsymbol{E}$.
3. Attenuation of forward power and reflected power.
4. Gas exhaust for emitted vapors from sample processing.
5. Water circulation to cool down components and dummy power loads.

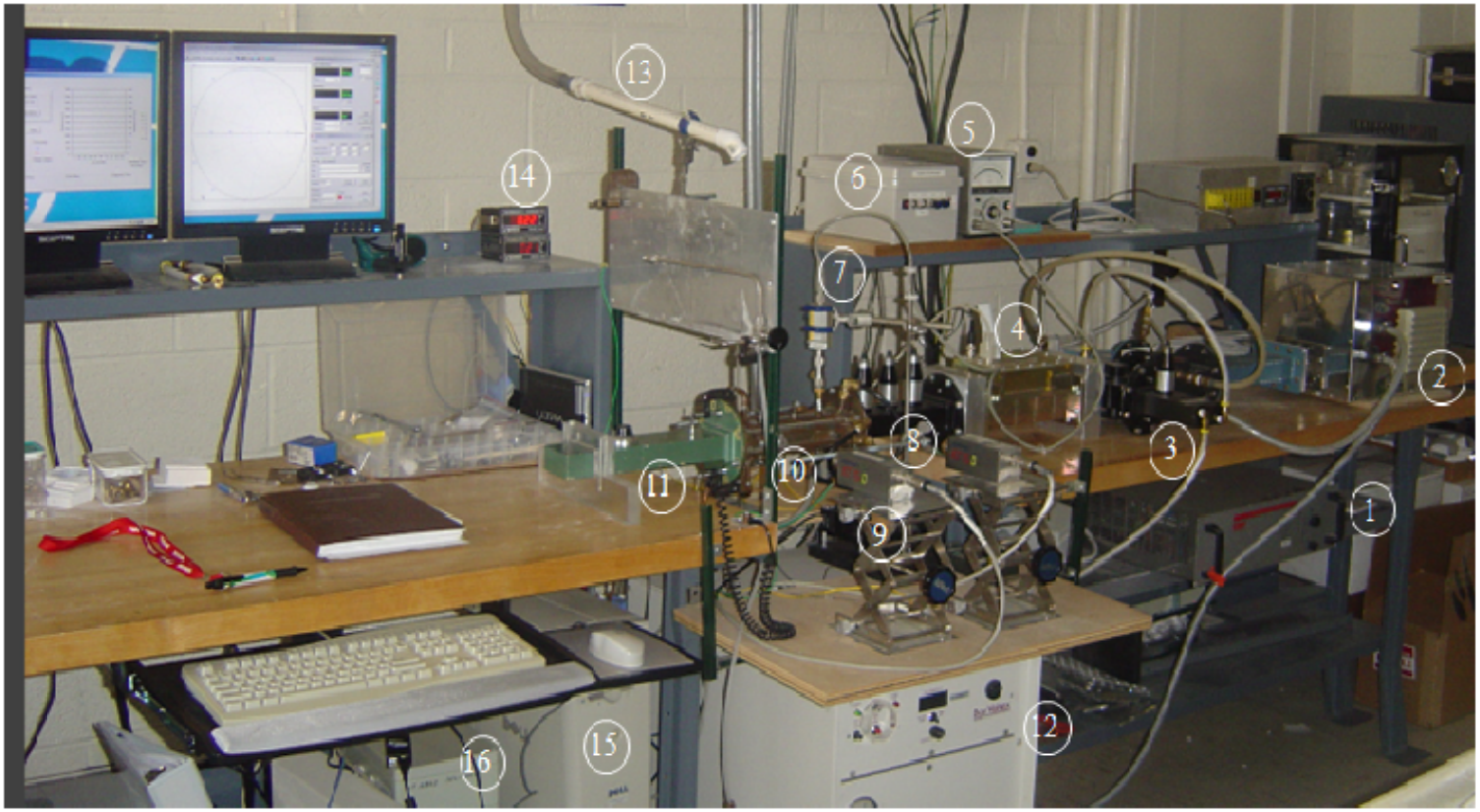

Fig. 4.8: Picture of the microwave heating system: 1) power control unit, 2) generator, 3) double circulator system, 4) impedance analyzer, 5) power meter, 6) power interface, 7) power probe, 8) tuner, 9) infrared temperature sensor, 10) cavity, 11) short circuit termination, 12) chiller, 13) exhaust system, 14) temperature monitors, 15) computer, 16) temperature interface.

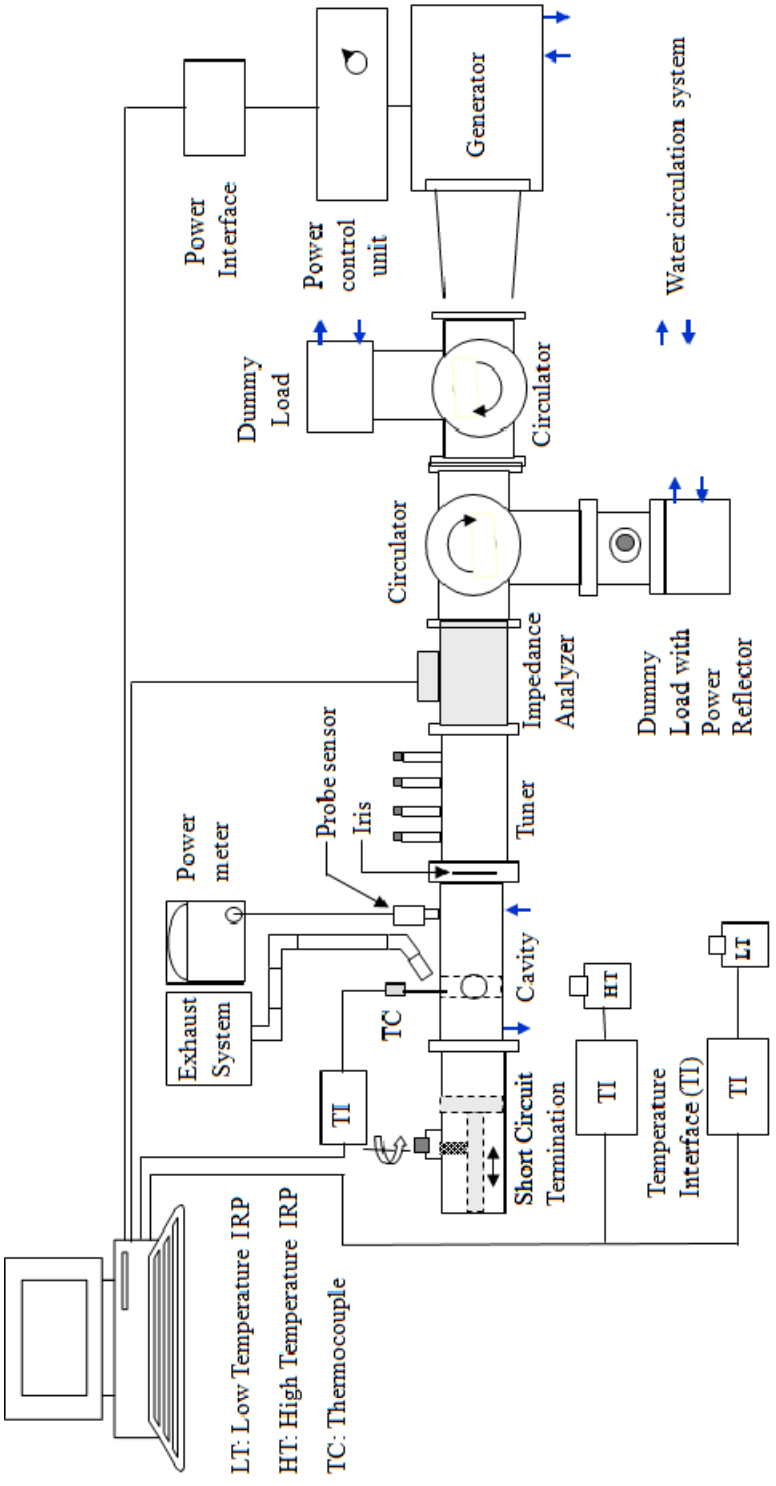

Fig. 4.9: Single mode microwave system.

Table 4.2 shows a summary of the main functions of the system, the parameters measured and how these measurements are performed. All the microwave components in this system use flange WR-284 which has the internal standard dimensions: *a*= 2.84 inch (7.21cm) and *b*=1.42 inch (3.60cm). Detailed information about the components is presented in the following section.

Table 4.2: Main features of the single mode microwave system.

Function	**Parameter**	**Performed by**
Control	I-Temperature II-Power III-Water flow	I, II- Computer III- Valves
Measure	I-Temperature II- Power III- Frequency IV- Equivalent electric of the load	I- Infrared sensors and thermocouples II, III, IV – Impedance analyzer
Tuning	I- Impedance II- Resonance	I- Tuner, iris II- Short circuit
Isolate	Reflected power	Circulator with dummy load
Attenuate	Forward power	Circulator with dummy load and power reflector
Exhaust	Exhaust air, gasses or vapor	Exhaust system
Cooling	Water flow	Chiller

4.2.1 Main components of the system

This section provides a brief description of the main components of the system and focuses on the features of the components that allow the system to perform and the criterion used to choose such components. Appendix B provides a list of the components and their

specifications, and further information can be obtained from their manufacturers. Components related with temperature measurement are described in the next section.

1. Power control unit

This unit provides the voltage and current to the generator and can vary the power from 450W to 3KW. Power can be controlled manually or using a remote control. This set-up uses the remote control, which is managed by the power interface or by a computer. It has sensors to detect arcing in any of the microwave components, overheating in the generator or power unit, and microwave leaks in the microwave source.

2. Generator

The generator is made up of a 3KW magnetron tube with its cooling system. The magnetron tube is the microwave source and, even though the technical manual maintains that the frequency is 2.45GHz, the actual frequency varies with the power output. According to microwave equipment manufacturers [5], this behavior is common when the magnetron works at powers much lower than its nominal power. The variation of frequency as a function of power output from 0.1 to 2KW was measured and is shown in Fig. 4.10. Appendix C presents the procedure regarding how this frequency-power relationship was obtained.

3. Power interface

The power interface is an electronic card that provides the control signals to the power unit to regulate the power output of the generator. The power interface used in this microwave system is the third version built (by the author). Originally, it was designed to control a

multimode microwave oven, but then it was substantially modified and adapted to the requirements of the single mode system. It was designed and built to work in two modes, manual and automatic. The manual mode regulates the power output of the generator very precisely, and the automatic mode is controlled by the computer.

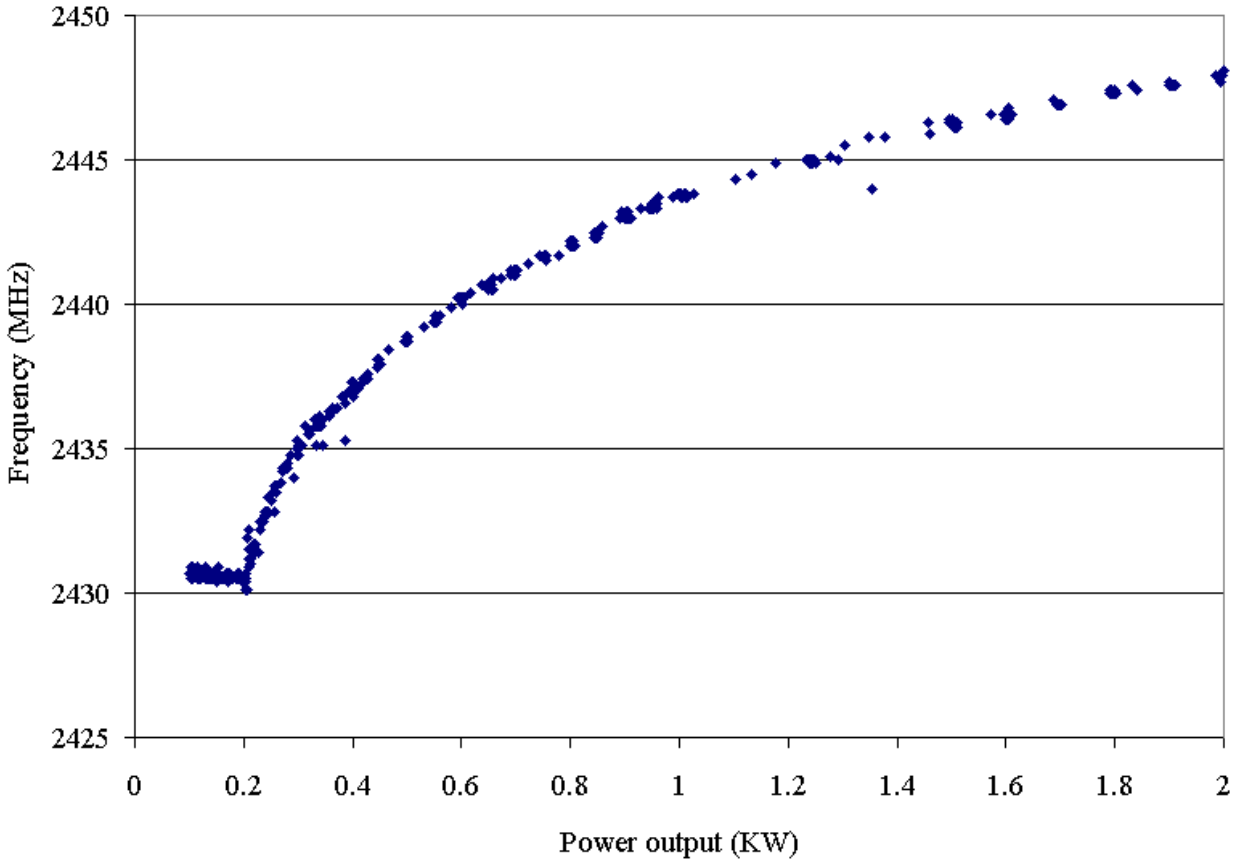

Fig. 4.10: Frequency of the generator as a function of its power output.

4. Double circulator system

This microwave set-up combines two circulators and is shown in Fig. 4.11. A circulator is a component that allows microwaves to pass in one direction, but not the other [6]. The circulators used in this system have three ports (Port 1, Port 2, and, Port 3) that direct the

microwave signal from Port 1 to Port 2, from Port 2 to Port 3, and from Port 3 to Port 1. For example, if a microwave signal enters Port 1, it is directed to Port 2.

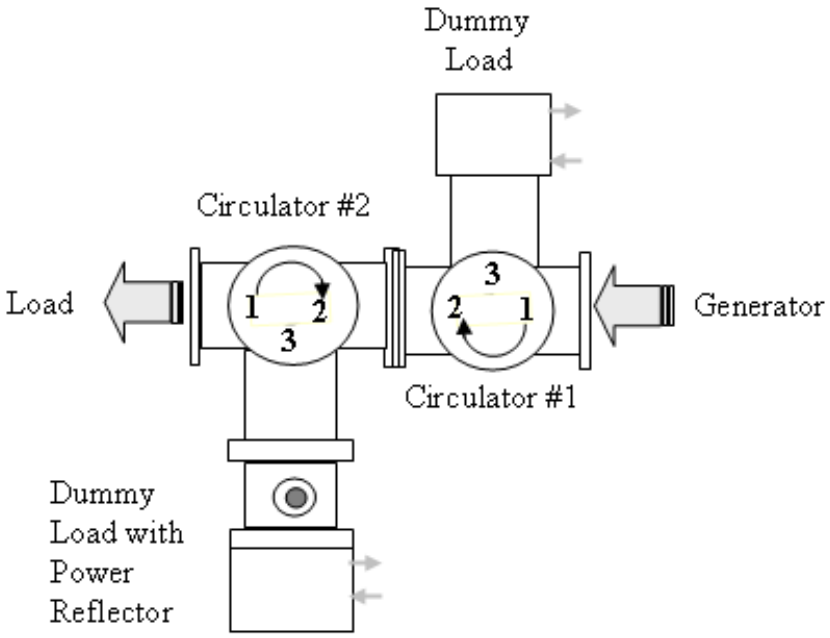

Fig. 4.11: Double circulator used in the microwave system.

In this system, the objective of Circulator #1 is to protect the generator. If reflected power (P_R) is sent back, this power is received by Port 2 which sends it to Port 3. This circulator has a dummy load (water passing through a microwave-transparent material) installed in Port 3 that adsorbs the P_R. In this way, Circulator #1 protects the microwave generator from being damaged by the P_R. For that reason, this circulator is called the isolator circulator.

The objective of Circulator #2 is to allow the microwave system to provide powers levels lower than the minimum power of the generator (Fig. 4.11). When the minimum microwave power from the generator is received in Port 2, it is sent to Port 3 that contains a power reflector. This device regulates how much power is reflected and sends it to Port 1. The power that is not reflected by this device is absorbed by a dummy load. Sometimes, it is necessary to attenuate the

power that is sent to the cavity or load to have better control over the heating and the distribution of the field on the load. Thus, this circulator works as an attenuator circulator.

5. Impedance analyzer

The main objective of this component is to provide a map, Smith chart, in which the optimum position of the tuner and short circuit termination can be ascertained. This component measures reflected power, forward power, and frequency.

6. Tuner

The objective of the tuner is to match the impedances before and after the tuner. When those impedances are the same, there is no P_R. Sometimes, it is not possible to match both impedances, so the best tuning is achieved when the lowest P_R is obtained. Tuning is performed by changing the position of the tuner stubs (variable tuner). By using the impedance analyzer, one can detect when the best tuning is reached. The tuner used in this system has three stubs; this configuration provides the capability of matching a broad range of impedances [7]. It can be installed anywhere along the propagation path of the microwaves, but ideally the tuner should be as close as possible to the load, so matching the impedance of the load vs. the microwave source would be the aim.

7. Iris

The iris has two functions in this system; one is similar to the tuner's function, but this device is a fixed tuner. The other is to determine the beginning of the cavity; therefore, one can know the size of the cavity for further calculations.

8. Short circuit termination

By using this component, one is able to physically change the size of the cavity. Any change in the dimensions of the cavity produces a variation in impedance; consequently, a change in the distribution of the electromagnetic field. In this research, the short circuit termination maintains the length of the cavity at three times $\lambda_g/2$ and in this way, the cavity conserves the TE_{103} distribution of the field and resonance (based on Eq. 3.28 and shown in Fig. 4.12).

9. Cavity

This is the most important component in the microwave system, and the place where the sample receives the microwave heat treatment. The cavity used is a TE_{103} cavity, and has an electric field distribution as shown in Fig. 3.7. The cavity has a cooling system (cold water passing around) that maintains its walls at temperatures lower than 70°C. It is common to think that the cavity is only that component between the tuner and the short circuit termination (Fig. 4.9); however, the entire cavity is between the iris and the internal wall of the short circuit termination, as shown in Fig. 4.12. This figure also illustrates the distribution of the electrical field in the direction of propagation, and the positions where the sample and a probe (electrical field sensor) are placed. It is important to point out that both elements, the sample and the probe, are positioned at a distance equal to $\lambda_g/2$ from each other, on a maximum electrical field location. Consequently, if the cavity contains a sample, the magnitude of $\boldsymbol{E}$ measured by the sensor would be approximately the magnitude of $\boldsymbol{E}$ on the surface of the sample.

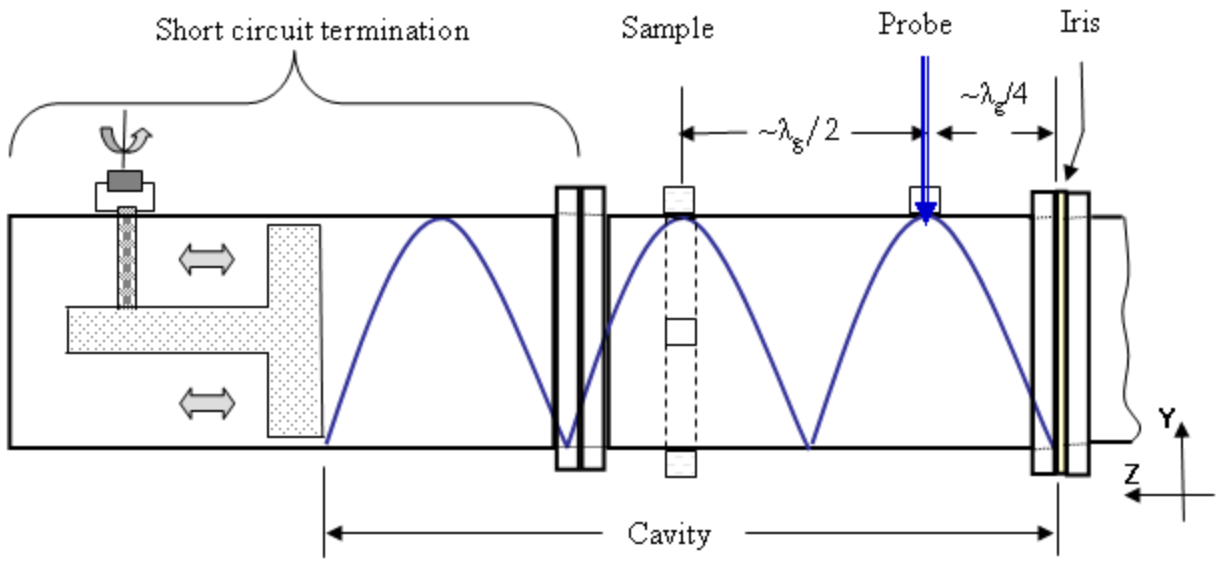

Fig. 4.12: Microwave cavity and its components.

10. Power meter

This component measures the power of the cavity at the position of the probe. It is important to know that the probe detects the strength of the electric field (*V*/m), and the power meter converts this signal into Watts [8]. To use this power meter, it must be calibrated with equipment that provides the power absorbed by the cavity. After calibrating this meter to read the power inside the cavity, its power scale (Watts) can be converted into an electric field scale (*V*/cm) by using Eqs. 3.35 and 3.36 (procedure is shown in Appendix D). Thus, the power meter in this set-up is used to indicate the electric field instead of power. Fig. 4.13 shows the electric field scale measurement equivalent to the power scale indicated by the power meter. In this way, the electric field on the port is measured, which is approximately the magnitude of ***E*** at the sample position.

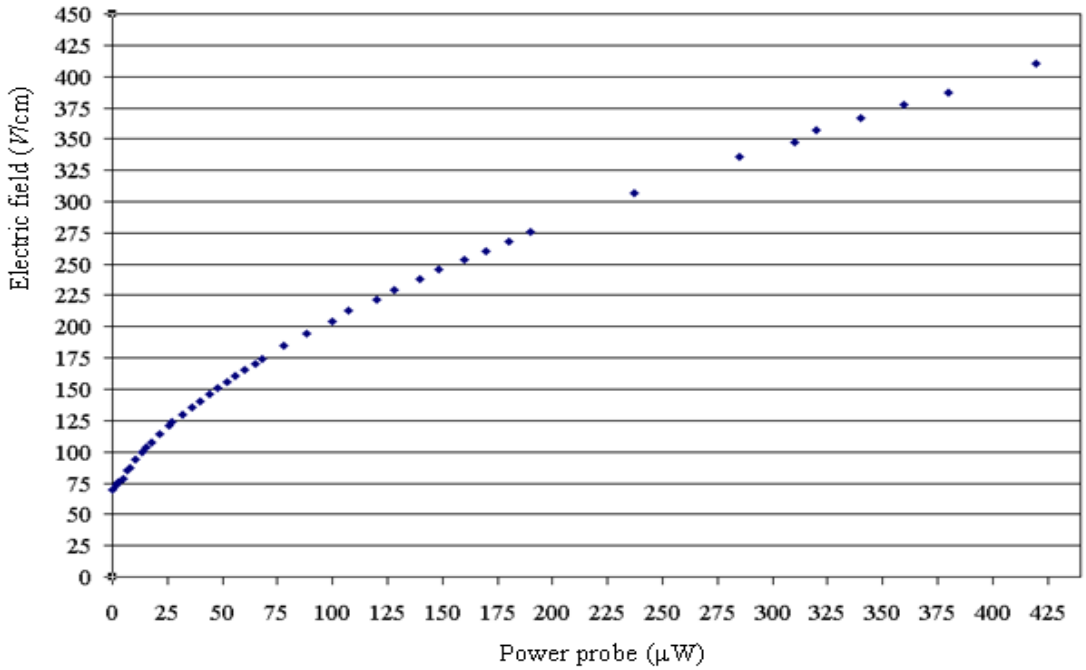

Fig. 4.13: Conversion of the power meter scale (Watts) into electric field scale (*V*/cm).

11. Microwave-controlled software

Software to control the microwave system and perform data acquisition features was developed for this project. The software uses Visual Basic programming and was designed by a former Ph.D. student, P. Mellodge. Originally, it was developed to control a multimode cavity. Major modifications were implemented to work with the requirements presented by the single mode system. During this research, several features were suggested (by the author) for integration into this software. Several versions of this software have been created; the version used by the single mode system in this project is the No. IV.

The single mode system was designed to have different capabilities, so microwave processing of materials could be performed using this equipment. A sample set-up was added, enabling silica aerogel processing. **This procedure design and implementation satisfied objective two proposed in Section 1.4.**

4.3 Sample set-up

Silica aerogel is a material with a low dielectric loss. The aerogel studied in this research had a ε''_{eff} equal to 0.27 at room temperature (2.45GHz). To trigger microwave absorption in this material, a hybrid heating set-up was designed to hold the sample in the single mode microwave cavity.

Basically, microwaves heated up a susceptor material (20 wt% (8 mol % yttria/ zirconia)/80% alumina) producing a conventional heating effect on the sample. When the sample increased in temperature, ε''_{eff} increased and the material absorbed more microwave energy. This behavior was confirmed when ε''_{eff} was measured on two samples (850°C and 1100°C) after they were cooled back (dashed lines in Fig. 5.9). These samples revealed that the dielectric loss increased at higher temperatures. Because the distribution of ***E*** in this cavity was known, the sample was placed in a position where ***E*** was maximum (Em), and the susceptor was at a position where ***E*** (Es) was lower than the one on the sample (Fig. 4.14). In this way, the sample experienced an ***E*** of larger magnitude than the susceptor and was more likely to absorb higher power.

Table 4.3 shows the parameters used to determine the relationship between Em and Es and the guide wavelength for a microwave frequency equal to 2.45GHz. It is important to keep in mind that this microwave system presented variations in frequency depending on the power output, so if the electric field was to be obtained, one had to know the real frequency at the time of measurements.

The susceptor was surrounded by a thermal insulator material that was also a microwave transparent material, porous alumina. This material protected the microwave cavity from

overheating and kept the heat in close proximity to the sample. The samples processed did not have a specific shape, but their weights were between 75 and 80 mg. The dimensions of the small cavity formed by the porous alumina that held the sample was 3x4x2 cm, as shown in Fig. 4.14.

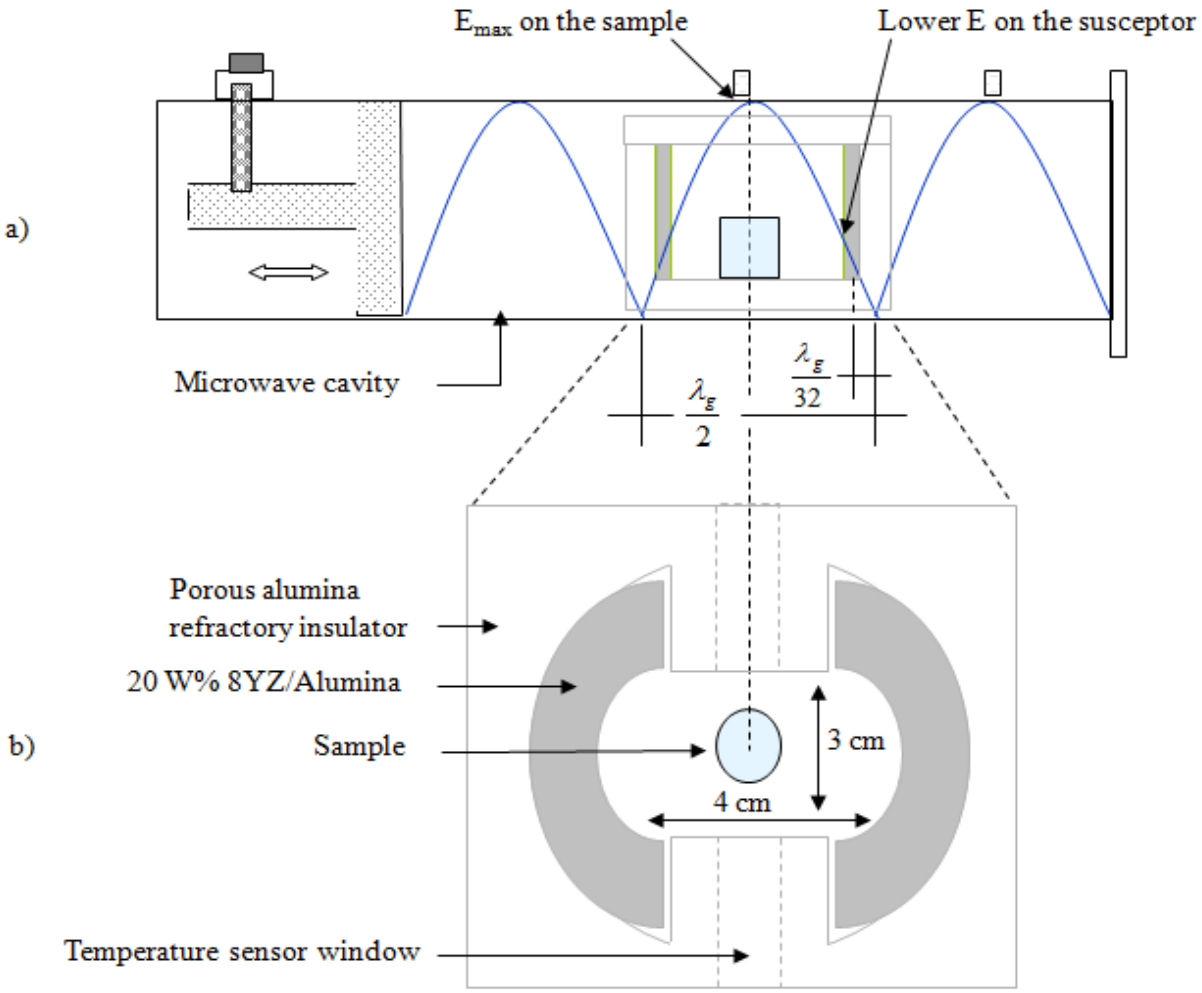

Fig. 4.14: Hybrid heating set-up used to trigger microwave absorption in the aerogel sample: a) schematic of the cavity with the E distribution and susceptor/sample locations, b) detailed schematic of the sample/susceptor/insulation set-up.

Table 4.3: Parameters to calculate the relationship between Em and Es.

Parameter	Value	Equation used
Microwave frequency (f_o)	2.45 GHz	n/a
Wavelength of f_o (λ_o)	12.24 cm	$\lambda_o = c/f_o$
Wavelength of the cut-off frequency (λ_c)	14.42 cm	(3.29)
Guide wavelength (λ_g)	23.15 cm	(3.28)
Electric field on the susceptor (Es)	~ 0.20 Em	(3.31)

4.4 Temperature measurement set-up

Temperature measurements were performed in the single mode cavity using two different methods. The first method employed infrared pyrometers (IRPs) and a thermocouple (TC), and the second method used only thermocouples. Both methods considered the requirements for these types of temperature sensors in a microwave cavity, as discussed in Appendix E.

4.4.1 Method using IRPs and TC

Temperature was measured with a TC and two single-color IRPs (a low- and a high-temperature IRP). The low-temperature pyrometer (LTP) measured temperatures from 20 to 500ºC and worked in the IR wavelength range from 8 to 14µm. The high-temperature pyrometer (HTP) measured temperatures from 350 to 2000ºC and worked in the IR range from 2.0 to 2.7µm. The thermocouple used was type K, internally grounded with a metallic shield. Appendix B provides more specifications about these components.

The experimental procedure was divided into two stages:

1. Stage I: During this stage, emittance (e_m) data was recorded for samples in a conventional tube furnace and inside the microwave cavity. In both cases, temperature was measured with a TC on one side of the sample and an IRP on the other side (Fig. 4.15). The objective of this stage is that once the emittance vs. temperature data was obtained for the material processed, then this information can be used in subsequent temperature measurements. In the case of the microwave temperature measurements, the TC was grounded to the cavity. The distances from the sample to the temperature sensors (Md) and field of view were kept the same in both cases (80 mm and 3mm from IRP and TC to the sample, respectively; and field of view of a target's diameter equal to 8mm). After e_m data was obtained, an equation that fits this data was calculated. This equation was used in the software that controled the microwave system to perform subsequent temperature measurements using IRPs. The procedure followed is illustrated in Fig. 4.16, and the e_m data obtained is shown in Fig. 4.17. This data can be represented by a constant value since the variation is very small (≤ 0.1), as is shown in Fig. 4.17 by a dashed line.

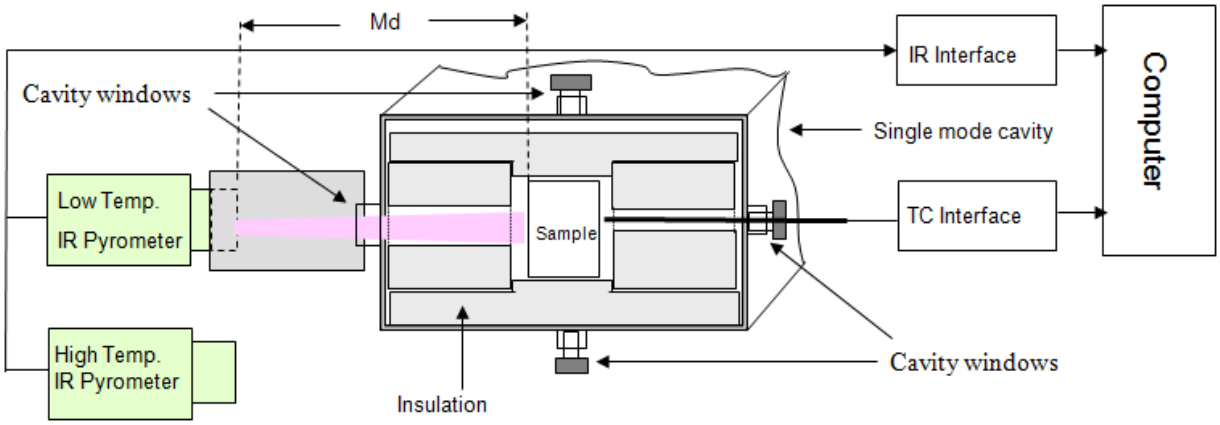

Fig. 4.15: Section of the TE_{103} cavity that shows the position of the temperature sensors.

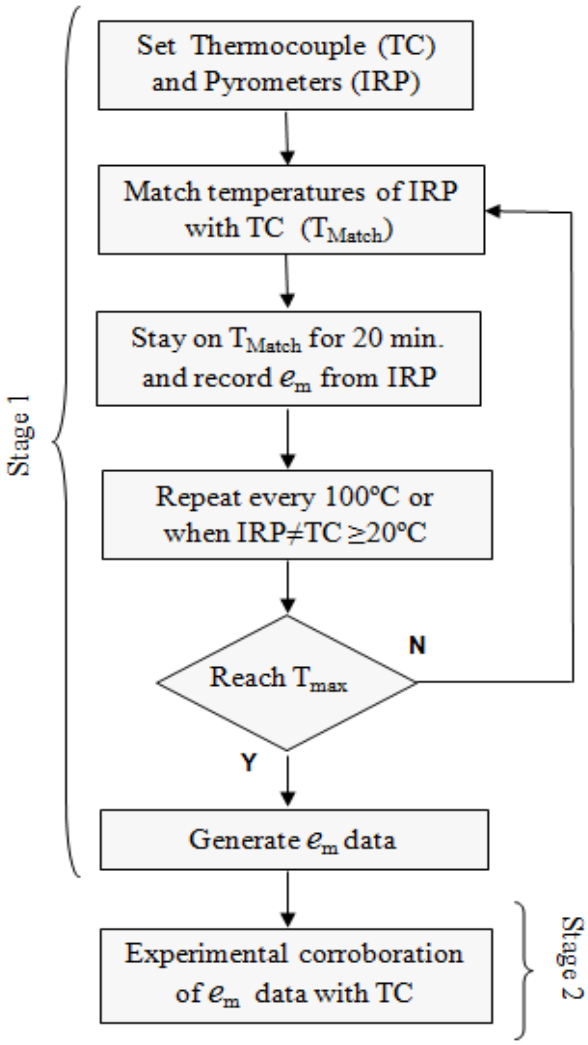

Fig. 4.16: Procedure followed to measure temperature using IRPs and TC.

2. Stage II: The emittance equation obtained in Stage 1 was corroborated experimentally. New samples were heated, up and the equation for e_m was used to generate the temperature measurements with the IRPs. The temperature of these samples also was measured with a TC, and both temperature profiles were compared to determine the precision of the temperature measurements obtained with the IRPs. A temperature profile that shows the performance of these sensors measuring temperature in a microwave cavity is shown in Fig.

4.18. Both pyrometers operate over two different wavelengths as a result, a discontinuity is observed on the plot (red dots circumferences in Fig. 4.18) when they are changed manually.

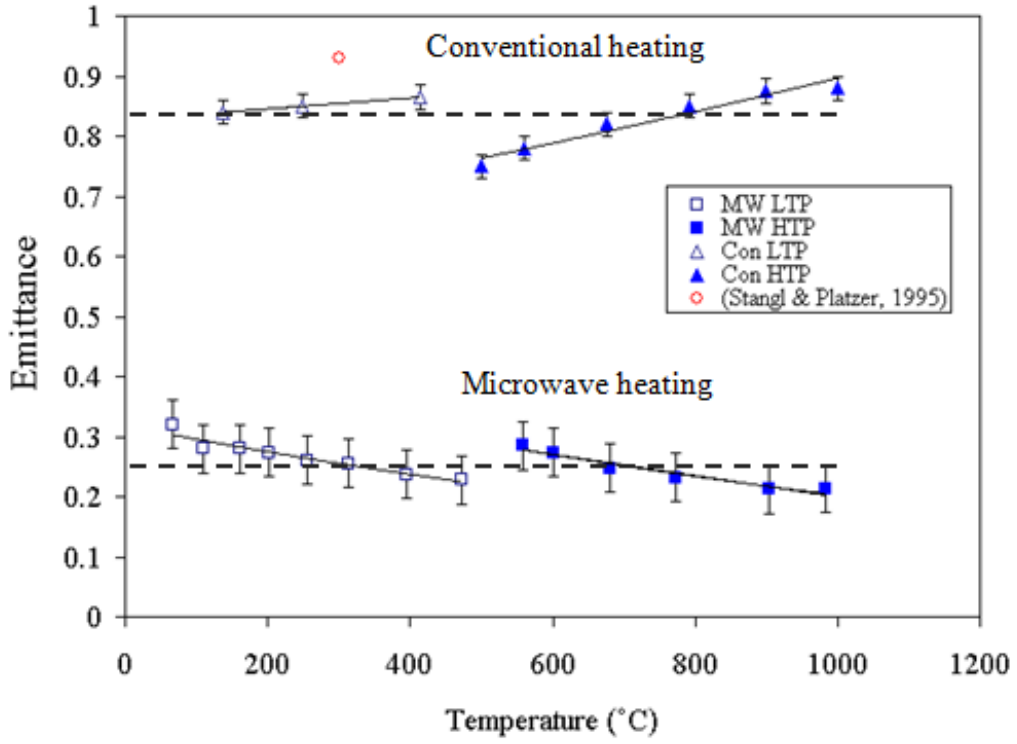

Fig. 4.17: Emittance data obtained for aerogel samples in a conventional oven and a single mode microwave oven.

Using the in situ emittance data, intentional variations in temperature were performed (by changing the input power of the cavity) in the temperature profile between 1800 and 3000 seconds to test the method under different conditions than the ones used to record the e_m. It can be seen that the TC and IRP- measured data were very close, falling within a temperature range of ±20ºC. The value of this method is that a practical way to perform reproducible measurements with a pyrometer in a microwave cavity is provided. It is important to note that after these two stages were accomplished, subsequent experiments on the tested material did not require use of the TC because the IRPs could provide the temperature data.

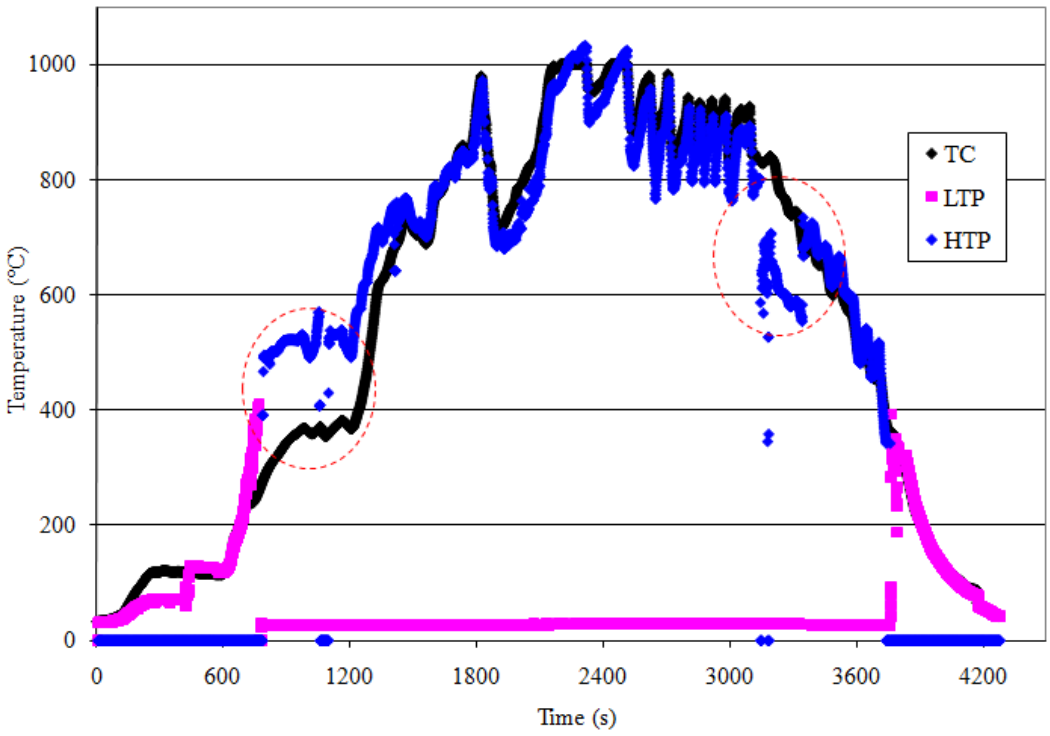

Fig. 4.18: Temperature profile on a silica gel sample obtained using a thermocouple and infrared pyrometers in a single mode microwave oven.

4.4.2 Method using thermocouples

Temperature was also measured using thermocouples in the single mode cavity. The thermocouple used was type K and more specifications about this component can be found in Appendix B. The set-up used in this method was similar to the one shown in Fig. 4.15. The difference was that if one wanted to use another thermocouple, it could have been installed in the cavity window where the IRP was placed. Fig. 4.15 shows that there was a window on every side of the cavity, but only the ones to the left and right sides were used to install the thermocouples. Electromagnetic boundary conditions in the microwave cavity require that ***E*** be normal to a metal body[9], so it was important to know the distribution of ***E*** in the cavity (Fig. 3.6c). Thus using the thermocouple in the position shown in Fig. 4.15, the ***E*** distribution was

perpendicular to the thermocouple, and the distortion of the field was substantially reduced. Therefore, the temperature reader showed steady measurements, and reliable temperature measurements could be performed. This observation was corroborated by installing a thermocouple in the upper window of the cavity, and no steady measurements were observed on the temperature reader due to the distortion that the metal body produced when it was parallel to $\boldsymbol{E}$ in the cavity. One of the advantages that a TE_{10} cavity offers is to have a functional distribution of the field that allows us to predict what would be the optimal position to introduce a thermocouple.

During this research, a comparison between the silica aerogel parameters observed under a conventional and microwave heat treatment was performed. Consequently, it was vital to minimize the differences between temperature measurements in both heat treatments. The method that used the IRPs sensors provided more reproducible measurements in the microwave oven than in the conventional furnace. Therefore, in this study, the results provided were measured using only thermocouples, which provided reliable measurements in both types of processes. To provide further confidence in the measurements, the same thermocouple was used in both types of processes. Thus temperature differences that could result due to different sensors in every system were reduced or eliminated. **Objective three, which was to develop a reliable method for measuring temperature inside a microwave cavity, was satisfied.**

4.5 Dielectric measurements

Dielectric measurements were performed using the cavity perturbation technique (CP), which measured dielectric constant and dielectric loss of a material in a resonant cavity with controlled atmosphere. The fundamental principle for this technique is that the electromagnetic

field (EM) out of the sample in the cavity is not significantly different from the EM of the empty cavity [9, 10]. Based on this principle, researchers have derived the variation in complex resonant frequency (ω*) when a sample is inserted in an empty resonant cavity, shown in Eq. 4.1 [10-13].

$$\frac{\omega_S - \omega_C^*}{\omega_C^*} = -\frac{\int_{V_S}[(\varepsilon_S - \varepsilon_C^*)E_S.E_C^* + (\mu_S - \mu_C^*)H_S.H_C^*]dV}{\int_{V_C}(\varepsilon_C E_C^*.E_S + \mu_C H_C^*.H_S)dV} \tag{4.1}$$

Where * denotes a complex identity, V is volume, and the subscripts S and C indicate parameters of the sample and the empty cavity, respectively (Other symbols in Eq. 4.1 have been defined in Chapter III).

Equation 4.1 is the basic cavity perturbation formula where the numerator on the right side represents the energy stored by the sample and the denominator represents the total energy stored in the cavity, with the assumption that the fields in the sample are uniform over its volume. This basic assumption is valid if V_S is very small compared to V_C, and smaller than the resonant wavelength. According to Hutcheon et al [14], to verify that this assumption has been met, the stored energy in the sample must be smaller than 1% of the energy stored in the cavity, which is usually observed when $\frac{\Delta f}{f}$ is less than 0.1% [15].

In addition, the complex resonant frequency can be expressed as [10, 13]

$$\frac{\omega_s - \omega_c^*}{\omega_c^*} = \frac{\Delta f}{f} + \left(\frac{1}{2\Delta Q}\right)i = \frac{f_s - f_c}{f_c} + \left(\frac{1}{2Q_s} - \frac{1}{2Q_c}\right)i \tag{4.2}$$

Knowing that the permittivity and permeability of the cavity are those of the free space (ε_o and μ_o), the complex electric and magnetic susceptibilities (χ_e and χ_m) are defined as

$$\chi_e = \frac{\varepsilon^* - \varepsilon_o}{\varepsilon_o} = \varepsilon_r - 1 \tag{4.3}$$

$$\chi_m = \frac{\mu^* - \mu_o}{\mu_o} = \mu_r - 1 \tag{4.4}$$

where,

$$\varepsilon_r = \varepsilon' - \varepsilon'' i \tag{4.5}$$

$$\mu_r = \mu' - \mu'' i \tag{4.6}$$

combining Eqs. 4.2 and 4.3, the difference in complex frequency expressed by Eq. 4.1 can be written as

$$\frac{f_S - f_C}{f_C} + \left(\frac{1}{2Q_S} - \frac{1}{2Q_C}\right) i = \frac{-\int_{V_s} \left(\chi_m \mu_o H_S . H_C^* + \chi_e \varepsilon_o E_S . E_C^*\right) dV}{\int_{V_c} \left(\varepsilon_o E_C^* . E_C^* + \mu_o H_C^* . H_C^*\right) dV} \tag{4.7}$$

If the resonant cavity used is a single mode cavity, one has the advantage of knowing where the maximum E and H are present, and the effect of the field on the sample can separate. Consequently, one can choose the field related to the property of interest. For example, if dielectric properties are obtained, the place for the insertion of the sample in the single mode cavity should be that position where the influence of E is maximum and the effect of H is almost negligible. Therefore, Eq. 4.7 can be reduced to

$$\frac{f_s - f_c}{f_c} + \left(\frac{1}{2Q_s} - \frac{1}{2Q_c}\right) i = -\chi_e . \frac{\int_{V_S} E_S . \varepsilon_o E_C dV}{2\int_{V_C} \varepsilon_o E_C . E_C dV} \tag{4.8}$$

Stratton et al [16] derived an expression for a static electric field in a sample (constant and uniform electric field in the sample) with the shape of an ellipsoid of rotation (Eq. 4.9).

$$E_S = \frac{E_C}{1 + \chi_e . F_{SH}} \tag{4.9}$$

Where, F_{SH} is the shape factor for the static electric field equal to

$$F_{SH} = \frac{\left(1-e^2\right)}{e^2}\left[\frac{1}{2e}\ln\left(\frac{1+e}{1-e}\right)-1\right] \tag{4.10}$$

and e is the eccentricity of the ellipsoid of rotation equal to

$$e = \sqrt{1-\left(\frac{c}{a}\right)^2} \tag{4.11}$$

Combining Eqs. 4.8 and 4.9, the change in complex frequency can be expressed as

$$\frac{f_s - f_c}{f_c} + \left(\frac{1}{2Q_s} - \frac{1}{2Q_c}\right)i = -\frac{-\chi_e}{\left(1+\chi_e F_{SH}\right)}\left(\frac{V_S}{V_C}\right)A \tag{4.12}$$

where,
$$A = \frac{\left|E_{C(SAMPLE)}\right|^2}{2\int_{V_C}\left|E_C\right|^2 dV} \tag{4.13}$$

Here, A is a real unitless constant that depends on the distribution of the electrical field in the empty cavity, and the field in the place of the sample when the cavity is empty ($E_{C(SAMPLE)}$).

If
$$K_C = \frac{V_C}{V_S A} \tag{4.14}$$

and
$$\delta f_{CF} = \frac{f_s - f_c}{f_c} + \left(\frac{1}{2Q_s} - \frac{1}{2Q_c}\right)i \tag{4.15}$$

combining Eqs. 4.12 to Eq. 4.15, χ_e can be expressed as

$$\chi_e = \frac{-K_C \delta f_{CF}}{1 + F_{SH} K_C \delta f_{CF}} \tag{4.16}$$

Based on Eqs. 4.3 and 4.5,
$$\varepsilon' = \text{Real part}(\chi_e) + 1 \tag{4.17}$$

and
$$\varepsilon'' = -\text{Imaginary part}(\chi_e) \tag{4.18}$$

During this research, a 2.45GHz TE_{103} single mode cavity was used to perform the cavity perturbation characterization (same type of cavity as used to heat the samples), as shown in Fig. 4.19. This cavity was designed and built (by the author) such that the sample could be

introduced in a location where *E* was maximum and negligible *H* consequently, the analysis was reduced to utilizing the electrical field only. The sample size was substantially smaller than the size of the cavity and size of the resonant wavelength, so the basic assumption was more likely to be met. However, in practice, the shape of the sample used was not an ellipsoid of rotation.

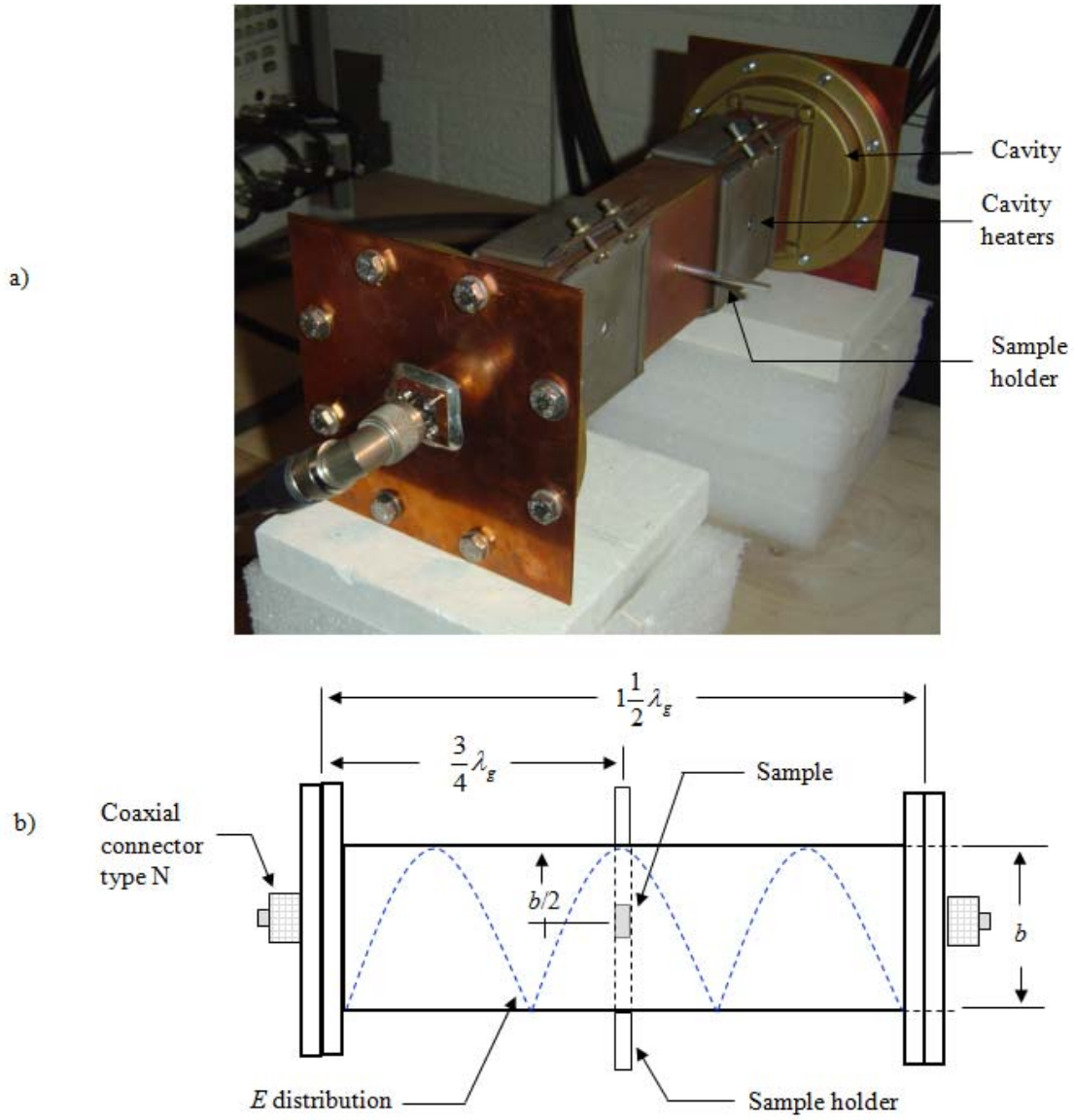

Fig. 4.19: Resonant cavity used to measure dielectric properties: a) picture of the cavity, b) schematic of the cavity with its dimensions (top view). This apparatus was designed and built by the author.

Therefore, a new calibration constant (F_m) has been used to adjust F_{SH} to the real shape of the sample (cylinder of 8.5 x 2.7mm, length x diameter), which transforms Eq. 4.16 into Eq. 4.19. In addition, the sample is held in the middle of the second variation of E by a sample holder producing a symmetric perturbation. The sample holder is made of fused silica (low ε' and ε") which presents an extremely low perturbation on E. However, the analysis carried out takes the information of the empty sample holder in the cavity as the f_c and Q_c. Therefore, the effect of the sample holder is subtracted (previously probed by researchers [17]) to reduce its influence in the analysis of the sample's dielectric properties.

$$\chi_e = \frac{-K_C \delta f_{CF}}{1 + F_m F_{SH} K_C \delta f_{CF}} \tag{4.19}$$

The complete set-up used to measure dielectric properties is shown in Fig. 4.20, which included a network analyzer (HP87531C from Hewlett-Packard) and a small furnace (1400A from Thermolyne). The network analyzer fed the cavity with a microwave frequency range from 2440 to 2460MHz and read the shift in resonant frequencies and Q of the empty and loaded cavity. The furnace heats the sample to a specific temperature and then the sample was introduced into the microwave cavity to carry out the dielectric measurements. Temperature differences when the sample was translated from the furnace to the cavity were recorded, and the data provided was at the actual temperature of the sample in the cavity.

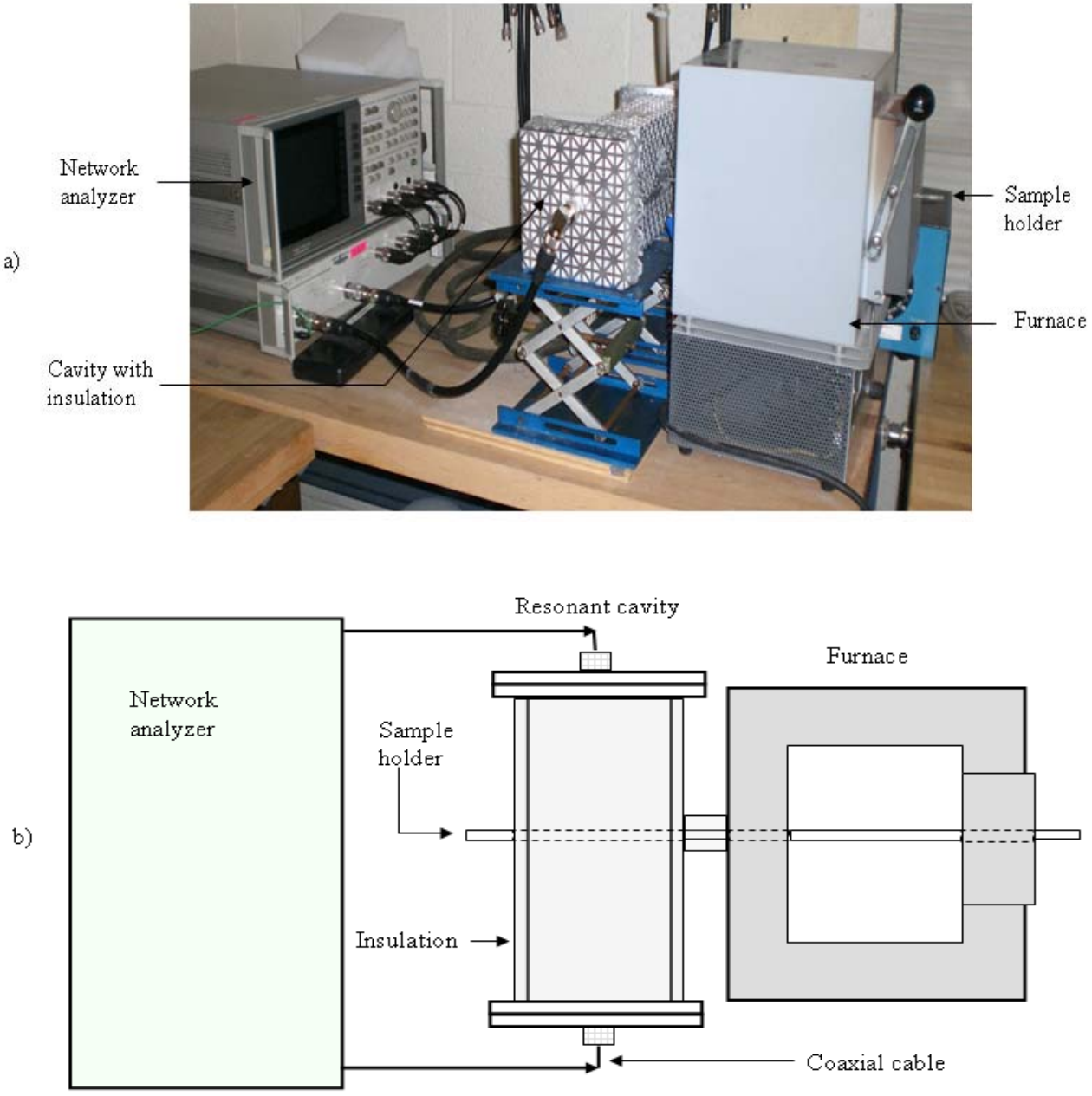

Fig. 4.20: Cavity perturbation set-up used to measure dielectric properties of silica aerogel: a) photography of set-up, b) schematic of the set-up (top view). This apparatus was designed and built by the author.

A program using Mathematica® software, DMeasurements, was developed to perform the dielectric measurement analysis. This program used dielectric constants of known materials with the same shape of the sample to estimate the values of A and F_m. Having these calibration constants, Eqs. 4.13 to 4.18 were used to calculate the dielectric constant and dielectric loss of the aerogel samples or other materials. **With the completion of this cavity perturbation system, objective four, the design and construction of a system capable of measuring dielectric properties of silica aerogel, was satisfied**.

4.6 Methodology for characterizing structure of aerogels

This section provides a brief description of the characterization techniques used in this research and the parameters obtained using these techniques. A summary of the techniques used is shown in Table 4.4.

Table 4.4: Characterization techniques used during this research project. The majority of the data collected in this study was obtained using the first four techniques.

No	Technique	Information Provided
1	Helium pycnometry	• Structural density
2	Adsorption/desorption surface analysis	• Surface area • Pore volume • Pore radius • Distribution of surface area
3	Archimedes principle	• Bulk density
4	Fourier transform infrared spectroscopy (FTIR)	• Structural bonding information
5	Differential scanning calorimetry (DSC)	• Phase change
6	Thermogravimetric analysis (TGA)	• Mass loss
7	Focus ion beam (FIB)	• Preparation of samples to use in transmission electron microscopy
8	Scanning electron microscopy (SEM)	• Surface structural features
9	Transmission electron microscopy (TEM)	• Onset of nucleation/crystallization
10	X-ray diffraction (XRD)	• Onset of crystallization • Crystalline phases present
11	Atomic force microscopy (AFM)	• Surface topography

4.6.1 Pycnometry

In this study, structural density was measured using a pycnometer, AccuPyc 1330 from Micromeritics. This instrument determined the volume of solid objects of irregular or regular shapes by measuring the pressure change of a gas in a known volume. The gas utilized by this system was helium because of its inertness and small molecular size, which could penetrate the finest pores to insure a better accuracy. Once the volume was obtained, the density could be calculated automatically if the sample weight was provided [18].

A simplified block diagram of the pycnometer system is shown at Fig. 4.21. Assuming the cell and the expansion chambers are at ambient temperature (T_a), the valve S_I is at position P_a (atmospheric pressure), and the valve S_{II} is close then the equation for the expansion volume (V_E) is

$$P_a V_E = n_E R T_a \tag{4.20}$$

where,

n_E = number of moles in the expansion chamber

R = gas constant

When the sample is introduced into the cell chamber, it is charged with a pressure P_1 by positioning S_I at P_H (helium gas pressure), and the valve S_{II} is open as a result the equation for the cell chamber is

$$P_1(V_C - V_S) = n_C R T_a \tag{4.21}$$

where,

V_C = volume of the cell chamber

$V_S =$ volume of the sample

$n_c =$ number of moles in the cell chamber

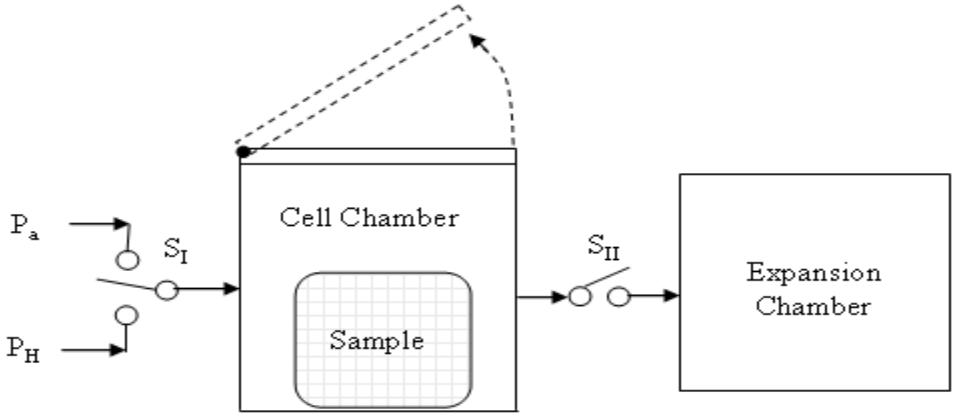

Fig. 4.21: Block diagram of a pycnometer.

When the valve S_{II} is closed, P_1 is reduced to a pressure P_2, and the new mass balance equation becomes

$$P_2(V_C - V_S + V_E) = n_C RT_a + n_E RT_a \tag{4.22}$$

Substituting Eqs. 4.20 and 4.21 into Eq. 4.22:

$$V_S = V_C - \frac{V_E}{\frac{P_{1g}}{P_{2g}} - 1} \tag{4.23}$$

where,

$$P_{1g} = P_1 - P_a \tag{4.24}$$

$$P_{2g} = P_2 - P_a \tag{4.25}$$

Equation 4.23 provides the volume of the sample as a function of two known volumes, and two pressures measured by the pressure sensor of the instrument. With the known sample weight (W_D), the structural density (ρ_S) can be calculated as expressed by Eq. 4.26.

$$\rho_S = \frac{W_D}{V_S} \tag{4.26}$$

4.6.2. Gas adsorption surface analysis

Gas adsorption surface analysis is a technique used for the surface and pore size characterization of porous materials. Basically, absorption can be considered as the enrichment of one or more components in an interfacial layer [19]. In the case of gas absorption, the gas/solid interface is the one involved, where the gas and solid are called the absorbed and the absorbent, respectively.

During the absorption surface analysis, the quantity of the gas (nitrogen) adsorbed (or desorbed) from a solid surface at equilibrium vapor pressure is measured. This information is obtained by allowing to enter (or removing) a known volume of gas into a sample cell containing the solid at a constant temperature. As adsorption or desorption takes place, the pressure in the sample cell changes until equilibrium is reached. The volume of gas absorbed (or desorbed) at the equilibrium pressure is the difference between the volume of gas admitted (or removed) and the volume required to fill the space around the adsorbent (void space) [20]. Once the volume-pressure data (absorption isotherm) is obtained, surface area (SA) of the solid tested can be calculated by using the Brunauer-Emmett-Teller (BET) equation (Eq. 4.27).

$$\frac{1}{W\left(\frac{P_o}{P}-1\right)} = \frac{1}{W_m C} + \frac{C-1}{W_m C}\left(\frac{P}{P_o}\right) \tag{4.27}$$

Where, $\frac{P}{P_o}$ = relative pressure

W = weight of the gas absorbed at a relative pressure

W_m = weight of the adsorbate monolayer that covers the surface

C = constant related to the energy of absorption of the first monolayer

A linear plot of $\frac{1}{W\left(\frac{P_o}{P}-1\right)}$ versus $\frac{P}{P_o}$, as shown in Fig. 4.22, will provide the slope (s, Eq. 4.28) and the intercept (i, Eq. 4.29).

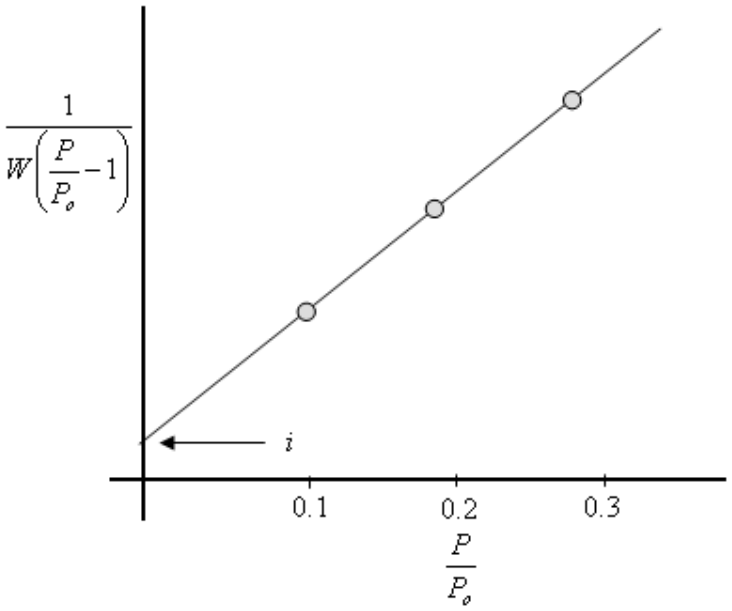

Fig. 4.22: Typical BET plot

$$s = \frac{C-1}{W_m C} \tag{4.28}$$

$$i = \frac{1}{W_m C} \tag{4.29}$$

By solving Eqs. 4.28 and 4.29, W_m can be obtained, and the total surface area of the sample (S_t) can be calculated using Eq. 4.30.

$$S_t = \frac{W_m N A_{cs}}{M} \tag{4.30}$$

Where, N = Avogadro's number (6.023×10^{23} molecules/mol)

A_{cs} = cross-sectional area of the adsorbate (for nitrogen is 16.2Å^2/molecule)

M = molecular weight of the adsorbate (for nitrogen is 28.0134 g/molecule)

The specific surface area (SA) can be obtained from the S_t and the sample weight (w), according to Eq. 4.31

$$SA = S_t/w \tag{4.31}$$

During this research, a surface area analyzer, Autosorb-1 from Quantachrome Instruments, was used to obtain the surface area (SA), pore volume (Vp), and distribution of pore volume. This characterization technique was performed on the samples heat treated in both systems, conventional and microwaves. After the sample cells were cleaned with ethanol, they were emptied and maintained in a drying oven at 150ºC for 1h. The cells were removed and allowed to cool for 30 minutes. The empty cells were filled with the bulk sample and allowed to outgas at 200°C for 2h, and then the cells were shifted to the testing section of the analyzer to perform the adsorption analysis. This procedure generally took between 10 to18h for the aerogel samples.

4.6.3 Archimedes principle

Archimedes principle states that when a body is submerged in a fluid, it experiences buoyancy, which is a force equal to the weight of the displaced fluid (W_{DL}). This principle is expressed in Eq. 4.32.

$$Vb = W_{DL} / \rho_L \tag{4.32}$$

Where Vb = volume of the body

ρ_L = density of the liquid

Using Archimedes principle, bulk density (ρ_B) and apparent density (ρ_A) of silica aerogel samples can be measured. The procedure followed is the standard test method described

in detail by the American Society for Testing and Materials Specification, ASTM C373 [21]. The main step to obtain ρ_B and ρ_A is to measure the bulk volume (V_B) and apparent volume (V_A), respectively, as seen in Eqs. 4.33 and 4.34.

$$\rho_B = \frac{W_D}{V_B} = \frac{W_D}{V_S + V_{OP} + V_{CP}} \tag{4.33}$$

$$\rho_A = \frac{W_D}{V_A} = \frac{W_D}{V_S + V_{OP}} \tag{4.34}$$

Where, W_D = weight of the sample (dry)

V_S = volume of the solid material (not including the pores)

V_{OP} = volume of the open pores

V_{CP} = volume of the closed pores

In addition,

$$V_B = \frac{Ws - Wss}{\rho_W} \tag{4.35}$$

$$V_A = \frac{Ws - W_D}{\rho_W} \tag{4.36}$$

where, W_S = weight of the sample with the open pores filled with liquid (saturated)

W_{SS} = weight of the saturated sample when it is submerged (suspended) in the liquid

The saturated weight was measured after the sample was maintained in boiling water for 8h and then allowed to cool in the water for 24h. The suspended saturated weight was obtained when the sample was suspended in water using a digital balance, Mettler Toledo AB204-S with a density measurement kit, Mettler Toledo PR803. In this study, Archimedes principle was used to measure bulk density of the silica aerogel samples.

4.6.4 Fourier transform infrared spectroscopy

Fourier transform infrared spectroscopy (FTIR) has been used in this research to provide information about the chemical bonding in selected silica aerogel samples. The equipment used was a FTIR Nicolet Avatar 330 working in specular reflectance mode with 45º angle of incidence beam, 7 mm sample mask, and 4000 to 400 cm^{-1} analysis range over 32 scans.

It has been reported by researchers that silica aerogel goes through a series of structural changes when it receives a heat treatment [22, 23]. These changes in the material modify its properties, and some of these properties can be determined by evaluating the shift in position or intensity of the FTIR spectrum. This spectrum provides a unique description of how an infrared beam interacts with the sample as a function of frequency or wavelength. The interaction between the IR energy and the sample reflects the vibration of the bonds within the molecule [24]. The vibration is generated by the absorption of infrared radiation that produces a net dipole moment, and it is classified in one of different types of vibrations (symmetric stretching, antisymmetrical stretching, scissoring, rocking, wagging, and twisting) depending on the symmetry of its motion. Therefore, the FTIR spectrum can be used as a fingerprint to identify molecules with bonds that vibrate with the interaction of the infrared energy. In this study, FTIR was used to evaluate changes in Si—O—Si and Si—OH bonds in aerogel as a function of processing conditions.

4.6.5 Differential scanning calorimetry

Differential scanning calorimetry (DSC) is a technique in which a test sample and a reference are subjected to the same temperature profile in a controlled atmosphere. As the sample goes through a physical transformation, such as a phase transition, it will require or

release heat to maintain the same temperature. If heat flows into the sample, then it undergoes an endothermic process. If heat flows out of the sample, the process is exothermic. Thus the DSC measures the differences in the amount of heat to maintain the same temperature [25]. In this study, DSC indicated phase changes, such as evaporation of water, combustion of organic materials, and crystallization.

4.6.6 Thermogravimetric analysis

Thermogravimetric analysis (TGA) is a technique that provides the change in weight of a sample as a function of temperature or time in a controlled atmosphere. During this research, the equipment used was a NETZSCH Jupiter STA 449C (the same equipment was used to obtain the DSC information) which provided information that was used to determinate the magnitude of material loss or gain as the sample heat up [25]. Knowledge about the weight changes suggested the nature of processes the materials underwent in various regions of the heating range. In this study, TGA was used to monitor the weight loss of water and alcohol residues from aerogel during heating.

4.6.7 Scanning electron microscopy

The scanning electron microscope (SEM) provides a highly magnified image of the sample surface by scanning it with an electron beam. As the electron beam penetrates the surface of the sample, it produces emissions of electrons and/or protons. Some of the electrons are collected by detectors that generate an output to create an image of the sample's surface on a monitor. The principles by which images are produced are of three types: secondary electron images, backscattered electron images, and elemental X-ray maps [24].

Secondary electrons (SE) are the result of the collision of the primary electrons (electron beam) with an atom which produces an inelastic scattering with the atomic electrons. During collision, some of the energy is transferred to the emitted electrons which have enough energy to leave the sample surface. Most of the emitted electrons are produced within a few nm of the surface. Those produced deeper inside the material suffer additional inelastic collisions that decrease their energy and may get trapped inside the sample.

Backscattered electrons (BSE) and X-ray imaging are also possible in the SEM but were not used in this study. During this research, the equipment used was a LEO 1550 from Carl Zeiss Company that generated images by scanning the secondary electrons. In this study, micrographs were taken to evaluate surface features on the silica aerogel samples.

4.6.8 Focused ion beam

The focused ion beam (FIB) system is an instrument used for specific analysis of materials, such as milling, imaging, and deposition. This instrument has a high degree of similarity with the SEM, but the FIB uses a different particle, ions, to generate the beam that interacts with the sample. Since ions are much larger, heavier and slower than electrons, their penetration depth is lower, so their interaction with the outer atomic shell is higher, resulting in atomic ionization and breaking chemical bonds of the sample atoms [26]. In addition, because ions are heavier than electrons, their momentum is higher. When the ion hits an atom, it will transfer a great part of its momentum because the ion's mass is comparable to that of the atom and, as a result, the atom moves with enough kinetic energy that it can leave the sample, a phenomenon known as sputtering or milling. Therefore, because the beam position, dwell time,

and ion size are precisely controlled, the FIB can be used to preferentially remove material from the sample.

During this research, the FIB (Helios 600 NanoLab from FEI Company) was used to prepare samples for analysis in the transmission electron microscope (TEM). The primary operation performed on the silica aerogel samples was milling the sample to micro-size dimensions. Figure 4.23 shows a preliminary sample milled on the surface of silica aerogel material, and Fig. 4.24 shows a sample milled further using FIB to be characterized in the TEM.

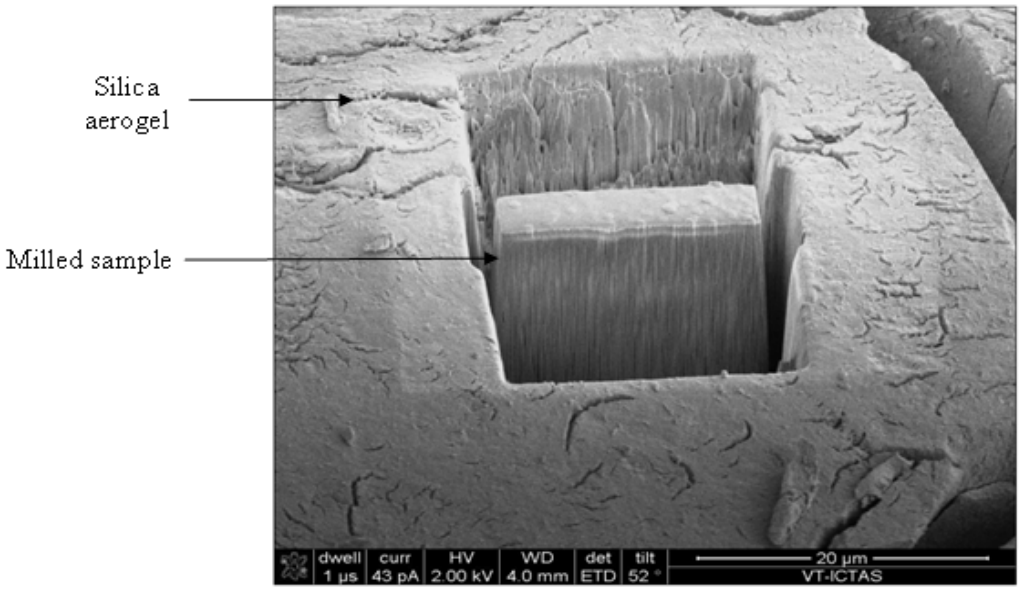

Fig. 4.23: Preliminary sample milled on the surface of a silica aerogel sample.

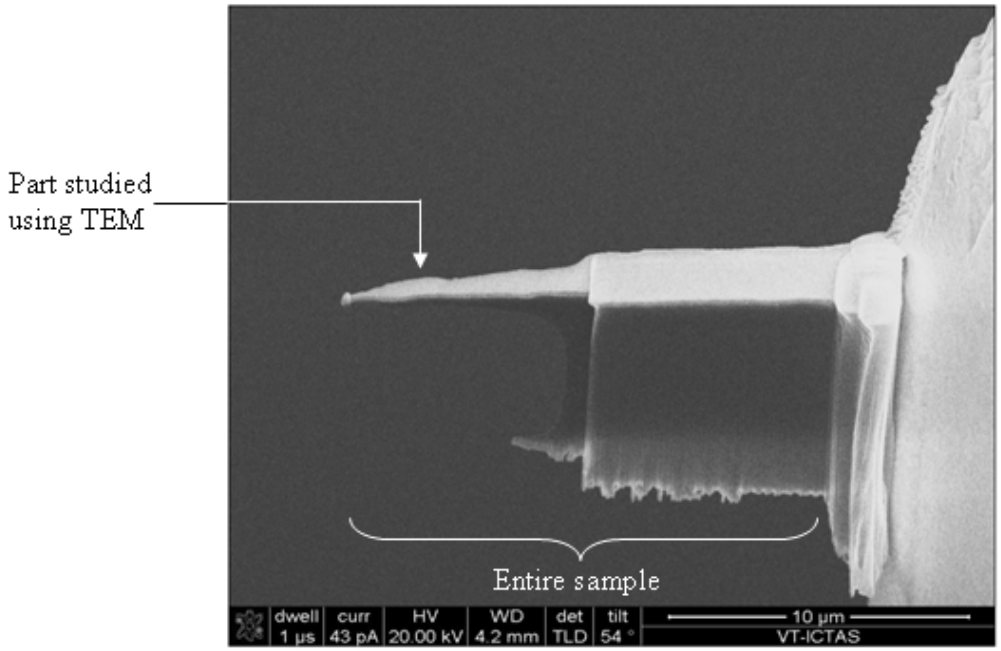

Fig. 4.24: Sample used in the transmission electron microscopy, prepared by further milling of the sample in Fig. 4.23 using FIB.

4.6.9 Transmission electron microscopy

Transmission electron microscopy (TEM) is a technique that provides high spatial resolution, and both image and diffraction information from a sample. The TEM scans the sample with a highly energetic beam of electrons. From this interaction, characteristic radiation and particles (i.e. X-rays, SE, BSE) are produced and measured to generate the material characterization.

With this technique, the sample used is very thin (< 200nm), and the signal obtained comes from both undeflected and deflected electrons that penetrate the sample thickness [24]. Several magnetic lenses are above and below the sample position, which receive and send the signal to a detector. The detector transforms and magnifies the signal into an output that describes the characteristic information of the sample, and this information is sent it to an output

device, such as camera or screen. The TEM can provide a magnification of the spatial information of the sample by as much as a factor of 10^6. However, one of its limitations is the low depth resolution. Because the electron scattering in a TEM is produced from a three-dimensional sample, but is projected onto a two dimensional devise (i.e. screen, camera), the resulting image is the superimposed spatial data at the image plane. Consequently, the operator has to use different techniques (i.e., tilt, specimen thickness, contour evaluation, different diffraction patterns) to determine the spatial information.

During this research, the TEM used was an EM 420 from Philips. Micrographs that revealed the onset of crystallization were obtained on samples that were approximately 100nm thin, as shown in Fig. 4.24.

4.6.10 X-ray diffraction

X-ray diffraction (XRD) is a technique used to identify the crystalline phases in a material and to measure structural properties of these phases [27]. In this research, XRD was used to determine if the material had undergone a change from amorphous to crystalline phase during the heat treatment, and was performed using an instrument model X'Pert PRO from PANalytical Inc. An X-ray tube generates X-rays when an electron beam is accelerated across a high voltage and bombards a stationary or moving solid target. When the electron beam hits the atom of the target, a spectrum of X-rays is emitted (Bremsstrahlung radiation). Normally, this continuous part of the X-ray spectrum is not used in the diffraction work unless an experiment with a number of different wavelengths is carried out. In addition, when the beam collides with the target material that ejects inner shell electrons from the atoms, a free electron needs to fill the hole in the shell then it is when X-ray photons with energy characteristic of the target material

are emitted. These characteristic X-rays are the most useful in the diffraction work and are the ones typically used in diffraction studies [28].

When the sample receives the incident beam of X-rays, the beam is diffracted by the crystalline phases of the specimen according to Bragg's law (Eq. 4.37).

$$\lambda = 2d\sin\theta \tag{4.37}$$

Where, λ = wavelength of the X-ray frequency

d = the spacing between atomic planes

θ = half of the angle between the incident and diffracted X rays

The intensity of the diffracted X-ray is measured as a function of the diffraction angle 2θ and the specimen's orientation. Each crystalline phase produces a set of X-ray peaks at different angles, depending on the atomic spacing between planes. In this study, the XRD was used to determine the onset of crystallization in silica aerogel and to identify the crystalline phases present.

4.6.11 Atomic force microscope

The atomic force microscope (AFM) is a high resolution instrument that scans the surface of the material with a probe. The probe is a cantilever with a tip that has a radius of curvature on the order of nanometers. When the tip is close to the surface of the sample, forces between the tip and the sample produce a deflection of the cantilever according to Hooke's law. Depending on the type of forces producing measured deflections, data can be obtained that describes the surface characteristic of the sample [24]. Typically, the deflection is measured using an infrared or laser bean that is reflected on the surface of the cantilever. The reflection of this beam is measured by an optic sensor that produces an electronic signal that provides the image of the

parameter present on the surface. In this study, the AFM was mainly used to provide information on the topography of the material surface.

Different techniques were applied to characterize monolithic aerogel samples. Results obtained following this methodology are presented in Chapter V. **Thus objective five of this study, to develop a suitable methodology for characterizing the structure of aerogels, was satisfied**.

References

1. Wang, S.-H., *Sol-gel derived silica optics*, *Ph.D. Dissertation in Materials Science and Engineering*. 1988. University of Florida: Gainesville, Florida.
2. Vasconcelos, W.L., *Topological Evolution and Properties of Sol-Gel Silica Monoliths*, *Ph.D. Dissertation in Materials Science and Engineering*. 1989. University of Florida: Gainesville, Florida.
3. Technologies, Q., *E3000 Series Critical Point Drying Apparatus, Operating Manual*. 2002. Quarum Technologies Ltd.: East Sussex, England.
4. Fricke, J., Editor. *Aerogels*. Springer Proceeding in Physics. Vol. 6. 1986. Springer-Verlan: Berlin, Germany.
5. Gerling, J., *Product user manual of the 3KW magnetron head*. 2008. Gerling Applied Engineering, Inc.: Modesto, CA.
6. Scott, A.W., *Understanding Microwaves*. 1993. New York, New York: John Wiley & Sons, Inc.
7. Gerling, J., *Precision 3-stub tuner manual*. 2003. Gerling Applied Engineering Inc: Modesto, CA.
8. Packard, H., *Operating manual 435B power meter*. 1983. Hewlett-Packard Co.: Oreland, PA.
9. Pozar, D.M., *Microwave Engineering*. 2005. Amherst, MA: John Wiley & Sons, Inc.
10. Altschuler, H.M., *Dielectric constant*, in *Handbook of microwave measurements*, Max Sucher and Jerome Fox, Editors. 1963. Polytechnic Press: New York, New York. p. 495-548.
11. Kumar, A. and S.Sharma, *Measurement of dielectric constant and loss factor of the dielectric material at microwave frequencies.* Progress in Electromagnetics Research, 2007. **69**: p. 47-54.
12. Baysar, A., J. Kuester, and S.El-Ghazaly, *Dielectric property measurement of polycrystalline silicon at high temperatures.* International Microwave Power Institute, 1991. **26**(3): p. 145-155.

13. Metaxas, A.C. and R.J. Meredith, *Industrial Microwave Heating*. 1983. London, United Kingdom: Peter Peregrinus Ltd.
14. Hutcheon, R. and M. Jong, *A system for rapid measurements of RF and microwave properties up to 1400C (Part 2).* Journal of Microwave Power and Electromagnetic Energy, 1992. **27**(3): p. 131.
15. Hutcheon, R., *A system for rapid measurement of RF and microwave properties up to 1400C (Part 1).* Journal of Microwave Power and Electromagnetic Energy.
16. Stratton, J.A., *Electromagnetic Theory*. 1941. New York, New York: McGraw-Hill.
17. Dejong, M., F. Adams, and R. Hutcheon, *Computation of RF fields for applicator design.* Journal of Microwave Power and Electromagnetic Energy, 1992. **27**(3): p. 136-142.
18. Micromeritics, *AccuPyc 1330 Pycnometer Operator's Manual*. 1996. Micromeritics Instrument Corporation.
19. Lowell, S., J.E. Shields, M.A. Thomas, and M. Thommes, *Characterization of porous solids and powders: surface area, pore size and density*. 2004. Norwell, MA: Kluwer Academic Publishers.
20. Quantachrome, *Autosorb-1 Operating Manual*. 2004. Quantachrome instruments: Boynton Beach, FL.
21. Astm, *Directory of testing laboratories, commercial-institutional/compiled by the American Society for Testing Materials*. 1975. ASTM: Philadelphia. p. C373-88.
22. Brinker, C.J. and G.W. Scherer, *Sol-Gel Science*. 1990. New York, New York: Academic Press.
23. Fricke J. and Tillotson T., *Aerogels: production, characterization, and applications.* Thin Solid Films, 1997. **297**: p. 212-223.
24. Brundle, C.R., C.A. Evans, and S. Wilson, Editors. *Encyclopedia of materials characterization*. 1992. Butterworth-Heinemann: Stoneham, MA.
25. Netzsch, *Thermal analysis, Instrument manual*. 2005. NETZSCH: Germany.
26. Company, F., *Focus ion beam technology, capabilities and applications*. 2001. FEI Company: Oregon.
27. Suryanarayana, C. and M.G. Norton, *X-Ray Diffraction: A practical approach*. 1998. New York: Plenum Press.
28. Cullity, B.D. and S.R. Stock, *Elements of X-ray diffraction*. Third edition ed. 2001. New Jersey: Prentice Hall.

CHAPTER V

Comparison of Structural Features during Conventional and Microwave Processing

This chapter presents the experimental results that show the structure evolution of silica aerogel processed in both conventional and single mode microwave ovens, between room temperature and 1200°C (greater than 1200°C in some cases). These results were obtained using the experimental procedures and characterization techniques explained in Chapter IV. In general, data from conventional tests were compared with results from the literature, and results from the microwave process were compared with those from the conventional system.

5.1 Adsorption/desorption surface analysis technique

Surface area and pore volume evolution as functions of temperature were recorded using nitrogen adsorption techniques. The results are presented in Figs. 5.1 and 5.2, respectively. Each figure presents two graphs: one represents the results obtained in a conventional furnace (open squares), and the other illustrates the results collected in a single mode microwave oven (solid squares). In order to observe a possible tendency, a trend line has been plotted on or next to the data obtained. Each data point is the average of three measurements. The same methodology has been followed for subsequent figures.

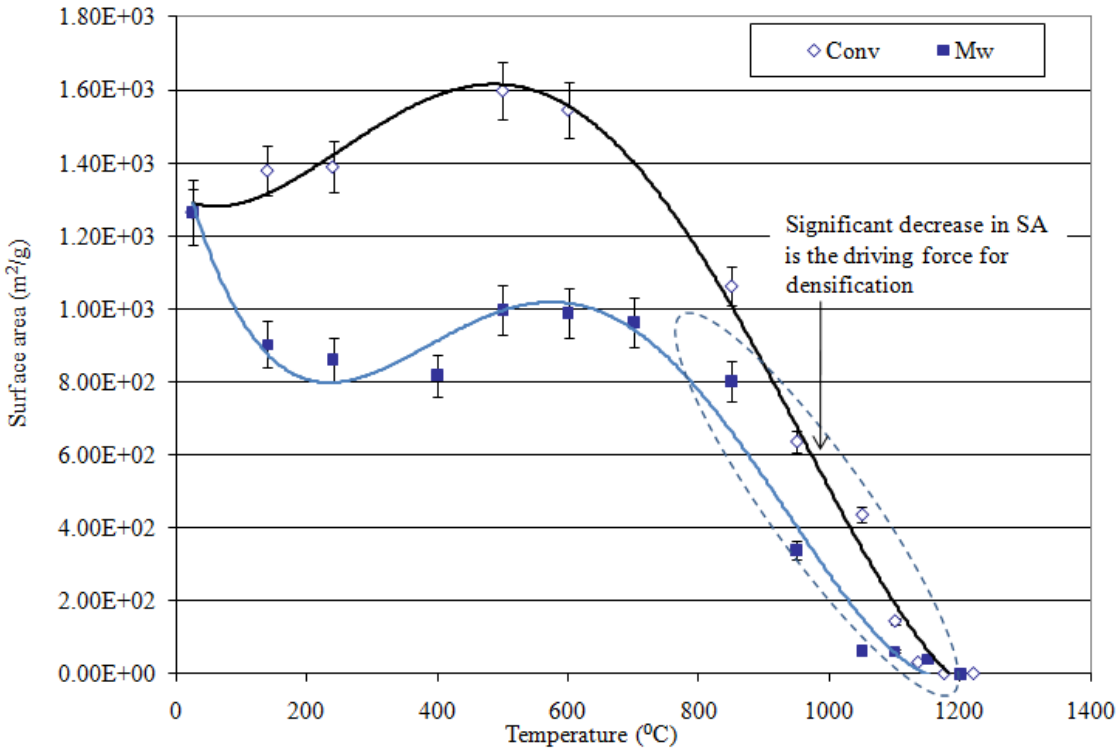

Fig. 5.1: Surface area of silica aerogel samples processed in conventional and microwave single mode ovens, measured using a surface area analyzer.

Figure 5.1 shows that the initial SA before processing by conventional or microwave methods was about 1300 m^2/g. Similar results were observed by Nogami and Moriya [1] when monolithic silica aerogel was produced by the hydrolysis of metal alkoxides. Additionally, Figs. 5.1 and 5.2 present differences in the evolution of SA and Pv between conventional and microwave processing throughout most of the temperature range. A substantial difference exists at temperatures from the beginning of the heat treatment to about 800°C, a moderate difference between 800 and 1100°C, and almost no difference at temperatures higher than 1100°C. Compared to conventional processing, microwave processing produced a greater reduction in SA and Pv at temperatures lower than 1100°C.

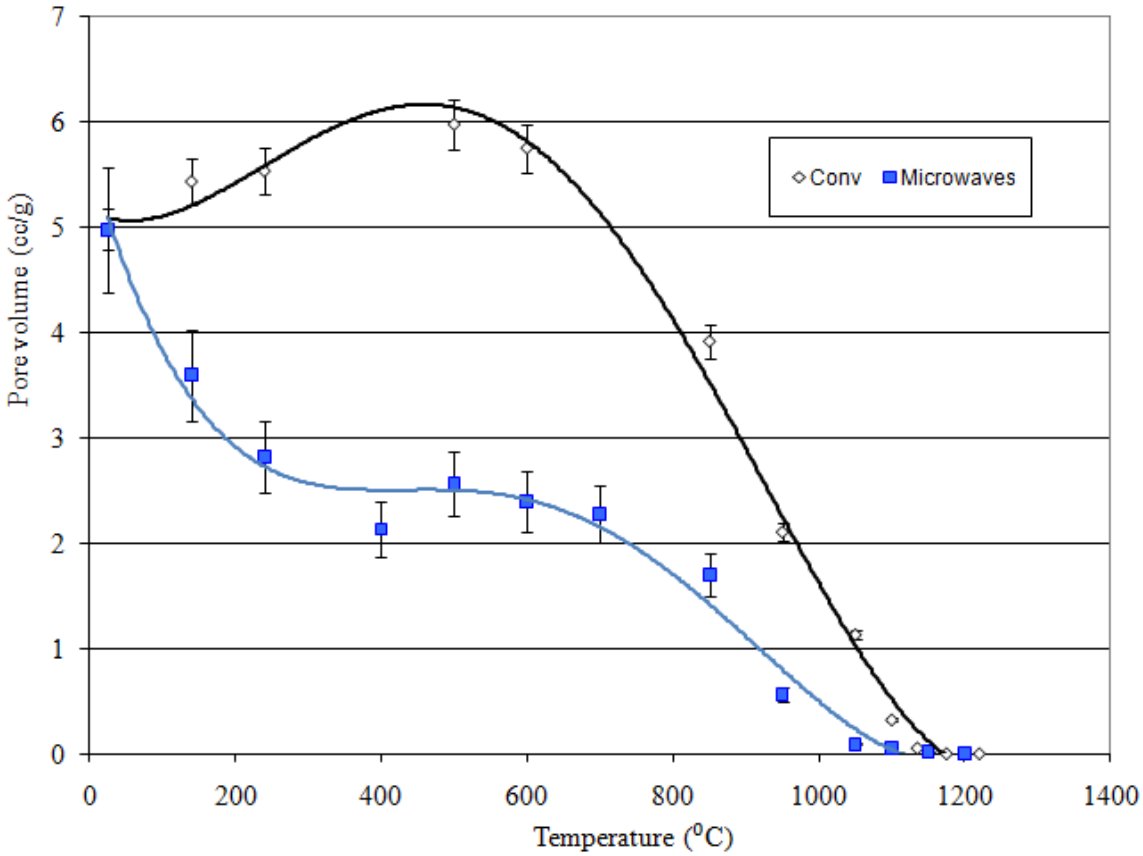

Fig. 5.2: Pore volume of silica aerogel samples processed in conventional and microwave single mode ovens, measured using a surface area analyzer.

5.2 Helium pycnometry

Structural density measured using He pycnometry is shown in Fig. 5.3. In this figure, the data plotted are also joined by a dashed line. In that way, one can see that some data points are not so close to the trend line. Notable observations can be obtained from the dashed and trend lines in this figure. For example, in conventional heating, silica aerogel changes in density between room temperature and 400°C at a much slower rate, while in microwave heating, the structural density evolves at a much higher rate. Silica aerogel reaches a structural density

similar to vitreous silica (2.2 g/cm^3) in a conventional system at around 1050°C, while in the single mode microwave cavity, that density is approached at 850°C. At temperatures above 1000°C, both processes present a similar behavior in structural density.

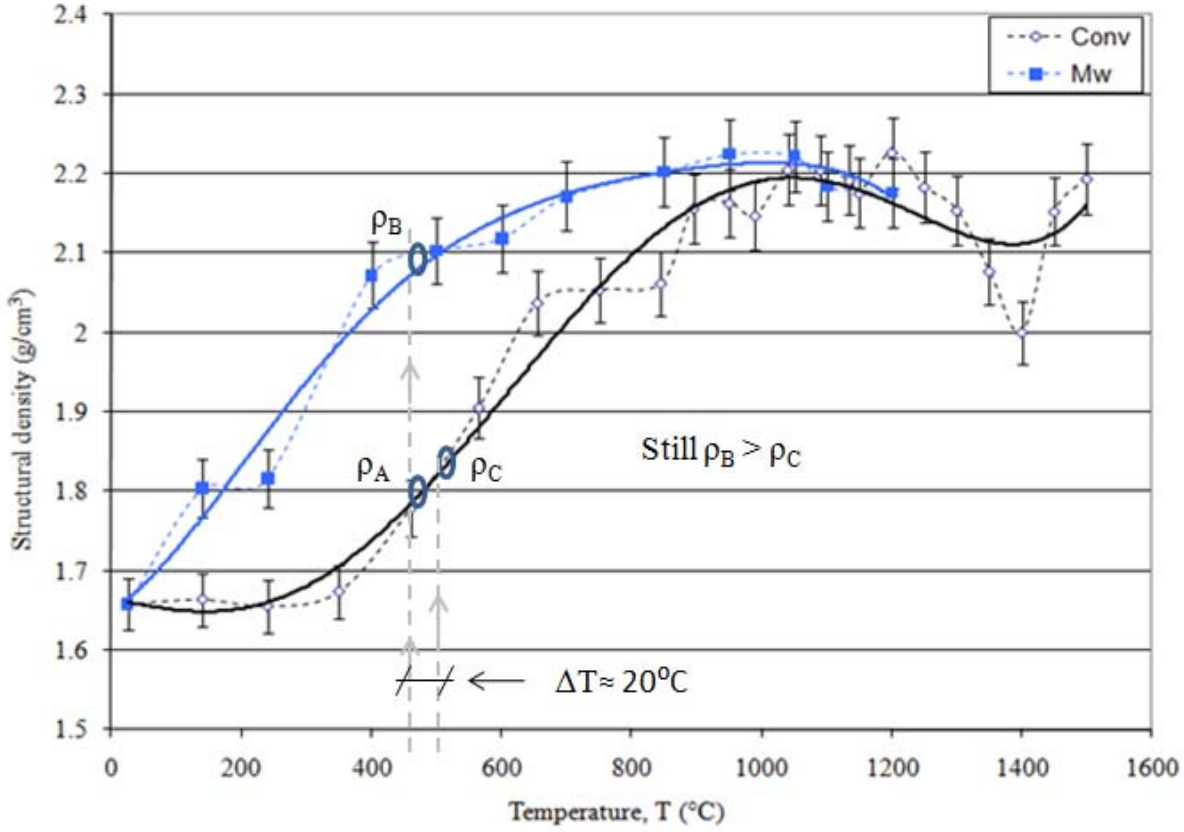

Fig. 5.3: Structural density of silica aerogel samples processed in a conventional oven and microwave single mode oven, obtained using He pycnometry.

5.3 Archimedes principle

Bulk density measurements using the Archimedes principle on silica aerogel samples are presented in Fig. 5.4. A moderate difference is observed with bulk density between conventional and microwave heating from room temperature to 850°C. In microwave heating, the bulk

density undergoes a progressive enhancement between 850 and 1050°C, while conventional heating results in a gradual increase. Above 1050°C, the slope of bulk density is greater for conventional than for microwave processing. Beyond 1150°C, a decrease in bulk density is observed for both microwave and conventional processes.

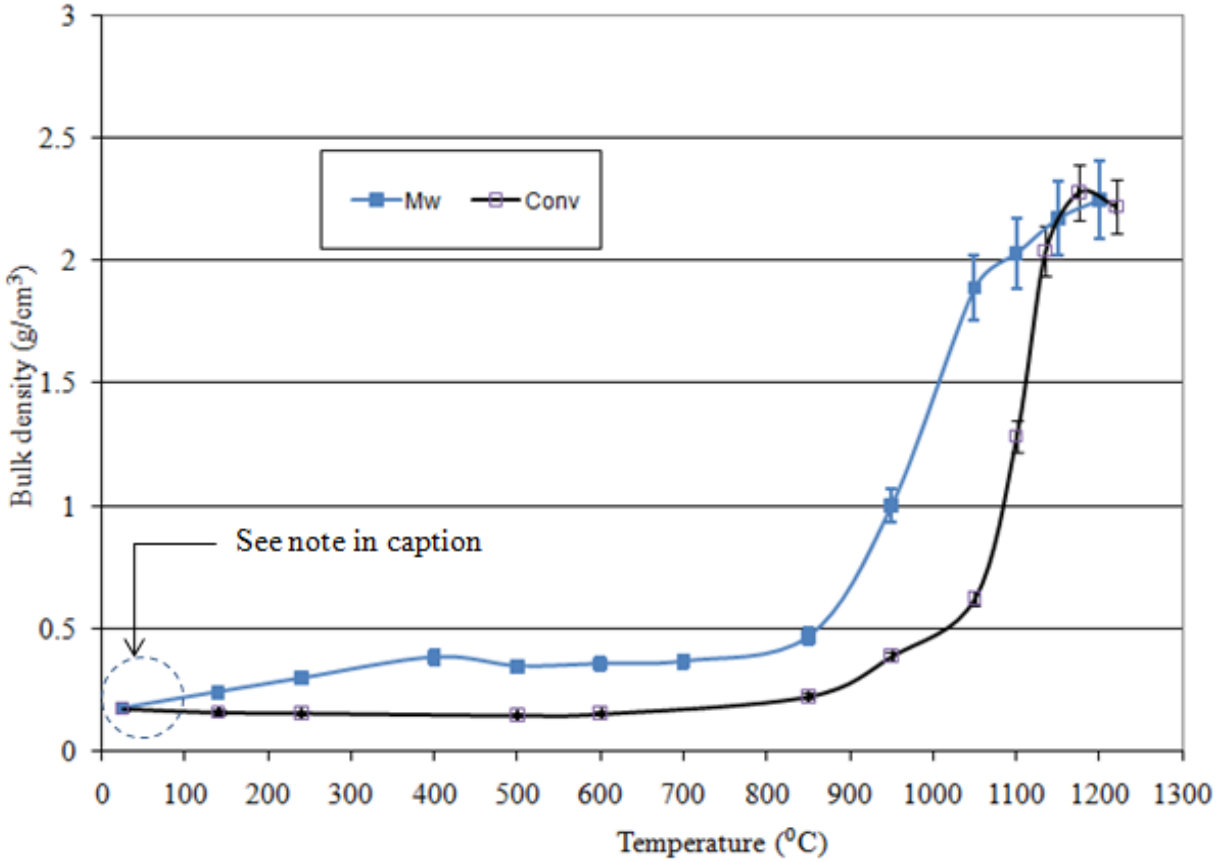

Fig. 5.4: Bulk density of silica aerogel samples processed in conventional and microwave single mode ovens. Note: the data point at room temperature was measured using geometrical dimensions of the samples and dried weight. All other data points were measured using Archimedes principle.

5.4 Percent porosity

By knowing ρ_B, ρ_S, and Vp, percent of total porosity (%P), percent of open pores (%Po), and percent of closed pores (%Pc) can be calculated by using Eqs. 5.1, 5.2, and 5.3, respectively [2, 3]. The results of the open and closed pores as a function of temperature are presented in Figs. 5.5 and 5.6. A figure for total porosity vs. temperature is not presented because it is almost identical to the %Po shown in Fig. 5.5.

$$\%P = \left(1 - \frac{\rho_B}{\rho_S}\right) \text{x}100 \tag{5.1}$$

$$\%Po = (V_p . \rho_B) \text{x}100 \tag{5.2}$$

$$\%Pc = \%P - \%Po \tag{5.3}$$

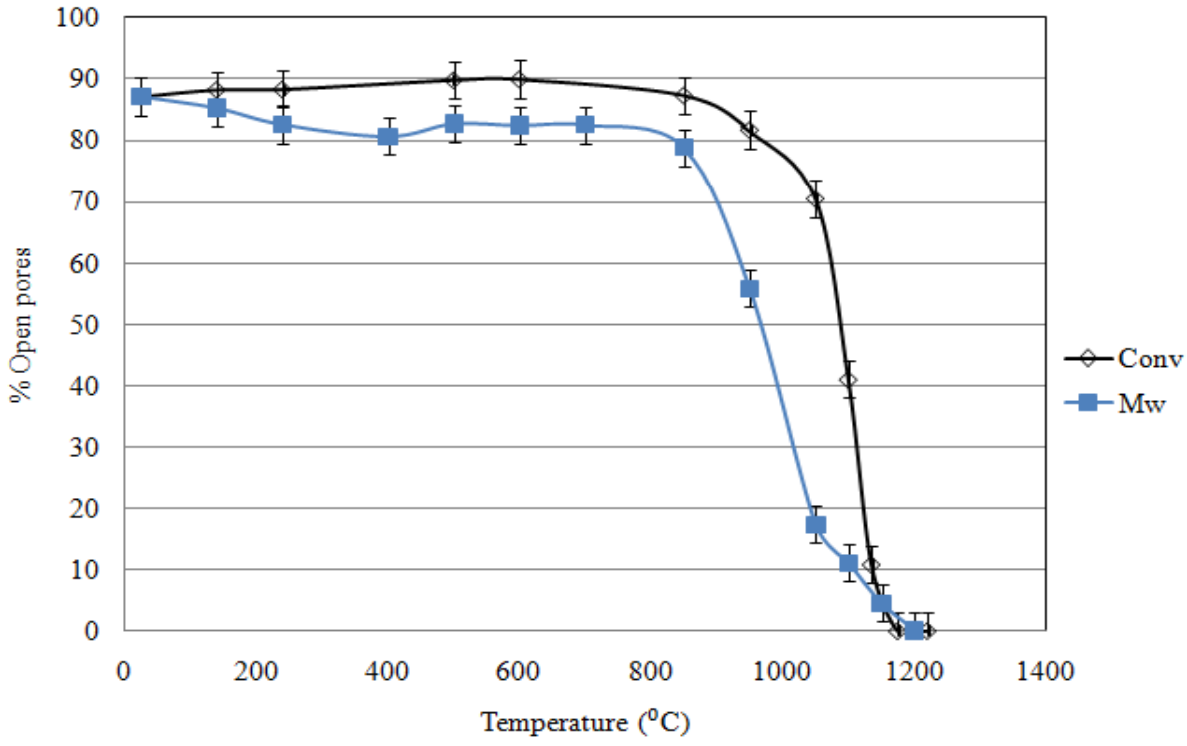

Fig. 5.5: Percent of open pores as a function of temperature of silica aerogel.

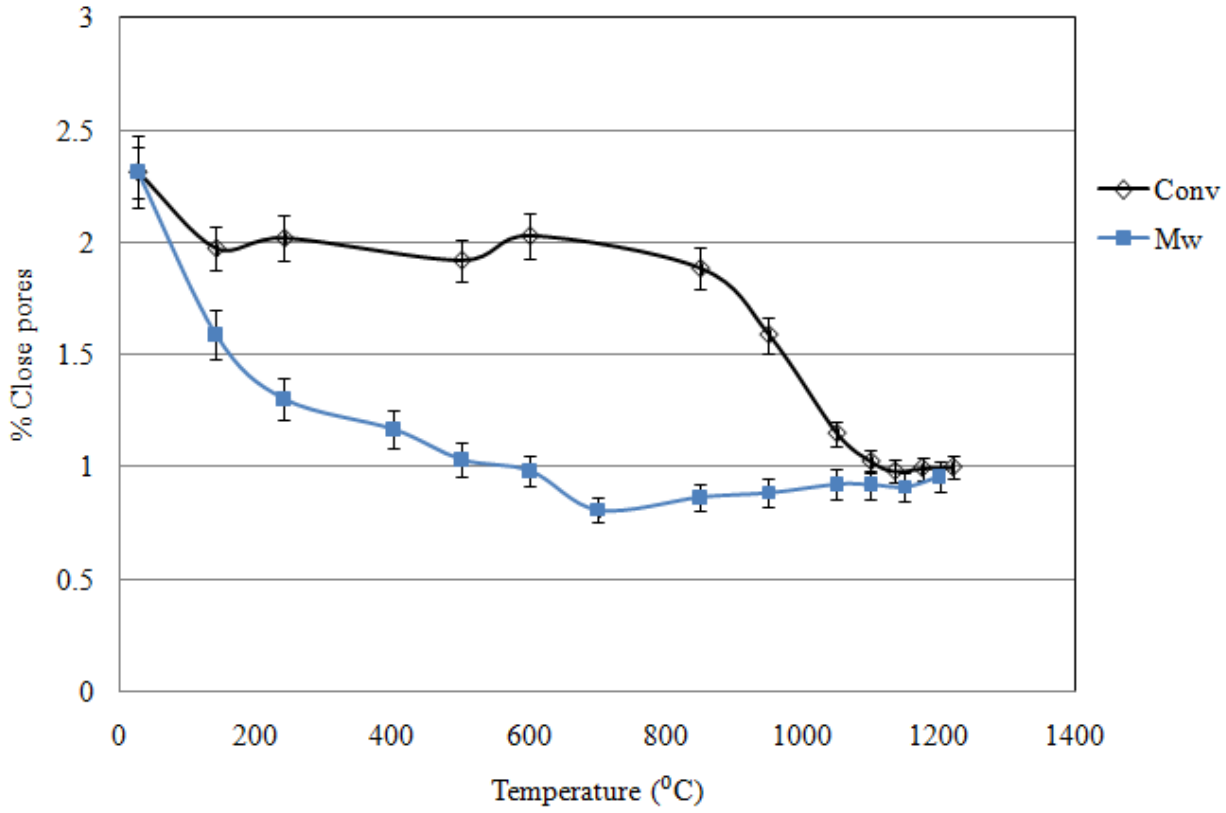

Fig. 5.6: Percent of closed pores as a function of temperature of silica aerogel.

Silica aerogel has been classified by many researchers as an open structure, mainly because of its high open porosity, as can be seen in Fig. 5.5 [4, 5]. However, it still contains some closed porosity (although very small), which is observed in Fig. 5.6. The main difference in the percentage of open pores between microwave and conventional heating is in the magnitude; however, they have similar trends. In contrast, the majority of the closed pores are eliminated in the early stages of microwave processing (< 700°C), as compared to conventional processing.

5.5 Thermogravimetric analysis and differential scanning calorimetry

Weight loss and phase changes were measured using TGA and DSC, respectively. There is a significant weight loss at temperatures lower than 200°C (≈12%, Fig. 5.7) and almost no densification is observed. This behavior can be associated with the evaporation of physically absorbed water and perhaps some residue of ethanol from the drying process. This is corroborated by the presence of an endothermic reaction observed during DSC (Fig. 5.8). Change in weight is observed in the range 200 to 500°C, which can be attributed to combustion of residual organics. This behavior is corroborated by an exothermic peak manifested in the DSC analysis (Fig. 5.8).

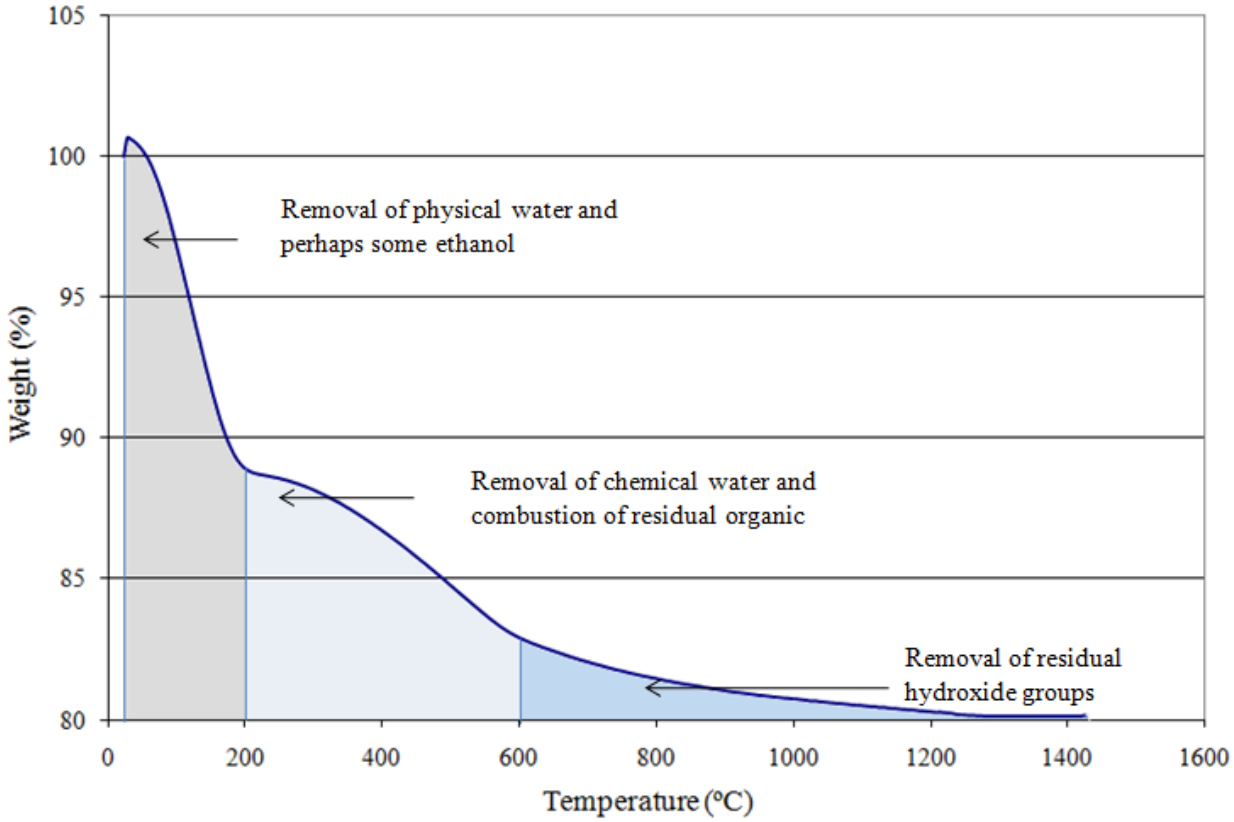

Fig. 5.7: Weight loss of silica aerogel measured by TGA.

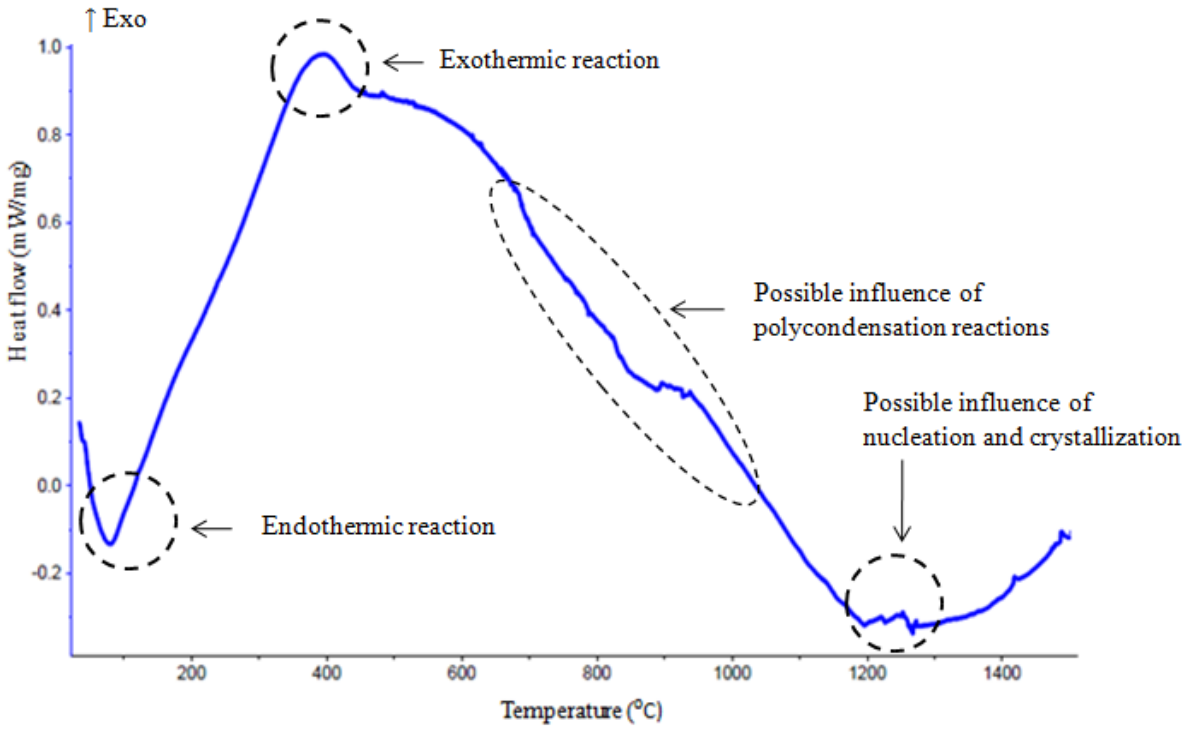

Fig. 5.8: DSC of a silica aerogel sample.

Above 600°C, small weight loss is observed. During this temperature range, removal of residual hydroxide groups is taking place. In addition, polycondensation reactions could be manifested in the DSC at about 800°C and possibly a phase change, such as nucleation and crystallization above 1200°C.

5.6 Dielectric measurements

Dielectric constant and dielectric loss were measured using the cavity perturbation technique, as described in Section 4.5. The apparatus that was designed and built by the author allows for the e' and e''_{eff} to be measured as a function of temperature at 2.45 GHz. The measurements of these properties are illustrated in Fig. 5.9. The effective dielectric loss is 0.27

at room temperature and decreases as the material is heated up to about 700°C. The samples heated to 850°C and 1100°C show lower e''_{eff} when they were cooled down to room temperature. These results indicate an influence of the composition, structure or temperature on the dielectric properties of silica aerogel which in turn could influence the microwave absorption of the material.

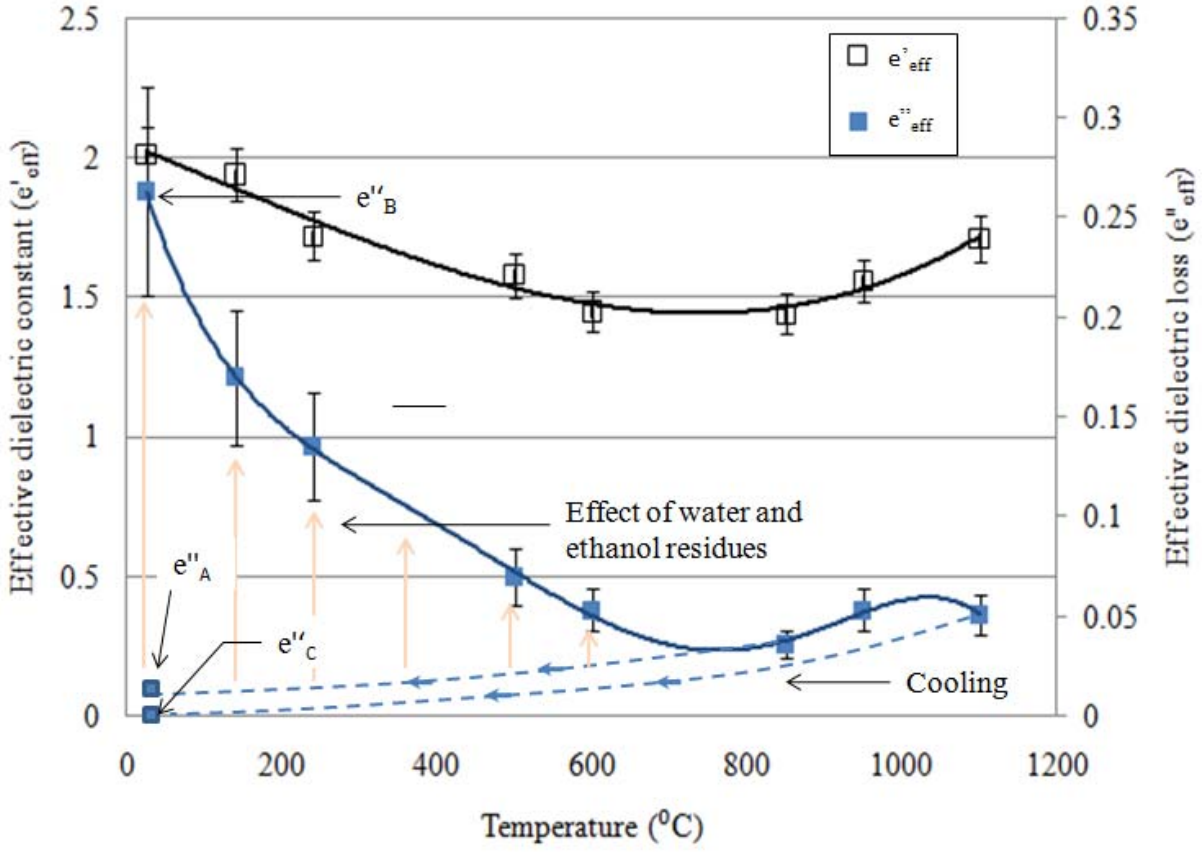

Fig. 5.9: Dielectric constant and dielectric loss of silica aerogel at 2.45GHz, measured using the cavity perturbation technique.

5.7 Electric field measurements

Electric fields on the samples were measured (Fig. 5.10) and confirmed that there was a high level of interaction between microwaves and the material at temperatures lower than 300°C. The intensity of the electric field is one of the main differences between microwave processing in a single mode and a multimode cavity. Multimode ovens (i.e. home microwave oven) are designed to have more than 40 modes of field distributions in order to improve the uniformity of the field on the load [6]. However, this large number of modes produces a reduction in the magnitude of the electric field. While in a single mode, much higher field intensities can be obtained at a specific location, compared with the same input power used in a multimode cavity [7, 8]. As seen in Fig. 5.10, the electric field ranged from 175 to 130 V/cm in the single mode microwave oven. In the case of a typical home microwave oven, the electric field would have been reduced to a factor of about 40, assuming the field was uniform (which it was not).

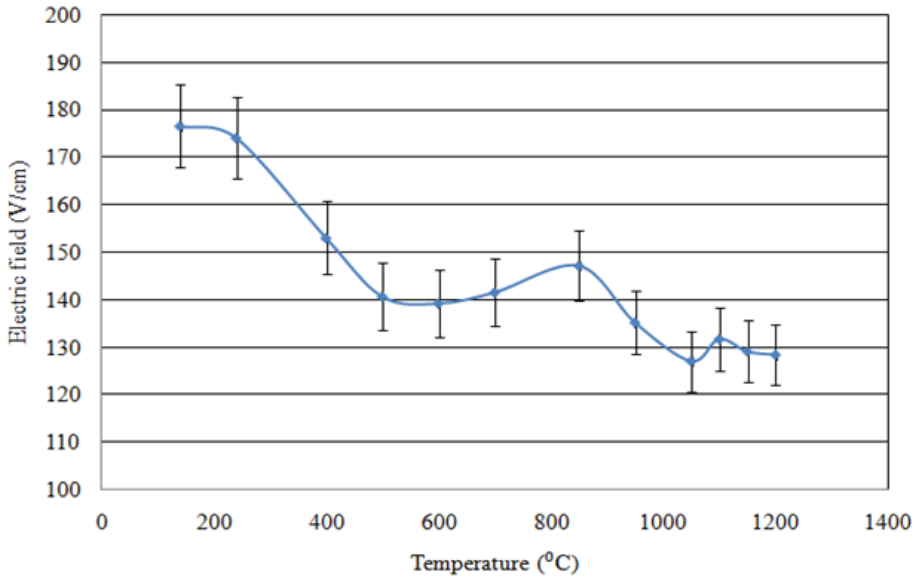

Fig. 5.10: Electric field measured on the aerogel sample during single mode microwave processing.

The microwave signal experiences a substantial amount of reflected power at 1200°C, shown in Table 5.1. The magnitude of the electric field and dielectric loss show the lowest values at this temperature. It is extremely difficult to process this material at 1200°C in the single mode microwave oven (2.45GHz) due to the high level of reflected power. The reflected power increased because the power absorbed decreased making it more difficult to heat the sample and maintain a given temperature.

Table 5.1: Typical electric fields and reflected powers.

Temperature (°C)	**Electric field (V/cm)**	**Power reflected (%)**
500	140	10
1100	130	50
1200	128	90

5.8 Fourier transform infrared spectroscopy

Fourier transforms infrared spectroscopy results are shown in Figs. 5.11 and 5.12 for conventionally and microwave-processed samples, respectively. Table 5.2 presents the FTIR bands of silica gel [9] used for interpreting these figures. The magnitude of the vibration produced by the interaction between infrared energy and the different bonds is associated with the number of bonds present. In the conventional process, Fig. 5.11 shows that during the transition between 300 and 600°C, there is a small variation in the number of siloxane (Si-O-Si) bonds (bands: 795 and 1200 cm^{-1}). There is a larger difference in siloxane bonds between 600

and 950°C; and there is a considerable increase between 950 and 1050°C, contributing to a higher density.

Table 5.2: FTIR bands observed for silica gel [9].

Frequency (cm^{-1})	**Assignment**
1640	Absorbed water (H_2O)
1200	Asymmetric stretching (Si—O—Si)
960	Symmetric stretching (Si—OH)
795	Symmetric stretching (Si-O-Si)
460	Bending mode (O—Si—O)

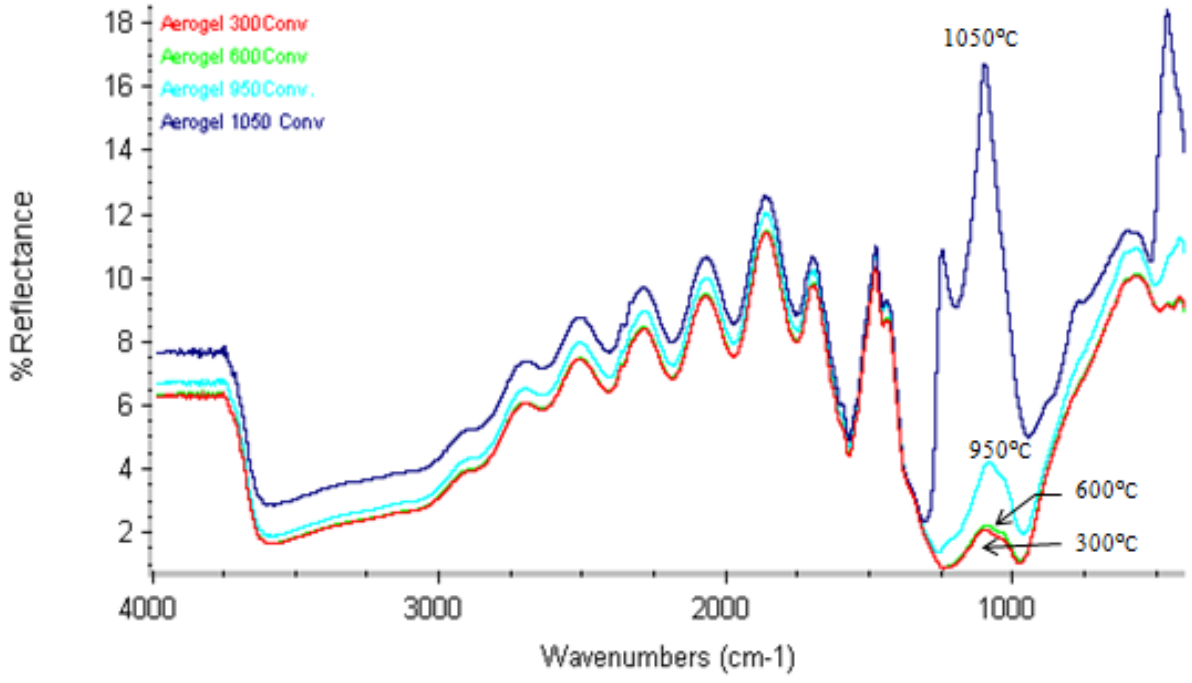

Fig. 5.11: FTIR bands of silica aerogel processed in a conventional furnace at 300, 600, 950, and 1050°C.

Above 400°C, microwave-processed samples show a substantial enhancement of the peaks at the 795 and 1200cm^{-1} (Fig. 5.12). These peaks represent the siloxane bonds. Their significant increase in magnitude can be observed at temperatures as low as 950°C, which is a characteristic not present at the same temperature in the conventional process (see peak at 950°C in Fig. 5.10).

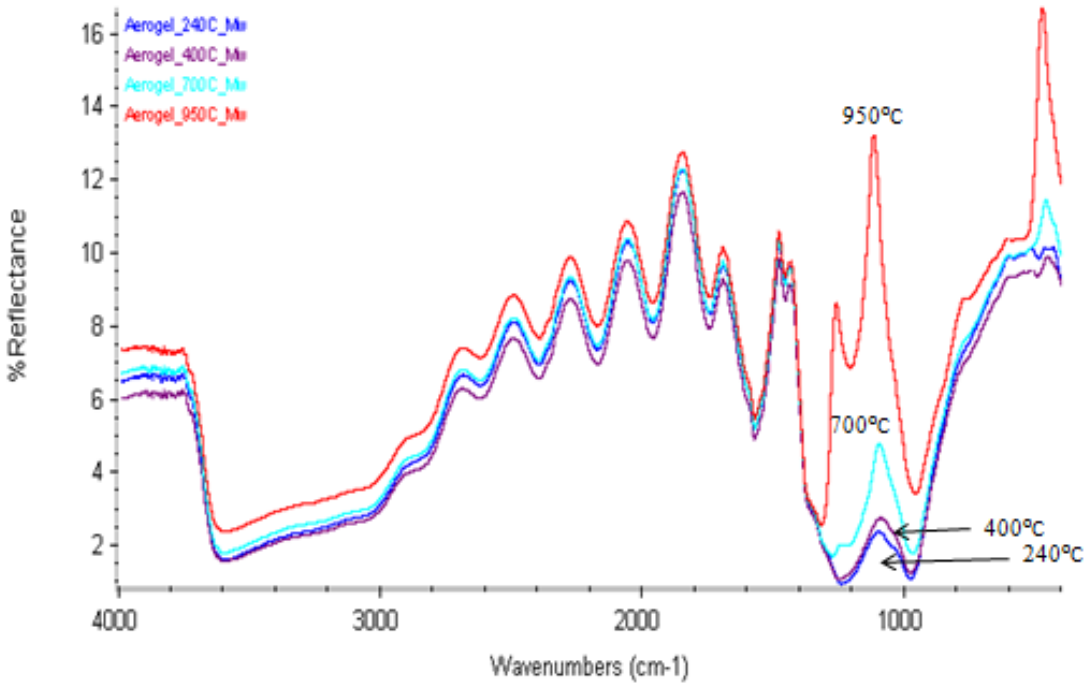

Fig. 5.12: FTIR bands of silica aerogel processed in a single mode microwave oven at 240, 400, 700, and 950°C.

5.9 X-ray diffraction

X-ray diffraction data was taken for both types of processed samples to evaluate if the material was still amorphous (Fig. 5.13 and 5.14). Microwave-processed silica aerogel, shown in Fig. 5.13a (1150°C), was still an amorphous material. The diffractogram observed in this figure is characteristic of amorphous silica gel [10]. However, at 1200°C, a few samples did not remain completely amorphous (Fig. 5.13b). Similar amorphous phase was observed in the XRD for samples conventionally processed at 1200 and 1300°C for 30min (Figs. 5.14a and 5.14b, respectively) and 1h (not completely amorphous, Fig. 5.14c). The peaks shown in Figs. 5.13b and 5.14c are similar to the XRD peaks of cristobalite [10] where the main characteristic peak (101) is at 21.09°. Thus, it appears that microwave processing resulted in crystallization at lower temperature and shorter processing times.

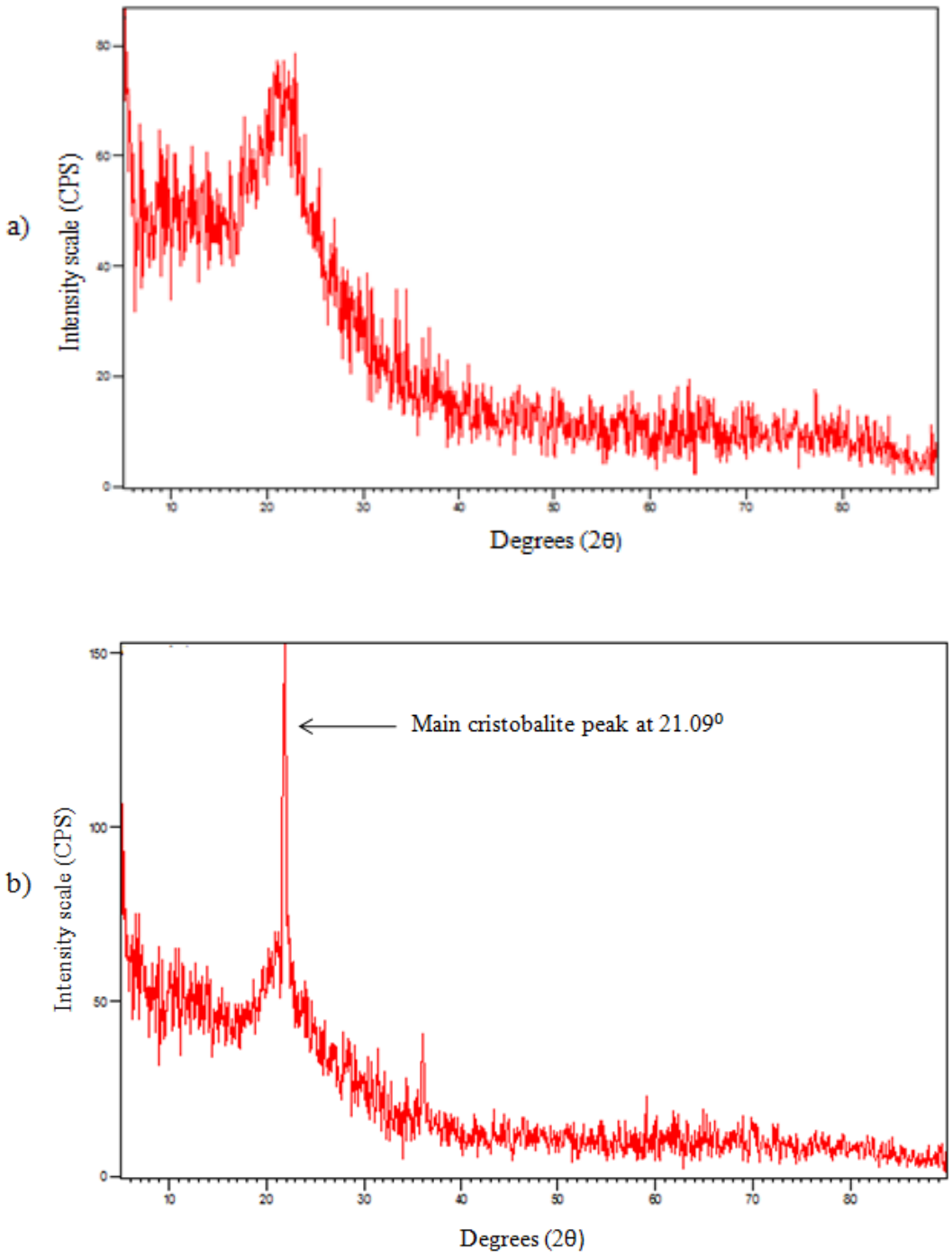

Fig. 5.13: XRD of silica aerogel samples processed in a single mode microwave oven at a) 1150°C, b) 1200°C. In both cases the sample was held for 30 min at the predetermined temperature.

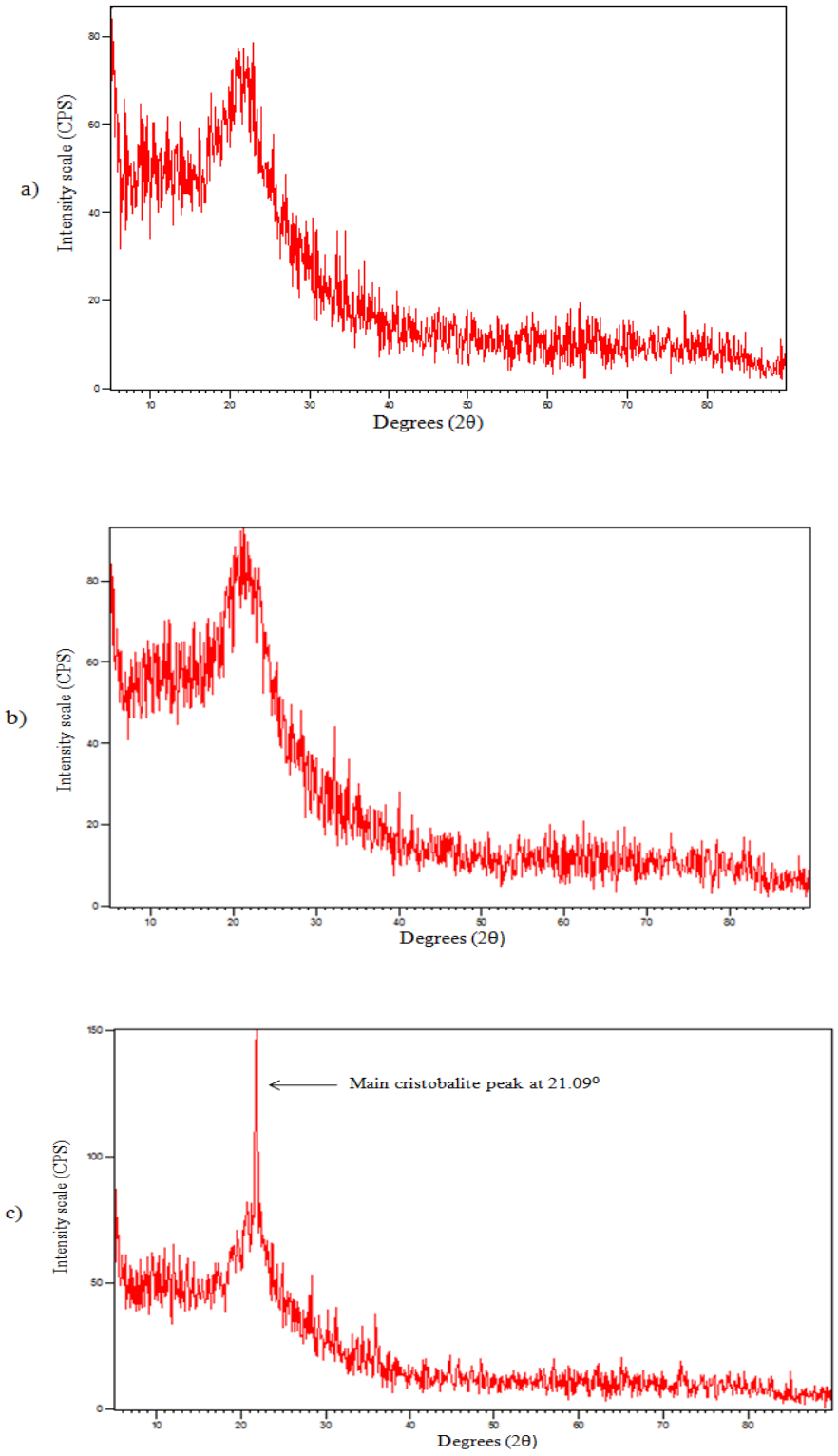

Fig. 5.14: XRD of silica aerogel samples processed in a conventional furnace at a) 1200°C for 30 min, b)1300°C for 30 min, c) 1300°C for 1h.

5.10 Transmission electron microscopy

Transmission electron micrographs were obtained for samples processed at 1200 and 1300°C (samples at which the reduction in structural density was observed) in the conventional and the microwave processes, respectively. On the surface of the material, the micrographs showed the presence of small inclusions (dots) that were smaller than 5nm in diameter. When a pore is observed using TEM, it has a characteristically lighter color than the rest of the material. However, the dots observed in Fig. 5.15 and 5.16b were darker. This observation combined with the XRD results suggest that these inclusions represent the characteristic seeds of nucleation.

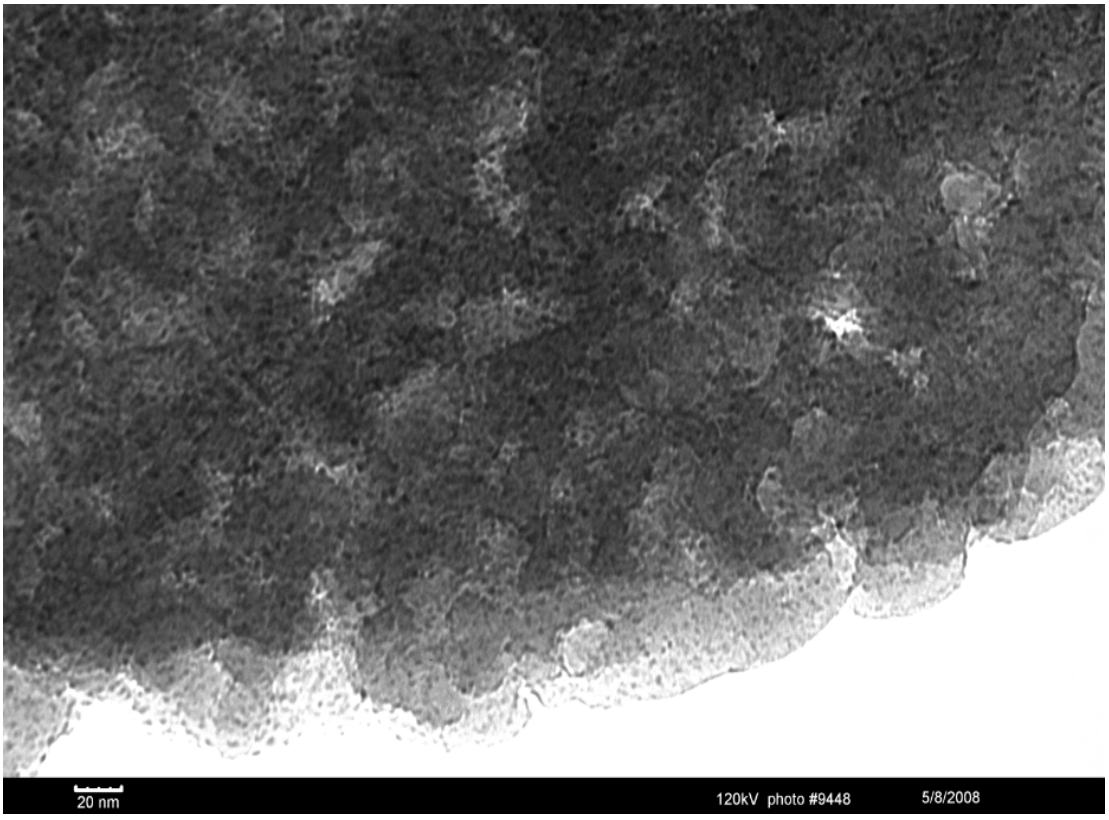

Fig. 5.15: TEM of silica aerogel sample processed in a conventional oven at 1300°C for 1h.

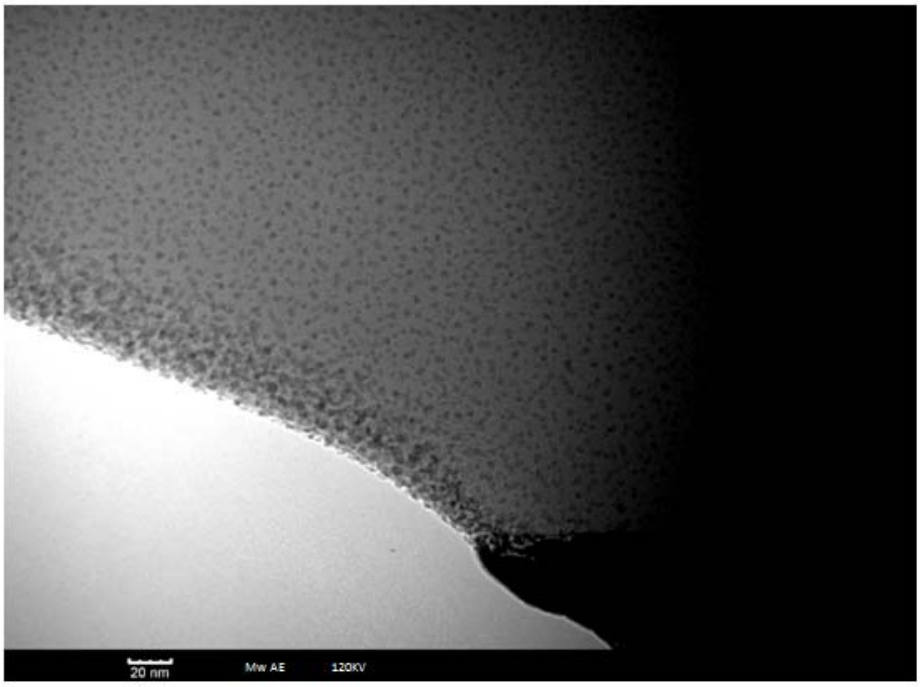

a)

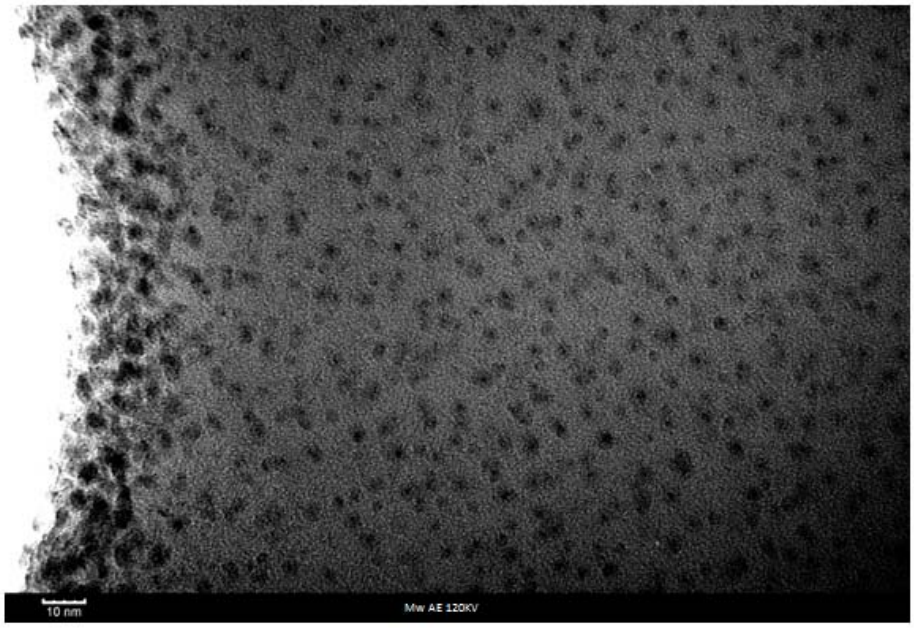

b)

Fig. 5.16: TEM of silica aerogel sample processed in a single mode microwave oven at 1200°C: a) 20nm scale, b) 10nm scale.

Reference

1. Nogami, M. and Y. Moriya, *Glass formation through hydrolysis of $Si(OC_2H_5)_4$ with NH_4OH and HCL solution.* Journal of Non-Crystalline Solids, 1980. **37**: p. 191-201.
2. Rao, A.V., et al, *Influence of temperature on the physical properties of TEOS silica xerogels.* Ceramics International, 1999. **25**: p. 505 - 509.
3. Barrett, E.P., L.G. Joyner, and P.P. Halenda, *The determination of pore volume and area distribution in porous substances. I. Computations from nitrogen isotherms.* Journal of The American Ceramic Society, 1951. **73**: p. 373 - 380.
4. Siouffi, A.M., *Silica gel-based monoliths prepared by the sol-gel method: facts and figures.* Journal of Chromatography A, 2003. **1000**: p. 808-818.
5. Iura, J., H. Hishikura, M. Kamikatano, and T. Kawaguchi, *Changes in the porous structure of silica gels during the gel-to-glass conversion.* Journal of Non-Crystalline Solids, 1988. **100**: p. 241-246.
6. Metaxas, A.C. and R.J. Meredith, *Industrial Microwave Heating*. 1983. London, United Kingdom: Peter Peregrinus Ltd.
7. James, C.R., W. Tinga, and W.A.G. Voss, *Energy conversion in closed microwave cavities*, in *Power Engineering*, E.C. Okress, Editor. 1968. Academic Press: New York, New York. p. 28-37.
8. Tian, Y.-L., *Practices of ultra-rapid sintering of ceramics using single mode applicators*, in *Microwaves: Theory and Application in Materials Processing*, Frank D. Gac David Clark, Willard H. Sutton, Editor. 1991. The American Ceramic Society, Inc.: Cincinnati, Ohio.
9. Brinker, C.J. and G.W. Scherer, *Sol-Gel Science*. 1990. New York, New York: Academic Press.
10. Kingery, W.D. and H.K. Bowen, *Introduction to ceramics*. 1976. New York, New York: John Wiley & Sons.

CHAPTER VI

The Effect of Microwave Processing on Structural Evolution

This chapter provides discussion and analysis of the results obtained in Chapter V. A comparison of the structural parameters (structural density, bulk density, surface area, volume of the pores, and porosity) obtained for both processes, microwave and conventional, reveals that the structural evolution of silica aerogel can be divided into three different regions. *Region I* covers from room temperature (25°C) to 850°C and is characterized by structural densification. *Region II* ranges from 850°C to 1200°C and is characterized by bulk densification. *Region III* lies above 1200°C and is characterized by crystallization of the material. Figure 6.1 illustrates some of the major structural features in these regions. Each of these regions is discussed in subsequent sections. However, the focus of this study is on the evolution observed in the first two regions.

6.1 Critical point dried aerogel

The study of microwave interactions begins after silica aerogel samples are dried using a critical point drier (CPD, procedure explained in Section 4.1.2). Based on Eqs. 2.1 - 2.3 and the information obtained from TGA and DSC (Fig. 5.7 and 5.8, respectively), monolithic silica aerogel can be represented as a composite formed by a matrix of "solid material," hydroxide groups, and some residues of absorbed water and ethanol.

Two of the major parameters in a structural evolution study are bulk density and structural density [1, 2]. These structural features are illustrated schematically in Fig. 6.2. The structural density includes the solid material only (with OH groups and residual alcohol). The bulk density includes the solid material as well as the pores.

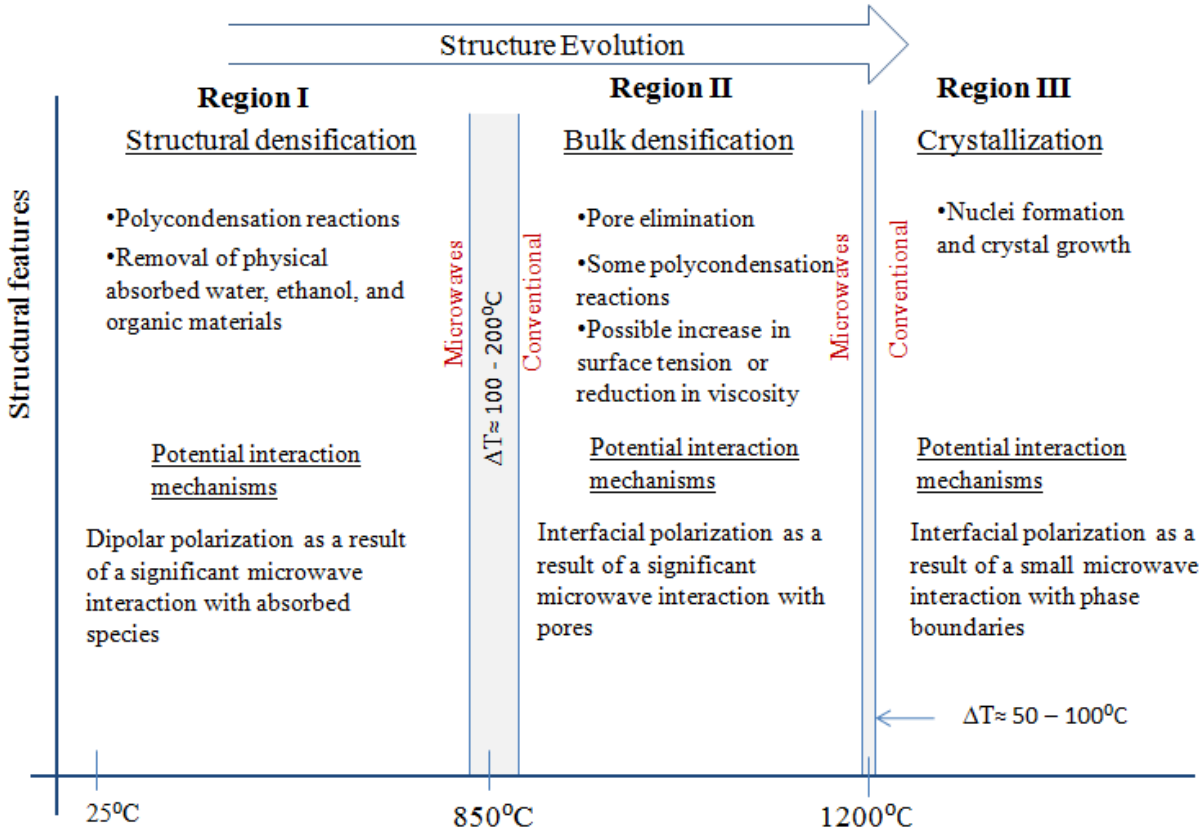

Fig. 6.1: Major regions of structural evolution in aerogels during heating. Note that the microwave heating results in transition between *Regions I* and *II* at a significant lower temperature than those observed for conventional heating, while the transition between *Regions II* and *III* is only slightly lower for microwave processing.

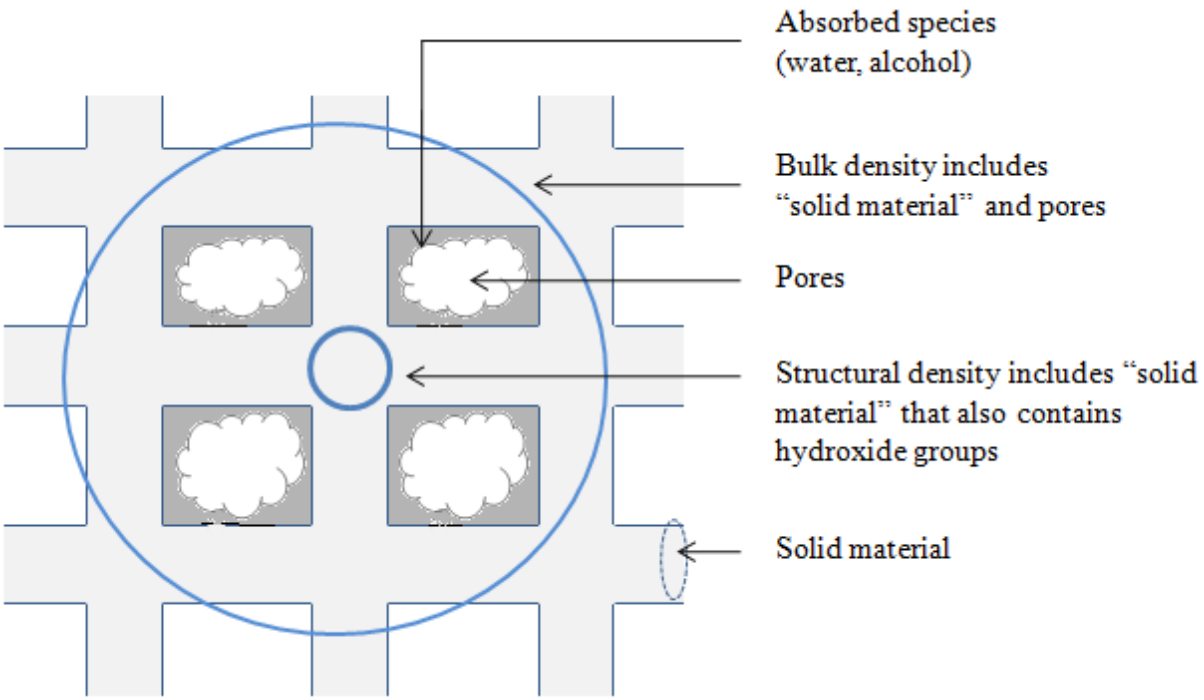

Fig. 6.2: Structure of critical point dried aerogel.

6.2 Temperature measurements during microwave processing of silica aerogel

Before the differences in the structural parameters can be explained, it is important to verify that these differences are not the result of unreliable temperature measurements, as discussed in Appendix E. In microwave processing of materials, temperature measurements play a crucial role when one is making a comparison between two different systems (i.e. conventional and microwave heating, or even in single mode microwave and multimode microwave cavities). In this study, the comparison is between processing using conventional and single mode microwave heating.

There are two cases where temperature measurements in microwaves could provide a substantial difference in the results. First, the temperature measured on the surface is lower than the one in the interior of the material. Second, the temperature sensor is experiencing interference with the electromagnetic field and providing a temperature reading different from the actual temperature.

The first case was evaluated by measuring the interior temperature of the material. Figure 6.3 represents one of these measurements. To minimize any possible thermal gradients throughout the sample, it was soaked for 30 min at constant temperature (this processing step was common for all the samples, conventional as well as microwave-processed). Even so, it was observed that the interior of the microwave-processed sample was about 20°C higher than the surface. This small temperature difference was not sufficient to account for the structural discrepancies observed between conventional and microwave-processed samples. For example, see densities at point A (ρ_A) and point B (ρ_B) in Fig. 5.3. Both densities were obtained at the same temperature in the conventional and microwave process, respectively. However, ρ_B was still higher than ρ_C which represents the density of a conventionally processed sample at 20°C higher than ρ_A. The second case was evaluated by changing the position of the thermocouple (TC) within the cavity (explained in Section 4.4.2). When the TC was localized in a position where it was not influenced by electrical perturbations from the electromagnetic field, the temperature monitor showed a steady signal. All the temperature measurements in this study were made in this way. Additional information about the appropriate location of the thermocouple in a single mode cavity is provided in Section 4.4.2. Therefore, observed differences in structural features between conventional and microwave-processed samples could

not have accounted for the differences in temperature between surface and interior or electromagnetic interferences in measurements.

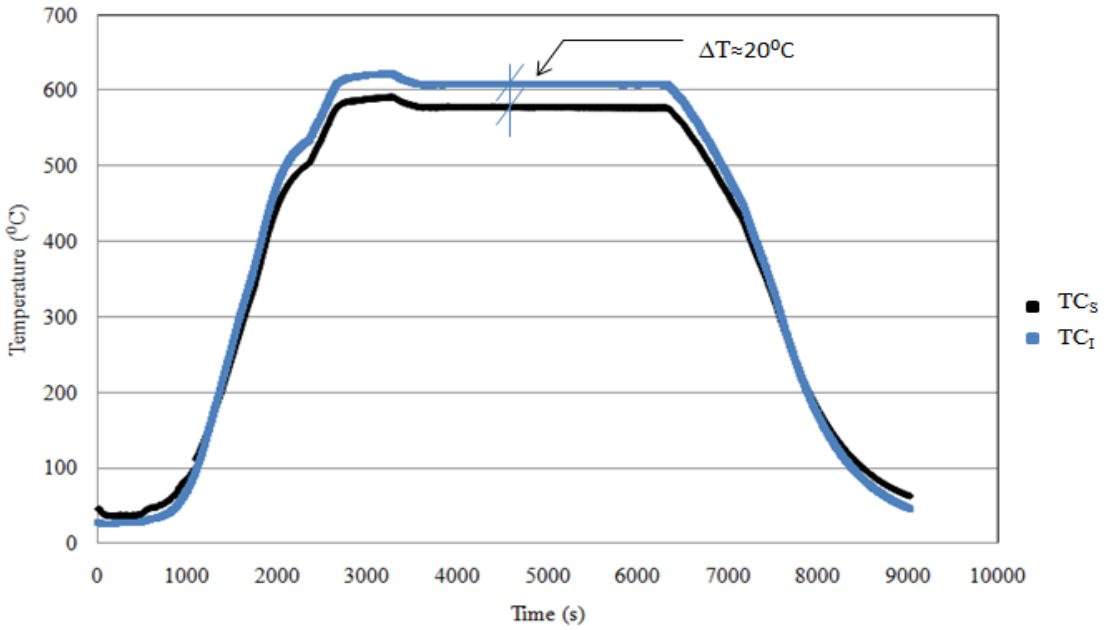

Fig. 6.3: Temperature profile of a silica aerogel sample in a single mode microwave oven where TC_S and TC_I are the surface and internal temperature of the sample, respectively. The internal temperature appears to be about 20°C higher than the surface.

6.3 ***Region I***

This region covered from room temperature to 850°C and was characterized by an increase in structural density and almost constant bulk density for both processes, but microwave processing exhibited a slightly higher bulk density. During conventional processing, the TGA and DSC results (Figs. 5.7 and 5.8, respectively) indicated that physical absorbed water, ethanol, and organic materials were present and then removed in this region. Similar behavior has been reported in the literature [3, 4]. The increase in structural density is attributed to the continuous

progress of the polycondensation reactions because these reactions increase the concentration of siloxane bonds [5, 6]. Above 500°C, the evaporation of the by-products generated by these reactions and the loss of OH groups due to the thermal stabilization (explained in Section 2.2.7) resulted in the gradual weight loss observed in Fig. 5.7. Also, an increase in SA is observed in the temperature range between 400 and 600°C in both processes. This change could be associated with the combination of the following factors: 1) combustion of organic materials and evaporation of by-products that leave a bigger Vp when they are removed, 2) dilatation of the structure due to structural relaxation. Similar changes were observed in SA and Vp in the literature [7].

In silica aerogel, changes in structural density also lead to changes in bulk density. When polymerization occurs, the solid structure tends to contract due to the removal of the hydroxide groups and rearrangement of the atoms, as shown in Fig. 6.4. The contraction of the solid material results in a smaller pore size and pore volume, and thus a potential increase in bulk density. Notice that "potential" increase in bulk density is used because if there is a weight loss during the contraction, it may partially compensate for the reduction of pore volume and sample size. Consequently, negligible or no increase in bulk density would result. *Region I* shows a small increase in bulk density, even though the main characteristic is a significant structural densification. This behavior is more evident in the microwave process at temperatures lower than 400°C (Fig. 5.4) suggesting that microwave processing is more effective in the reduction of hydroxide groups or other species (such as water and ethanol) present in the silica gel structure.

There was a substantial difference in structural density between the conventional and microwave heating (Fig. 5.3). This behavior suggests that there was a significant interaction between microwaves and silica aerogel. Part of this interaction can be explained by observing the dielectric properties of silica aerogel (Fig. 5.9) at the microwave frequency used, 2.45GHz. These properties were measured using the cavity perturbation technique described in Section 4.5.

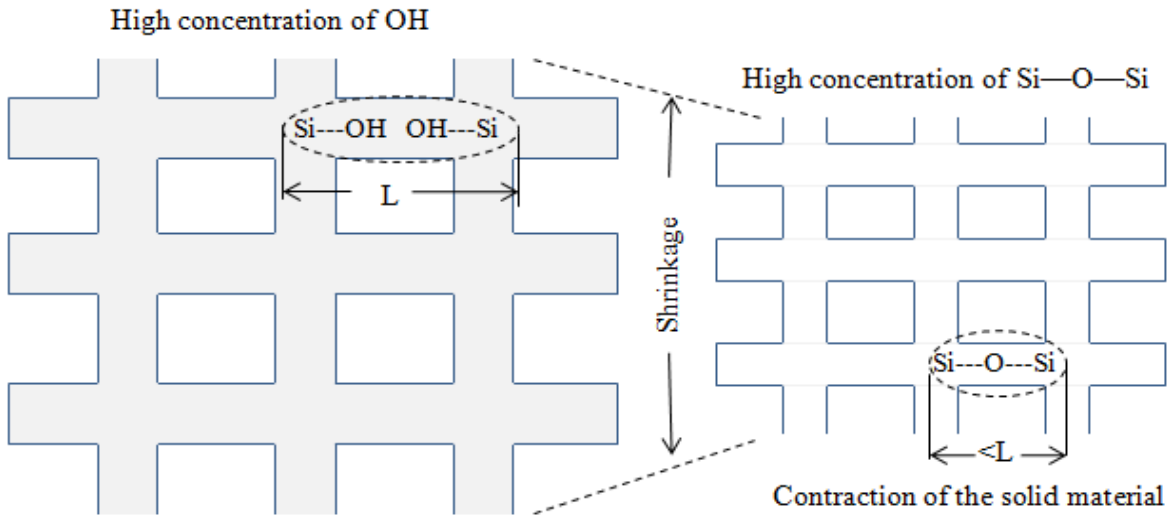

a) b)

Fig. 6.4: The effect of polycondensation on structural and bulk densities: a) sample after critical point drying, b) sample after heated to temperatures less than 850°C (i.e. before viscous flow).

As presented in Eq. 3.22, the dielectric loss of the material is a factor that influences the microwave power absorbed. In *Region I*, the aerogel was a partial absorbed material composed of a nearly transparent silica material with water and alcohol dispersed throughout, as shown in Fig. 3.1d. The measured effective dielectric loss (e''_{eff}) factor represented all the mechanisms that could have lead to heating (explained in Section 3.4). The highest dielectric losses were recorded along *Region I*. Water and ethanol experienced much higher dielectric losses than

silica at frequencies close to 2.45GHz (Table 6.1), and these losses contributed to higher dielectric loss of the silica aerogel (Fig. 5.9).

Several researchers have shown that the variation of the percentage of water in silica aerogel substantially influenced the dielectric loss of the material and its microwave absorption properties [8, 9]. Figure 5.9 and Table 6.1 show that e''_{eff} measured at 25°C for silica aerogel heated at 850°C and then cooled down (Point A in Fig. 5.9, e''_A) to room temperature (0.01) was much lower than the e''_{eff} (0.27) at 25°C when water and ethanol were present (Point B in Fig. 5.9, e''_B). These data corroborate that the presence of water and ethanol species in silica aerogel enhanced the microwave absorbing capacity of the material in *Region I*. This absorbed microwave energy was apparently dissipated through the enhancement of polycondensation.

The measured electric field on the samples processed in a single mode cavity (Fig. 5.10) confirmed that there was a high level of interaction between microwaves and silica aerogel in *Region I*. Note the similarity of the shape of Fig. 5.10 with the weight loss curve shown in Fig. 5.7. This behavior suggests a higher interaction in those regions where water, ethanol, and organic species were present. It is appropriate to mention that a few samples were heated in a multimode microwave oven under similar conditions (time, sample set-up) at 200, 600, and 900°C. No significant differences between multimode and conventional ovens were observed in structural or bulk densities during these particular experiments. It is known that the intensity of the electric field on the location of the sample was higher in the single mode cavity [9-11] (explained in Section 4.3 and 5.7). This behavior suggests that the interaction between silica aerogel and the high electric field induced by a single mode cavity was most likely responsible

for enhanced microwave absorption in the material (expressed in Eq. 3.22), and this is one of the main factors that influenced the increase in structural density.

Table 6.1: Dielectric parameters at frequencies close to 2.45GHz.

Material	**Temp. (°C)**	**Frequency (GHz)**	**Dielectric constant (e')**	**Dielectric loss (e''_{eff})**
Water [12]	25	3.0	76.60	12
Ethanol [13]	60	2.8	11.15	6.76
Fused silica [9]	25	3.0	3.78	0.002
Aerogel (e''_B, this study)	25	2.45	2.10	0.27
Aerogel (this study)	850	2.45	1.48	0.04
Aerogel (this study)	1100	2.45	1.70	0.05
Aerogel heated up to 850°C and cooled down to 25°C (e''_A, this study)	25	2.45	1.4	0.01
Aerogel heated up to 1100°C and cooled down to 25°C (e''_C, this study)	25	2.45	1.65	0.004

Substantial reduction of closed pores is observed over *Region I* (Fig. 5.6) for microwave processing. Similar behavior was reported in microwave sintering of porous alumina by Willert-Porada et al [14]. Reduction of closed porosity affected bulk density, but only to a small extent due to the fact that the percentage of closed pores was small (≈1.5%). It may be significant that, in *Region I,* microwave-processed samples revealed a reduction of closed porosity of about 50% with only 10% decrease in open porosity. In contrast, the conventionally processed samples

presented a 10% decrease in closed porosity and 5% reduction in open porosity. It appears that microwave energy interacts more with the closed pores. More research is required to explain why this should be the case, and this phenomenon is left for future investigators to explore.

It has been confirmed that silica aerogel manifested significant microwave absorption during *Region I*, which lead to the effect of a higher structural densification when compared to conventional processing. Absorbed species present in the monolithic silica aerogel and a high electric field enhanced the microwave absorption. This behavior suggests that, in this region, the microwave effects observed were a result of dipolar polarization mechanisms as discussed in Section 3.3. Dipolar polarization is known to be the main mechanism for microwave interaction with water and other polar materials [9].

Region I is particularly important in the structure evolution of microwave-processed aerogel because at the end of this region (about 850°C) there are structural parameters that contribute to the behavior of *Region II*. For example, the slightly higher bulk density (due to an increase in the polymerization reactions and some relaxation) in the microwave process results in a smaller pore size. This observation is confirmed in Fig.6.5 that shows the hydraulic radius (r_H). At 850°C, r_H is much smaller in the microwave-processed aerogel than in the conventionally processed. The hydraulic radius represents the average pore size of the silica aerogel calculated using Eq. 6.1 and Fig. 5.1 – 5.2 [15]. This difference in pore size will influence the bulk densification in *Region II* as discussed in subsequent sections.

$$r_H = 2V_p/SA \tag{6.1}$$

Where, V_p = Pore volume

SA = Surface area

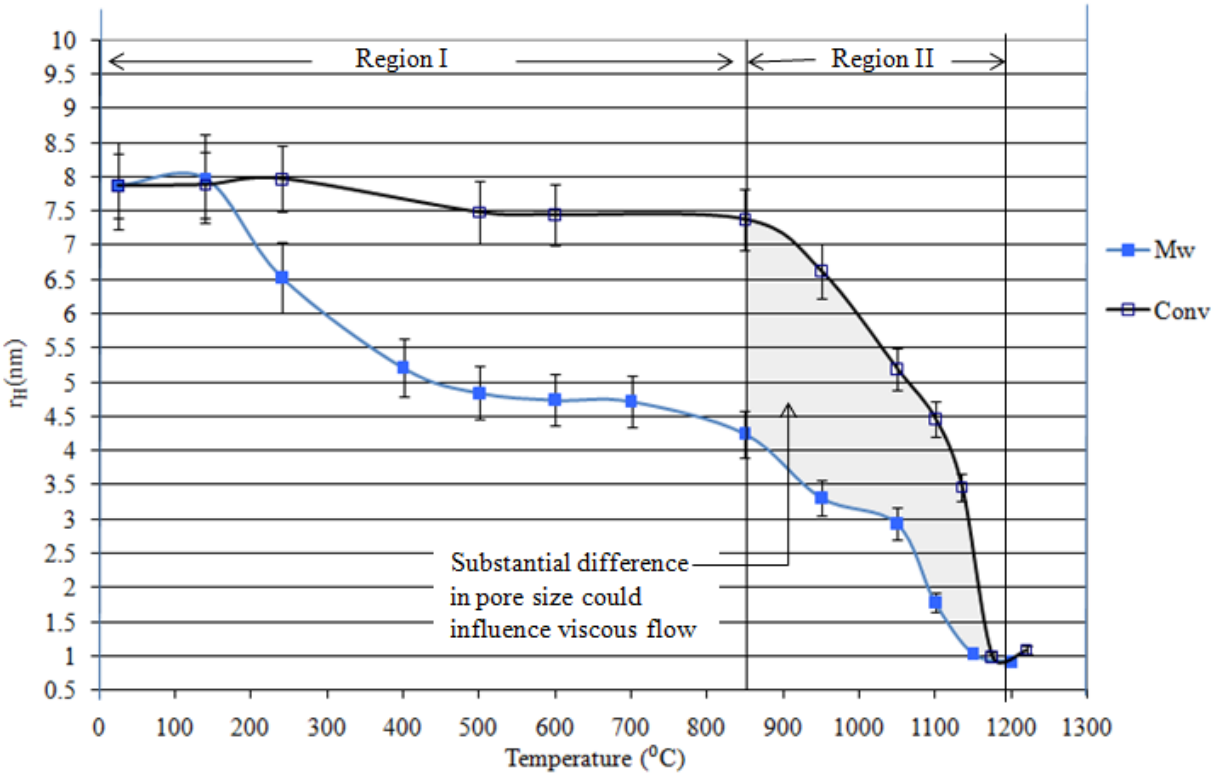

Fig. 6.5: Hydraulic radius vs. temperature for silica aerogel samples processed in conventional and microwave single mode ovens.

6.4 ***Region II***

This region ranged from 850 to 1200°C and was characterized by a significant increase in bulk density due primarily to the elimination of open pores. This behavior was observed (Fig. 5.4) for both processes as a greater increase in slope than observed in the previous region. During conventional heating, minimal weight losses (Fig. 5.7) continued even at the end of this region, probably as a result of the slow removal of water due to the residual condensation

reactions. Silica aerogel experienced a significant reduction in SA and open pores, shown in Figs. 5.1 and 5.5, respectively. This behavior indicated that mass transport and densification were taking place throughout this region. In silica gels, the mechanism responsible for densification due to the mass transport is viscous flow [16-18]. The driving force for viscous flow is the decrease in surface area of the highly porous gel [19], as shown in Fig. 5.1 between 850 and 1200°C. The presence of OH groups produced non-bridging oxygen bonds between adjacent Si atoms. Significant surface tension produced by the highly porous silica aerogel presented a constant stress resulting in a continuous deformation and fracture of the bonds, which resulted in viscous flow. This mass transport resulted in a shorter (n in Fig. 6.6b) and thicker (m in Fig. 6.6b) walls in the structure, while maintaining a constant solid volume.

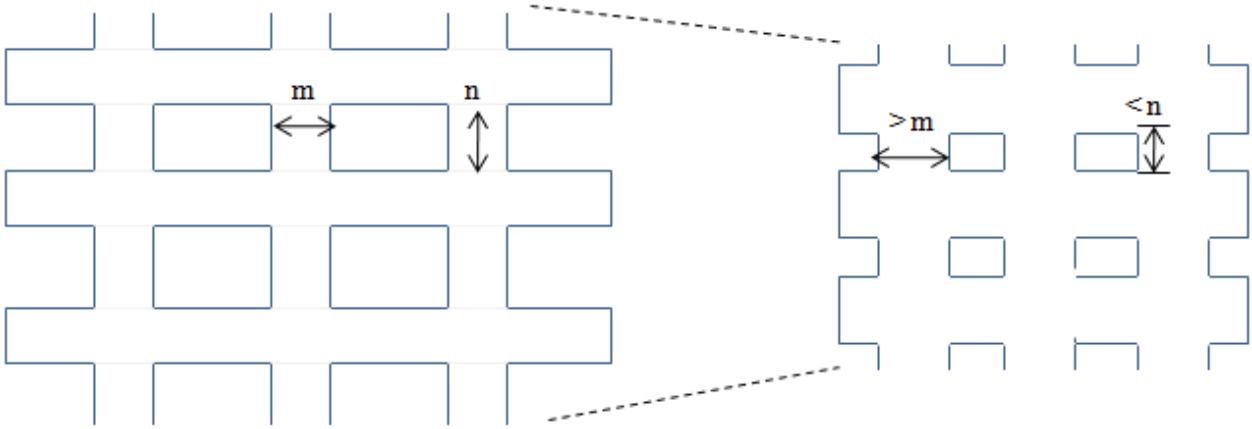

Fig. 6.6. Viscous flow densification during *Region II*: a) dried gel, b) partially densified structure after the beginning of viscous flow at temperatures higher than 850°C. Note that surface area of the pores is smaller after partial densification.

In microwave heating, above 850°C, the variation of structural density was minimal and suggests that the material achieved its maximum structural density (Fig. 5.3, 2.2 g/cm^3). Even though most of the microwave-absorbing species (water, ethanol, organics) appeared to have been removed in *Region I,* substantial reduction in %Po (Fig. 5.5) in *Region II* indicated that there was a significant interaction between microwaves and silica aerogel. This interaction was most likely due to the structural features, such as porosity, becoming more microwave-absorbing in this region. This supposition was supported by the change in the slope's direction, observed in the dielectric constants (e' and e"$_{eff}$) at the beginning of this temperature range (850°C, Fig. 5.9). Similar behavior of the dielectric properties was reported by Hrubesh et al [20]. In addition, Table 6.1 and Fig. 5.9 show that the dielectric losses of silica aerogel measured at 25°C for samples processed at 850°C (e"$_A$) and 1100°C (e"$_C$) were much lower than when these parameters were measured at the same processing temperature. This behavior indicates that the dielectric loss of silica aerogel samples increased as the temperature increased, a typical behavior of many ceramic materials, as pointed out in Section 3.6. Moreover, Table 6.1 shows that e"$_{eff}$ at 850°C (e"$_A$) was much higher than the e"$_{eff}$ heated at 1100°C (e"$_C$) when both samples were cooled back to room temperature (Fig. 5.9). Higher e"$_{eff}$ is related to higher microwave absorption, as expressed in Eq. 3.22 [21, 22]. Therefore, this data suggest that porosity (%P≈80% at 850°C and %P≈10% at 1100°C, Fig. 5.5) contributed to microwave absorption, most likely due to the interfacial polarization discussed in Section 3.3.

The substantial increase of Si-O-Si bonds observed in the FTIR spectroscopy at 950°C (Fig. 5.12) and the increase in bulk density also indicate that densification, governed by viscous flow, was present in this region in the microwave-processed aerogel. The effect of viscous flow can be observed in Fig.6.7, that shows the surface topography of two aerogel samples. One was

processed at 850°C (Fig. 6.7a) and shows a much rougher surface than the other sample processed at 1050°C (Fig. 6.7b). This change of surface topography is typical of a densification process via viscous flow [23]. The silica aerogel processed at 1050°C should have shown no features on the surface because most of the pores had collapsed. However, there were some surface pores (Fig. 6.7b) that were most likely due to OH groups trapped as a result of rapid densification. As the temperature increased, the pressure inside the pores also increased, creating defects (pores or features) on the surface of the material. Similar behavior was observed by researchers in silica gel when a large number of pores had closed before complete release of OH groups [16, 24].

Densification by viscous flow is a process that is influenced by several factors, such as temperature, viscosity, surface tension, and porosity, as previously reported in the literature [1, 3, 25]. This process is driven by the energy dissipated in the reduction of surface area [2, 16], which is very large (1300 m^2/g at room temperature in this study) for silica aerogel. In order to better understand the role of microwave processing in densification, a cylindrical model of viscous flow was adopted (previously used for conventional processing [2, 26, 27]).

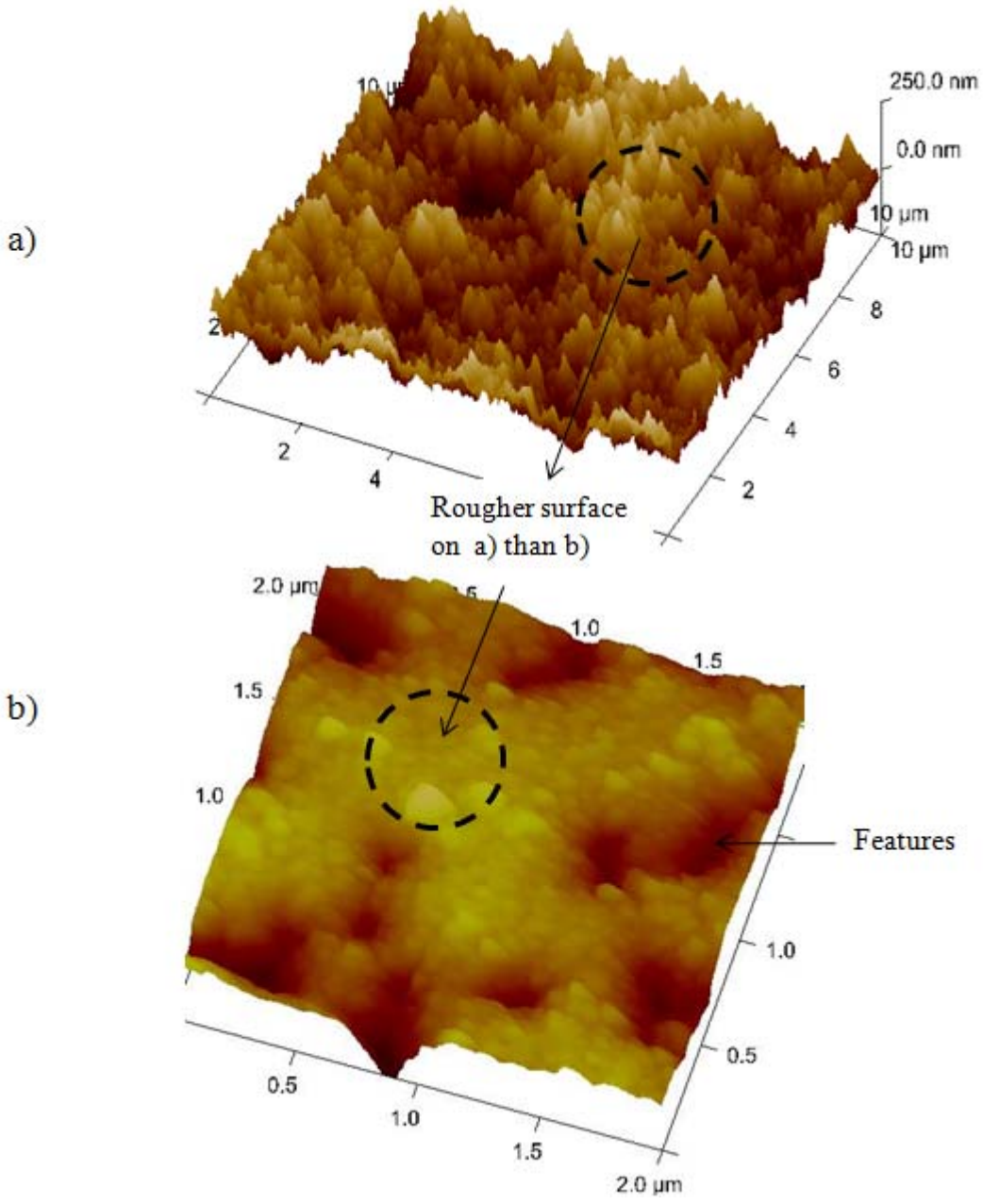

Fig. 6.7: Surface topography of microwave-processed silica aerogel: a) at 850°C, b) at 1050°C. Note the smoother texture in (b) which is characteristic of viscous flow.

6.4.1 Cylindrical model for the structure of low-density, open-pore materials

Several studies have verified that densification of amorphous porous materials is governed by viscous flow [26, 28]. Exact analysis of viscous flow densification is sometimes difficult due to the complex geometry of the porous body. A model that describes the rate at which a material containing open pores densified by viscous flow was proposed by Scherer [18, 27]. This model is based on the Frenkel approach, i.e. that the energy dissipated in viscous flow is equal to the energy gained by the decrease in surface area of the porous body [28]. This model was used to analyze the data in *Region II.* Although other models describe the densification of silica gel, most are qualitative in nature. In contrast, the Scherer-Frenkel model provides a more quantitative approach and relates measurable structural characteristics, such as density and pore size, to geometric features. This model has been used successfully by several researchers [2, 29], and while it makes some basic assumptions, these apparently do not significantly reduce its ability to describe the densification process.

The model approximates a series of bonded particles to cylinders (Fig. 6.8a.), then a cubic array of cylinders (Fig. 6.8b) is used to analyze the densification as the material changes in dimensions. The particles that make up the cylinders are assumed to be small spheres, as shown in Fig. 6.8a. This scenario is known to be the case for silica aerogel, which is composed of nano-sized spherical particles that agglomerate into larger spheres (several hundred nanometers) as the gelation process progresses [30, 31]. Scanning electron micrographs of the larger particles are shown in Fig. 6.9. In these micrographs, the observable pores range in size from about 20-200nm, which correspond to the larger pores shown in Fig. 2.4 for dried aerogels. The smaller pores (<20nm) cannot be seen in these micrographs.

Based on this model, the volume of the solid material of a single cylinder cell (V_S) is expressed by Eq. 6.2 [27].

$$V_S = 3\pi a^2 l - 8\sqrt{2}a^3 \tag{6.2}$$

Where, a = radius of the unit cell cylinder where

2a represents the particle size

l = length of the unit cell's edge

and $$\rho_B = \rho_S V_S / l^3 \tag{6.3}$$

Combining Eqs. 6.2 and 6.3, relative density (${}^{\rho_B}/_{\rho_S}$) can be expressed as

$${}^{\rho_B}/_{\rho_S} = 3\pi x^2 - 8\sqrt{2}x^3 \tag{6.4}$$

where, $x = a/l$

In addition, l is related to the size of the pore (d) by [27, 32]

$$\frac{\pi d^2}{4} \approx (l - 2a)^2 \tag{6.5}$$

$$d = 2r_H \tag{6.6}$$

where, r_H is the hydraulic radius (Eq. 6.1 and Fig. 6.5)

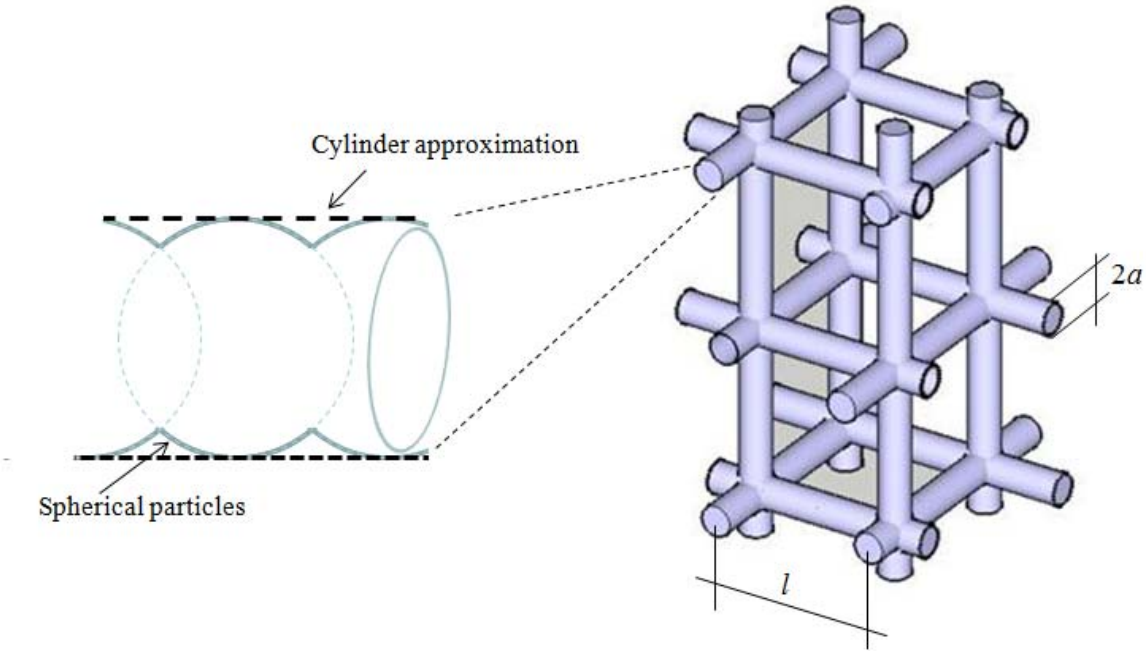

a) b)

Fig. 6.8: Cylindrical cubic array model: a) approximation of bonded particles to cylinders, b) cylindrical array of the cell.

Note that when a/l = ½, the neighboring cylinders touch and the cell contains a closed pore. The relative density at that instant is equal to 0.942 (using Eq. 6.4), which corresponds to about 6% of total porosity. Consequently, for greater relative densities, the structure is no longer described by the model.

To calculate the rate of densification of the model structure, Frenkel's approach was used. Frenkel derived the rate of energy dissipated during viscous flow and set this rate equal to the energy change resulting from the reduction in surface area for a cylindrical body [2]. From the combination of the Scherer model and Frenkel's energy analysis, an expression that describes the rate at which the dimensions of the cylindrical cell change is obtained (Eq. 6.7) [27, 29].

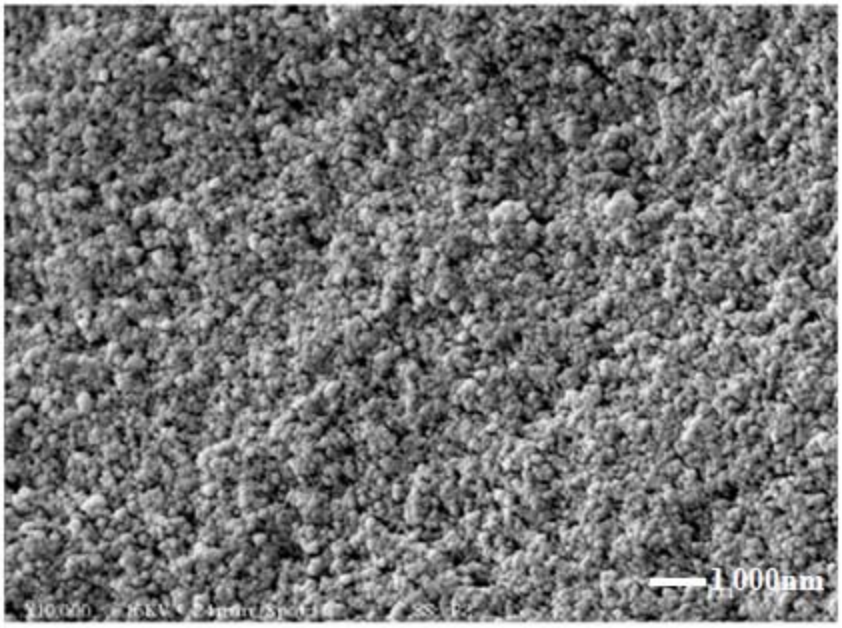

a)

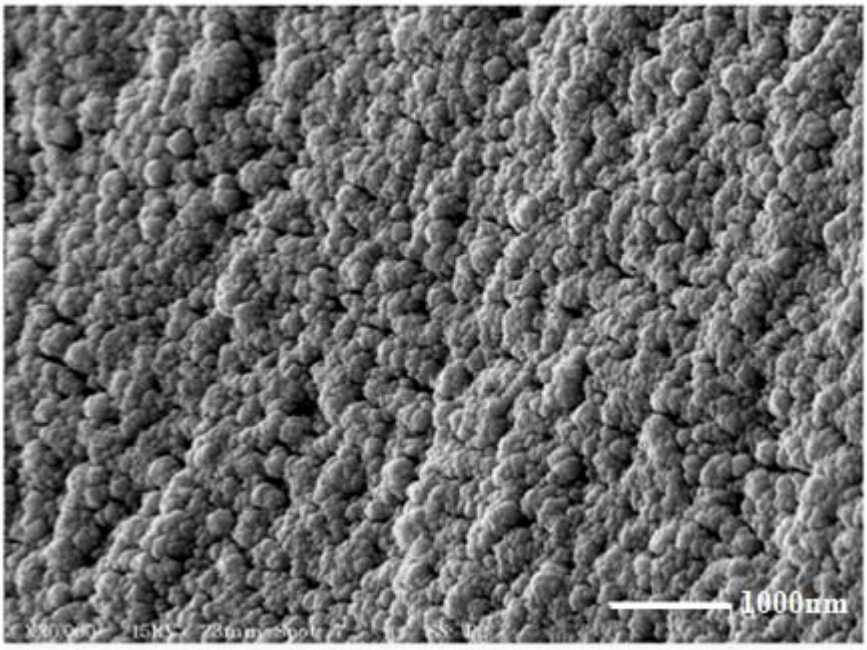

b)

Fig. 6.9: SEM micrograph of silica aerogel at room temperature revealed that silica aerogel was formed of large spherical particles (made of agglomerates of smaller particles) with diameters smaller than 200 nm: a) magnification 10,000X, and b) magnification 30,000X.

$$\frac{dx}{dt} = \left(\frac{\gamma}{2\eta}\right)\left(\frac{1}{l_{(t)}}\right) \tag{6.7}$$

Where, γ = surface tension (ergs/cm^2)

η = viscosity (Poises)

Recognizing that *Vs* is constant and using Eqs. 6.3 and 6.4, *l* as a function of time ($l_{(t)}$) can be obtained (Eq. 6.9).

$$Vs = l\left(\frac{\rho_B}{\rho_S}\right)^{1/3} = (3\pi x^2 - 8\sqrt{2}x^3)^{1/3} l_{(t)} \tag{6.8}$$

$$l_{(t)} = \frac{l(\rho_B/\rho_S)^{1/3}}{(3\pi x^2 - 8\sqrt{2}x^3)^{1/3}} \tag{6.9}$$

Combining Eqs. 6.7 and 6.9 leads to

$$\frac{2dx}{(3\pi x^2 - 8\sqrt{2}x^3)^{1/3}} = \frac{\gamma}{\eta l(\rho_B/\rho_S)^{1/3}}\, dt \tag{6.10}$$

Equation 6.7 presents *x* as a function of time. In addition, relative density is expressed as a function of *x* (Eq. 6.4), so Eq. 6.7 can be used to present relative density as a function of time.

Solving Eq. 6.10 leads to

$$\frac{\gamma}{\eta l\left(\frac{\rho_B}{\rho_S}\right)^{\frac{1}{3}}}(t - t_o) = \int_0^x \frac{2dx}{(3\pi x^2 - 8\sqrt{2}x^3)^{1/3}} \tag{6.11a}$$

$$\frac{\gamma}{\eta l\left(\frac{\rho_B}{\rho_S}\right)^{\frac{1}{3}}}(t - t_o) = -\frac{2}{\alpha}\left(\frac{1}{2} ln \frac{\alpha^2 - \alpha y + y^2}{(\alpha + y)^2} + \sqrt{3} tan^{-1} \frac{2y - \alpha}{\alpha\sqrt{3}}\right) \tag{6.11b}$$

Equation 6.11b relates the geometrical features of the cylindrical cell (i.e. size of cylinders and separated distance) to the structural features (structural and bulk densities) during densification. To further simplify,

$$K(t - t_o) = -\frac{2}{\alpha}\left(\frac{1}{2} ln \frac{\alpha^2 - \alpha y + y^2}{(\alpha + y)^2} + \sqrt{3} tan^{-1} \frac{2y - \alpha}{\alpha\sqrt{3}}\right) \qquad (6.11c)$$

where, α is a constant equal to $(8\sqrt{2})^{1/3}$

t_o is a fictitious time at which x=0

$$y^3 = \left(\frac{3\pi}{x}\right) - 8\sqrt{2} \qquad (6.12)$$

$$K = \left(\frac{\gamma}{\eta l}\right)(\rho_B/\rho_S)^{-1/3} \qquad (\text{sec}^{-1}) \qquad (6.13)$$

The product of *K(t-to)* is referred to as the reduced time at which the relationship *a/l* is achieved for a specific relative density. Also, it represents the extent of densification for a specific processing time. Using Eqs. 6.4 and 6.12 and assuming values for the relative density, the corresponding set of *x* values can be obtained. A theoretical plot of relative density vs. *K(t-to)* can be obtained from this procedure, as shown in Fig. 6.10. This plot represents the trend of densification as a function of reduced time for the model. If either *a* or *l* in Eq. 6.5 could be determined experimentally, an experimental plot of ρ_B/ρ_S vs *K(t-to)* could be obtained. Presently, neither of these values could be obtained with sufficient accuracy to determine *K(t-to)* with confidence. Using the measured values of relative density (Fig. 6.11), the reduced times for the processed samples can be determined graphically from the theoretical plot, as pointed out by the arrows in Fig. 6.10. This data is also shown in Table 6.2 for several processing temperatures and times. Based on this model, Table 6.2 and Fig. 6.10 reveal that the conventionally processed

samples require a longer time and/or higher temperature to achieve the same relative density of the microwave process.

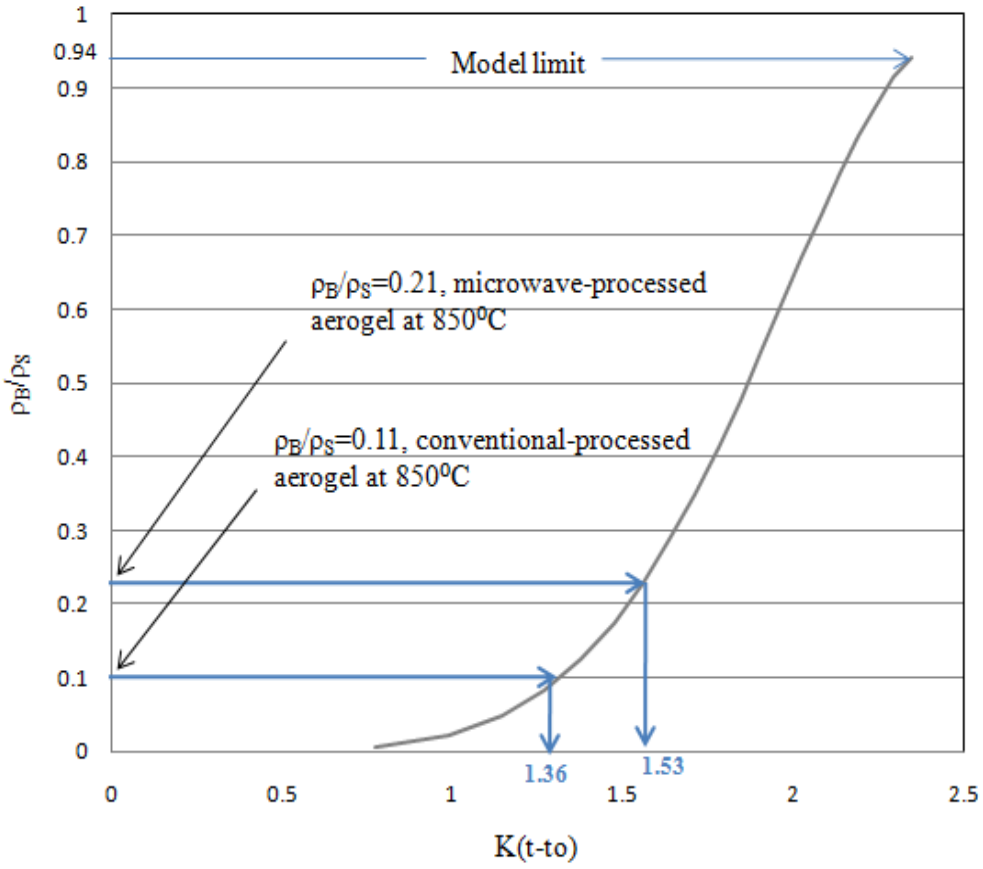

Fig. 6.10: Theoretical plot of relative density vs. *K(t-to)*. Examples of how to obtain the *K(t-to)* value having the measured relative density also are illustrated.

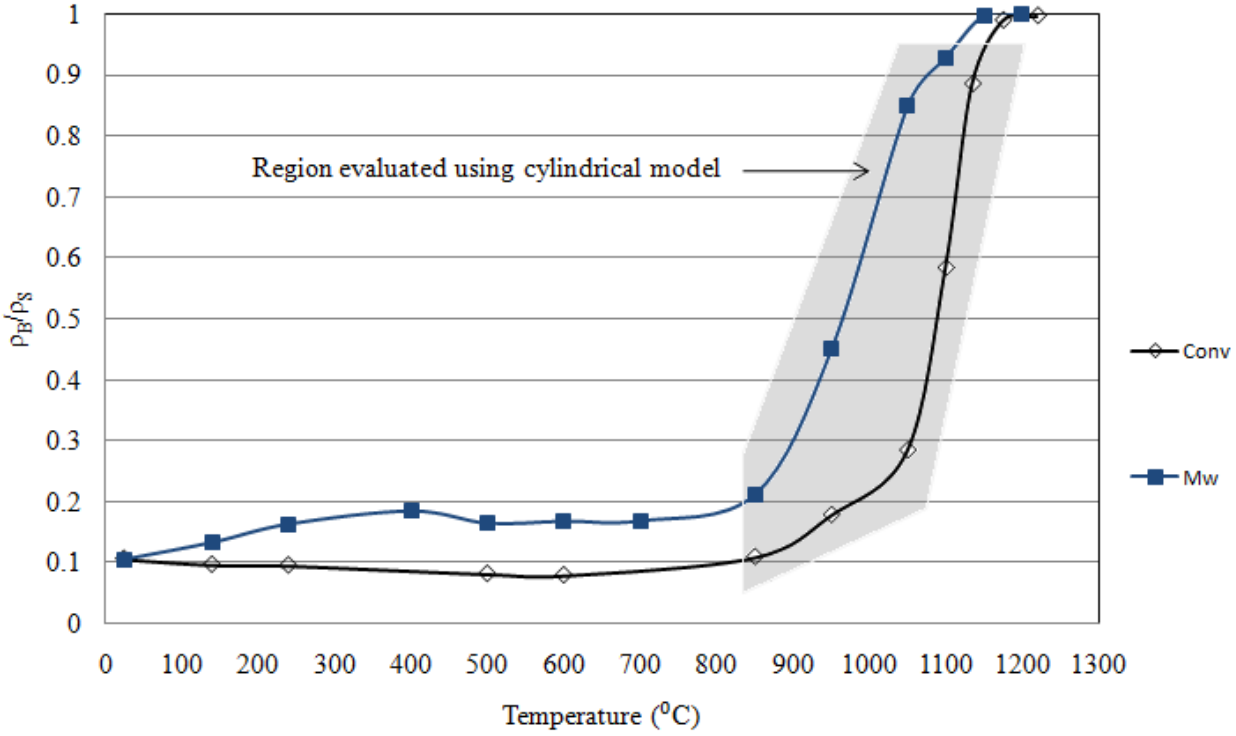

Fig. 6.11: Relative density of silica aerogel samples processed at different temperatures in conventional and microwave ovens. Notice that the maximum relative densities at which this model was evaluated were 0.93 (at 1100°C) and 0.88 (at 1135°C) for the microwave and conventional processes, respectively. Therefore, the criterion that the model should be used for relatively densities lower than 0.94 was met.

Table 6.2: Reduced times obtained for different temperatures and processing times.

Temperature (°C)	**Processing time (min)**	**Conventional**		**Microwaves**	
		ρ_B/ρ_S	***K(t-to)***	**ρ_B/ρ_S**	***K(t-to)***
850	30	0.108	1.33	0.212	1.53
950	30	0.177	1.46	0.450	1.76
950	60	0.188	1.49	0.492	1.86
1050	30	0.283	1.63	0.850	2.20
1100	30	0.583	1.79	0.920	2.19
1100	60	0.62	2.02	0.940	2.38

Reduced time (*K(t-to)*) vs. real processing time (soak time) is shown in Fig. 6.12. Note that at t=0, the reduced time has a finite value, which is greater for the microwave-processed samples at the beginning of viscous flow (also the beginning of *Region II*). A higher value of *K(t-to)* indicates that the extent of densification is greater for that time. The slope of a specific line in Fig. 6.12 is equal to *K* (Eq. 6.13) [27, 29] and is related to the rate of densification for that specific process and temperature. This figure shows that the microwave-processed samples not only have a higher initial extent of densification, but also have rates of densification about a factor of two greater (Table 6.3) than the conventionally processed samples.

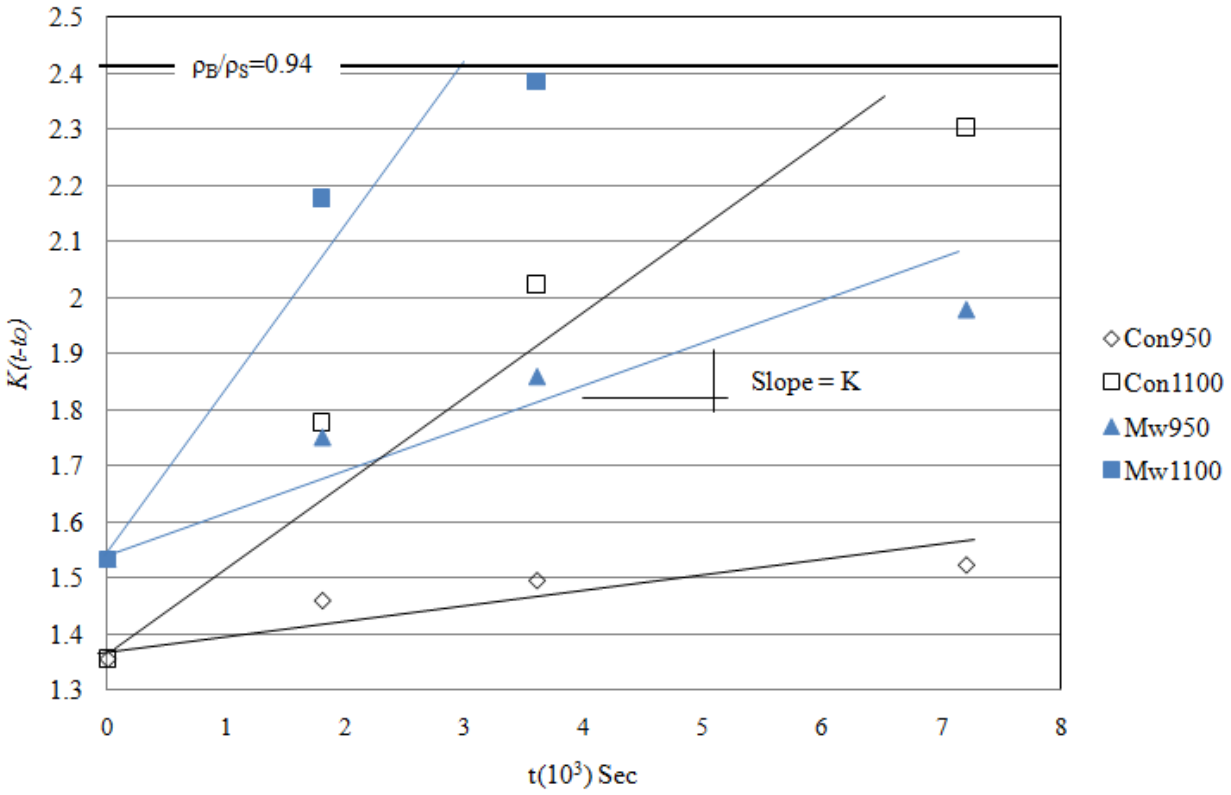

Fig.6.12: Reduced time vs. different processing times (30, 60, 120 min) for two different temperatures, 950 and 1100°C. Notice that the microwave-processed sample at 1100°C for 120 min was not evaluated because, at that time, the relative density was higher than 0.94.

Table 6.3: Initial parameters used to calculate viscosity based on the cylindrical model.

Parameter	Conventional	Microwave
Initial bulk density (ρ_{Bo})	0.22 g/cm^3	0.46 g/cm^3
Initial structural density (ρ_{So})	2.07 g/cm^3	2.20 g/cm^3
Initial length of the unit cell's edge (*lo*)	17.19 nm	11.32 nm
Surface tension in silica gel (γ, temperature range: 850 – 1100°C)	280 ergs/cm^2 [29]	280 ergs/cm^2 (assumed)
K at 950°C	2.3x10^{-5}	5.8x10^{-5}
K at 1100°C	1.3x10^{-4}	2.3x10^{-4}

In order to understand why the rate of densification is greater for the microwave-processed samples, Eq. 6.13 must be carefully evaluated. It can be seen that *K* depends on four parameters; surface tension (γ), viscosity (η), initial cell size (*lo*), and the initial relative density (ρ_B/ρ_S). The initial relative densities can be obtained from Fig. 6.11, and Eqs. 6.4 – 6.6 can be used to determine *lo*. The last two parameters are constant for a given process and are presented in Table 6.3. The product of $\left(\frac{1}{lo}\right)\left(\frac{\rho_{Bo}}{\rho_{So}}\right)^{-1/3}$ for the microwave process is 22% higher than for the conventional process, which is not sufficient to account for a factor of two higher value of K observed during the microwave process in *Region II*. Therefore, either viscosity or surface tension must be different for the two processes.

The literature provides the surface tension for silica gel (conventionally processed) in the range between 800-1200°C where viscous flow occurs as 280 ergs/cm^2 [29]. Assuming this

parameter is the same for both processes and rearranging Eq. 6.13, the viscosity can be represented as

$$\eta = (\gamma)\left(\frac{1}{K}\right)\left(\frac{1}{l_o(\rho_{Bo}/\rho_{So})^{1/3}}\right) \tag{6.14}$$

If the slope *K* (for each temperature and process) is obtained from Fig. 6.12, then viscosity can be calculated using Eq. 6.14. Initial values used to obtain viscosity in the conventional and microwave processes are shown in Table 6.3. A plot for viscosity vs. temperature is shown in Fig. 6.13. The same procedure was followed to calculate viscosity in both conventional and microwave processes. No variation bars are shown in this figure because viscosity is calculated using the average values of the relative density and size of the pores. The viscosity obtained using the experimental data and the cylindrical model is within the range reported by the literature, plotted in Fig. 6.13 as silica gel I and II [25, 29].

Figure 6.12 shows that viscosity is apparently lower during the microwave process than during the conventional process. Viscosity is a property that depends on the strength of the bonds in the structure. As the concentration of hydroxide groups increases, the overall strength of the structure decreases, resulting in a lower viscosity [3, 25]. As a result, viscosity in the microwave process should be higher according to the FTIR results (Fig. 6.13) that show higher concentration of siloxane bonds, which also is associated with lower concentration of hydroxide groups. Therefore, either the original assumption that surface tension was the same for both processes is incorrect, or there is a "microwave effect" on viscosity that outweighs the lower concentration of hydroxide groups.

A microwave effect is one that cannot be explained based on existing knowledge and theory. For example, volumetric and selected heating phenomena that occur during microwave

heating are not considered to be a microwave effect because their origins are understood. In contrast, the observation that chemical reactions or sintering occur at lower temperature in a microwave oven are considered microwave effects because these phenomena are not understood.

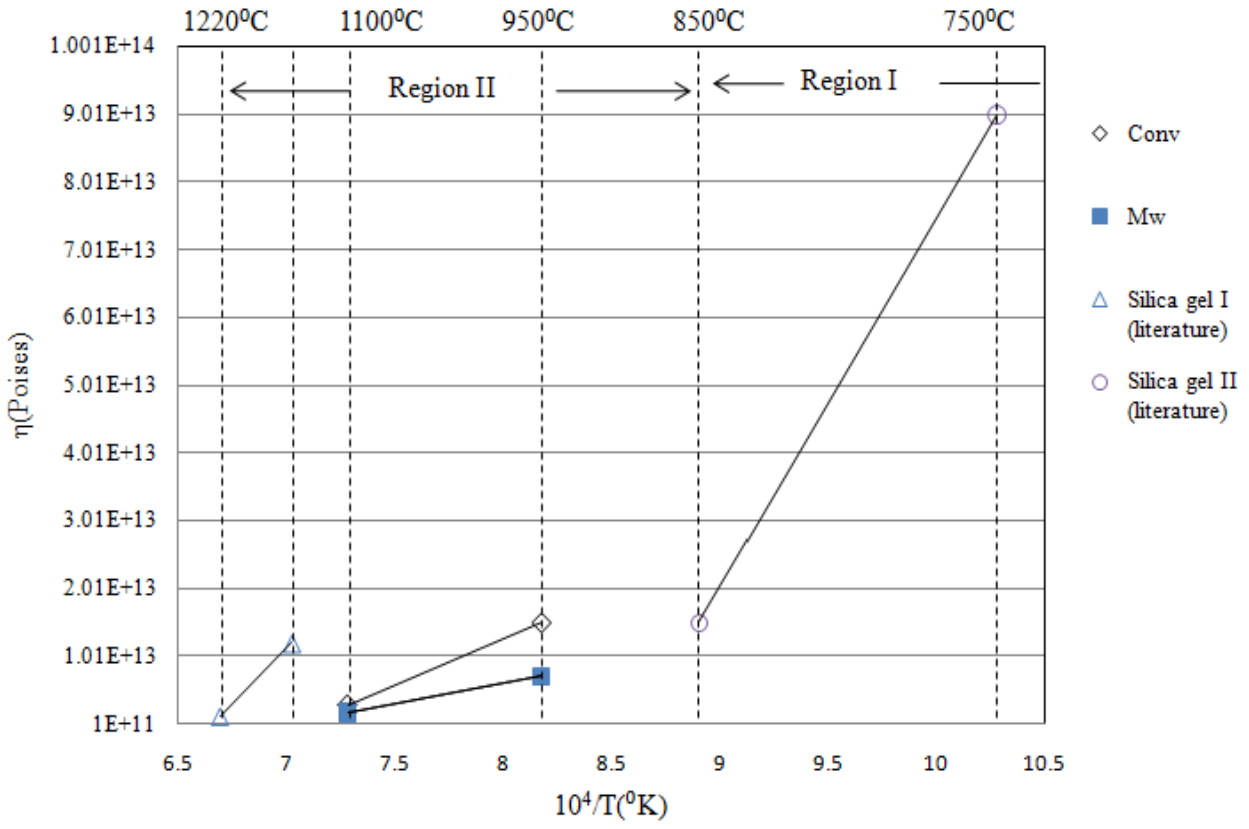

Fig. 6.13: Viscosity of microwave- and conventionally processed silica aerogel calculated for two different temperatures, 950 and 1100°C. Viscosity of silica gel from the literature also is plotted [25, 29].

Surface tension may be different in the microwave process based on the fact that silica aerogel, in this region, has less hydroxide groups, as is pointed out previously. Researchers have shown that surface tension increases when the concentration of hydroxide groups is reduced [3,

17], and this increase favors viscous flow densification [33]. Additionally, if surface tension is higher, a higher densification rate (K) is obtained, as expressed in Eq. 6.13, which was observed during the microwave process.

On the other hand, to further investigate if a microwave effect could be possible during viscous flow densification, the activation energy (Q) was calculated. Viscosity for silica gel in the range of 900 to 1400°C can be expressed by an Andrade-type equation (Eq. 6.15) [34].

$$\eta = \eta_o \exp\left(\frac{Q}{RT}\right) \tag{6.15a}$$

Where, η_o = constant

R = gas constant (1.985 cal/Kmol)

T = absolute temperature

Eq. 6.15a also can be expressed as

$$LN(\eta) = \frac{Q}{R}\left(\frac{1}{T}\right) + LN(\eta_o) \tag{6.15b}$$

Knowing the viscosity values for silica aerogel at 950 and 1100°C from Fig. 6.13, $LN(\eta)$ vs. 1/T can be plotted, as shown in Fig. 6.14. Based on Eq. 6.15b, the slope of this graph is equal to Q/R, so activation energy can be calculated, as shown in Table 6.4. Figure 6.14 also plots two silica gels from the literature, each with a different level of dehydration (hydroxide concentration) as shown in Table 6.4. According to the literature, vitreous silica (fully dehydrated) has an activation energy between 120 and 170 kcal/mol [2], which is consistent with the value obtained for silica gel I. Notice that microwave and conventionally processed samples (this study) have an activation energy between the fully and non-dehydrated samples from the

literature. This result is because these samples (this study) were partially dehydrated during the 30 min soak thermal treatment at 950 and 1100°C. As the concentration of hydroxide groups increases, lower activation energy is required to fracture the bonds, because the presence of hydroxide groups weakens the silica network. Most of the bonds present in the fully dehydrated silica gel are siloxane bonds. Comparing the energy of the Si-O bond (148 Kcal/mol, [6]) with the activation energy of fully dehydrated samples (Table 6.4), both energies are similar indicating that the barrier of energy necessary to densify the material was primary related with a structural rearrangement of Si-O bonds.

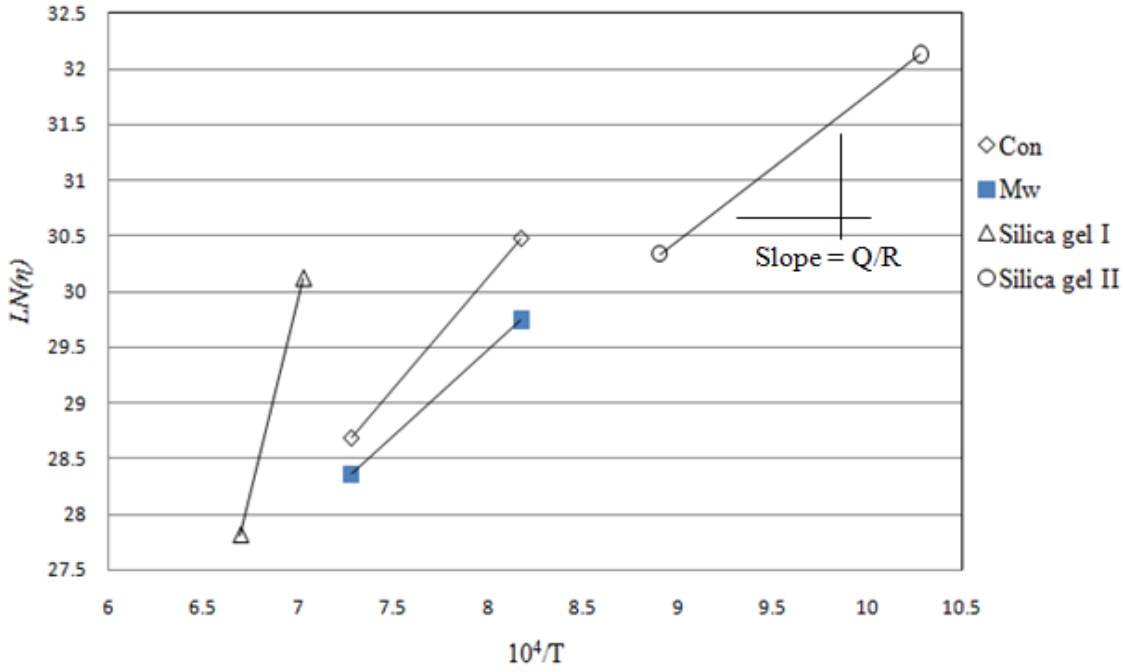

Fig. 6.14: Activation energies can be calculated from the slope of these graphs for microwave- and conventionally processed silica aerogel. Also, activation energies for silica gels from the literature were calculated.

Knowing that microwave-processed aerogel has lower concentration of hydroxide groups than the conventionally processed, the activation energy should be higher. However, an

"apparent" lower activation energy was obtained for the microwave process (Table 6.4). Similar results have been observed for different ceramic materials using microwave processing [35, 36]. The term apparent is used because the activation energy obtained could have been influenced by a non-thermal source such as the electric field, as suggested by other researchers [35-38]. Thus the fact that a lower activation energy was obtained for the microwave-processed samples supports the possibility that a microwave effect could be present during viscous flow densification of silica aerogel. Further investigation is required to prove the existence and mechanisms of a non-thermal effect.

Table 6.4: Activation energies calculated for different silica gels. The data are ranked in order of increasing levels of dehydration.

Process	**Temperature range (°C)**	**Activation energy (kcal/mol)**	**Level of dehydration**
Conventional (literature) [25]	700 - 850	26	No dehydration
Conventional (this study)	950 - 1100	40	Partial dehydration
Microwaves (this study)	950 - 1100	31	More dehydration
Conventional (literature) [29]	1150 - 1220	139	Fully dehydrated

It should be mentioned that structural differences observed in *Region I* between microwaves and conventional processing were not associated with a "microwave effect." This is because these differences could be understood based on enhanced electric fields in the presence of water and alcohol resulting in more extensive polymerization reactions.

6.5 ***Region III***

This region existed at temperatures greater than or equal to 1200°C and showed a small variation in bulk density for both processes. X–ray diffraction data indicated that silica aerogel in *Region* I and II was an amorphous material for both microwave and conventional heating (Figs. 5.13a and 5.14a, respectively). However, at 1200°C, microwave-processed aerogel showed the presence of the characteristic peak of cristobalite, suggesting that the material was at the beginning of a phase change (Fig. 5.13b). In addition, inclusions observed in the TEM (Fig. 5.16) and XRD data most likely corresponded to the beginning of a nucleation stage. In order to evaluate whether a similar situation was manifested in the conventionally heated silica aerogel, several samples were processed beyond the temperature range covered by this study for times longer than 30 min (30 min was the standard soak time for all the other samples, as was shown in Fig. 4.5). Similar behavior was observed in the conventional process between 1300 and 1400°C, as shown in the XRD and TEM (Figs. 5.14c and 5.15, respectively). Wang and Tsai reported that xerogel (another type of silica gel) crystallized at temperatures between 1250 and 1350°C with conventional heating, which required times longer than 800 min to reach a transformed cristobalite of higher than 20% [39, 40]. Also, researchers have reported that cristobalite formed from amorphous silica at low temperature (≈ 1200°C) has a lower density than the density of amorphous silica [41], as shown in the structural density (Fig. 5.3). Therefore, the data obtained and the information from the literature suggest that this region is characterized by a nucleation and crystallization phase dependent on the incubation time (in this case, the soak time).

During microwave processing, the microwave signal experienced a substantial amount of reflected power (90%), shown in Table 5.1. This data indicates that the absorption of microwave

energy in *Region III* was lower than in the previous regions. The reflected power increased because the power absorbed decreased due to the reduction of dielectric loss of the sample, as expressed in Eq. 3.24. In other words, the loaded cavity behaved as an empty cavity because the sample became transparent to the microwaves (Fig. 3.1a).

In an extensive study of crystallization using microwaves conducted by M. Mahmoud [42], it was found that crystalline lithium disilicate had a much lower dielectric loss than the amorphous glass state, and that its microwave absorption was substantially reduced during the crystallization process. Amrhein and Muller verified experimentally that tan δ (explained in Section 3.4) of quartz silica (crystalline form) at microwave frequencies was much lower (2 orders of magnitude) than vitreous silica (amorphous form) [43]. Silica aerogel had a low dielectric loss during the whole temperature range in this study ($e'' < 0.3$). If silica aerogel crystallized, it follows that its dielectric loss would have decreased. The decrease in dielectric loss would have produced a reduction in microwave absorption. When the power applied was kept constant and the microwave absorption decreased, the reflected power increases, as expressed by Eq. 3.24, which was the behavior observed in *Region III* (Table 5.1). Thus it is likely that, at temperatures greater than 1200°C, silica aerogel could have been at the beginning of a crystallization stage characterized by the reduction in dielectric loss, which produced a reduction in the interaction between microwave energy and silica aerogel. The onset of crystallization appears to have been in the range of 50 -100°C lower in the microwave- processed sample as compared to the conventionally processed sample in this study.

6.6 Summary

The study of the effect of microwave energy on structural evolution of silica aerogel was performed over the temperature range from 25 to 1200°C. A few conventional processing experiments were conducted at temperatures beyond the range used in the microwave process to determine whether the structural evolution behavior was the same or different from microwave processing at 1200°C. A schematic that compares the structure evolution in microwave and conventional processing is shown in Fig. 6.15. Results obtained during the characterization of silica aerogel revealed that the structure evolution could be represented in three different regions.

Region I ranged from room temperature to 850°C. The strong interaction between the silica aerogel and microwave energy lead to a faster (than conventional processing) increase in structural density. This densification was the result of the combination of the following factors: 1) water and ethanol residues within porous silica aerogel resulted in a composite silica matrix with high dielectric loss, 2) interaction of high electrical field with high microwave-absorbed species (water, alcohol, and organic) resulted in a high microwave interaction, and 3) possible acceleration of polycondensation reactions enhanced structural density.

Region II rangeed from 850 to 1200°C and presented a rapid increase in bulk density. Densification governed by viscous flow characterized this region. The accelerated kinetics in this region for the microwave process were attributed to several factors. First, at the beginning of *Region II,* the microwave-processed sample had a smaller pore size and higher structural density due to more effective polycondensation reactions in *Region I*. Second, the more effective elimination of the hydroxide groups could have increased the surface tension and increased the rate of densification. Third, there was most likely a non-thermal microwave effect which could

have reduced viscosity, even though the hydroxide concentration had decreased. The origin of the non-thermal effect is left for future investigators to determine.

Region III covered temperatures greater than 1200°C. This region presented a similar structural behavior for both processes. Significant increase of the power reflected during microwave processing indicated that the dielectric loss decreased at these temperatures, which reduced the microwave energy absorption. The XRD data revealed the presence of cristobalite peaks, and the TEM showed small inclusions in the microwave-processed sample heated to 1200°C. These factors indicated the beginning of a nucleation/crystallization phase around 1200°C, which was about 50 – 100°C lower than the results observed in the conventionally processed samples. The onset of crystallization at lower temperature during microwave processing and the reduction of microwave absorption as a result of crystallization have been previously reported for lithium disilicate glass [42].

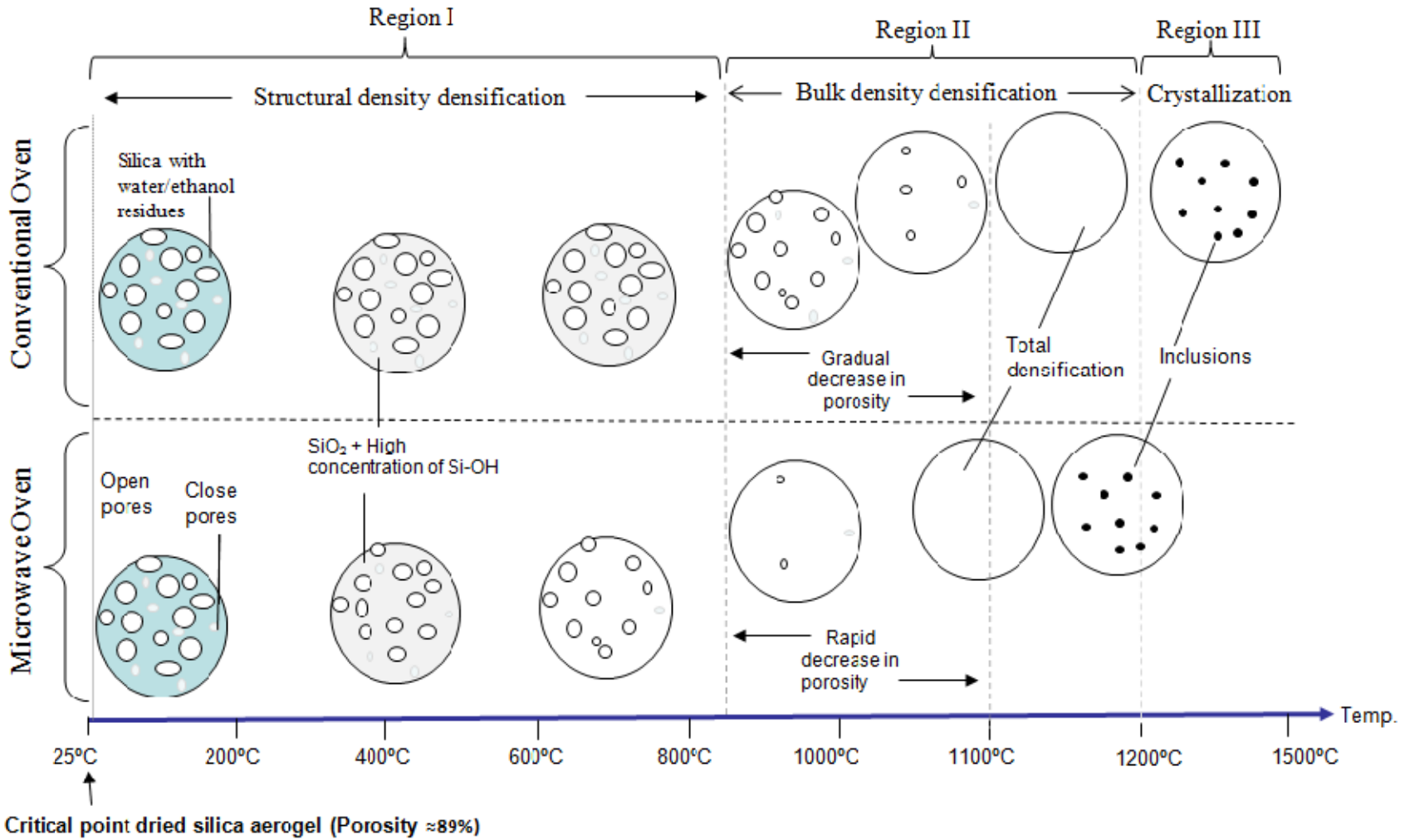

Fig. 6.15: Schematic of the structure evolution of silica aerogel in conventional and single mode microwave ovens.

References

1. Kingery, W.D. and H.K. Bowen, *Introduction to ceramics*. 1976. New York, New York: John Wiley & Sons.
2. Brinker, C.J. and G.W. Scherer, *Sol-Gel Science*. 1990. New York, New York: Academic Press.
3. James, P.F., *The gel to glass transition: chemical and microstructural evolution.* Journal of Non-Crystalline Solids, 1988. **100**: p. 93-114.
4. Colby, M.W., A. Osaka, and J.D. Mackenzie, *Effect of temperature on formation of silica gel.* Journal of Non-Crystalline Solids, 1986. **82**: p. 37-41.
5. Araujo, F.G., G.P. Latorre, and L.L. Hench, *Structural evolution of porous type-VI sol gel silica glass.* Journal of Non-Crystalline Solids, 1995. **185**: p. 41-48.
6. Iler, R.K., *The Chemistry of Silica*. 1979: John Wiley & Sons.
7. Hench, L.L. and J.K. West, *The sol-gel process.* Chem. Rev., 1990. **90**: p. 33-72.
8. Hench, L.L. and J.K. West, *Principles of Electronic Ceramics*. 1990: John Wiley & Sons, Inc.
9. Metaxas, A.C. and R.J. Meredith, *Industrial Microwave Heating*. 1983. London, United Kingdom: Peter Peregrinus Ltd.
10. Roussy, G. and J.A. Pearce, *Foundations and Industrial Applications of Microwaves and Radio Frequency Fields*. 1995. West Sussex, England: John Wiley & Sons Ltd.
11. Balanis, C.A., *Advanced engineering electromagnetics*. 1989. New York, New York: John Wiley & Sons.
12. Oree, S., *A modified cavity perturbation technique for measurement of the dielectric constant of high permitivity materials*, in *Advances in microwave and radio frequency processing*, M. Willet-Porada, Editor. 2006. Springer-Verag: Germany.
13. Gabriel, C., et al, *Dielectric parameters relevant to microwave dielectric heating.* Chemical Society Reviews, 1998. **27**: p. 213-223.
14. Porada, M.W., *A microstructural approach to the origin of "microwave effects" in sintering of ceramics and composites*, in *Microwaves:Theory and Application in Materials Processing IV*, David Clark, Williard H. Sutton, and David A. Lewis, Editors. 1997. The American Ceramic Society: Westerville, Ohio.
15. Scherer, G.W. and D.M. Smith, *Cavitation during drying of a gel.* Journal of Non-Crystalline Solids, 1995. **189**: p. 197-211.
16. Fricke, J., Editor. *Aerogels*. Springer Proceeding in Physics. Vol. 6. 1986. Springer-Verlan: Berlin, Germany.
17. Maniar, P.D., et al, *Energetics and structure of sol-gel silicas.* Journal of Non-Crystalline Solids, 1990. **124**: p. 101-111.
18. Brinker, C.J. and G.W. Scherer, *Sol - Gel - Glass: I. Gelation and Gel Structure.* Journal of Non-Crystalline Solids, 1985. **70**: p. 301-322.
19. Orgaz-Orgaz, F., *Gel to Glass Conversion:Densification Kinetics and Controlling Mechanisms* Journal of Non-Crystalline Solids, 1988. **100**: p. 115-141.
20. Hrubesh, L.W., L.E. Keene, and V.R. Latorre, *Dielectric properties of aerogels.* Material Research Society, 1993. **8**: p. 1736 - 1741.
21. Chan, C.T. and H.C. Reader, *Understanding Microwave Heating Cavities*. 2000. Boston, Massachusetts: Artech House, Inc.

22. Hirao, K., M.I. Jones, M.E. Brito, and M. Toriyama, *Microwave Sintering of Silicon Nitride Ceramics*, in *Advances in Microwave and Radio Frequency Processing*, Monika Willert-Porada, Editor. 2001. Springer: Bayreuth, Germany. p. 533 - 540.
23. Richerson, D.W., *Modern Ceramic Engineering*. 2006. Boca Raton, Fl: Taylor & Francis.
24. Hrubesh, L.W., T.M. Tillotson, and J.F. Poco, *Characterization of ultralow-density silica aerogels made from a condensed silica precursor*, in *Better Ceramics through chemistry IV*, Brian Zelinski, Jeffrey Brinker, David Clark, and Donald Ulrich, Editors. 1990. Materials Research Society: San Francisco, California. p. 315-320.
25. Gallo, T.A. and L.C. Klein, *Apparent viscosity of sol-gel processed silica.* Journal of Non-Crystalline Solids, 1986. **82**: p. 198-204.
26. Klein, L.C. and T.A. Gallo, *Densification of sol-gel silica: Constant rate heating, isothermal and step heat treatments.* Journal of Non-Crystalline Solids, 1990. **121**: p. 119-123.
27. Scherer, G.W., *Sintering of low-density glasses: I, Theory.* Journal of The American Ceramic Society, 1977. **60**(5): p. 236-239.
28. Mackenzie, J.K. and R. Shuttleworth, *A phenomenological theory of sintering.* Proceedings of the Physical Society. Section B, 1949. **62**: p. 833-852.
29. Scherer, G.W. and D.L. Bachman, *Sintering of low-density glasses:II, experimental study.* Journal of The American Ceramic Society, 1977. **60**(5-6): p. 239-243.
30. Zarzycki, J., *Structural aspects of sol-gel synthesis.* Journal of Non-Crystalline Solids, 1990. **121**: p. 110-118.
31. Lours, T., J. Zarzycki, A.F. Craievich, and M.A. Aegerter, *Textural characteristics of silica aerogels from SAXS experiments.* Journal of Non-Crystalline Solids, 1990. **121**: p. 216-220.
32. Iura, J., H. Hishikura, M. Kamikatano, and T. Kawaguchi, *Changes in the porous structure of silica gels during the gel-to-glass conversion.* Journal of Non-Crystalline Solids, 1988. **100**: p. 241-246.
33. Mulder, C.A.M., J.G.V. Lierop, and G. Frens, *Densification of SiO2-xerogels to glass by Ostwald ripening.* Journal of Non-Crystalline Solids, 1986. **82**: p. 92-96.
34. Hetherington, G., K.H. Jack, and J.C. Kennedy, *The viscosity of vitreous silica.* Physics and Chemistry of Glasses, 1964. **5**(5): p. 130 - 136.
35. Janney, M.A., H.D. Kimrey, W.R. Allen, and J.O. Kiggans, *Enhanced diffusion in sapphire during microwave heating.* Journal of Material Science, 1997. **32**: p. 1347-1355.
36. Janney, M.A. and H.D. Kimrey, *Diffusion-controlled processes in microwave-fired oxide ceramics.* Oak Ridge National Laboratory, 1992(Conf - 900466-103).
37. Agraval, D., J. Cheng, and R. Roy, *Microwave processing of ceramic and metallic materials in single mode E field and H field.*, in *10th International Ceramic Congress, 2002, Part B*. 2003. Advances in Ceramics and Technology Faenza, Italy. p. 381-388.
38. Gu, X.M., W. Liu, and K.M. Liang, *The effect of the electric field in glasses.* Materials Science and Engineering A, 1999. **265**(1-2): p. 177-185.
39. Bouajaj, A., M. Ferrari, and M. Montagna, *Crystallization of Silica Xerogels: A Study by Raman and Fluorescence Spectroscopy.* Journal of Sol-Gel Science and Technology, 1997. **8**: p. 391-395.
40. Wang, L.H. and B.J. Tsai, *The sintering and crystallization of colloidal silica gel.* Material letters, 2000. **43**: p. 309 - 314.

41. Pavlov, V.F., *Effect of cristobalite on the properties of acid-resistant materials.* Glass and ceramics, 1971. **28**(12): p. 727 - 730.
42. Mahmoud, M.M., *Crystallization of lithium disilicate glass using variable frequency microwave processing*, *Dissertation in Material science and engineering*. 2007. Virginia Polytechnic Institute and State University: Blacksburg, VA.
43. Amrhein, E.M. and F.H. Muller, *Low-temperature microwave absortion in insulating materials.* Journal of The American Chemical Society, 1967. **90**(12): p. 3146-3149.

CHAPTER VII

Conclusions and Original Contributions

The goal of this investigation was to determine if there were differences in structure of silica aerogel produced using microwave and conventional processes. If so, then explain the reasons behind the observed differences. This research provided evidence that differences in structure did exist when silica aerogel was processed using microwave energy. At the same time, this study confirmed that microwave energy absorption could be obtained in silica aerogel using a single mode microwave oven at 2.45GHz over the temperature range from room temperature (25°C) to 1200°C.

A systematic study of structure evolution in silica aerogel was performed in conventional and microwave ovens. Structure values (structural density, bulk density, surface area, volume of the pores, hydraulic radius, porosity) obtained during the conventional process were in reasonable agreement with data observed in the literature. A comparison of structural parameters obtained for both processes, microwave and conventional, revealed that the structure evolution could be divided into three distinct regions. Explanations of the structure evolution results were provided for each region.

The evolution of the structural parameters observed in the microwave process was similar to the one observed in the conventional process, but in microwave processing, the evolution occurred at lower temperatures. In some cases, the differences in temperature reached 200°C.

Water and perhaps ethanol species were still present at low temperature (< 850°C) in the silica aerogel samples after the material was dried under supercritical conditions. The combination of these species and high electrical field enhanced the microwave adsorption in silica aerogel most likely due to dipolar polarization. Between 850 and 1200°C, a combination of interfacial interaction (due to porosity) and possible lower viscosity (or higher surface tension) in microwave processing increased the bulk densification rate. Around 1200°C, the onset of crystallization was identified for the microwave-processed samples, which was about 100°C lower than the conventional process. In *Region* III, the microwave interaction with the material was substantially reduced as a result of crystallization. This is an interesting phenomenon because it suggests that microwave absorption can be controlled by the structure, in addition to the composition.

Five objectives were proposed at the beginning of this investigation. All of them were successfully accomplished. A list of the main contributions provided by these objectives follows:

1. This study provided a detailed procedure for drying silica aerogel using a critical point dryer. Most existing literature showed a general procedure, but the procedure in this study specified temperature, pressure and heating rate to obtain monolithic silica aerogel samples with no cracking. Monolithic samples were obtained with no cracks, which allowed for better characterization and more consistent data.
2. A single mode microwave system was built and adapted to perform research. A control system was designed and built to obtain a precise variation of temperature and microwave power. In addition, a detailed description of the microwave components was provided so users could understand better the level of complexity required in the process system.

3. A procedure to perform temperature measurements in a single mode microwave oven was suggested. The procedure recommended infrared sensors or/and thermocouples. It was shown that this procedure could provide a foundation to perform reliable temperature measurements in multimode cavities.
4. A dielectric characterization system using the cavity perturbation technique was designed and built. This system was designed to work using a rectangular TE_{103} cavity. The system used coefficients that compensated for the non-uniformity of the electric field and the shape of the sample. Dr. Ronald Hutcheon[1] developed this analysis for a circular cavity and provided vital assistance during the development of the system used in this study.
5. This study provided reliable data of the structural evolution of silica aerogel. This data included the structural characterization in both systems, conventional and microwave. This information could be used as a tool to develop silica aerogel with different properties.

The present investigation combined two advance material processing techniques, sol-gel and microwave. The results obtained revealed that microwave- absorbed species (water and ethanol) introduced during sol-gel processing were still present after the drying stage. During subsequent heat treatments, the presence of these species favored the microwave interaction and contributed to a higher densification. If other microwave-absorbed species were introduced during sol-gel processing, the properties of silica aerogel could be modified, tailored, or controlled at a different temperature or frequency range. This is a significant phenomenon that can be used for better understanding of microwave interaction with gels and future development of materials.

[1] From Microwave Properties North, Canada.

CHAPTER VIII

Future Work

Microwave processing of sol-gel materials has the potential to improve the material properties or enhance processing relative to conventional methods. Characterization of microwave effects on the structure and chemistry could lead to a greater understanding of densification and kinetics in a variety of materials. However, a limitation in many studies on microwave processing of materials is that microwave-specific characterization equipment (characterization equipment using microwave heating) is usually non-existent. The development of these tools is important to produce scientifically grounded studies on the fundamental interactions between microwaves and materials. In addition, these tools could lead to scalable and more reliable production processes.

Although a significant enhancement in understanding of structural evolution has been achieved with this study, several questions have been raised that require further study: 1) What effect does the susceptor have in the structure evolution? 2) What role does closed porosity have in microwave-material interactions? and 3) Is there a microwave effect on viscosity?

As a continuation of this study, the research areas proposed include:

1. Susceptor effect and the relationship between microwave absorption and densification.

Composite glass powders that absorb sufficient microwave energy at room temperature could be designed to eliminate the use of a susceptor. Each powder should have a different level of

microwave absorption. Compacts of these powders can be made, and they can receive a heat treatment in single mode microwave and conventional ovens. Structural parameters could be measured to re-evaluate the cylindrical model (similar experiments used in this study) in a more controlled manner. The difference in densification could be correlated with the intensity of the electric field and a quantitative correlation could be established between microwave absorption and densification.

2. The role of closed porosity in microwave-material interactions.

Using one of the powders developed above, samples with near full densification (containing only closed porosity) could be prepared using conventional heating. Subsequently, these samples could be heat treated in a microwave oven at different temperatures. The microwave oven should be equipped with a power meter capable of measuring forward and reflected power, so power absorbed could be calculated. Structural parameters to obtain data about closed porosity, pore size, and pore shape should be measured. A correlation between power absorbed and structural parameters (shape, size, and distribution of pores) could be obtained. This information could provide more quantitative data to explain the microwave-interaction with the closed pores.

3- Is there a microwave effect on viscosity?

Powders (mentioned previously) of different particle sizes could be used to make compacts. Heat treatment could be applied to the compacts using conventional and microwave ovens at

different temperatures in *Region II*. Structure information should be measured to determine if the cylindrical model could be used. Viscosity could be calculated from the cylindrical model. This information would allow for evaluation of the effects of different particle size on viscosity, and the possible presence of a non-thermal effect produced by the microwave-interactions with the material.

APPENDIX A

Power absorbed inside a material

The power flow through a closed surface can be obtained from integration of the Poynting vector (P) [1, 2].

$$P = ExH \tag{A.1}$$

Where E = electric field

H = magnetic field

$$P = \int_S (ExH).dS \tag{A.2}$$

Using the divergence theorem, $$\oint_S \bar{A}.d\,\bar{S} = \oint_V \nabla.\bar{A}dV \tag{A.3}$$

Equation A.2 can be expressed as $$\oint_S (ExH).dS = \oint_V \nabla.(ExH)dV \tag{A.4}$$

Using the vector identity, $$\nabla.(\bar{A}\,x\,\bar{B}) = (\nabla x\,\bar{A}).\bar{B} - (\nabla x\,\bar{B}).\bar{A} \tag{A.5}$$

Then, Eq. A.4 becomes $$\oint_S (ExH^*).dS = \oint_V [(\nabla xE).H^* - (\nabla xH^*).E]dV \tag{A.6}$$

Maxwell's third law says that $\nabla xE = -jw\mu_o\mu' H$ (A.7)

Then, $(\nabla xE).H* = -jw\mu_o\mu' H.H*$ (A.8)

Maxwell's current law says that $\nabla xH = J + jw\varepsilon_o\varepsilon * E$ (A.8)

Knowing that $J = \sigma E$ (A.9)

Where, J = current density due to conduction effects

σ = conductivity of the medium

and $\varepsilon* = \varepsilon' - j\varepsilon''$ (mentioned in Eq. 3.17) (A.10)

Inserting Eq. A.9 and A.10 into A.8, Eq. A.11 is obtained.

$$\nabla xH = \sigma E + (w\varepsilon_o\varepsilon'' + jw\varepsilon_o\varepsilon')E = w\varepsilon_o(\frac{\sigma}{w\varepsilon_o} + \varepsilon'')E + jw\varepsilon_o\varepsilon' E \quad \text{(A.11)}$$

If $\varepsilon''_{eff} = \frac{\sigma}{w\varepsilon_o} + \varepsilon''$ as mentioned in Eq. 3.20, then Eq. A.11 becomes

$$\nabla xH = w\varepsilon_o\varepsilon''_{eff}E + jw\varepsilon_o\varepsilon' E \quad \text{(A.12)}$$

and $$(\nabla xH).E = w\varepsilon_o \varepsilon''_{eff} E.E^* - jw\varepsilon_o E^*.E \quad \text{(A.13)}$$

Inserting Eqs. A.7 and A.13 into Eq. A.6, the power flow through a closed surface can be expressed as

$$\oint_S (ExH^*).dS = \oint_V [(\nabla xE).H^* - (\nabla xH^*).E]dV =$$

$$-jw\int_V \mu_o \mu' H.H^* dV - \oint_V w\varepsilon_o \varepsilon''_{eff} E.E^* + jw\oint_V \varepsilon_o E^*.E \quad \text{(A.14)}$$

By definition, the average power is $$P_{AV} = -\frac{1}{2}\oint_S real(ExH^*).dS \quad \text{(A.15)}$$

Then, $$P_{AV} = \frac{1}{2} w\varepsilon_o \varepsilon''_{eff} \oint_V (E^*.E)dV \quad \text{(A.16)}$$

Equation A.16 shows the electric field in integral form, since in most of the cases, E is not a constant quantity and changes according to the position in the microwave cavity. If the electric field is assumed to be constant, then $E^*.E$ becomes E^2. The value E_{RMS} has been taken as the constant and average value of the electric field. Where, $E_{rms} = \frac{E_o}{\sqrt{2}}$ and E_o is the maximum that E takes in the volume analyzed. Thus Eq. A16 can be expressed as

$$P_{AV} = w\varepsilon_o \varepsilon''_{eff} E^2_{rms} V \quad \text{(A.17)}$$

APPENDIX B

Technical specifications of the main components of the microwave system.

Table B.1: Main components of the single mode microwave system.

Component	Manufacture	Specifications
Control power unit	Cober Electronics Inc.	SM 1545, 208V, 3 phases, 3KW
Generator	Cober Electronics Inc.	Magnetron CWM-4S, water cooled
Power interface	Made by the author	232 digital input, 120V
Circulator #1	Cober Electronics Inc.	Model: WG 284-3PC, 2450 MHz
Dummy load	GAE	Model: GA1201, 3KW incident power
Dummy load with power reflector	GAE	Model: GA1213, 3KW incident power
Impedance analyzer	MUEGGE	Model: Homer, MW-HMD 2450
Tuner	GAE	Model: GA100x, precision 3 stub tuner
Iris	Custom made by Los Alamos Laboratory	¼ x 1 in. aperture
Cavity	Custom made by Los Alamos Laboratory	WR 284 waveguide, 12 in long with 3 ports to measure electric signals.
Short circuit terminator	Microlab/FXR	Model: S630C
Power meter	Hewlett-Packard	Model: 435B
Prove sensor	Hewlett-Packard	Model: 8481A
Low temperature IR pyrometer	Heitronics	Model: KT15.82D, temperature range: 20-500°C
High temperature IR pyrometer	Heitronics	Model: KT15.01D, temperature range: 350-2000°C
IR pyrometer interface	Heitronics	Model: PSJB12 300 24
Thermocouple	Omega engineering	XCIB-K-1-4-3

APPENDIX C

Procedure for measuring frequency-power output relationship

As was explained in Chapter IV, Section 4.2.1, the impedance analyzer was used to measure reflected and forward power. If the reflected power (P_R) was minimum (almost zero), the forward power measured was almost equal to the output power of the generator.

To obtain $P_R \approx 0$, the iris and the tuner were removed from the system, and a water load was connected at the end of the cavity to absorb all the power applied. A schematic of the set-up used is shown in Fig. C.1. Having this set-up, the power output of the generator was applied gradually using the manual control, and frequency and power forward to the cavity were measured using the impedance analyzer. The measurements obtained are presented in Chapter V, Fig. 5.10.

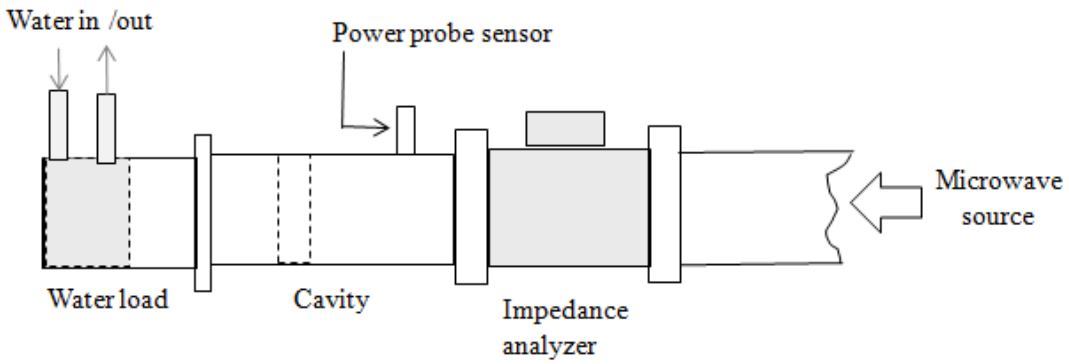

Fig. C.1: Set- up used to measure the variation of frequency as a function of output power of the generator.

APPENDIX D

Procedure to calibrate the power meter and convert its scale to V/m

A power meter was used to measure the electric field in the cavity at the position of the power probe sensor [3]. This meter had a scale to measure power (Watts), but to measure electric field, the power scale was converted into a scale to measure electric field (Voltage/meter). The set-up used was similar to the one described in Appendix C, and basically, this procedure was performed in two important steps, as follows:

1. Calibration of the power meter. Power was applied gradually to the cavity and was measured using the network analyzer and the power meter. This data is presented in Fig. D.1 which shows the power applied (measured by the network analyzer) on the *x* axes, and the power measured by the power meter through the power probe sensor and a 20dB attenuator on the *y* axes.
2. The power probe had a 20dB attenuator, so its measurements were converted to the dimension of the cavity power. This conversion was carried out using Eq. D.1 [4].

$$P_{out} = P_m 10^{(\frac{Att}{10})} \quad \text{(D.1)}$$

Where, P_{out} = actual power on the measured point

P_m = power measured (power measured by the power probe in this case)

Att = value of the attenuation produced to measure the actual power

For example, for a power applied to the cavity equal to 1500W, the power probe measured 2.85μW. Using Eq. D.1 and knowing that Att=20dB, the actual power where the sensor was placed was equal to 0.0285W.

1) The impedance of the cavity or waveguide was calculated using Eq. 3.40 for all the different levels of power applied in Fig. D.1. Table D.1 shows an example and the equations to complete this step.

Table D1: Example how the impedance of the cavity was obtained for a value of power applied.

Parameter	**Value**
Power applied	1500 W
Impedance characteristic of the medium (η, air)	377Ω
Cut-off frequency (calculated using Eq. 3.29)	2080 MHz
Frequency at the power applied (Obtained from Fig. 4.10)	2446.3 MHz
Impedance of the cavity (Z_{TE})	974.27Ω

2) Knowing the impedance of the cavity, the electric field was calculated using Eq. 3.39. A record of these calculations for different power applied to the cavity is shown in Fig. D.2.

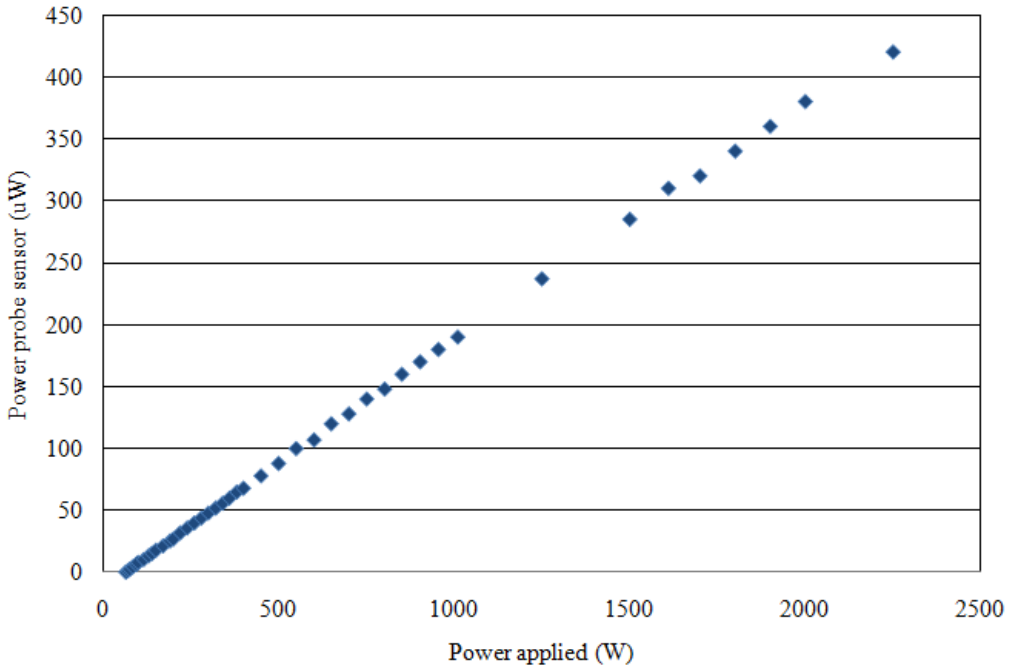

Fig. D.1: Power measured by the power probe sensor at different power levels applied to the cavity.

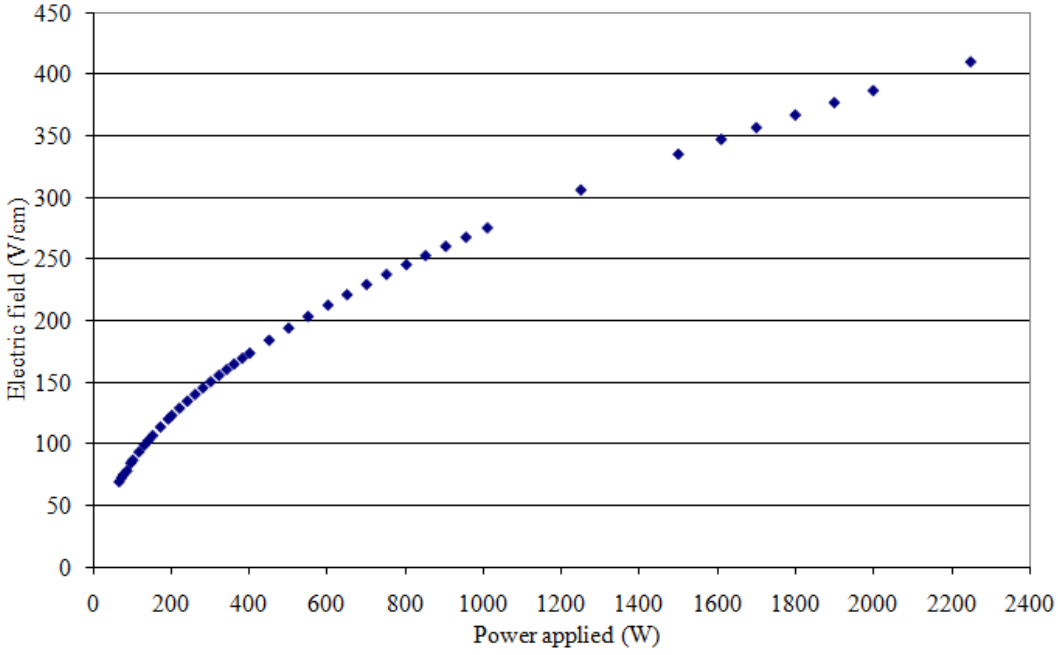

Fig. D.2: Electric field calculated for different powers applied to the cavity.

3) Having Figs. D.1 and D.2, the electric field for the power measured by the sensor can be obtained and is shown in Fig. D.3.

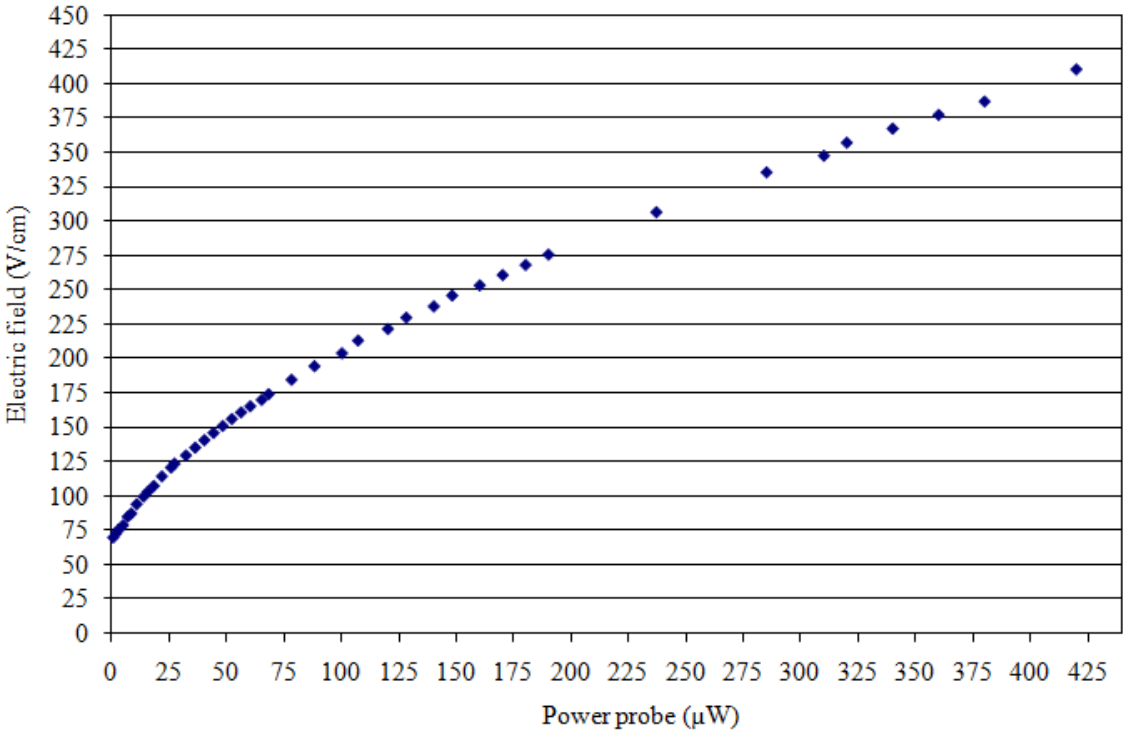

Fig. D.3: Electric field for the power measured by the power probe (sensor) on the cavity.

Knowing the data from Fig. D.3, the measurements provided by the power meter were converted into values of the electric field. It is important to point out that these measurements must be performed when the sensor (probe) is in the location shown in Fig. 4.12, and there was a 20dB attenuator connected to the sensor.

APPENDIX E

Temperature Measurements in a Microwave Cavity

E.1 Temperature measurements between conventional and microwave systems

One of the most difficult and important parameters to measure in a microwave cavity is temperature. Traditional temperature measurement techniques used in conventional ovens and furnaces may not provide the optimal solution for monitoring temperature in a microwave field. Concerns are based on the fact that comparisons between microwave and conventional processing results use a common temperature as the base parameter because data for materials processing are mainly presented as a function of thermal history. However, achieving accurate temperature measurements during microwave processing is challenging. The objective of this appendix is to provide a practical methodology for measuring temperature in a microwave environment.

When a sensor measures the temperature of an object in a system or specific environment, it indicates the thermal energy [5] level of the object. The object and the environment surrounding it are not necessarily at the same temperature. Furthermore, if the sensor causes a perturbation in the environment or vice versa, the information obtained by the sensor may not report or measure the correct temperature of the object. For example, an infrared pyrometer in a dusty room will have interference from the environment, or a thermocouple in a microwave cavity may experience an electrical discharge or "arc." Consequently, one of the keys to performing a reliable temperature measurement is to minimize or eliminate the interference caused between the system and the temperature sensor.

Since microwaves heat the sample itself rather than the entire cavity, as in conventional processing, temperature measurements must be performed directly on, in, or very close to the sample. Comparisons between conventional and microwave temperature measurements must be performed carefully. The physical location of the temperature measurements in the sample should be specified. When the surface temperature measured in both systems (conventional and microwaves) is the same, the internal temperature in the microwave-processed sample may be different. Consequently, comparisons should take these differences into consideration. To perform temperature measurements in a microwave environment, this appendix focuses on two types of temperature sensors: thermocouples (TC) and infrared pyrometers (IRP).

E.2 Thermocouples

Thermocouples are made from two dissimilar metals or metallic alloy wires connected at the tip, and their junction serves as the temperature device that converts a temperature difference into an electric signal known as the Seebeck voltage (V_s). Depending on the compositions of the wires, the junction produces different V_s. The Seebeck voltage-temperature relationship must be known in order to obtain the temperature (T) sensed at the junction. Approximation formulas for this relationship are presented in a polynomial form similar to [6]

$$T = A + BV_s + CV_s^2 + DV_s^3 + EV_s^4 \quad \text{(E.1)}$$

Thermocouple manufacturers usually provide tables with the Seebeck coefficients (A, B, C, D, E) and V_s to calculate T. However, electronic temperature readouts are the most common method used today. These instruments convert the TC signal into a temperature scale that can be read directly by the user.

Figure E.1 shows a schematic of a TC probe with some of the most common accessories. Every one of these parts is selected according to the temperature range and environment in which the probe will be used. The main component of the probe is the wire element, which is formed by the TC wires and the junction. The sheath and insulation provide protection to the element from chemical contamination, electrical interferences and mechanical shock. Table E.1 presents a summary of the materials (typical data) used for the parts of a TC. However, depending on the TC manufacturer, the compositions or temperature range of these materials may change.

E.2.1 Thermocouples in a microwave environment

Thermocouples are probably the most common temperature sensors used in materials research and manufacture. However, in a microwave cavity, there are several conditions that must be met to make reliable measurements:

1. Shielding and proper grounding improve the performance of this sensor, preventing electrical interference. Grounding may be the most important factor and should be performed in two locations: inside the sheath with the TC junction and outside the sheath, preferably with the microwave cavity. If the TC is not grounded inside, the signal could suffer some distortion from electrical noise. There are some electronic readouts that can deal with this problem. However, if the TC is not grounded outside, it may arc when the cavity receives the electromagnetic energy and providing a false and unstable signal.

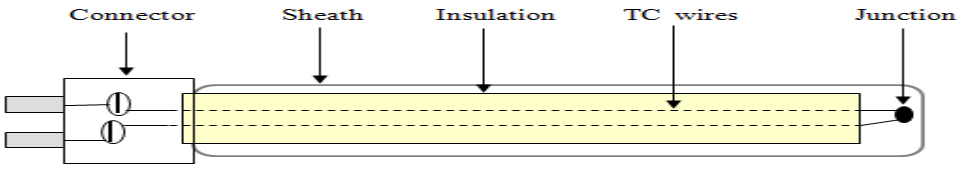

Fig. E.1: Schematic of thermocouple probe and common accessories.

Table E.1: Materials used in thermocouples parts [7].

I - Element Materials		
Element type	**Composition**	**Service Temperature**
N	Ni-14.2%Cr-1.4%Si / Ni-4.4%Si-0.1Mg	982 °C
K	Ni-Cr / Ni-Al	1100 °C
R	Pt 13%Rh / Pt	1450 °C
S	Pt 10%Rh / Pt	1450 °C
B	Pt 6%Rh / Pt 30%Rh	1700 °C
II - Sheath Materials		
Materials	**Max. Operating Temp.**	**Working Environment**
304, 310, 316, 312SS	900 °C	Oxidizing, inert, vacuum
Ni-Cr Alloy (Inconel 600)	1150 °C	Oxidizing, inert, vacuum
Pt-Rh Alloy	1650 °C	Oxidizing, inert
Tantalum	2300 °C	Vacuum
Molybdenum	2200 °C	Inert, vacuum
III - Insulation Materials		
Material	**Max. Operating Temp.**	**Approx. Melting Point**
Alumina	1450 °C	2010 °C
Magnesia	1650 °C	2790 °C
Hafnia	2500 °C	2830 °C

2. The thermocouple should not be in contact with the sample unless it is properly shielded. In conventional systems, the TC preferably should be set as close as possible to the sample, but in a microwave cavity, the TC could produce arcing due to a substantial difference of charge built-up on both surfaces that could damage the sample and/or the TC. If surface temperature is measured, arcing can be avoided by locating the TC approximately 3-6 mm from the target, at which a reliable temperature measurement still can be obtained. Other researchers have observed a similar distance range for positioning the TC from the sample [8].
3. Drift in the calibration of the TC is a common effect after several experiments are performed under a microwave field [7]. This phenomenon could be the product of thermal stresses and fatigue in the TC metals, producing changes in the properties of the TC wire materials and generating inaccurate readings.
4. A TC inside a microwave cavity always produces a perturbation in the field. However, the position of the TC can reduce perturbation of the electric field (***E***). The perturbation is even higher when the TC is placed at a location where ***E*** is parallel to the conductor, because electromagnetic boundary conditions in a microwave cavity require that ***E*** be normal to a metal body[2, 5]. For the same reason, the distortion of the field can be minimized if the TC is localized perpendicular to ***E***. In a multimode cavity, it is more difficult to identify the distribution of ***E***; however, some single mode cavities allow for positioning the TC in a place where it is perpendicular to ***E***, and the perturbation can be substantially reduced. Chapter IV, Section 4.4.1 shows a schematic (Fig. 4.15) with the TC positioned perpendicular to the electric field in a TE_{103} cavity. In addition, a perturbation of the field may produce a non-uniform temperature distribution in the

sample[9, 10]; consequently, it is recommended that measurements be carried out after the temperature has been kept constant for some time. In this investigation, the sample was soaked at the temperature programmed for 30 min.

5. Thermocouples can be used to measure internal temperature of the samples. When a TC is used inside a sample, it should be surrounded by a metal sheath. This sheath provides a smooth surface that produces a uniform distribution of $\boldsymbol{E}$ on the TC; more so than with only the two TC wires. Additionally, there is a concentration of $\boldsymbol{E}$ around the TC, but the sample acts as a shield, attenuating $\boldsymbol{E}$ and minimizing the effects of localized heating.

In addition, it is a common practice that the TC in conventional ovens and furnaces is located in a place far from the sample processed. It is assumed that the temperature in the entire chamber is uniform, but this is not always the case for all the temperature ranges and processing times. Consequently, comparison between different systems (conventional and microwaves) should verify that the temperature measured reflects the temperature on/in the sample.

One of the main advantages of using a TC is its relative low cost. When this sensor is used in a conventional system, a ceramic sheath can be used. However, at temperatures higher than 1200ºC in a microwave environment, a TC requires shielding using expensive high-temperature metals, such as platinum, molybdenum or tantalum, as observed in Section II of Table E.1.

E.3 Infrared sensors

Infrared sensors are non-contact devices for intercepting and measuring thermal radiation coming from an object to determine surface temperature. Primarily, they consist of an optical

system and a detector, as represented in Fig. E.2. The optical system focuses the energy coming from an object onto the detector, which is sensitive to the radiation in the IR range of frequencies. The output of the detector is then amplified and filtered. Once the processor receives the signal, it is transformed into an output that is proportional to the amount of energy radiated (W_λ) by the target for specific wavelengths (λ). The processor takes the signal from the filter and computes the temperature by using Planck's law (Eq. E.2).

$$W_\lambda = \frac{2\pi hc^2}{\lambda^5}\frac{1}{e^{hc/\lambda KT}-1} = \frac{C_1}{\lambda^5}\frac{1}{e^{C_2/\lambda T}-1} \qquad \text{(E.2)}$$

Where, c = speed of light = 3.00 x 10^8 m/s

C_1 = 3.74 x 10^{-16} W m^2

C_2 = 1.44 x 10^{-2} K m

h = Planck's constant = 6.63 x 10^{-34} J s

K = Boltzmann's constant = 1.38 x 10^{-23} J/K

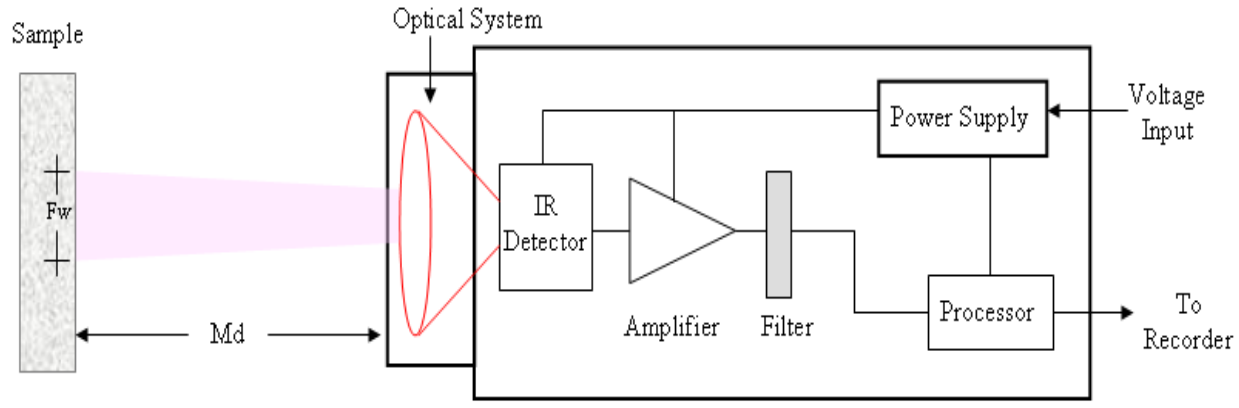

Fig. E.2: Typical representation of an IR sensor.

Figure E.3 shows a graphic illustration of Planck's formula as a function of λ at different absolute temperatures. It shows that increasing the temperature shifts the maximum energy radiated by a black body to a shorter wavelength. A black body is an ideal radiator, which absorbs all incoming radiation and shows neither reflection nor transmission [6]. As a result, the energy emitted is the same as that absorbed. Most of the correlations for describing the infrared energy are established using this concept.

By integrating the spectral radiation for all the wavelengths from 0 to infinity for a specific temperature in Fig. E.3, one can obtain the emitted radiation of a black body. This relationship is called the Stefan-Boltzmann law and is defined in Eq. E.3.

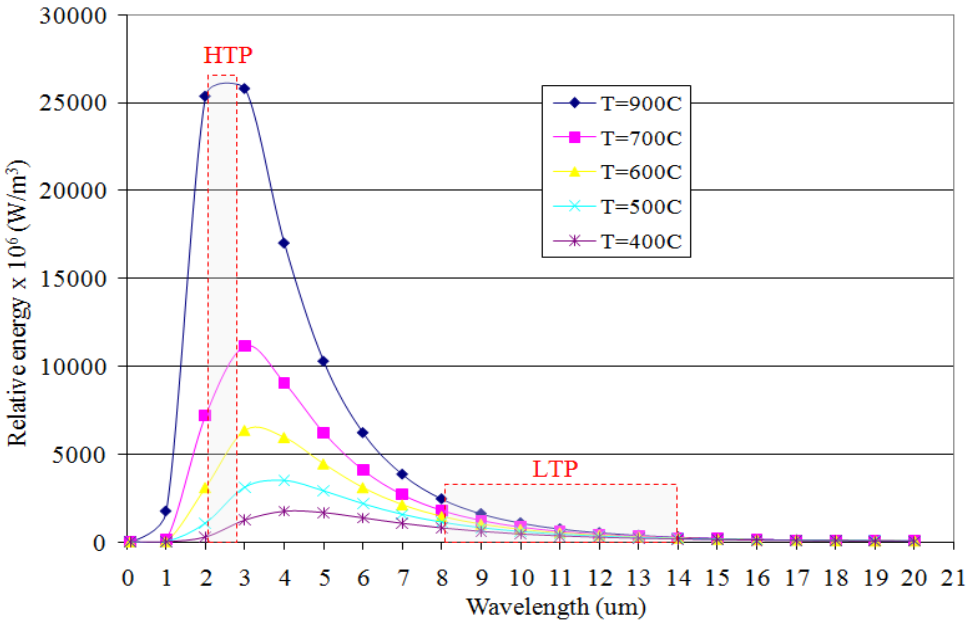

Fig. E.3: Planck's law spectral radiation representation where HTP and LTP point out the wavelength ranges over which the high-temperature and low-temperature pyrometers work (explained in Chapter IV, Section 4.4), respectively.

$$W_{\lambda} = \sigma T^4 \ [\text{Watt/m}^2] \tag{E.3}$$

Where, σ = Stefan-Boltzmann constant = 5.669x 10^{-8} Watt / K^4 m^2

The Stefan-Boltzmann law shows that the radiant energy over the entire wavelength range (area under a curve in Fig. E.3) increases to the fourth power of its absolute temperature and illustrates that temperature can be measured from the radiation signal. Infrared temperature sensors rely on this principle.

E.3.1 From black bodies to real objects

The IR range lies between 0.7 and 1000μm wavelengths. Infrared temperature sensors measure the energy radiated by an object in the 0.7 to 20μm wavelength range because above 20μm, the energy level is too low for detection.

Infrared sensors do not cover the entire spectrum. They use a narrow wavelength band, so the integration of Planck's equation lies between certain wavelengths (band of the sensor)[6, 11]. Additionally, the radiation detected comes from a material that is not a black body. Consequently, instead of σ in Eq. E.3, two constants are used. One depends on the material and the other depends on the detector used. Therefore, the equations that describe the output $W_{(T,\lambda)}$ of an IR temperature sensor are in the form of Eq. E.4 [12].

$$W_{(T,\lambda)} = \varepsilon_m k T^N \tag{E.4}$$

Where, ε_m = emissivity of the material

k = device specific constant

N = exponent that depends on the T and λ range used

Equation E.4 introduces a new concept, emissivity, which is a fundamental property of a material under optimal conditions, such as perfectly flat even on a molecular scale, free of oxide coating, no porosity, or any other physical or chemical features that would alter its properties. For such a perfect material, ε_m is defined as the ratio of the thermal radiation emitted by the material's surface (W_{NB}) to that of a black body (W_{BB}) at a given T and λ, as expressed in Eq. E.5.

$$\varepsilon_m = \frac{W_{NB}}{W_{BB}} \tag{E.5}$$

Since a black body is an ideal radiator, $\varepsilon_m = 1$. However, real materials are not ideal radiators, so $\varepsilon_m < 1$ and they are known as non-black bodies (NB). Non-black bodies are divided in two categories, gray bodies (GB) and non-gray bodies (NG). Gray bodies are NB with ε_m constant, and NG are NB for which their ε_m changes at different wavelengths in the electromagnetic spectrum [13], as shown in Fig. E.4.

Most of the materials do not meet the optimal conditions under which emissivity must be obtained, so the ratio of the radiation emitted by them to that of a black body is known as emittance (e_m). It has the same form of ε_m, but e_m is coming from a real body as it exists with oxide coating, curvature, imperfect surface, or other conditions. Most cases deal with emittance rather than emissivity, and much of the data tabulated in the literature as emissivity is, in fact, emittance [6, 14].

It is crucial to properly determine the e_m of the material being studied to obtain temperature from radiant energy measurements. Moreover, the e_m obtained for a material must be used with caution, because it may not work consistently for the same material under different conditions (i.e. shape, environment, porosity). It is important to keep in mind that accurate e_m values from different samples (same material) are difficult to achieve. However, precise e_m values that still provide reliable temperature measurements are possible.

In this document, the ε_m concept is used to explain the theoretical relationships for IR temperature measurements. However, the reader must know that, for experiments performed, emittance is the appropriate concept for the samples used.

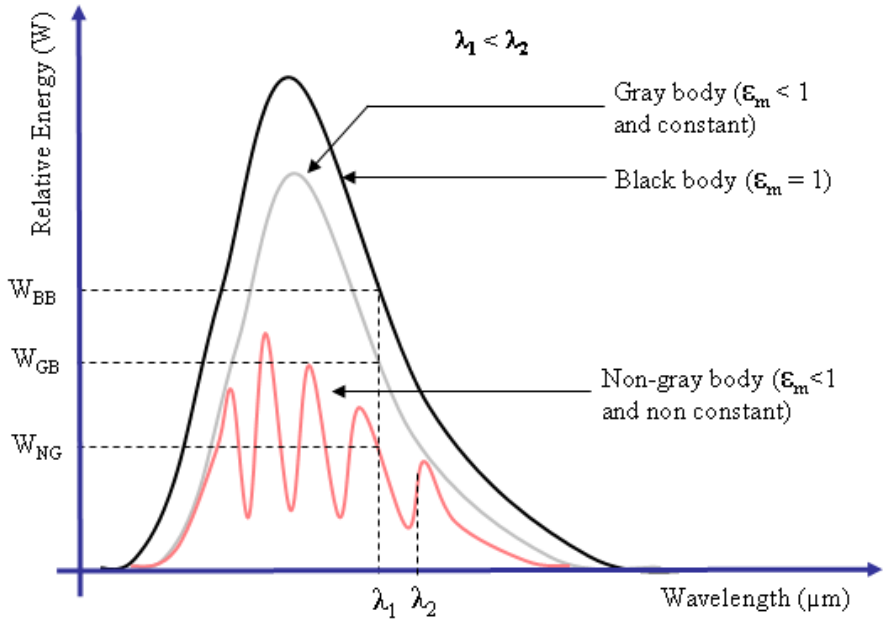

Fig. E.4: Spectral distribution of different optical bodies.

E.3.2 Single- and dual-color infrared pyrometers

Common IRPs are designated as single-color and dual-color based on their mode of operation. Single-color pyrometers determine the temperature by measuring the energy emitted by a material at a single wavelength (in reality, the IR sensors detect a small range where the target frequency is the central frequency) in the infrared spectrum. To perform this task, this pyrometer requires the ε_m value. The ε_m required is the one at the wavelength used by the IRP and at the temperature of the sample (target). A dual-color IRP measures the energy emitted at two different wavelengths. This pyrometer requires the ratios of the emissivities at both wavelengths ($\varepsilon_R = \varepsilon_{m1} / \varepsilon_{m2}$). This sensor design is based on the ratio of the sample's energy at two different wavelengths obtained using Planck's equation, and is discussed extensively in the literature [11, 15]. If the ε_m is the same at both wavelengths (GB), $\varepsilon_R = 1$ and the temperature provided by the dual-color IRP can be determined directly from the sensor. However, if the emissivities at both wavelengths are different (NG), ε_R or both emissivities must be known so the temperature can be recorded. If the dual-color pyrometer uses two close wavelengths, ε_R is approximately equal to one and the temperature will be more accurate. This design works well for some temperature ranges of the NG, but not in all cases. Because of the restrictions with using the dual IRPs, a common misunderstanding is that this pyrometer does not need ε_m or ε_R data, and that the temperature can always be obtained directly. An advantage of the dual-color pyrometer is that interference in the path between the sample and the sensor usually affects the measurements similarly at both wavelengths and, consequently, does not change the results [15].

E.3.3 Multi-wavelength pyrometers

During the early 1990s, a new group of pyrometers known as multi-wavelength pyrometers was conceived at the National Institute of Standards and Technology (NIST, USA) [16]. As an analogy with the two-color pyrometer, the multi-wavelength pyrometer measures the temperature at several wavelengths. The method used by this pyrometer is described in the literature [17-19], which consists of obtaining the true temperature of a body (T_t) by using an equation (Eq. E.6) derived from Wien's law.

$$T_t^{-1} = T_c^{-1} - \left(\frac{\lambda_i}{C_2}\right) ln\varepsilon_{m(\lambda)} \tag{E.6}$$

Where, T_c = calculated temperature

λ_i = wavelengths

$\varepsilon_{m(\lambda)} = a+b\lambda+c\lambda^2+\ldots m\lambda^n$ = emissivity function (E.7)

The emissivity is expressed as a function of the wavelength and is called the emissivity function. This function has coefficients (a, b, c,…m) that are obtained by measuring the IR intensities at a number of wavelengths. Therefore, ε_m can be known at a specific λ_i and a temperature can be calculated (T_c) for every single wavelength used by the pyrometer. From Eq. E.6, it can be seen that, if $\lambda_i \rightarrow 0$, then $T_t \rightarrow T_c$, as illustrated in Fig. E.5. Consequently, the true temperature can be obtained by extrapolating to $\lambda=0$. In this way, the effect of the unknown emissivity is reduced as the wavelength approaches zero.

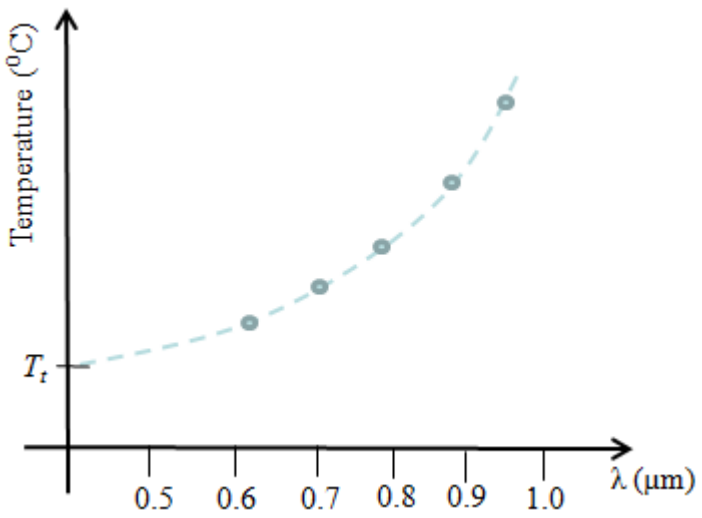

Fig. E.5: Temperature vs. wavelength that shows T_t at λ=0.

One of the limitations of multi-wavelength pyrometers with non-gray targets is that the analytical process of extrapolating data at relatively long wavelengths to zero (where there is significant energy to measure it) could be inaccurate. Nevertheless, Donnan and Samandi [20] showed a comparison between different temperature measurement methods inside a microwave cavity using a thermocouple, two-color pyrometer and multi-wavelength pyrometer. Their results suggested that multi-wavelength pyrometers provide an accurate alternative for measure temperature in a microwave environment. This type of pyrometer was not used in the present study because it was not commercially available.

E.3.4 Infrared pyrometers in a microwave environment

Infrared pyrometers offer advantages for performing temperature measurements in a microwave cavity, especially because they do not need to be located inside the cavity. Pyrometers that measure surface temperature can be used from room temperature to temperatures greater than 1300ºC and do not require close proximity to the sample, but some important parameters must be considered when using these sensors:

1. Field of view of the pyrometer (F_w). This parameter is defined as the area over which the sensor measures the temperature and is determined by the distance from the sensor to the sample (M_d), as shown in Fig. E.2. The field of view usually changes as M_d changes, and it must be less than the size of the target to ensure that background or/and other interference do not provide false readings.
2. Surface of the sample. Measurements on samples of the same material with different surface finishes may provide different readings [21]. For some materials, measurements may differ throughout thermal cycling of the same samples. This phenomenon could be due to changes in surface area and topography of the sample after a thermal treatment.
3. Environment surrounding the sample and the sensor. Gases, dust, smoke, vapor, suspended matter, and light from ambient radiation in the transmission path between the target and the sensor can result in false measured values.
4. Emissivity or emittance data. Most of the infrared sensors require ε_m data for the material. This data should specify temperature and wavelength ranges. The lack of ε_m data for many materials is one of the significant limitations to using this technique.

Furthermore, researchers have found differences in structure and distribution of energy for some materials at the same temperature in conventional and microwave systems [22, 23]. Consequently, emittance, the property of the material used by the IR sensors, could be different in both systems. It is recommended that this property be measured in situ on the system under study.

As microwave processing of materials plays a more important role in many industrial applications, and IRPs provide the advantages of not perturbing the field neither affecting the target, it becomes more apparent that ε_m data is crucial [19, 24]. Consequently, it is important to know or develop a procedure for measuring this value.

The recommendations suggested in this chapter were applied when measuring temperature in the experiments described in Chapter IV. Many of these recommendations also apply to measurements in conventional systems. Based on this brief review of temperature measurements in a microwave environment, is implied that this operation is a non-trivial procedure and must be reported in detail for validation of the results.

APPENDIX F

Permissions

F.1- Permission granted to use Fig. 2.4

October 27, 2008

Carlos Eduardo Folgar
509-2 Essex Ct.
Blacksburg, VA 24060

Dear Carlos:

Per your request, I am pleased to hereby grant permission allowing you to copy and use for your doctoral dissertation any all information contained in the technical paper titled "Drying Silica-Gel Using Microwaves" as published by the Microwave Working Group, Ltd. in the *Proceedings of the Fourth World Congress on Microwave and Radio Frequency Applications*, R.L. Schulz and D.C. Folz, editors, ISBN:0-97862222-0-0.

This permission extends to any future revisions and editions of your dissertation, including non-exclusive world rights in all languages, and to the prospective publication of your dissertation by UMI Company. These rights will in no way restrict republication of the material in any other form by the MWG, Ltd. or by others authorized by the MWG, Ltd.

Regards,

John F Gerling
Treasurer
The Microwave Working Group, Ltd.

F.2- Permission granted to use Fig. 2.6

From: Essenpreis, Alice, Springer DE
To: cfolgar@vt.edu
Subject: AW: Permission to publish an excerpt
Date: Monday, November 23, 2009 9:01:49 AM

Dear Mr. Folgar,

With reference to your request (copy herewith) to re-use material on which Springer controls the copyright, our permission is granted free of charge, on the following conditions:

* it concerns original material which does not carry references to other sources,
* if material in question appears with credit to another source, authorization from and reference to that source is required as well,
* permission is also obtained from the author (address is given on the imprint page or with the article);
* allows you non-exclusive reproduction rights throughout the world,
* permission includes use in an electronic form, on the condition that content is
  - password protected,
  - at Intranet or
  - in CD-ROM/E-book;
* full credit (book title, volume, year of publication, page, chapter/article title, name(s) of author(s), figure number(s), original copyright notice) is given to the publication in which the material was originally published by adding: With kind permission of Springer Science+Business Media.

Permission free of charge does not prejudice any rights we might have to charge for reproduction of our copyrighted material in the future.

With best regards,

–

Alice Essenpreis
Springer
Rights and Permissions

F.3- Permission granted to use Fig. 3.3

Goldweber, Paulette - Hoboken

From: PermissionsUS@wiley.com on www.wiley.com [webmaster@wiley.com]
Sent: Tuesday, November 17, 2009 7:11 AM
To: Permissions - US
Subject: Republication/Electronic Request Form

A01_First_Name: Carlos
A02_Last_Name: Folgar
A03_Company_Name: Virginia Tech
A04_Address: 2000 Broken Oak Dr
A05_City: Blacksburg
A06_State: VA
A07_Zip: 24060
A08_Country: USA
A09_Contact_Phone_Number: (540)808-6729
A10_Fax:
A11_Emails: cfolgar@vt.edu
A12_Reference:
A13_Book_Title: Principles of electronic ceramics
A40_Book_or_Journal: Book
A14_Book_Author: L.L. Hench & J.K. West
A15_Book_ISBN: 0-471-61821-7
A16_Journal_Month: NA
A17_Journal_Year: NA
A18_Journal_Volume: NA
A19_Journal_Issue_Number: NA
A20_Copy_Pages: Pag. 192, Fig. 5.4
A21_Maximum_Copies: only the Fig. 5.4
A22_Your_Publisher: Virginia Tech
A23_Your_Title: Microstructure Evolution of Silica Aerogel under a Microwave Field
A24_Publication_Date: 2010
A25_Format: WWW
A41_Ebook_Reader_Type:
A26_If_WWW_URL: www.vt.edu
A27_If_WWW_From_Adopted_Book:
A28_If_WWW_Password_Access: Yes
A45_WWW_Users: Virginia Tech community
A29_If_WWW_Material_Posted_From: permanet
A30_If_WWW_Material_Posted_To: permanet
A42_If_Intranet_URL: www.vt.edu
A32_If_Intranet_From_Adopted_Book:
A33_If_Intranet_Password_Access: Yes
A48_Intranet_Users: Virginia Tech community
A34_If_Intranet_Material_Posted_From: Permanent
A35_If_Intranet_Material_Posted_To: permanent
A50_If_Software_Print_Type:
A60_If_Other_Type:
A37_Comments_For_Request: I request a permission to reprint in my PhD dissertation an excerpt (Fig 5.4 in Pag 192)from the book Principles of Electronic Ceramics. Please send me the autorization to publish this excerpt as soon as possible.

PERMISSION GRANTED
BY: _____
Global Rights Dept., John Wiley & Sons, Inc.

NOTE: No rights are granted to use content that appears in the work with credit to another source

References for the appendices

1. Balanis, C.A., *Advanced Engineering Electromagnetics*. 1989. NY: John Wiley & Sons Inc.
2. Pozar, D.M., *Microwave Engineering*. 2005. Amherst, MA: John Wiley & Sons, Inc.
3. Roussy, G. and J.A. Pearce, *Foundations and Industrial Applications of Microwaves and Radio Frequency Fields*. 1995. West Sussex, England: John Wiley & Sons Ltd.
4. Scott, A.W., *Understanding Microwaves*. 1993. New York, New York: John Wiley & Sons, Inc.
5. *Microwave Processing of Materials*. Committee on Microwave Processing of Materials. 1994. Washington, D.C.: National Academy Press.
6. Mcgee, T.D., *Principles and Methods of Temperature Measurements*. 1988. Ames, Iowa: John Wiley & Sons, Inc.
7. Company, H.P., *Practical Temperature Measurements*, in *The Temperature Handbook*. 2004. Omega Engineering Inc.: Stamford, CT. p. Z-19 - Z-32.
8. Moore, J.M., *Microwave Firing of Low-Purity Alumina*, *Ph.D. Dissertation in Materials Science and Engineering*. 1999. University of Florida: Gainesville, Florida.
9. Pert, E., et al, *Temperature Measurements during Microwave Processing: The Significance of Thermocouple Effects.* Journal of The American Ceramic Society, 2001. **84**(9): p. 1981-1986.
10. Grellinger, D.J. and M.A. Janney, *Microwave Measurements in a 2.45GHz Microwave Furnace*, in *Microwaves: Theory and Application in Materials Processing II*, David E. Clark, Wayne A. Tinga, and Joseph A. Laia., Editors. 1993. American Ceramic Society: Westerville, Ohio.
11. Lawton, B. and G. Klingenberg, *Transient Temperature in Engineering and Science*. 1996. New York, New York: Oxford University Press.
12. Micro-Epsilon, *Basic of noncontac temperature measurement*. 2005: Raleigh, North Carolina.
13. Gruner, K.-D., *Principles of Non-Contact Temperature Measurement*. 2003. Raytek Corporation.
14. Nicholas, J.V. and D.R. White, *Traceable Temperatures*. 2001. West Sussex, England: John Wiley and Sons Ltd.
15. Benton, R.D. and P.-R. Jang, *A Multi-Sensor Two Color Pyrometer.* American Institute of Aerospace and Astronautics, 1993.
16. Cezairliyan, A., G.M. Foley, M.S. Morse, and A.P. Miller, *Six-wavelength millisecond-resolution pyrometer.* Temperature: Its measurements and control in science and industry, 1992. **6**(2): p. 757-762.
17. Michalski, L., K. Eckersdorf, J.Kucharski, and J. Mcghee, *Temperature Measurement*. 2001. Chichester, England: John Wiley & Sons Ltd.
18. Dewitt, D.P. and G.D. Nutter, Editors. *Theory and Practice of Radiation Thermometry*. 1988. John Willer & Sons, Inc.: New York, New York.
19. Neuer, G., L. Fiessler, M. Groll, and E. Schreiber, *Critical analysis of the different methods of multiwavelength pyrometry.* Temperature: Its measurements and control in science and industry, 1992. **6**(1): p. 787-789.
20. Donnan, R.S. and M. Samandi, *A critical assessment of thermometric accuracy during microwave sintering of engineering ceramics*, in *Microwaves: Theory and Application in*

Materials Processing V, David Clark, Jon Binner, and David Lewis, Editors. 2000. The American Ceramic Society: Westerville, Ohio. p. 363-370.
21. Metaxas, A.C. and R.J. Meredith, *Industrial Microwave Heating*. 1983. London, United Kingdom: Peter Peregrinus Ltd.
22. Zhong, J.P., et al, *Microwave Densification of Porous Silica Gel*, in *Microwaves: Theory and Application in Materials Processing II*, Clark David, Wayne Tinga, and Jr. Joseph Laia, Editors. 1993. The American Ceramic Society: Westerville, Ohio.
23. Roth, M.D., et al, *Vibrational Spectroscopy of Silica Sol-Gel Components During Microwave Irradiation*, in *Microwaves:Theory and Application in Materials Processing III*, Diane Folz David Clark, Steven Oda, Richard Silberglitt, Editor. 1995. The American Ceramic Society: Westerville, Ohio.
24. Blair, G.R., *Determination of Spectral Emissivity of Ceramic Bodies at Elevated Temperatures.* Journal of The American Ceramic Society, 1960. **43**(4): p. 197-203.